VALVE REGULATED IMPLANTABLE INTRATHECAL DRUG DELIVERY FOR CHRONIC PAIN MANAGEMENT

By

Allan T. Evans

A dissertation submitted in partial fulfillment
of the requirements for the degree of
Doctor of Philosophy
(Electrical Engineering)
in The University of Michigan
2010

Doctoral Committee:

Professor Yogesh B. Gianchandani, Chair
Professor Kevin K. Tremper
Professor Kensall Wise
Associate Professor Euisik Yoon
Assistant Professor Srinivas Chiravuri

DEDICATION

To my family

ACKNOWLEDGEMENTS

I would like to give my utmost thanks to my advisor, Professor Yogesh Gianchandani, for giving me the opportunity to work on the exciting project and also for his teaching, guidance, and support. I also thank my committee members, Prof. Wise, Prof. Yoon, Prof. Tremper, and Prof. Chiravuri for their interest and valuable insights in various aspects of this work.

I also would like to express my thanks to Prof. Klein and Prof. Nellis and their students, Ryan Taylor, Tyler Brosten, Kristian Rasmussen, and Nick Guldan at University of Wisconsin at Madison for their contribution in numerical modeling related to this work. I am thankful to many former Ph.D. students in my group, Dr. Kabir Udeshi, Dr. Kenichi Takahata, Dr. Bhaskar Mitra, Dr. Scott Wright, Dr. Scott Green, Dr. Mark Richardson, Dr. Tao Li, Dr. Weiben Zhu, and Dr. Amar Basu, who have helped me with my research. I would like to especially thank my mentor and collaborator, Dr. Jong Moon Park for his symbiotic efforts and guidance in the early stages of my career. I also thank all my friends and colleagues in my group and SSEL for their companionship, support, and encouragement: Christine, Naveen, Karthik, Jae Yoong, Heidi, Tzeno, Kevin King, Bobby, John Brown, Emine, Ed, Neil, Pat Shea, Scott Hanson, Andy, Razi, Sang-Hyun, Ruba, Jay, SangWon, Hanseup, and many others.

I would like to acknowledge the SSEL, WIMS, and Lurie Nanofabrication Facility (LNF) staff members for keeping everything running, tolerating me, and making the cleanroom a safe and enjoyable place to work.

Finally, I want to thank my parents and my brother and sisters for their endless love and support without which I would never have written this.

TABLE OF CONTENTS

List of Figures

List of Tables

List of Appendices

ABSTRACT

VALVE REGULATED IMPLANTABLE INTRATHECAL DRUG DELIVERY FOR CHRONIC PAIN MANAGEMENT

By

Allan T. Evans

Chair: Yogesh B. Gianchandani

Chronic pain afflicts an estimated 100 million people in the United States with annual costs exceeding $100 billion. Treatment modalities for severe chronic pain include implantation of an intrathecal drug delivery device (IDDD). Conventionally, these devices are of two types: passive, permitting the delivery of a single analgesic mixture at a fixed rate; or active, permitting variable delivery by virtue of a peristaltic pump. This thesis presents an implantable system for medication delivery from multiple reservoirs with micromachined components. These components permit the use of an architecture that can provide superior volume efficiency and permit complex multi-drug delivery protocols. The system comprises three main components: regulatory valves, pressurized reservoirs, and control electronics. Important design considerations for each of these components are emphasized.

Piezoelectric microvalves were designed and tested for use with aqueous flows. Two types of spring pressurized reservoirs were also designed and tested for feasibility in an IDDD. Reservoirs were pressurized using springs fabricated from silicon and generated up to 80kPa of pressure. Alternative reservoirs were pressurized using compressive metal springs and generated up to 18kPa of pressure.

A first-generation system was developed that demonstrated controlled diffusion into agar gel. Water flow was regulated from 0.2-5mL/day, and bolus delivery was demonstrated. A second-generation system utilizing a two-valve manifold with embedded sensors was used to independently regulate isopropyl alcohol flow at set rates between 0.05-1mL/hr. Both systems demonstrated liquid delivery at intrathecal flow rates using continuous and duty-cycle flow regulation. Outlet pressure sensors were used to detect acute catheter occlusions and disconnects. A smart refill port was developed to allow for power transfer rates necessary to recharge batteries during a reservoir refill session. Recharging at current rates up to 500mA was demonstrated.

The proposed valve-regulated architecture and two preliminary prototypes allowed evaluation of potential solutions to challenges for application of the architecture in an IDDD. Recommendations for future systems and plans for bench-top and *in vitro* testing are detailed. The proposed work may lead to a system that provides the functionality of commercially available implantable drug delivery devices with high volume efficiency, and the ability to independently regulate multiple medications.

CHAPTER 1:
INTRODUCTION

The focus of this work is the development of a new drug delivery system for the treatment of severe chronic pain. The work is motivated by the need to advance treatment for a condition that has wide ranging impact on all levels of society. Chronic pain afflicts an estimated 100 million people in the United States with annual costs exceeding $100 billion [JCT99, Phi03]. The continuum of treatment modalities for severe chronic pain may include implantation of an intrathecal drug delivery device (IDDD) [Win96, Wer05, Sch06, Rau03, Deer07]. The system level design aspects of these devices have remained relatively unchanged for over 20 years. An IDDD that allows active control of the delivery rate is comprised of several components like a battery, a peristaltic pump, and control circuitry that occupy a significant portion of the system volume. The inclusion of these components reduces the ratio of the medication in the system as compared to the volume of the system itself; this is considered the volume efficiency ratio (VER). A system implemented using throttles to regulate flow from drug reservoirs allow for systems with greater volume efficiency (~70%) than current architectures (~30%). Improvements in the VER of an IDDD will allow for systems that have the functionality and drug volume of current solutions in a housing that is half the size.

Delivery of multiple drugs into the intrathecal space is utilized in clinical practice when mono-drug therapy with opioids fails, either due to tolerance, opioid non-

responsiveness (neuropathic pain) and/or hyperalgesia [Has04, Kra99]. Current practice consists of mixing multiple drugs in a single chamber for simultaneous delivery into spinal fluid [Rai07, Gra01, And99]. This imposes limitations on the type and concentration of drugs that can be administered. A system with multiple independently regulated drug reservoirs may permit combination therapy in a manner that will improve drug synergistic effects. This method of combination therapy also limits side effects because it uses the lowest possible doses of each drug. A multiple reservoir design can improve analgesic efficacy, reduce cost and improve patient satisfaction [ASH00]. The primary goal of this research is the development of a volume efficient IDDD with the capacity for multi-drug protocols that could allow further study of clinical pain treatment with combination therapy.

In section 1.1, the benefits and limitations of various chronic pain management techniques are discussed. Section 1.2 describes advantages and disadvantages of various implantable drug delivery devices and their topologies with regard to intrathecal delivery. In section 1.3, the focus of the current and proposed work is discussed. Additionally, past work in valve regulation is highlighted with a view toward application in implantable drug delivery.

1.1 Chronic Pain Management Techniques

1.1.1 Overview of Chronic Pain

Although pain is a symptom of many diseases, it might be regarded as the primary disorder in conditions such as migraines, trigeminal neuralgia and other forms of nerve damage. In these conditions, pain is the overwhelming predominant symptom. The

International Association for Study of Pain (IASP), a body concerned with pain research and clinical management of pain, has classified at least 600 types of pain syndromes. The IASP also defines pain based on its duration: acute being less than one month, subacute lasting one to six months, and chronic lasting six months or more. Pain is generally catergorized as being either harmful stimulus induced in sense receptors or the nervous system (nociceptive pain) or pain not related to the activation of pain receptor cells (neuropathic). Common types of chronic pain include back pain, headaches, arthritis, cancer pain, and neuropathic pain resulting from nerve injuries.

Neuropathic pain is caused by actual damage or altered function of nerves or nerve pathways. Neuropathic pain is most often described by patients as electrical-like sensations. Examples of these pathological changes that may cause chronic pain include the sensitization of nociceptors, central sensitization (or "wind-up"), abnormal sympathetic somatic nervous system interactions, and abnormal activation of N-methyl-D-aspartate (NMDA) receptors. Some common examples include failed back syndrome, neuralgias, neuropathies, etc.

Nociceptive pain is defined as pain mediated by nociceptors, widely distributed in the soma of the body. The pain is often described by patients as a dull, aching, sharp, or throbbing pain. Nociceptive pain is often responsive to opioid therapies, whether delivered orally, parenterally, or spinally. Examples include bone pain (fractures, arthritis, metastatic).

1.1.2 Impact and treatment of Chronic Pain

Comprehensive management of chronic pain involves multiple medical disciplines which often use pharmacological and non-pharmacological methods [Rai07, Tur07]. When pain is not well controlled with oral pain medications, or if a patient develops side effects, treatment options like intrathecal drug delivery are considered [Kra97].

The continuum of care pain therapy ranges from conservative to more advanced treatments. Conservative non-invasive options include use of various medications (non-steroidal anti-inflammatory drugs, muscle relaxants, opioids), physical therapy, and psychological counseling. Not all patients respond to these measures; some require more advanced treatment like nerve blocks, steroid injections, neurolysis, neurostimulation and intrathecal drug delivery devices.

Intrathecal drug delivery is a safe and effective therapy for well selected patients [Erd06]. It improves spastic symptoms, provides pain relief, reduces drug-related side effects, decreases the need for oral analgesia, and enhances quality of life in a segment of chronic pain patients whose pain has not been controlled with more conservative therapies [Lik06]. The benefits of IDDDs include potent analgesic response with stable therapeutic drug levels, decreased latency, increased duration of action, and decreased pharmacological complications like sedation, constipation, nausea and vomiting.

1.1.3 Current Implantable Intrathecal Drug Delivery Technology

Implantable pain pumps function by delivering medication into the cerebrospinal fluid (CSF) that is in the intrathecal space (Figure 1-1). Pumps are significantly more efficient then other forms of medication delivery because they have a direct path into the CSF. Drug pumps require about $1/300^{th}$ of the amount of medication used in oral

delivery to achieve the same level of analgesia. The central action on opioid receptors of the substantia gelatinosa of Rolando allows intrathecal opioids to significantly affect pain anywhere inferior to the cranial nerves. These medications have a low coefficient of distribution in lipids and do not cross the blood-brain barrier; resulting in prolonged action. This is a major advantage for patients who require higher order mental faculties and control.

Current pumps generally range from 100-180 cm^3, contain a single reservoir, and are implanted beneath the skin of the abdomen. A catheter is connected to the pump and is inserted into the spine. The implantation is done in an operating room under sterile conditions. A new catheter is inserted into intrathecal space. The catheter tubing is tunneled underneath the skin to the abdomen where it is connected to the implanted pump. A 4-6 inch incision is made in the abdomen, and a cavity for the pump is made between the patient's skin and muscle tissue. The pump is connected to the catheter, placed inside this cavity, and sutured to the fascial tissue above the stomach muscles. The entire operation generally takes 2 to 4 hours.

Fig. 1-1: The intrathecal pump is implanted in an abdominal pocket and the catheter is subcutaneously routed around the side, up the back, and inserted into the intrathecal space.

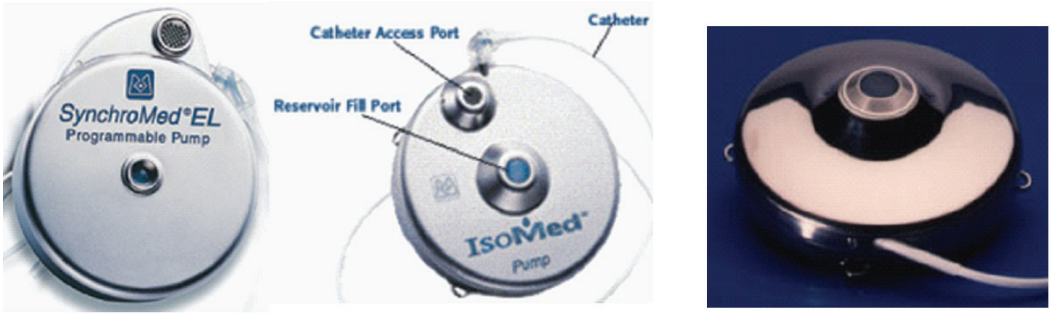

Fig. 1-2: Left: The SynchroMed EL made by Medtronic. Center: The IsoMed intrathecal pump made by Medtronic. Right: The CODMAN 3000 continuous flow pump manufactured by Codman. [Med08]

Several companies have developed intrathecal implantable pumps (Figure 1-2), the specifications of which are summarized in Table 1-1. IsoMed from Medtronic and the CODMAN 3000 series do not require a battery, provide long implant life, and require fewer replacement surgeries than active pumps. However, the flow rate is restricted to one of a few default delivery rates, and the only method of adjusting dosing after implantation is to alter the concentration of the medication. The SynchroMed is the most versatile system in terms of programmability. It uses a peristaltic pump controlled by microprocessor that can be programmed for infusion mode (bolus, multi-step bolus, continuous, etc.) and delivery rate depending on patient needs. The battery life is dependent on the infusion rate, but it exceeds three years at a delivery rate of 1.5 mL/day.

Table 1-1: Comparison of current commercial intrathecal implantable pumps.

	SynchroMed II	**SynchroMed EL**	**IsoMed**	**CODMAN 3000**
Manufacturer	Medtronic	Medtronic	Medtronic	Codman
Volume (cm^3)	91, 121	123, 156.7	111.7, 135,172	94, 219.3
Weight (empty, g)	165, 175	185, 205	113, 116, 120	98, 173
Reservoir Size (mL)	20, 40	10, 18	20, 35, 60	16, 50
Battery Life	5-7 years	5-7 years	No battery	No battery

The most effective pain relief generally comes from drug combinations. This is typically a mix of an opiod, like morphine, and a local anesthetic. Providing combination therapy is very challenging because single reservoir pump technology requires manually

mixing of the medications. This has to be done at a pharmacy under the physician's direction before the mixture can be injected into the refill port of the intrathecal pump. Not all pharmacies do this because of issues like the lack of a clean room facility, liabilities associated with unknown long-term drug stability, and unknown interactions mixed medications may undergo between implant refills. Additionally, any change in the delivery ratio of the mixed medications requires the pump and the delivery catheter to be completely emptied and re-filled with the new mixture. Greater infection risks may occur during the early adjustment phase of an implant. This is due to an increased frequency of needle punctures required to empty and refill the system to the medication constitution [Lob07]. Additionally, applying a bridge bolus necessary to clear the delivery catheter is a process that has direct access to the CSF and is often conducted if significant changes to the medication are made. Changing pump technology to allow for simultaneous delivery of two or more medications would make drug combination therapy safer and easier. Current implantable drug delivery device architectures do not allow for easy adaptation to multiple independently regulated drug reservoirs. An alternative device architecture allows for the development of an intrathecal drug pump that actively delivers an adjustable ratio of mixed medications from separate reservoirs.

1.2 Other Drug Delivery Devices

There are several different types of devices - implantable and external - that have been used to deliver medication. Exploring these possible alternative devices may yield insight into potential architectures for an alternative IDDD.

Over the last decade, advances in subcutaneous and implantable reservoirs and pumps have assisted with long term drug management. Various treatment technologies may be

implanted under the skin or deliver medication subcutaneously, often through a catheter [Rai07]. Some drug delivery mechanisms that do not consume electrical power, like polymer implants, allow for the medication rate to be pre-programmed for the duration of delivery between refills or replacement [Gra01, And99, ASH00, Cra80, Bar82, Coo91, Has00]. These medication technologies deliver solid-phase medication and are unable to respond to changes in the patient's needs. This type of drug therapy is not as effective as active pumping for treating some medical conditions like chronic pain because patients' needs may adjust daily in ways that are difficult to anticipate. Active devices, like the SyncroMed II, generally pump an aqueous medication from a reservoir at a very controlled rate that allows for precise dosing [Pai96, Sau94, Deer02, Sak05]. These pumps allow for flexible control over the medication rate, but are increased in both size and weight because of pump and battery needs. This is particularly apparent for medications that require a relatively large amount of solution because the power consumption is related to the volume that must be pumped. These active systems present significant opportunity for miniaturization, power savings, and increased versatility while maintaining precise dosing control [Mer01].

Many other passive delivery devices, like the CODMAN 3000, use a pressurized reservoir in conjunction with a restrictive opening to regulate dosing [Mer03]. If the restrictive opening is replaced with an active valve, electronic control of the delivery rate can be achieved [Eva07, Eva08, Par07]. This throttled device allows active delivery rate control while utilizing mechanical energy for the delivery of the fluid.

1.2.1 External Drug Delivery Devices

External drug pumps are in common use for the regulation of insulin in diabetics [FDA08]. These typically work with disposable infusions sets that include a cannula and small reservoirs that are either replaced or re-filled regularly. Insulin pumps can deliver both basal and bolus deliveries according to a pre-set schedule. Recent devices advance delivery ease by monitoring glucose levels and using feedback to provide well balanced therapy regardless of consumption or the daily lifestyle of the patient.

Insulin pumps typically operate using a peristaltic pump to deliver medication from a reservoir into subcutaneous space via tubing connected to the disposable cannula. The infusion set is replaced every 2-3 days, and the battery lasts 2-10 weeks depending on the pump and manufacturer. Some devices, particularly the Paradigm series by Medtronic, have the capacity to wirelessly communicate with sensors that detect glucose levels. These sensors have a permanent component that processes the information and transmits to the insulin pump, and a disposable glucose sensing element that is replaced every three days. When using this feedback mechanism, the Paradigm drug pumps respond to the patients needs in real-time with no user input. This allows for therapeutic regulation of the insulin glucose cycle while providing no inconvenience beyond the act of physically wearing the pump.

External insulin pumps have less battery life and smaller reservoirs than current intrathecal pumps of a similar size. They do, however, provide greater delivery flexibility and exhibit more pump and physiological sensor sophistication that might be adaptable to implantable therapy. There are several other external devices that are used to deliver medication to patients, like the gravity powered intravenous (IV) bag. These

types of devices are generally too large to consider when determining advantages that can be gleaned for use in intrathecal pumps, and other external, portable delivery mechanisms tend to lack the sophistication of insulin delivery systems.

1.2.2 Implantable Drug Delivery Devices

Research into implantable drug delivery mechanisms is multi-disciplinary and has generated several new approaches to regulation. Advances in the integration of medication into biodegradable polymers for delayed targeted release were achieved by Langer *et al.* [Lan76]. This type of polymer delivery technology has continued in development since inception [Gra03]. In short, polymers that have a known degradation and release rate are combined with a concentration of a targeted medication, and are inserted into the location where release is desired. Initial polymer delivery systems provided uncontrolled dissolvable release, but advances that incorporate varying concentrations, well depths, or polymer thicknesses allow the ability to pre-program a release profile [Lan90]. A commercial realization of this type of drug delivery is the Norplant contraceptive implant. The most recent contraceptive implant in this family of devices is Jadelle by the Population Council [PoC08]. It has an outer biodegradable sheath, and an internal drug imbued polymer that slowly dissolves over the lifetime of the device (5 years). Dissolving polymeric implants are generally small and provide no dynamic control, feedback, and are not refillable.

Another type of implantable drug delivery devices are silicon microreservoir systems. This delivery mechanism (Figure 1-3) was introduced in 1999 by Santini *et al.* [San99]. The device utilized reservoirs fabricated in silicon wafers that were filled with the desired

drug. The reservoirs were covered with a gold membrane that was dissolved by applying an anodic voltage to the membrane when chloride ions were present. The membrane could also be removed by rapid heating. The reservoirs could each be filled with different medications or even sensors. Programmed release from these types of devices requires either an internally programmed controller, or it can be achieved via wireless communication [Mal05]. Additionally, work has been done to create microreservoir delivery devices from substrates other than silicon [Gra03]. This implantable technology offers greater release control than polymer devices, but it requires embedded electronics that complicate the device. It is also not refillable. Microreservoir drug delivery is currently being commercialized for subcutaneous delivery by MicroCHIPS [Mic08].

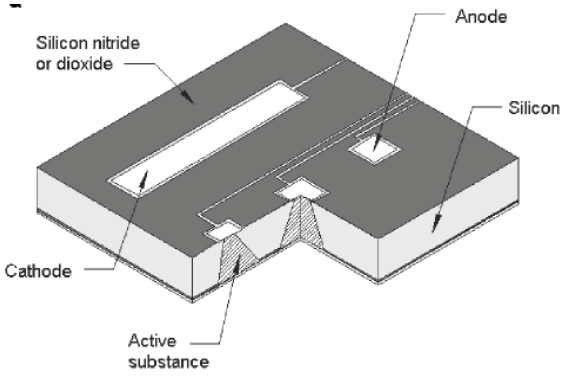

Fig. 1-3: Gold membrane silicon microreservoirs originally developed by Santini *et al.* and now being commercialized by MicroCHIPS. [San99]

Several other technologies are being developed for implantable drug delivery. In some other systems, osmotic force is used as a pressure generation mechanism to drive delivery (Figure 1-4) [Won07]. The pumps available from Alzet [Alz08] are cylindrical with an outer semi-permeable layer, followed by a salt layer, an inner impermeable layer, and a core that functions as the reservoir for the drug to be delivered. The salt layer creates an osmotic pressure that drives water from the body into the salt layer. This forces medication out of the device by compressing the inner reservoir core. The

delivery rates of these types of pumps are determined by the permeability of the outer layer. They are implantable but are difficult to refill or reprogram once they are implanted.

Fig. 1-4: Various sizes of the single use implantable osmotic pump made by Alzet. [Alz08]

Several drug delivery techniques provide controlled delivery to a target location, but they are difficult to regularly refill and replace. Adjustments of the delivery profile after implantation are also difficult to achieve without wireless communication and/or embedded circuitry. The advantage of polymer and microreservoir delivery is the volume efficiency that results from the large percentage of device volume that is utilized for medication. Current intrathecal drug pumps may be improved by increasing volume efficiency to approach these devices.

1.3 Focus of the Current and Proposed Work

As described in section 1.1, techniques for providing intrathecal drugs for the treatment of chronic pain are reaching device limits. Thus, a new drug pump architecture should be developed that provides the ability to control delivery to facilitate current therapy practices. Ideally, the system should have greater functional control than current solutions, but it should also improve upon general safety, and increase volume efficiency. Functional control of a drug implant can be qualitatively defined across a range of

devices based upon the relative capacity to be utilized in a specific way. For example, a gravity driven IV bag with no regulation would have a functional control metric of 1 and a volume efficiency of almost 100%. An insulin pump that automatically detected and delivered insulin to regulate glucose levels in a diabetic would have a function control metric of 10. As illustrated in Fig. 1-5, current drug delivery devices either provide a very high level of control, or they sacrifice control to improve the volume efficiency to make it practical for implantation. The focus of this work is to design a novel drug delivery architecture and develop an implantable pump that allows for greater control over intrathecal treatment while improving volume efficiency.

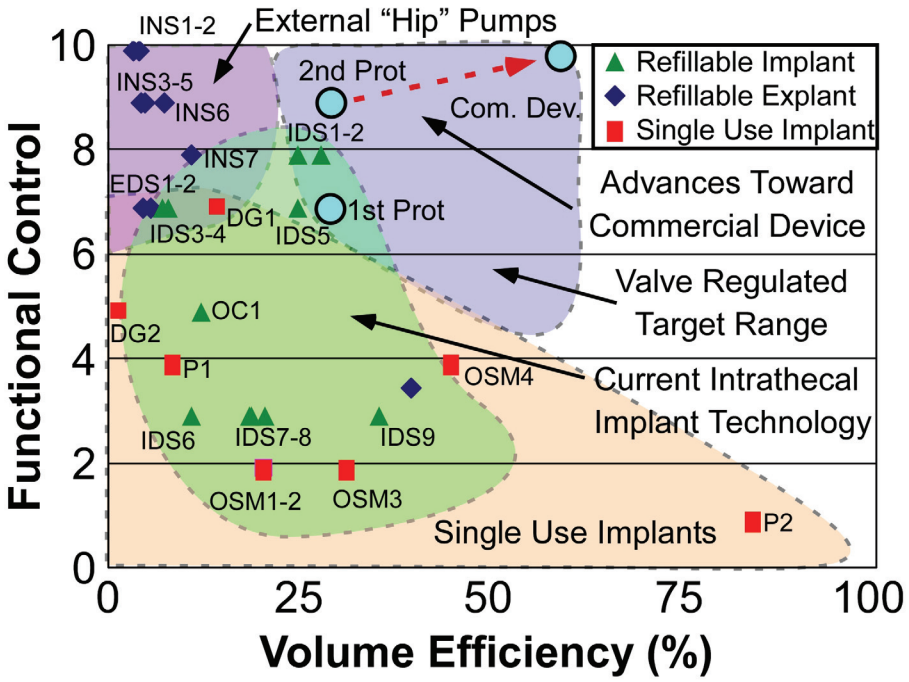

Fig: 1-5: Current drug delivery devices trade functionality and control for size. This work seeks to develop a new topology that improves the intrathecal implant class of devices in both functional control and volume efficiency. Device specifics can be found in Table 1-2.

As illustrated with the brief review in section 1.2, current intrathecal drug delivery devices can be modified to offer greater functionality with significant size reduction.

Notably, an architecture utilizing multiple regulatory mechanisms with separate reservoirs may allow clinicians to dose medications as described in section 1.1. The work documented here focuses on developing a pump architecture with multiple reservoirs that improves safety and volume efficiency. Early prototypes target a VER of 25% and specific functional control of 8 with the potential for commercial devices to have a VER of at least 60% and specific functional control of 10. Focusing the work in this way allows detailed design specifications to be developed and addressed in order to create a device that will allow physicians to implement and further evaluate the medicinal benefits of multiple chamber drug regulation into the intrathecal space.

Table 1-2: Overview of the drug delivery devices in Figure 1-5

ID Tag	Name	Description	Ref
INS1	Paradigm 522	Insulin pump made by MiniMed	[Dia08]
INS2	Paradigm 722	Insulin pump made by MiniMed	[Dia08]
INS3	IR-2020	Insulin pump made by Animas	[Dia08]
INS4	Deltec Cozmo 1800	Insulin pump made by Smiths Medical	[Dia08]
INS5	Spirit	Insulin pump made by Disetronic	[Dia08]
INS6	Diabecarell	Insulin pump made by Sooil USA	[Dia08]
INS7	OmniPod	Insulin pump made by Insulet	[Dia08]
EDS1	Alpha Infusion Pump	External intrathecal drug pump from Advanced Infusion	[Adv08]
EDS2	Alpha Infusion Pump	External intrathecal drug pump from Advanced Infusion	[Adv08]
IDS1	Synchromed II	Internal intrathecal drug pump made by Medtronic	[Med08]
IDS2	Synchromed II	Internal intrathecal drug pump made by Medtronic	[Med08]
IDS3	Synchromed EL	Internal intrathecal drug pump made by Medtronic	[Med08]
IDS4	Synchromed EL	Internal intrathecal drug pump made by Medtronic	[Med08]
IDS5	Jo2004	Reseach intrathecal drug pump done in Seoul	[Hon04]
IDS6	Codman 3000	Internal intrathecal drug pump made by Codman	[Cod03]
IDS7	IsoMed	Internal intrathecal drug pump made by Medtronic	[Med08]
IDS8	Codman 3000	Internal intrathecal drug pump made by Codman	[Cod03]
IDS9	IsoMed	Internal intrathecal drug pump made by Medtronic	[Med08]
OC1	Meng08	Research ocular drug implant done at USC	[Lo08]
DG1	Walt2007	Dissolving gold research drug implant done in Edinburgh	[Smi07]
DG2	Lang99	Dissolving gold research drug implant done at MIT	[Lan99]
P1	Lang03	Dissolving polymer research drug implant done at MIT	[Gra03]
P2	Jadelle	Contraceptive implant made by Population Council	[PoC08]
OSM1	Alzet 1003D	Osmotic drug pump made by Alzet	[Alz08]
OSM2	Alzet 2003D	Osmotic drug pump made by Alzet	[Alz08]
OSM3	Alzet 2ML1	Osmotic drug pump made by Alzet	[Alz08]
OSM4	Fasch2007	Research osmotic drug pump made at Stanford	[Won07]

1.3.1 Structure of this Work

Chapter 2 of this work presents a conceptual vision for a new implantable drug delivery architecture and the key system components for achieving this vision. Subsequently, each component and the related design considerations are discussed in a more detailed manner. Additionally, analytical and finite element design tools that have been developed are described and important results highlighted. Chapter 3 presents the design, fabrication, and testing of three generations of piezoelectric microvalves. This includes the development of a two-valve manifold with embedded sensors. Chapter 4 presents the design, fabrication, and testing of two variations of spring pressurized drug reservoirs. Chapter 5 contains the assembly, testing, and characterization of a prototype device utilizing a single valve to demonstrate feasibility. Chapter 6 presents the assembly, testing, and characterization of a second prototype device utilizing a two-valve manifold and multiple reservoirs to demonstrate protocol versatility. Chapter 7 presents a battery recharging mechanism using power transfer across a reservoir refill port. Finally, Chapter 8 summarizes and discusses continuation of this work.

CHAPTER 2:

GENERAL DESIGN CONSIDERATIONS

As noted in Chapter 1, a new implantable drug pump architecture could improve intrathecal medical therapy and improve on the volume efficiency of current devices. The device architecture outlined in Fig. 2-1, potentially achieves both goals [Eva08]. In this concept, two independently regulated microvalves throttle drug flow from separate mechanically pressurized reservoirs. Mechanically pressurized reservoirs allow for mechanical power to be recharged when the reservoir is refilled. This, coupled with low-power valves, reduces the overall electrical energy required; this allows for longer device lifetimes from a smaller battery. Regulating pressurized reservoirs allows for a full flow range and a high VER. Reduced flow controller size allows for multiple reservoirs to be regulated independently while maintaining volume efficiency. Independent regulation of multiple medications increases the therapeutic returns from a set volume of different drugs.

There are three main components of this system that warrant detailed design consideration. First and foremost, the throttle valves need to be able to regulate flow at rates necessary for intrathecal drug delivery. Additionally, they must be able to withstand reservoir pressures, have a small form factor, and be energy efficient. The second component of the system is the mechanical pressurization of the reservoir. The reservoirs have to be mechanically recharged when the medication is refilled. The third component of the system is the power management and control circuitry and that

regulates the operation of the throttles. The circuitry must minimize power consumption and could include a mechanism for recharging the battery. Each of these components will be described in more detail in the following sections.

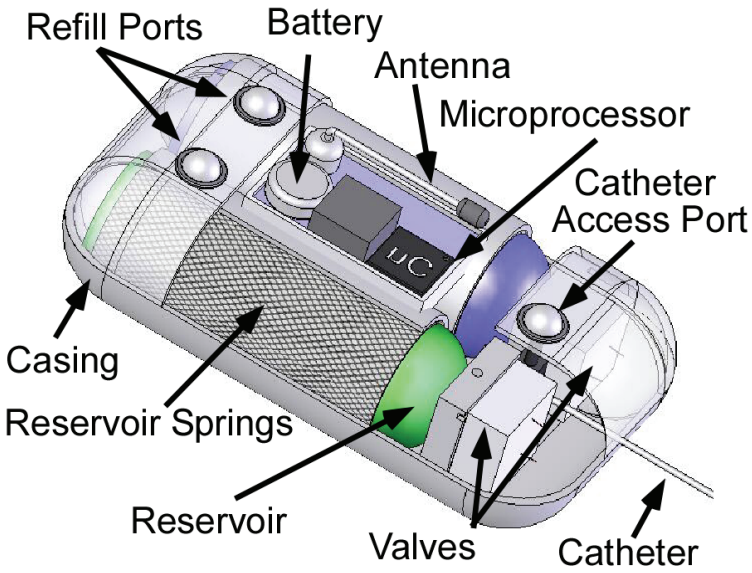

Fig. 2-1: Conceptual design of an implantable intrathecal drug delivery device that uses two valves to independently regulate the medication delivered from spring pressurized reservoirs.

2.1 Regulatory Microvalve Design

Microvalves for this system are designed to regulate medication and flow rates necessary for clinical efficacy. Device size and power consumption are minimized within this constraint. Embedded sensors can be included in the valves to simplify the integration of multiple system components and reduce overall device volume. All elements of the valve that come into contact with the medication are biologically compatible.

An active valve is necessary to regulate flow from a varying pressure source. Active microvalves are generally composed of a variable flow channel and an actuator. Current microvalve designs yield insight into valve mechanisms that meet the needs of a drug

delivery system. For convenience, the valves are categorized by their actuation mechanisms. Various actuation methods have been explored for use in active microvalves: electromagnetic, electrostatic, piezoelectric, and thermal actuation. These will be discussed in more detail in the following subsections.

2.1.1 Electromagnetic Actuation

Electromagnetic actuation utilizes force generated by magnetic induction. The magnetic field is often applied by a permanent magnet or an external electromagnetic coil. The main advantage of magnetic actuation is the ability to create a relatively large force and large deflections with low driving voltages. One of the first active micromachined valves was reported by Terry *et al.* in 1979, to be used in an integrated gas chromatography system [Ter79]. The valve consisted of an etched silicon orifice, a nickel diaphragm, and a solenoid actuator and plunger assembly. When the solenoid was energized, the plunger was pulled, allowing the diaphragm to relax and gas to flow. Other examples of early work in magnetically actuated microvalves are described in references [Ike97, Shi97, Smi90, Hir97, Yan95]. These valves utilized external magnetic fields provided by external coils or permanent magnets to actuate flow blockers made of magnetic material. More recent work involves fully integrated electromagnetic actuation without the aid of any other external components [Bin05, Sut06, Sad98]. A ball-type microvalve using an iron ball driven by external solenoid has been reported by Fu et al. [Rum03]. Bae et al. developed a pressure-regulating microvalve as an implant for use in the treatment of glaucoma [Bae04]. Electromagnetic actuation typically generates forces in the range of 1-100 mN with supply of 100-600 mA of DC current. Flow rates as large as 8.8 L/min have been successfully modulated with this actuation scheme with a valve

stroke of 0.1 mm [Ike97], but high power consumption (up to 6 W [Rum03]) is a drawback of electromagnetically driven valves. Electromagnetic actuation also demonstrates relatively slow response time ranging from 3 ms [Ike97] to 10 ms [Bin05, Sut06, Rum03].

2.1.2 Electrostatic Actuation

Electrostatic actuation is frequently employed in microvalves. The electrostatic force generated between two conductors depends on the applied voltage and the separation distance between them. The force is generally small (microNewtons) and requires a small gap between two conductors. This small displacement may hinder the microvalve performance by limiting the flow rate. Electrostatic valves generally consume little power, but they require high voltages and have small displacements. Ohnstein *et al.* has demonstrated an electrostatically actuated microvalve with a cantilever closure plate [Ohn90]. The closure plate was made from silicon nitride by surface micromachining; a metal electrode was embedded in it. The valve provided up to 150 sccm flow with a 30 V drive. An electrostatically actuated microvalve with an S-shaped film was demonstrated by Shikida *et al.* [Sat94, Shi94]. The conductive film between a pair of planar electrodes was elastically bent in an S-shape and the S-bend moves back and forth as voltage is applied. This particular type of valve demonstrated a large vertical displacement by utilizing the electrostatic force at the edge of the S-bend. A flow rate variation of several sccm was obtained under a pressure difference of 100 Pa with an actuation voltage of 150 V. A pressure-balanced microvalve was reported by Huff *et al.* [Huf90, Huf93]; this overcame the limited force generated by the electrostatic method,

and closed against high pressures. The valve was tested up to 80 psi differential pressure with an applied voltage of 210 V. A polymer microvalve with a flexible membrane was presented by Goll *et al.* [Gol97]. A voltage of 60-150 V was needed to modulate the membrane and flow rates of 12 mL/min at a differential pressure of 110 kPa have been measured. Wijngaart *et al.* [Wij02] combined a pressure balancing concept with a flexible membrane to demonstrate a large stroke electrostatic microvalve for high pressure control. Simulation showed that it is possible to control 500 kPa of air pressure while ensuring a 15 μm gas flow gap at an actuation of 366 V. A Ta-Si-N membrane was used to achieve fast switching valves by Dubois *et al.* [Dub01, Dub01-2]. Such valves were developed to be used at differential pressures greater than 200 kPa. Pulse width modulation was used to control the flow rate up to 30 mL/min with an actuation voltage of 30 V. A bulk-micromachined integratable electrostatic microvalve with a curved-compliant structure was demonstrated by Yobas *et al.* [Yob03, Yob01] for a tactile display system. Due to its unique curved-compliant structure, the valve required a relatively low closing voltage of 72.9 Vrms for 19.3 kPa of pressure with 86 mL/min flow. A group from MIT demonstrated an electrostatic microvalve for gas fuel delivery of a microengine [Yan94]. The valve was fabricated using direct bonding of three wafers and deep reactive ion etching techniques. A 136 V actuation was required to open the valve against a 0.9 MPa pressure difference, and a flow rate of 45 sccm was measured when opened. Electrostatic microvalves are often used as binary valves due to pull-in characteristics. Robertson *et al.* [Rob98, Rob94] integrated an array of electrostatic microvalves with a micromachined 3 μm thick silicon beam to build a gas modulator.

The gas flow modulator was able to deliver sub-sccm gas flow in the range from 3.8×10^{-3} sccm to 0.7 sccm.

2.1.3 Piezoelectric Actuation

Certain crystals have the ability to produce mechanical deformation by a change in the electrical polarization of the crystal. This is referred to as a piezoelectric effect. This effect has been widely used in microvalve and micropump fabrication because it can generate large forces. Piezoelectric actuation has an added advantage in power consumption because DC actuation only draws power when the actuator is adjusted to turn on or off the valve. One of the earliest works on fabrication of a piezoelectric microvalve was presented by Esashi *et al.* [Sho91, Esa89, Esa90]. The valve was constructed from a silicon mesa suspended with a flexible silicon diaphragm. The diaphragm was pressed against a glass plate by a stack piezoelectric actuator with dimensions of $3\times1.4\times9$ mm^3. The valve was capable of modulating gas flow from 0.1 to 85 mL/min with 73.5 kPa inlet pressure. It exhibited a response time of less than 2 ms.

A major disadvantage of piezoelectric actuation is the small stroke for even large voltages. This drawback can be overcome by hydraulic amplification of the piezoelectric actuator [Rob03, Li04]. A compact, high-frequency, high differential-pressure microvalve reported by Roberts *et al.* utilized a hydraulic amplification mechanism to achieve 40-fold amplification of the limited stroke provided by the piezoelectric material. The valve had a nine layer structure composed of glass, silicon, and silicon on insulator (SOI) layers assembled by wafer-level fusion bonding, wafer-level anodic bonding, die-level anodic bonding, and eutectic bonding. Valve strokes as large as 20 μm were realized and a flow rate of 12.6 mL/min was realized. Another microvalve with a 25-fold

hydraulic amplification was reported by Rogge *et al.* [Rog04, Sha04]. A valve made from a surface macromachined piezodisk actuator was described by Watanabe *et al.* [Wat97]. The valve was constructed in a thin beam with a round valve cap at the center and a valve seat comprised of a thin film piezoelectric. Each valve, smaller than 1×1 mm^2, handled up to 2.4 mL/min of flow. NASA's Jet Propulsion Laboratory has developed piezoelectric microvalves for space applications [Cha00, Lee04, Yan04-2, Lee06]. A series of concentric rings was defined around the orifice to create a leak-tight seal. An extremely low leak rate of 5×10^{-3} mL/min at an inlet pressure of 5.5 MPa was demonstrated. At an inlet pressure of 2 MPa, flow rates of 52 mL/min were measured with 10 V actuation.

2.1.4 Thermopneumatic Actuation

Bi-metallic, thermopneumatic, and shape memory alloy actuation mechanisms use thermal properties of materials to generate displacements. These actuation schemes generally produce considerable force while simultaneously achieving large strokes. However, they have relatively high power consumption rates (100 mW) and slow response times (100 ms). In some bi-metallically actuated valves, thin-film heater elements are placed on a diaphragm. When they are heated, a difference in thermal expansion coefficients bends the diaphragm. Bi-metallic actuators are often easy to fabricate, but they draw relatively large amount of power and are sensitive to ambient temperatures. Jerman [Jer94] showed Al/Si bi-metallic driven diaphragms in a valve structure and demonstrated flows up to 100 mL/min using 400 mW of power. Barth *et al.* [Bar94] developed a Ni-Si bi-metallic microvalve which successfully opened against 1300 kPa of pressure and achieved a 600 mL/min flow rate with power consumption of 1

W. Messner *et al.* [Mes98] demonstrated a bi-metallically actuated 3-way microvalve which successfully achieved flow rates up to 800 mL/min at 600 kPa with power consumption of about 1 W.

The shape memory effect is due to a crystalline transformation between a high-temperature phase and a low-temperature phase. It is an attractive actuation mechanism because it allows simple and compact structures to generate high forces which can be used in high pressure applications. Further advantages of shape memory alloys (SMAs) are low voltage operation, high reliability, no additional moving parts, and high chemical resistance. Kohl *et al.* demonstrated gas microvalves using Ti-Ni SMA thin films [Koh00, Koh99, Koh99-2, Skr97]. Maximum gas flows of 1.6 L/min and work output of 35 μN-m were achieved with a driving power of 210 mW at a pressure difference of 120 kPa. The response time for closing the valves varied between 0.5 and 1.2 s, and between 1 and 2 s for opening. This response depends on the applied pressure difference.

Thermopneumatic microvalves are operated by volumetric thermal expansion or a phase-change phenomena coupled to membrane deflection. This actuation method can provide relatively large deflections. However, this type of valve typically has a relatively longer response time, and the fabrication process is often complicated due to the necessity to fill the chamber with fluid and provide a hermetic seal. Zdeblick *et al.* demonstrated the idea of heating an encapsulated liquid with a miniature resistive heater in order to move a diaphragm [Zde87]. Takao *et al.* employed PDMS as a diaphragm material for a long stroke actuation and demonstrated good sealing performance [Tak05]. At 50 kPa of inlet pressure, a microheater powered with 100 mW was required to cut-off the flow, and a flow rate of 17 mL/min was achieved when the valve was fully open. The

transient time necessary to open the valve was about 23 s and the transient time necessary to close the valve was 1.5 s. Rich *et al.* also reported a high-flow thermopneumatic microvalve constructed from a three-wafer stack with a corrugated diaphragm [Ric03]. Flow rates as high as 400 mL/min were achieved at 200 kPa differential pressure; 500 mW of input power raised the cavity pressure by 260 kPa. Potkay *et al.* used a combination of thermopneumatic actuation with an electrostatic hold so that the valve only required power during the transition from open to closed and consumed no static power [Pot05]. The thermopneumatic actuator closed the valve in 1 second at 200 mW of input power and the open flow rate was 3.3 mL/min at 17 kPa.

As highlighted in section 2.1.1-2.1.4, electrostatic and piezoelectric actuation mechanisms consume much less power than electromagnetic or other thermal actuation mechanisms. However, the reported electrostatic and piezoelectric microvalves provide much lower flow rates than the other actuation mechanisms. Piezoelectric actuation is appealing for implantable systems because it offers high force that can overcome high reservoir pressure and low power consumption. The principal drawback of the lower flow rates due to a reduced displacement can be overcome with proper design. One aspect of this research is to develop microvalves that meet the requirement of delivering intrathecal medication at medically viable delivery rates. These microvalves should regulate the flow of saline from 0.1 - 5 mL/day. Additionally, the valves should minimize power consumption and a have a small size, preferably less than 1 mW and 3 cm^3 respectively.

2.2 MECHANICALLY PRESSURIZED RESERVOIR SPECIFICATIONS

There are several factors that need to be accommodated in the design of refillable pressurized reservoirs. These include the pressurization mechanism, the pressure-volume relationship (PVR), and the dead volume. The force mechanism that generates pressure can either be actively controlled, like a motorized screw, or it can be passive, like the constriction of a balloon. The PVR is the relationship between the liquid pressure in the reservoir compared to the volume remaining in the reservoir. The unusable reservoir volume is related to the PVR because it represents the volume of liquid in the reservoir that is not deliverable. The dead volume of the reservoir is the unusable reservoir volume and the volume of the reservoir that is not liquid. The various design constraints for these elements are detailed in the following subsections.

2.2.1 Pressurizing Mechanism

Active mechanisms are often liquid pumps that generate a pressure gradient, physical systems that squeeze the reservoir in a manner similar to a toothpaste tube, or systems that create volume expansion within the reservoir itself like a bubble generator [Coo04]. These systems all require power for increases in reservoir pressure, but they can create precise reservoir pressures because of the monotonic relationship between reservoir pressure and volume. This controllable pressure can be used to regulate drug delivery through a fixed aperture. An architecture that utilizes an active throttle is volume efficient because it does not need controlled reservoir pressures or the associated active mechanisms.

Passive reservoir pressure is often generated by mechanical compression, pressurized

gas, osmotic pressure gradients, or surface tension effects like capillary pressure [Bor06]. Capillary pressure is relatively difficult to use to create a large reservoir with uniform pressures. Osmotic pressure is used in the Alzet drug pumps to pressurize reservoir liquid and drive it through a fixed aperture; this technique takes advantage of interactions with the subject across a permeable membrane.

Current intrathecal drug devices use a combination of mechanical constriction and gas pressure across a membrane to pressurize medication in the reservoir. The un-powered devices like the CODMAN 3000 and the IsoMed utilize a propellant gas in conjunction with a bellows spring network to create a relatively constant pressure over most of the delivered volume of the reservoir. Additionally, this bellows mechanism is reversible, and the energy used to drive delivery is mechanically stored and recharged every time the reservoir is refilled from a higher pressure source. One problem with this style of reservoir is that the loss of one element (gas or spring) or the other causes serious deviations from the set PVR and subsequently results in faulty medication delivery to the patient [Med06]. Additionally, the bellows and propellant are designed such that a relatively constant pressure is generated and driven through a flow restrictor [Eth05]. This sophisticated mechanisms requires significant volume that does not contain medication. The dead volume can be reduced by eliminating the constraint that the reservoir has to generate a constant pressure.

2.2.2 Pressure Volume Relationship (PVR)

Current intrathecal pumps have reservoirs that aim at maintaining a constant pressure regardless of the undepleted drug volume. This constant pressure is necessary to

maintain a constant flow rate through a set aperture, in the case of passive devices; or to maintain a set pressure differential for a pump, in the case of active devices. This is no longer a necessary constraint when using an active throttle. The benefits of potential pressure to volume relationships can be explored.

PVR allows the throttle to be characterized before system assembly. Flow can then be modulated by setting the throttle to a particular effective aperture size without needing any information about the state of the reservoir. Constant pressure reservoirs require significant dead volume, and do not allow the PVR to be used as an indicator of the undepleted drug volume.

Reservoirs with a repeatable PVR in which the reservoir generates decreasing pressure with decreasing volume can be used to indirectly measure the undepleted drug volume by measuring the pressure. MEMS pressure sensors can be integrated into either the reservoir or the flow channel to provide feedback about the remaining volume and average flow rate. Reservoirs with this type of PVR can be easily fabricated and realize volume efficiencies greater than 80%. A varying pressure reservoir requires feedback control to account for pressure variations and achieve accurate dosing. A passive, variable pressure reservoir works well for implantable systems because it is volume efficient and allows for accurate dosing using embedded sensors.

2.2.3 Dead Volume

Almost every reservoir has both unusable liquid volume in the reservoir and dead volume created by the mechanisms used to pressurize the reservoir. The unusable liquid volume, in the case of intrathecal drug pumps, is the volume below which the drug can no

longer be properly delivered. The dead volume also includes all the volume of the device that is not occupied by medication. In the case of a bellow pressurized reservoir, the dead volume would be the volume of the bellow springs, the space taken up by the propellant gas, and the volume of the reservoir casing. The most volume efficient reservoir is one that minimizes dead volume while meeting the application needs.

Unusable volume in a valve-regulated drug delivery device is dictated by the pressure below which medication can no longer be delivered across the entire flow rate range. Worst case delivery conditions for an intrathecal drug pump involve the delivery of medication into a spinal column at pressures of 15 cm/H_2O (1500 Pa) [Hea08]. The medication is delivered through a one meter long catheter with a 0.5 mm diameter [Med06]. Assuming the throttle valve is much less constrictive than the catheter when fully open, and the maximum necessary flow rate for clinical efficacy is 5 mL/day; the minimum necessary reservoir pressure can be estimated using hydraulic resistance theory - further detail in Section 5.2.2 [Bra03]. The minimum reservoir pressure necessary to ensure the full delivery range is 200 Pa, if the system is not throttle limited. Anything less than this is considered unusable volume.

Dead volume includes the volume that the pressure mechanism requires. This is the significant limiting factor in the volume efficiency of intrathecal pumps that utilize constant pressure reservoirs. In order to maintain a constant pressure across the delivery volume, space is utilized for a propellant gas, bellows, and a unique housing. This creates a situation in which devices like the CODMAN 3000 have reservoirs that hold 50 mL of medication but require 220 cm^3 of total volume. As previously discussed, reservoir designs with non-uniform pressures are more volume efficient. An example of

this type of reservoir is a compressive balloon. The only dead volume is the thickness of the elastic polymer that contracts against the volume inside of the balloon. The reservoirs represent a large portion of the volume of an intrathecal drug delivery device, and the dead volume should be minimized.

In summary, sections 2.2.1-2.2.3 cover issues related to reservoir design for a throttled intrathecal drug delivery device. The proposed system architecture requires a reservoir designed for use in valve regulated delivery. Various compressive mechanical pressure generation systems that use springs have been reported. Current intrathecal pumps have unusable reservoir volumes that vary from 1-3 mL (10-20% of the total volume). Assuming the throttle is ten-fold more constrictive than the catheter and 20% unusable reservoir volume is acceptable, the compressive pressure systems should generate differential pressures above 600 Pa for 80% of the volume. Additionally, pressures greater than 200 kPa would likely overwhelm the valve. Reservoirs should contain between 10-30 mL of deliverable liquid to be medically viable over a three month refill period without being unnecessarily large.

2.3 Electronic Control and Power Management

In order to regulate delivery from a variable pressure reservoir with an adjustable throttle, sensors and related circuitry are needed to control the valve. These circuit elements need to operate from a battery for the lifetime of the device (5 years). This power constraint is imposed upon the control system, and it is the most important design factor aside from assuring functionality required for proper medical viability.

The electronic components include physical sensors with associated analog conditioning, central processing, communications, memory, analog amplification for valve output, and the power supply. The physical sensors are embedded in the valve and have known output ranges and sensitivities that need to be accounted for in the analog readout circuitry for proper data collection. The central processing unit is the microprocessor and associated components that allow the system to utilize sensor information to provide feedback regulation of the microvalve. The communications and memory represent the interface for a clinician to receive system data and modify the delivery schedule to provide the patient with the best care possible. Analog amplification and power regulation are comprised of the battery regulator and power amplifiers used to drive high voltage or current to actuate the valves. It also regulates the voltage provided from the battery to the remaining electronic elements. Power management electronics can be provided to recharge the battery during the refill sessions. This relaxes energy constraints on control circuitry because devices need run from the same battery for 6 months rather than for five years. Recharging can be done by wireless power transfer or through direct connection mechanisms. The design constraints for these components are detailed in the following subsections.

2.3.1 Physical Sensors and Conditioning

Physical sensors and the associated analog conditioning are necessary to collect data from the system in order to actively control flow via feedback. Pressure is the most important physical property to sense for flow regulation. Additional sensors may include temperature, acceleration, and other devices to sense phenomenon related to patient

health. Temperature sensors can be used to compensate the pressure sensors for small variations, and can, along with an accelerometer, provide information about the state of the patient. Regardless, the design constraints for the pressure sensors dominate the requirements for sensor conditioning.

Two common methods of sensing pressure across a membrane are piezoresistive sensing of membrane stress and capacitive measurements of membrane deflection. Piezoresistive sensors are usually configured in a Wheatstone bridge and tend to have a linear voltage to pressure relationship. Capacitive sensors are more sensitive with smaller gaps and generally need conditioning to adjust for non-linearity. The sensor specifics are covered more in depth in section 3.2.3, and it is assumed that the pressure sensors are linearized before they interface with the analog conditioning circuitry.

Piezoresistive pressure sensors can typically operate with a wide power supply that includes 3–5 V. The analog to digital converter (ADC) will share this same voltage range; thus, the output of the analog conditioning circuitry can be specified as a percentage of the supply voltage (Vdd) rather than as a specific voltage. Additional constraints can be placed on the range of the sensors. The full scale pressure sensor range should be the full range of reservoir pressures. This is from 50 kPa down to 0 kPa. The inputs into the ADC should span the entire supply range for the pressure range in order to maximize sensitivity.

Typical ADCs provide 12-bit resolution. This allows for 4096 discrete input voltages that can be independently determined, with each point separated from the next by 0.0244% of the supply voltage. The first requirement of the analog conditioning circuitry is that it should not generate noise greater than half of this value. Assuming a minimum

supply of 3V, the noise voltage generated by the conditioning circuitry should be less than 0.0244% of 3V (366 μV). Also, a single bit change (or increase of 0.732 mV) in a 12-bit ADC equates to a measured change of 12.21 Pa. The analog circuitry must change the output from the sensor for a shift of 12.21 Pa into a voltage change of at least 0.732 mV. This will define the amplification necessary between the sensor and the ADC, and this could easily be amplification of three orders of magnitude.

The necessity of a wide dynamic range, high accuracy, and good precision in the pressure sensors will dominate the requirements of the analog conditioning circuitry. It is important to meet the necessary requirements, but it is also important to minimize power consumption. This can be accomplished by adding the ability to turn on and off the sensors and circuitry. Pressure will be sampled no more than once a minute, so the 'sleep' mode and startup power costs of the circuitry will dominate the power budget allocated to the electronics. If the system has a sleep state where it draws almost no power, time average power consumption should meet the system requirements.

2.3.2 Processing, Communications, and Memory

Physical sensors provide the data necessary for a central unit to process and alter the output. The algorithm that the central processing unit (CPU) undertakes to adjust the output based on current conditions is stored in the memory along with other information. The memory and the control process are updated by the clinician through the communications system. Due to the inter-related nature of these elements in function and in design, it is important to consider them as a single functional block.

There are several different realizations of this functional block. The processor can be independent from the other elements, everything can be integrated in a single chip, or partial integration between these components can exist. Regardless of the specific elements within the functional block, the requirements are the same. The block has to read and process the sensor data and the memory information, communicate that information, control output, and use as little power as possible. Minimizing power is particularly important for the control elements because they will draw power at all times.

The power requirement can be specified if it is assumed that the circuitry requires a very significant portion of the total power budget (>80%). Further, assuming that the continuous nature of the processor will require half of the total power of the circuitry and the supply is the equivalent of two AA batteries, (4800 mAh at 1.8V) allows the determination of the power draw for a set time. The continuous power consumption of the processing unit for the device lifetime (5 years) has to be less than 27.5 mW. This is the most significant constraint on this system block, and the communications are restricted because of this.

Most memory elements easily fall within the power consumption requirements, so the remaining specifications are applicable only to communications. The communications must be in one of the industrial, scientific, and medical (ISM) bands approved for medical devices, and they have to meet all government requirements for medical wireless communication. Aside from that, the communications have very significant power draw. To compensate for this, the transmitter has to be completely shut down when not in use (it will only be used once every three months). Additionally, the receiver needs to consume as little power as possible while allowing communication at any time. This

'wake on receive' functionality is very important in any communications circuitry used in this implant. Initial lifetime of the device can be 100 days for demonstration purposes if it can be increased to five years with program optimization.

2.3.3 Power Supply and Valve Output

The battery, supply regulator, and power amplifiers for the valves are dependent upon the other system needs. It is imperative for space and power efficiency that all circuit elements are able to operate from a common supply voltage. This allows a single power supply regulator to provide voltage for every element from a single battery. This supply regulator and the power amplifiers both need to maximize their respective power efficiencies before meeting other performance metrics.

Standard batteries range from 1.2 – 12 V. Battery selection is dependent upon power density and maximum current draw as long as the nominal voltage is within this range. The initial batteries selected are not vital in determining overall system performance because medical devices of this nature tend to have specifically molded high density batteries. The standard batteries need to accurately mimic the current supply and voltage levels of a custom designed battery.

The supply regulator must provide a relatively level voltage to all of the circuit elements. In sharing a common supply across several circuit elements, digital noise will make it very difficult to provide a noise free analog supply. More importantly, it needs to be as efficient as possible in regulating the battery. A reasonable target for the supply regulation is 85% power efficient with the ability to determine the remaining power in the battery.

Many piezoelectric actuators can require up to 100 V to drive them across their full scale range. Current is required primarily during the transients of activation and deactivation. The power amplifies used to drive the valves should have a programmable output from 0 – 100 V, should operate from the supply voltage, and should be as energy efficient as possible. A good topology for controlling piezoelectric valves from a low voltage source is a controllable capacitive charge pump. A circuit of this nature should be designed to drive two valves at up to 100 V.

Power regulation is completely dependent upon the other circuit elements. Once an acceptable supply voltage is determined, the battery, supply regulator, and amplifiers must be selected to use this same supply while being as efficient as possible. In maximizing capacitive and inductive regulation topologies, loss can be minimized while power is provided across the system.

2.3.4 Recharging Mechanisms

The battery within current intrathecal drug delivery devices currently takes up about one quarter of the total volume. This is because the current systems are designed to run continuously from the same battery for at least five years. If the battery can be recharged, the size of the battery in the device can be reduced. This would lead to significant volume efficiency improvements without sacrificing functionality. Designing a system with a recharging mechanism allows for a smaller implant and more power for subsystems.

Traditionally, implantable devices with rechargeable batteries use wireless power transfer [Bov08]. This can be done by using an inductively couple link, RF frequency

energy scavenging, or magnetic fields that induce recharge currents in the implantable device. Wireless methods have been developed for several years and are commonly used in applications ranging from cell phone stations to nodal sensor networks. There are two barriers to wireless recharging that need to be addressed with an implantable drug pump. First, the power necessary to operate the pump is significant. Wireless recharging would have to occur regularly to provide enough energy to continuously run the pump. Second, the device is implanted, and there are federal regulations are the type and density of energy that can be transferred into the body.

An alternative to wireless recharging is to use a direct connection [Vip07]. Typically, a patient must go to their clinician every three to six months to have the drug reservoir refilled. This refill is accomplished by inserting a needle into a subcutaneous access port located on the implant. The process usually takes between fifteen and thirty minutes [And90, Str86]. The physical connection made between the needle and the system during refills can be exploited to also allow for a physical connection for energy transfer. The difficulty with this technique is that the medication and the patient need to be electrically isolated from the recharge current.

Recharging the implant battery allows for the battery size to be reduced and more power to be consumed in the operation of the system. Wireless or physical connections are required to provide this functionality. This comes at the expense of a more complicated device and increased circuitry volume. Providing a recharging mechanism that can be activated during a reservoir refill session improves the volume efficiency and functionality of the system without adding patient inconvenience.

In summary, sections 2.3.1-2.3.4 presents an overview of the circuitry necessary for

system functionality. Input pressure sensors need to be linearized across their full-scale range and output a voltage from zero up to the supply rail. The conditioning circuitry has to generate less noise than the input ADC. A CPU needs to be able to process the sensor measurements, control output amplifiers, and consume as little power as possible. Every functional block of the circuit needs to conform to a single supply voltage, and power regulation has to minimize loss. A recharging mechanism is necessary to minimize battery size. The circuit needs to provide the full range of clinical functionality as efficiently as possible to further reduce battery volume.

CHAPTER 3:

VALVE DESIGN, FABRICATION, AND PERFORMANCE

The piezoelectric microvalves used to regulate drug delivery should conform to the design constraints for the system (Fig 2-1). Three types of valves were designed in this work. The first two valve types have similar actuation mechanisms but different suspension mechanisms*. The third type uses the same suspension mechanism as one of the former types, but it has a several different features and can be assembled in a manifold. More detail on the design, fabrication, operation and modeling of flexure suspended valves, membrane suspended valves, and starburst manifold valves are in the following sections.

3.1 Flexure Suspension Valves

3.1.1 Device Structure and Operation

The valve operates by pushing a bulk silicon (Si) micromachined plate against a Corning #7740 Pyrex glass substrate that has the inlet and outlet holes in it (Fig. 3-1). A commercially-available multilayered PZT stack is used to drive the silicon valve plate (Physik Instrumente, Germany).

The PZT stack has footprint of 5×5 mm^2 and a height of 6 mm. Macor™, a glass mica ceramic, is used as the primary packaging material. It can be easily machined with precision, and has a thermal expansion coefficient of 7.4 ppm/K. In addition, it has zero porosity, does not outgas in vacuum environment, and can be used with epoxy to provide

* This work was done in close collaboration with Dr. Jong Moon Park, while he was a Ph.D. student at the University of Michigan

a hermetic seal. The ceramic enclosure measures 1×1×1 cm^3, and has 6 mm deep cavity with 1 mm thick walls on all four sides.

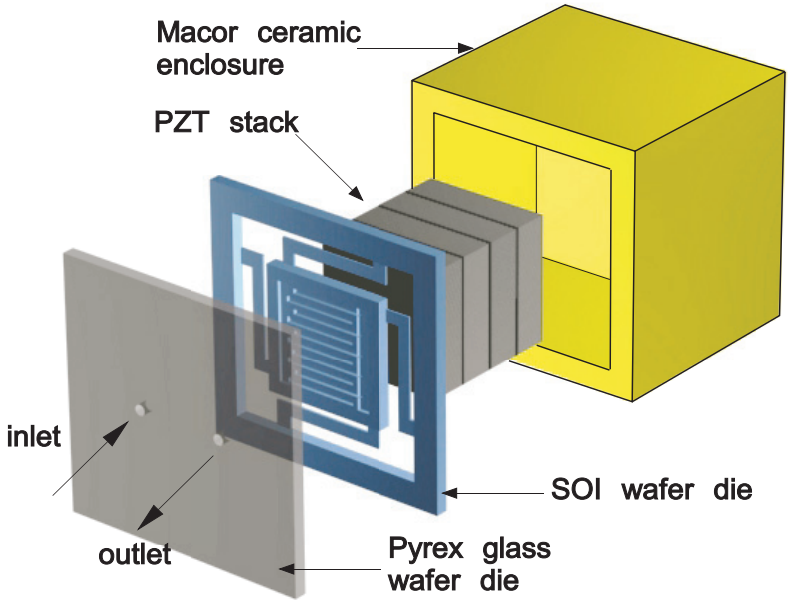

Fig. 3-1: Microvalve concepts: The valve consists of ceramic-PZT-Si-glass structure. A PZT stack actuator moves the silicon plate to open or close the valve. Micro-groove patterns are fabricated on the silicon plate to increase the flow area.

The limited displacement of PZT poses a major design challenge for this microvalve in providing sufficient flow rates for drug therapy. In this case, the flow area is given by the product of valve seat perimeter surrounding inlet or outlet hole (p) and the separation between silicon valve plate and glass seat (δ).

$$A_{valve} = \delta \cdot p \qquad (3\text{-}1)$$

The required flow area is quite large considering that the PZT actuator can provide at most 6 μm of displacement at room temperature. To achieve this large flow area, the perimeter of the valve seat is substantially increased by implementing serpentine groove patterns on the silicon valve plate (5×5 mm^2), as shown schematically in Fig 3-1. Each

groove measures 50 μm wide and 120 μm deep, and the perimeter measures about 127 mm, allowing much higher flow rates.

The silicon valve plate is suspended by four flexures in crab-leg formation; each measures 500 μm wide, 4200 μm long, and 50 μm thick. These flexures are flexible enough to move freely upon the actuation of PZT (spring constant ≈ 500 N/m) but are rigid enough to hold the plate in place. In addition, the crab-leg formation can relieve any stress that is caused by temperature or process variations. This characteristic was verified by finite element analysis of the structure. Assuming that the anodic bonding between the silicon and glass was done at 400ºC, at room temperature, a maximum stress of 21 MPa was observed at the corners of bonding rim but the stress on the flexure and silicon valve plate was negligible.

The bonded die, PZT actuator, and ceramic enclosures are joined using Stycast epoxy. The PZT actuator is not bonded to the Si plate, which helps to accommodate variations in height caused by expansion mismatch between the PZT and the Macor housing.

3.1.2 Device Fabrication

To ensure control of material properties, the final device is comprised of only bulk materials. Deposited thin films are not used for any structural layer, although they are used in intermediate steps. The fabrication process uses two wafers: a silicon-on-insulator (SOI) wafer which has device layer, buried oxide layer, and carrier wafer thicknesses of 50 μm, 0.5 μm, and 450 μm, respectively, and a 500 μm thick Pyrex glass wafer. The fabrication processes for SOI and glass wafers are illustrated in Fig. 3-2, and the assembly with the PZT and the ceramic housing is discussed in Section 3.2.2.

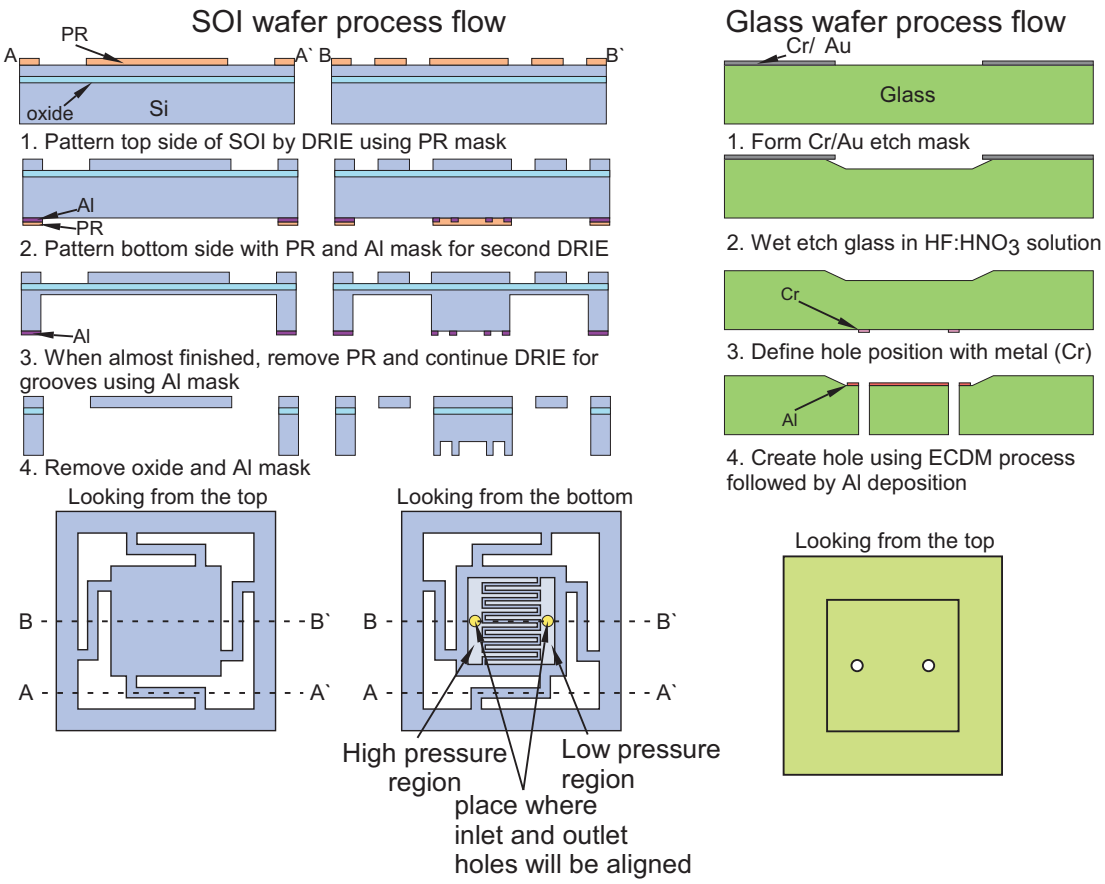

Fig. 3-2: Si-glass micromachining process: The buried oxide layer in a SOI wafer acts as an etch stop for DRIE. A three-step DRIE process is illustrated for the SOI wafer. A glass wafer undergoes a wet etch process and electrochemical discharge machining (ECDM) for inlet and outlet hole creation. Finally, an Al metal layer is deposited and patterned in preparation for anodic bonding to prevent bonding of the valve seat to the glass substrate.

Deep reactive ion etching (DRIE) of silicon was used to form flexures, the valve plate, and groove patterns in the plate. DRIE provides high etching speed, high aspect ratio capabilities, and good selectivity. However, the uniformity of DRIE is not reliable across a full wafer [Tay06, Fas99]. The buried oxide layer in SOI wafers provides an etch stop for DRIE, while the epitaxial layer provides a well-controlled flexure thickness, smooth surfaces, and bulk Si properties. The first DRIE step etches down to the buried oxide layer from the top and defines the flexure structures. Then the bottom side is patterned with Al and photoresist. The photoresist acts as an etch mask for the second DRIE step

that is approximately 400 μm deep. Next, the photoresist is removed and Al is used as an etch mask for the final DRIE step which engraves serpentine grooves for perimeter augmentation. The Al layer is then removed and the wafer is prepared for bonding. A scanning electron microscope (SEM) image of a valve plate after these three-step DRIE is shown in Fig. 5a. Each groove width is 50 μm, and they are etched approximately 120 μm deep.

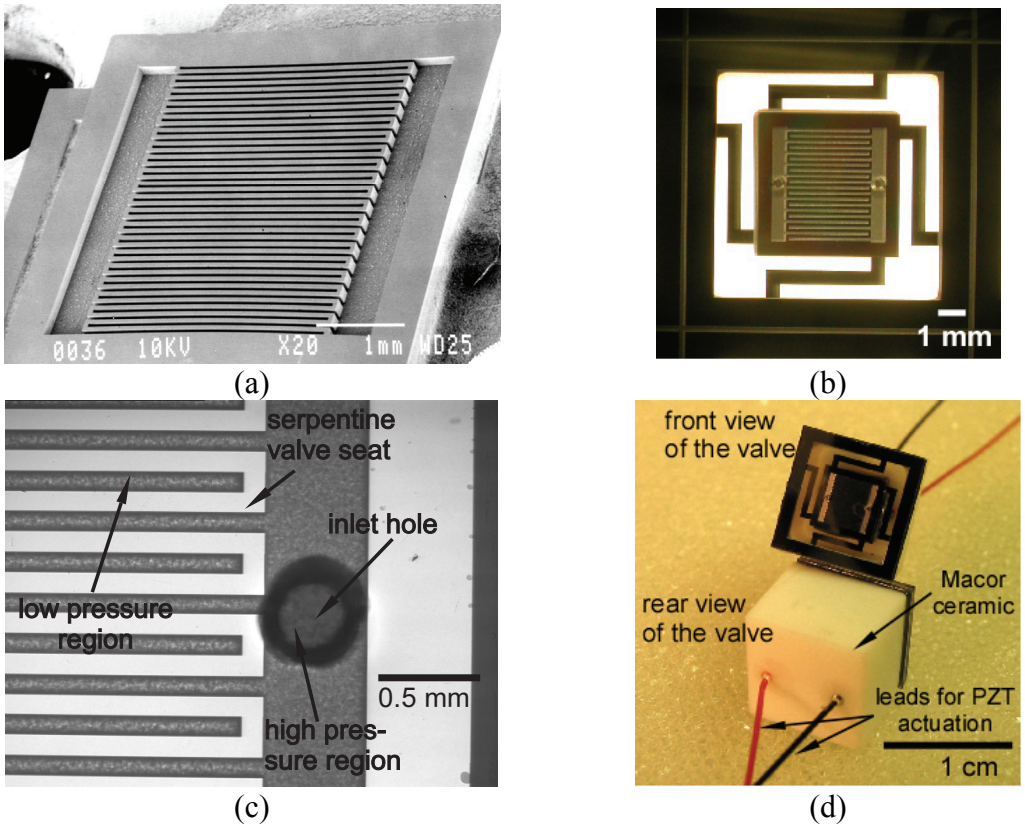

Fig. 3-3: Photographs of the fabricated device. (a) SEM photograph of the silicon valve plate with groove patterns right after the three-step DRIE process. (b) Picture of a die after the anodic bond. (c) Close-up view near the hole with serpentine groove patterns for perimeter augmentation. (d) Completely assembled valve structure. Two valves (front and back) are shown.

For the glass wafer, a recess of 2 μm is made to accommodate the PZT displacement. The recess is formed by wet etching the glass in H_2O:HF:HNO_3=10:7:3 solution, using

Cr/Au/PR layer as an etch mask. After the recess formation, the etch mask is removed and a thin Cr layer (100 nm) is patterned to define the position of inlet and outlet holes that are formed using electrochemical discharge machining (ECDM). ECDM was chosen for through-hole formation against wet etching the glass because wet etching results in significant undercut. ECDM of glass is a rapid, low-cost method that provides a near-vertical profile and is suitable for hole formation. The procedure is performed in 40% NaOH solution at room temperature, and the glass is machined using approximately 300 μm diameter tungsten cathode and 37 V bias.

Before performing the bonding of the Si and glass wafers, a thin layer of Al must be deposited into the glass recess to prevent inadvertent bonding of the valve plate to the glass substrate due to a shallow recess depth and very compliant flexures. Anodic bonding is performed at 400˚C and 800 V, after which the Al layer on SOI wafer is dissolved. The bonded wafers are then diced and prepared for assembly with the ceramic structure and PZT.

The final step is to attach the PZT stack and ceramic cap by epoxy. The piezoelectric actuation provides enough force to displace the Si against inlet pressures that can reach several atmospheres for some cases. The PZT does not need to be bonded to the Si. This may also relieve stress on flexures. The completed valve structure with final dimension of $1\times1\times1$ cm^3 is pictured in Fig. 3-3.

3.1.3 Modeling and Experimental Results

A flow model was based upon the solution of the Navier-Stokes equations using computational fluid dynamic (CFD) software applied to the critical valve components.

The results of the CFD models were used to generate empirical formulas of these components which could be interfaced in order to predict the flow rate through the valve and are discussed in more detail in Section 5.2.2. The valve specific model was obtained by assuming that the diameters for the inlet and outlet are 350 µm and the displacement of PZT at 60 V is 4 µm. In addition, a linear relationship between PZT displacement and voltage was assumed. Thus, seat clearance from the glass substrate can be expressed as in Eq. (3-2).

$$Clearance(\mu m) = 4 - Voltage(\mathrm{V}) \cdot 0.067 \qquad (3\text{-}2)$$

First, room temperature tests were conducted to verify the model and establish baseline performance characteristics of the valve at low and high pressures. Additionally, high and low temperature testing was performed to yield more information on dependencies of the valve.

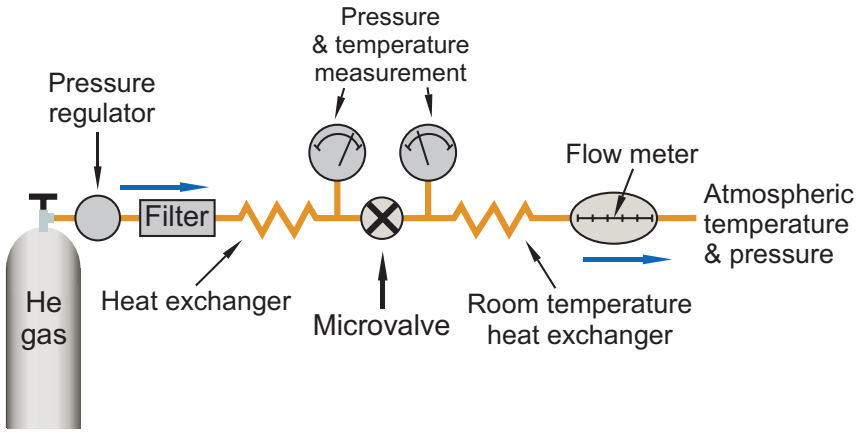

Fig. 3-4: Schematic of the test setup for the He gas flow measurement. Flow rate through the valve is measured while monitoring the inlet and outlet pressure. For low or high temperature testing, heat exchangers are placed to cool or heat the He gas.

Tests were performed at room temperature with He gas flow. Figure 3-4 is a schematic of the test. An in-line thermoplastic filter is placed upstream of the device to trap any particles or moisture. Pressure gauges are mounted so that inlet and outlet

pressure can be monitored. Copper piping (6.35 mm diameter) is connected to 0.4 mm holes in glass through an aluminum header. A ball valve is added at the end so that the outlet pressure can be controlled if necessary.

In the first set of tests, the inlet pressure was regulated (21-55 kPa, gauge), and the outlet was maintained at atmosphere, while the flow rate was measured over 0-60 V actuation. As shown in Fig. 3-5, as actuation voltage increases, the PZT expands, the clearance between the silicon valve seat and glass substrate decreases, and thus, flow rate decreases. With the gauge pressure of 55 kPa at the inlet, flow rate could be modulated from 0 to 980 mL/min. At 60 V, the valve leakage was below the measurement limit (< 0.1 mL/min.).

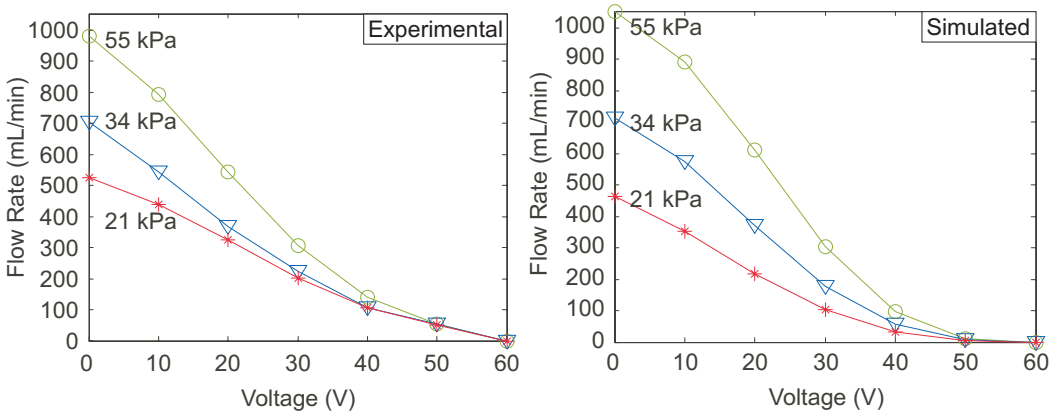

(a) (b)

Fig. 3-5: Flow rates as a function of voltage at room temperature from experimental results (a) and analytic model (b). As the actuation voltage increases, the valve is closed and results in a decreased flow rate.

In a separate experiment, the valve was tested at a higher inlet pressure of 345 kPa gauge pressure to verify high pressure operation, but the pressure difference between the inlet and outlet was kept at 34.5 kPa. A pressure vessel was used to obtain a high absolute pressure while maintaining a relatively low pressure differential across the valve

at room temperature. Absolute pressure was measured at the inlet of the valve while the pressure difference across the valve and volumetric flow rates were measured. Multiple throttling valves were utilized downstream of the valve to allow precise regulation of the pressure difference at high absolute line pressure. Tests were conducted by holding the inlet pressure and differential pressure constant while increasing the valve actuation voltage from 0 to 100 V, and then reducing voltage back to 0 V in 10 V increments. The test result comparison with the model prediction is shown in Fig. 3-6. The flow rate measurements reveal the hysteretic behavior of the PZT actuator. The model and the experimental results show good agreement.

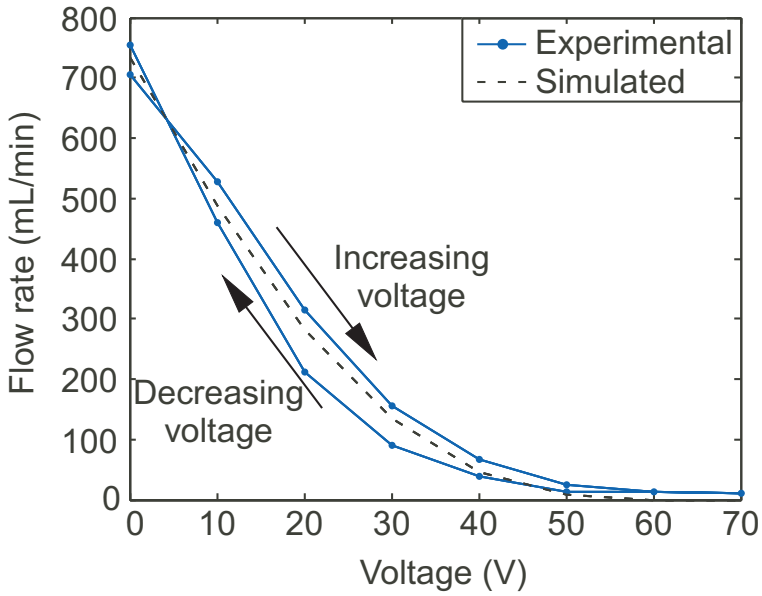

Fig. 3-6: Flow rates as a function of actuation voltage measured at room temperature with an inlet pressure of 345 kPaG and an inlet to outlet pressure differential of 34 kPa. Experimental data is shown with the numerical modeling results. Flow rate measurements show the hysteretic behavior of the PZT actuator.

The flow rates from the model tend to be slightly larger than the experimental results, but in general, they match reasonably well (Fig. 3-5). The main discrepancy comes from uncertainties in seat clearance and inaccurate inlet and outlet hole sizes used in the model.

Compressibility of He gas and hysteretic behavior of PZT also contribute to the difference between the model and experimental data.

Preliminary liquid flow tests were performed at room temperature using oil (viscosity 4.5 cP) to provide solution viscosity greater then saline water. For every test, a liquid reservoir was pressurized with regulated nitrogen gas to control and simulate varying pressures that might be generated from a passive source. The valve outlet was exposed to atmospheric pressure to create a pressure difference across the valve. Flow rates were determined by calculating the mass change in an outlet reservoir over a two minute time period.

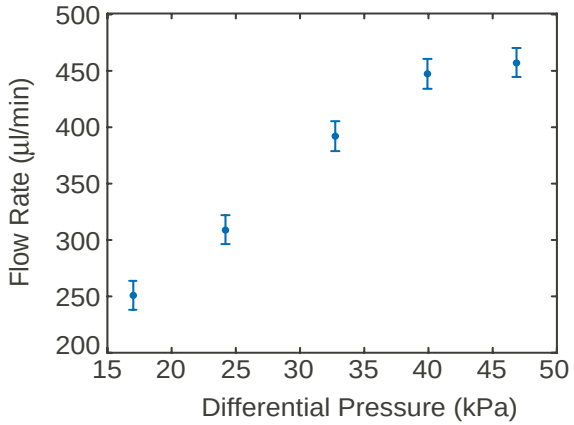

Fig. 3-7: Flow rate through un-actuated valve (0 V) across various pressures. At lower pressures the flow rate changes linearly with pressure.

The liquid flow rate was monitored as input pressure was varied (Fig. 3-7). The flow rate varied linearly with the differential pressure over a range of 250-460 µl/min; the corresponding differential pressure drop was 16 - 47 kPa. Additionally, the valve was actuated by increasing and decreasing the voltage with different inlet pressures (Fig. 3-8). Flow rates were tested over a range of input pressures (108 - 142 kPa), and could be altered from the un-powered, partially open flow rate by as much as 50 µl/min.

Frequency tests were conducted in which the microvalve was actuated with a 50 Hz, 0-60 V square wave with varying duty cycle (Fig. 3-9). This actuation strategy provided more uniform linear control across inlet pressure than DC control. These results suggest that either voltage or frequency can be used to regulate the flow rate. DC operation consumed 0.136 μW and AC operation used 45 mW. As expected, DC regulation consumes less power. AC modulation is less efficient because of capacitive losses in the piezoelectric actuator.

The liquid flow results fail to exhibit necessary performance characteristics for drug regulation. The valve is unable to completely stop liquid flow when actuated at voltages as high as 60 V and regulation range is highly pressure dependent. Additionally, the valve topology has significant dead volume in the cavity of the housing. The difficulty in regulating fluid flow is likely due to the unsealed valve, and dictates the need for a design that addresses these issues. Most performance issues can be addressed by altering the suspension mechanism.

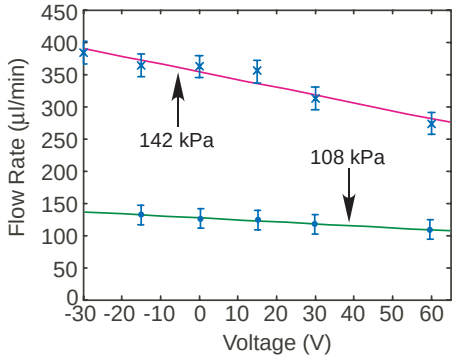

Fig. 3-8: Flow rate versus voltage actuation from -30 V to 60 V. Results are recorded for two inlet pressures, while the outlet is held constant at 101 kPa. Actuation is more pronounced with greater inlet pressure.

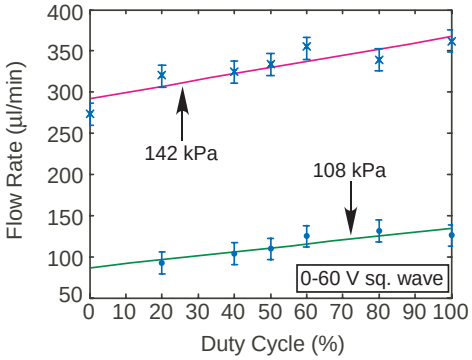

Fig. 3-9: Flow rate changes versus duty cycle for two inlet pressures. The actuation voltage was a 50 Hz square wave from 0-60 V. This method does not rely on the linearity of piezoelectric actuation.

3.2 Membrane Suspension Valves with Embedded Sensors

3.2.1 Device Structure and Operation

The device consists of three main components; a membrane suspended valve for flow modulation, a pressure sensor, and a temperature sensor. Similar to the flexure suspended valves, the valve operates by pressing a suspended silicon plate against a glass plate using piezoelectric actuation. Piezoelectric actuation provides enough force to displace the silicon plate against large inlet pressures (above 1 atm) with negligible DC power consumption and acceptable performance. The membrane suspension greatly reduces the dead volume of the valve and allows for easy integration of sensors. The shape of the valve seat was altered to a circular shape to evenly distribute the stress on the membrane. The valve and actuator are housed inside a Macor structure. Macor was also used to create the fluidic header that is used to connect the inlet and outlet of the valve to the rest of the flow path.

The limited displacement provided by the PZT actuator has been overcome using a valve flow passage design referred to as a perimeter augmentation [Bro07]. The flow area for an out-of-plane valve (A_{valve}) is given by the product of the valve stroke (δ) and the perimeter of the valve seat (p).

$$A_{valve} = \delta \cdot p \qquad (3\text{-}3)$$

Thus, by increasing the perimeter of the valve seat, flow area can be increased substantially, which results in larger flow modulation. Extended serpentine grooves (> 30 cm in length) are fabricated on the valve plate as shown schematically in Fig. 3-10, to increase flow area.

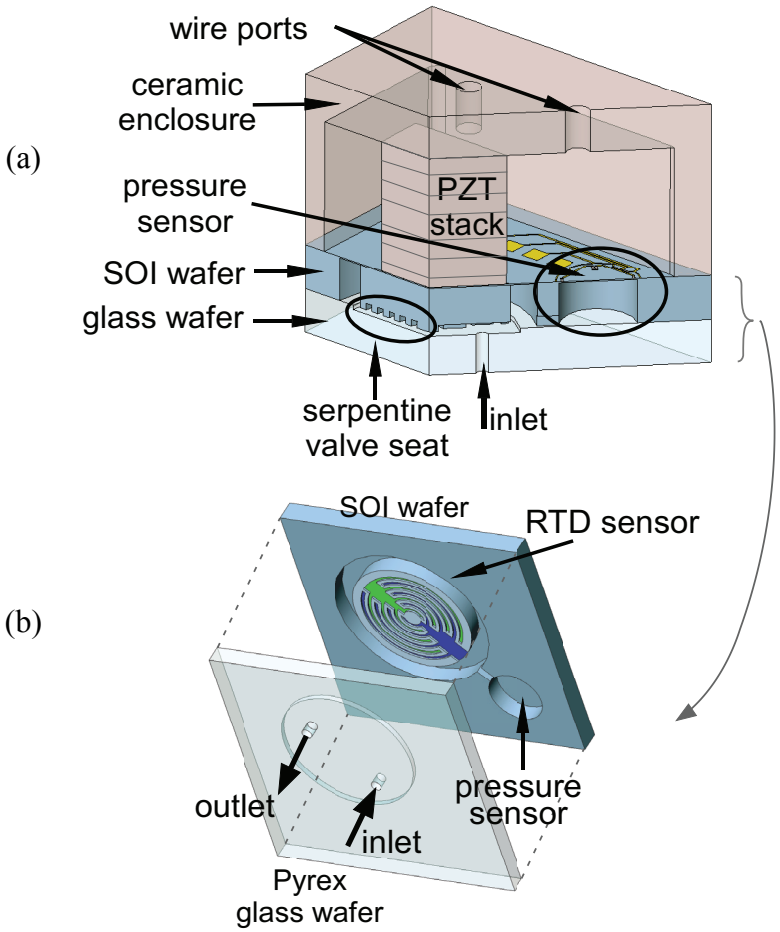

Fig. 3-10: Microvalve concepts: (a) A cut away view of assembled ceramic-PZT-Si-glass valve structure. (b) A valve plate suspended by Si membrane with integrated sensors viewed from the bottom. RTD sensor is located on the back of the wafer

The embedded temperature and pressure sensors enable closed loop control of a drug delivery system. The most common methods of measuring temperature are thermocouples, diodes, and resistance temperature detectors (RTDs) [Yea01]. As the entire device is exposed to the operating temperature of the valve, the requirement of temperature reference junction prevents the use of a thermocouple for the temperature sensor. Diode thermometry uses the temperature dependence of forward voltage drop in a p-n junction biased at constant current. A platinum RTD is chosen as the temperature sensor because of its linear response in the range of our interest, industry standard robustness, and ease of implementation. The RTD is fabricated on the back side of the

valve plate to prevent electrical conduction paths from interacting with the fluid channel. It is strategically placed on back of the valve to measure the temperature of the inlet. Thin silicon between flow path and the sensor element provide a thermal conduction path to accurately measure the temperature while preventing direct contact with the fluid.

The membrane suspension creates a valve with little dead volume in the fluid path. The dead volume in the device is only 0.021 cubic centimeters which is less than 1% of the total valve volume. This is an order of magnitude reduction of the dead volume compared to the flexure suspended valves despite a slight increase in overall valve size. The membrane is also designed to remain closed during a reservoir refill in which back pressures of up to 100 kPa may be experienced. The membrane suspension is fabricated using a process that is easy to integrate with a diaphragm pressure sensor. This allows a feedback control circuit to access pressure data without substantial volume increases. A channel routes the medication from the inlet to the pressure sensor diaphragm.

3.2.2 Device Fabrication

The fabrication process is a variant of the process previously used to create flexure suspended microvalves. Steps have been added to the process to create the embedded sensors, and other steps have been altered to increase yield and decrease process complexity. The valve is fabricated from a silicon-on-insulator (SOI) wafer with layer thicknesses of 50 μm, 0.5 μm, and 450 μm and a 500 μm thick Pyrex glass wafer. The SOI and glass wafers are independently processed, bonded, and then cut into individual die. The fabrication processes for SOI and glass wafers are illustrated in Fig. 3-11.

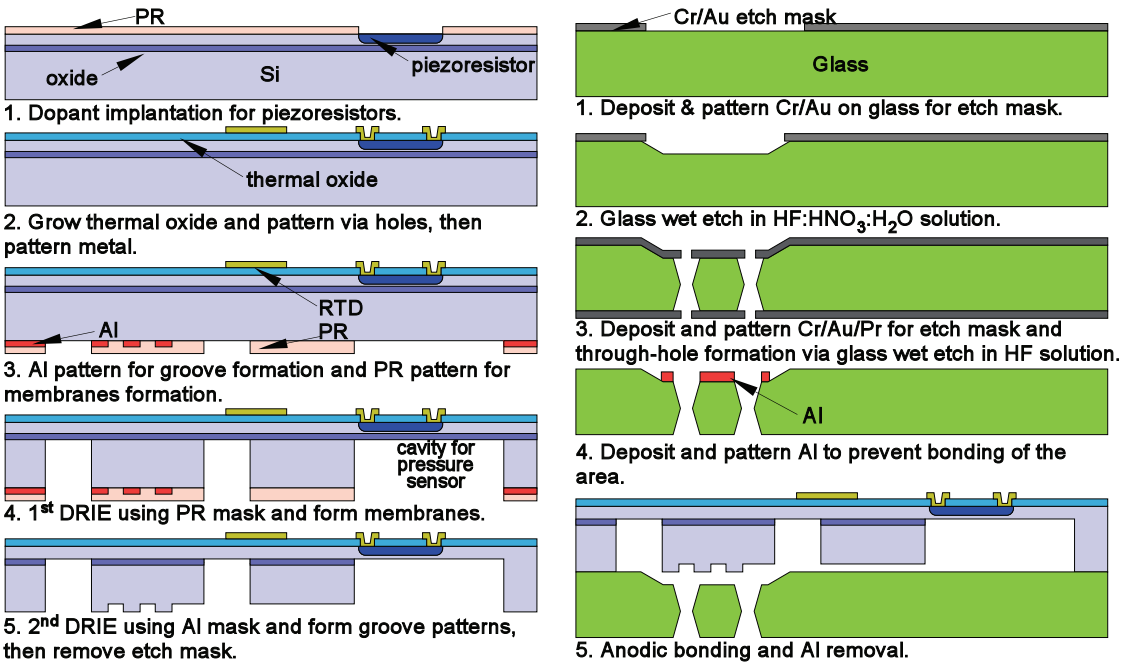

Fig. 3-11: Si-glass micromachining process: sensors are formed on the device layer of the SOI wafer by various surface micromachining techniques. The buried oxide layer in SOI wafer acts as an etch stop for DRIE when forming membranes. A two step DRIE process is illustrated for SOI wafer. A glass wafer undergoes two wet etch steps for a recess and through-hole formation. Next, the two wafers are bonded and diced.

Surface micromachining is done at the very beginning of the process to create the embedded sensors. The SOI wafer is initially patterned with photoresist and exposed to create the pattern for the piezoresistors. The wafer is then sent to Innovion Corporation for dopant implantation. The implantation power level was selected to yield the correct carrier profile after implantation and annealing using the T-SUPREM 4 implantation simulator.

After Boron implantation, the wafers are prepared for oxidation and annealing. An oxide layer provides insulation between metals and silicon substrate. Annealing is necessary in order to activate the implanted dopants, and it also heals damage to the Si crystal structures that occurred during the high energy ion bombardment. A thermal oxide was grown to both provide the necessary isolation and act as the high temperature

anneal needed to activate and diffuse the implanted boron. A 2000 Å oxide was grown at 1000°C for 50 minutes and the wafer was left at the temperature additional 20 minutes in nitrogen environment to allow for enough diffusion time for the implanted Boron.

After the thermal oxidation and anneal, vias are etched in the oxide using buffered hydoflouric acid (BHF) to create contacts to the buried piezoresistors and metal is deposited on the wafers to form the RTD. A platinum layer with titanium adhesion layer are evaporated and put in acetone to pattern via lift off. Lastly, gold is deposited on the contact pads for easier electrical contact with external wiring. Figure 3-12 shows the fabricated die with pressure and temperature sensors.

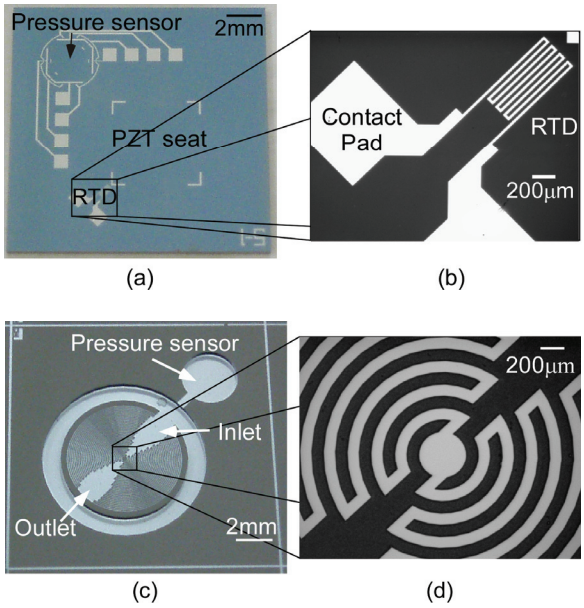

Fig. 3-12: (a) Photograph of the top of the SOI wafer showing metal contact layer with (b) an expanded view of the platinum RTD. (c) Wide and (d) expanded views of the circular serpentine groove patterns for perimeter augmentation from the bottom of the SOI wafer. This side bonds to the glass wafer

After the device side is processed, the back side of the wafer undergoes a two step Deep Reactive Ion Etch (DRIE) process to create the pressure sensor diaphragm, the membrane suspension, and the serpentine groves that increase the flow perimeter. The

two step DRIE process uses aluminum and photoresist masks to achieve desired groove and membrane structures. Figure 3-12(c) and (d) shows the bottom view of the silicon die after these processes. The resulting grooves are 100 μm in depth and provide seat perimeter that longer than 30 cm in length to provide larger flow area when the valve opens.

A Pyrex glass wafer is patterned with a recess, and then undergoes an HF etch to form through vias that act as the valve inlets and outlets. A wet etch method was chosen instead of ECDM to offer a repeatable batch process. After a 2 μm recess is formed, both sides of the glass wafer are patterned with chrome, gold, and thick photoresist. The wafer is then placed in HF until the through holes are etched. The SOI wafer and the glass wafer are anodically bonded at 400ºC, and the wafers are diced to create the final valve die.

After the valves are fabricated, electrical connections are made to the sensors, and they are assembled with a piezoelectric actuator stack and a ceramic Macor cap. The PZT stack is bonded inside the Macor cap using epoxy. Next, the valve is bonded to the PZT stack and the Macor cap using epoxy. The epoxy not only bonds, but also creates a layer that compensates for height differences between the actuator and ceramic housing. At this stage, different methods can be used during the valve bond step to create a normally open, partially open, or normally closed valve. Figure 3-13 illustrates this process.

To create a normally open valve, the PZT stack is energized at 100 V during the last step so the actuator stack shortens after the epoxy has cured. To create a normally closed valve, a stage is used to press down the valve die until it comes into contact with the

unactuated PZT stack. The voltage produced when PZT stack is pressurized is a good indication that contact is made. For the normally closed valve, a reverse polarity voltage is applied to open the valve, so that PZT stack contracts upon actuation. A partially open valve is assembled by using the stage to drive the valve into contact, and then moving the stage away from contact the desired initial gap distance. The final valve structure measures 1.5 x 1.5 x 1.1 cm^3 and is pictured in Fig.3-14.

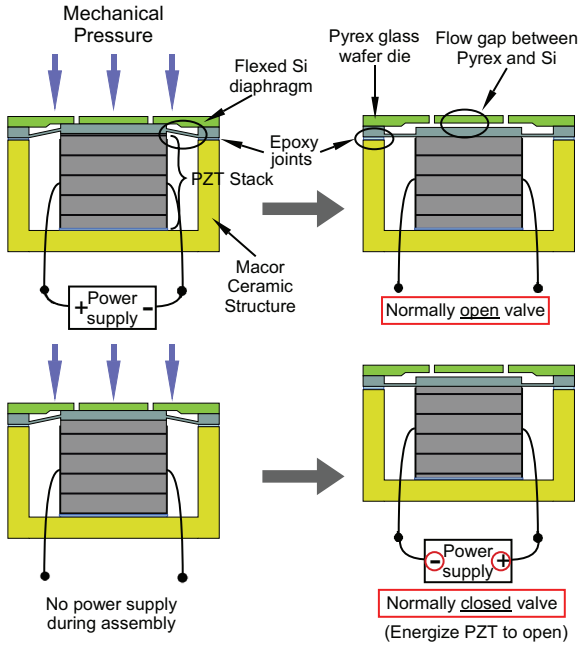

Fig. 3-13: Assembly process can result in either normally closed or normally open valve. Energizing the PZT actuator during assembly results in normally open configuration (top), while no PZT actuation during assembly yields normally closed valve (bottom). For normally closed valve configuration, reverse polarity actuation voltage is applied to the piezoelectric actuator to shorten the PZT stack and open the valve.

3.2.3 Experimental Results

Room temperature tests were conducted on the normally-open and normally-closed valves. The valves were tested at various pressures and temperatures. The temperature sensor was tested across varying differential pressures at several temperatures.

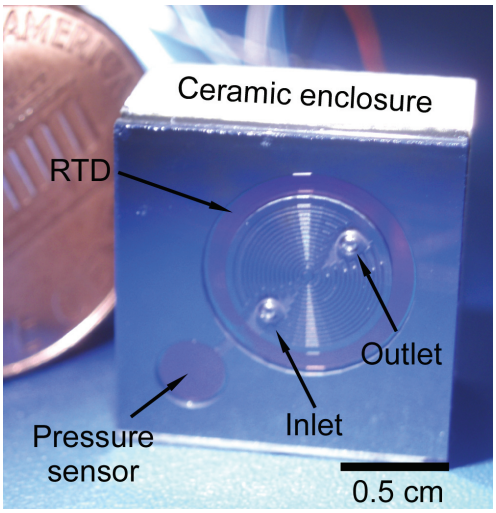

Fig. 3-14: Assembled valve from the glass side with US penny. The pressure sensor cavity is connected to the inlet through a passage. The valve is 1.5×1.5×1.1 cm^3.

The mechanics of the valve diaphragms were studied using a finite element analysis (FEA) tool, Ansys®. The spring constant of the valve diaphragm is about 3.8×10^6 N/m. It is important to note the thermal stress on the membrane as the valve will experience large differences in temperature, because the anodic bonding is done at 400 ºC and the application of the valve is targeted to body temperatures. In the worst case scenario of 6 µm maximum displacement and 10 atmospheres of pressure, the maximum stress was about 0.5 GPa, which is a fraction of silicon's yield strength (≈ 7 GPa), showing the membrane has enough structural integrity to be used for the targeted application.

A normally-open and a normally-closed valve were tested at room temperature with N_2 gas flow. The N_2 gas was introduced to the inlet of the valve at the gage pressure of 52 kPa, while the outlet was connected to a flow meter and vented to the atmosphere. The flow rate was measured as the valves were actuated from 0–40 V. The hysteresis due to the piezoelectric actuator can be seen in the flow rate variations for various set voltages (Fig. 3-15). Additionally, the difference in the hysteresis curve directions is due

to the opposite polarities applied to the normally-open versus normally-closed valves and was as expected. The flow rate went from below the measurement limit (< 1 mL/min) to above 200 mL/min in the normally open valve and above 100 mL/min in the normally-closed valve.

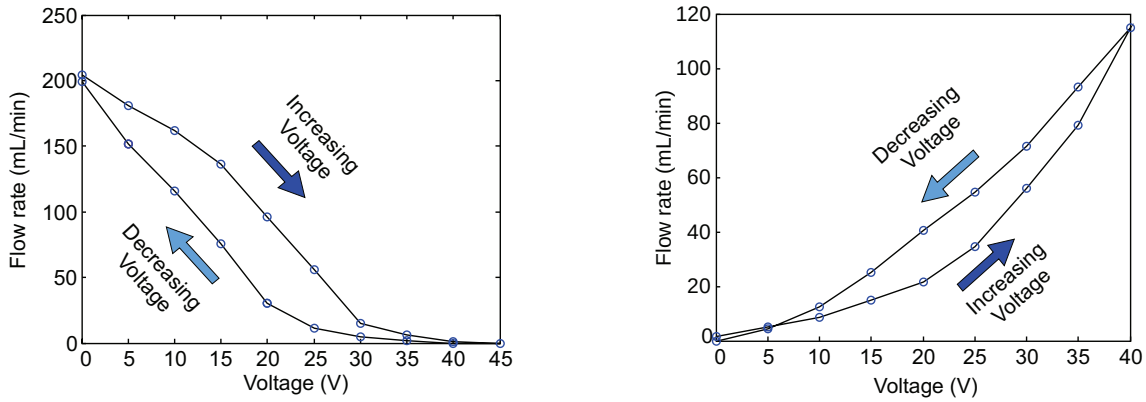

Fig. 3-15: Flow rates as a function of voltage measured. (a) normally open valve, and (b) normally closed valve measured at differential inlet pressure of 52 kPa.

Liquid flow tests were conducted using the valve as part of a complete system. These results conform to the expectations presented by the gas testing and the initial testing using the flexure style valves. Details on the liquid delivery experiments, system modeling, and delivery results are presented in Section 5.1.1 and Section 5.4.1.

The pressure sensor is comprised of four Boron doped piezoresistors on a silicon diaphragm. T-Supreme 4 was used to simulate the Boron piezoresistors. . The pressure sensor was powered at 5 V as the differential output voltage was monitored. Simulations of the resistors suggest a sheet resistance of about 2.97×10^3 Ω/□ and an actual resistance of 26.7 kΩ. Several resistors were tested at room temperature and they averaged a resistance around 23.5 kΩ. This indicates these resistors correspond closely with

simulation and suggest successful ion implantation. The resistors are arranged in a Wheatstone bridge configuration

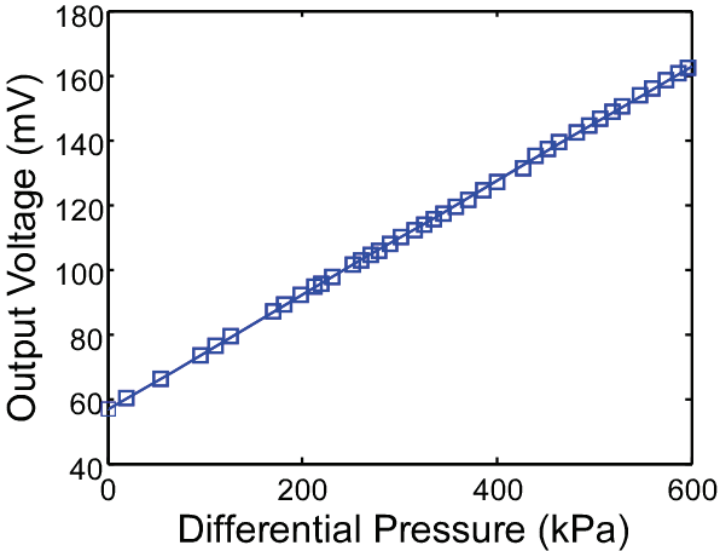

Fig. 3-16: Output voltage from piezoresistive pressure sensor at various differential pressures.

Linearity of the pressure sensor is good. At room temperature, the sensitivity is 356 ppm/kPa with an offset of 59 mV. The device does exhibit a change in offset and sensitivity associated with temperature that needs to be accounted for once it is implanted. The Temperature Coefficient of the pressure Sensitivity (TCS) is defined as,

$$TCS = \frac{1}{S}\frac{\delta S}{\delta T} \qquad (3\text{-}4)$$

where S is sensitivity and T is temperature, and measures how much sensitivity changes with temperature. In our case, the TCS is –6507 ppm/K and is referenced to the sensitivity at room temperature. This behavior is almost entirely dominated by temperature coefficient of piezoresistive coefficient [Kim83].

The offset voltage also changes as temperature increases. Initial offset is introduced due to mismatched resistors. Most mismatches come from geometric difference of

splitting the resistor in transverse direction into two segments to have them placed close to the rim. The temperature effects on individual resistor can be represented as

$$\Delta R = R_{T0}\alpha_R \Delta T + \Delta R\left(\pi(T), \sigma(T)\right) \qquad (3\text{-}5)$$

where R_{T0} is resistance at reference temperature, α_R is temperature coefficient of resistance and the last term describes the change of resistance due to temperature induced stress on membrane [Alj02]. Temperature Coefficient of Offset (TCO) is defined as

$$TCO = \frac{1}{V_{cc}} \frac{\delta V_o}{\delta T} \qquad (3\text{-}6)$$

where V_{cc} is supply voltage and V_o is the output voltage when no pressure differential is applied. We calculated the TCO of 652 ppm/K over the temperature range tested.

3.3 Starburst Valves and Manifolds with Embedded Sensors

3.3.1 Device Structure and Operation

The valve consists of two main components: a membrane suspended boss with a starburst pattern valve seat for flow modulation and multiple pressure sensors. A manifold was made that contains two valve plates with a common outlet and two inlets. These devices were very similar to both the flexure and membrane suspended valves in that the valve operated by pressing a silicon plate against glass. The actuating mechanism was also a PZT stack because of the high force and low power consumption. The membrane suspension maintained the reduction in dead volume, prevented liquid from interfering with the actuator, and simplified the integration of multiple pressure sensors. The shape of the valve seat was altered to a starburst pattern, and the outlet was moved off of the actuation membrane to evenly distribute the stress on the valve walls and increase the flow rate. Aside from mixing, this change also allowed the manifold to

function like a single valve (Fig. 3-17). The valve (or manifold) and actuator were housed inside a Macor structure. Macor was also used to create the fluidic header that was used to connect the inlet and outlet of the valve to the rest of the flow path.

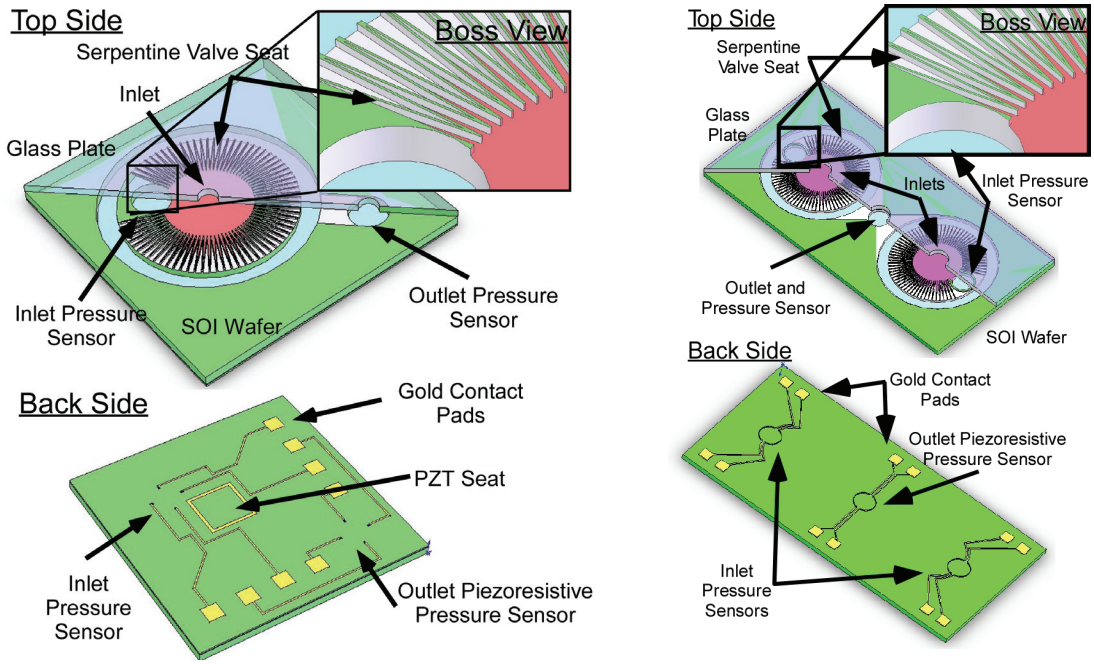

Fig. 3-17: Starburst manifold concepts: (left) A top and back side view of the SOI wafer with the centralized inlet, dual pressure sensors, and starburst valve seat arrangement. (b) A manifold designed with the starburst valve seat used to regulate flow from two inlets. The manifold has a common outlet with a single pressure sensor for mixing in the device and common flow control.

The pressure sensors enable closed loop control of a drug delivery system and have the potential to detect dosing errors. The sensors allow reservoir pressure and the outlet pressure to be measured using the same device on the same substrate. This allows for differential pressure measurements across the membrane with two benefits. First, the effects of common error sources like supply drift, thermal effects, substrate noise, and geometric mismatches are reduced because the same sensor geometries are powered from the same source on the same substrate. Second, errors do to leakage, the fluidic resistance of the catheter, and the fluidic resistance of the reservoir interconnects are

eliminated by placing the sensors as close to the valve channel as possible. This can provide usable information even with drift in the patient's CSF pressure. Additonally, implantation reduces effects related to temperature drift because individuals exhibit relatively little internal temperature variation. Like the membrane suspended valve, Wheatstone bridges using piezoresistors are used for all the pressure sensors because they are easy to interface and have lower output impedance than capacitive readouts.

3.3.2 Device Fabrication

The fabrication process is a variant of the process previously used to create membrane suspended microvalves. Steps have been removed from the process because temperature sensors are no longer being fabricated on the valve die. Additionally, other steps have been modified to increase yield and decrease process complexity. The valve is fabricated from a silicon-on-insulator (SOI) wafer with layer thicknesses of 20 μm, 2 μm, and 450 μm and a 500 μm thick Pyrex glass wafer. The SOI and glass wafers are independently processed, bonded, and then cut into individual die. The fabrication processes for SOI and glass wafers are illustrated in Fig. 3-18.

Surface micromachining is done at the very beginning of the process to create the embedded sensors. The SOI wafer initially undergoes thermal oxidation. A 2400 Å oxide is grown at 1000°C for 50 minutes and then is patterned with photoresist and exposed to create the pattern for the piezoresistors. The oxide is selectively removed with a 9 min BHF etchant step. The wafer is then sent to Innovion Corporation for dopant implantation. Boron implantation was done with a 1×10^{13} cm^{-2} dose at an energy level of 20 Kev with a 7° tilt. The implantation parameters were selected to yield a carrier profile that makes it twice as sensitive as the sensor on the membrane suspended

valve type while measuring pressure in the targeted reservoir range. The implantation, drive-in, and annealing temperatures were calculated using the T-SUPREM 4 implantation simulator.

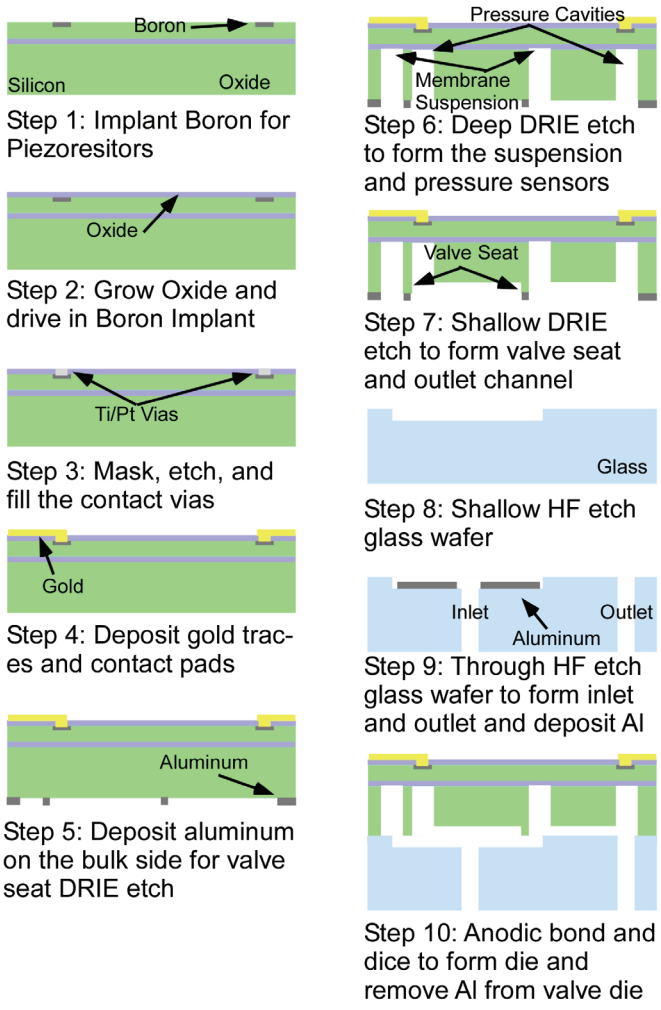

Fig. 3-18: Si-glass micromachining process: sensors are formed on the device layer of the SOI wafer by implanting boron and making ohmic connections through a field oxide to gold contact pads on the device perimeter. The buried oxide layer in SOI wafer acts as an etch stop for DRIE when forming membranes. A two step DRIE process is illustrated for SOI wafer. A glass wafer undergoes two wet etch steps for a recess and through-hole formation. Next, the two wafers are bonded and diced.

After the Boron implantation, the wafers are prepared for oxidation and annealing. An oxide layer provides insulation between metals and silicon substrate. Annealing is necessary in order to activate the implanted dopants, and it also heals damage to the Si

crystal structures that occurred during the high energy ion bombardment. A thermal oxide was grown to both provide the necessary isolation and act as the high temperature anneal needed to activate and diffuse the implanted boron. A 1000 Å oxide was grown at 1000°C for 20 minutes and the wafer was left at the temperature additional 5 minutes in nitrogen environment to allow for enough diffusion time for the implanted Boron.

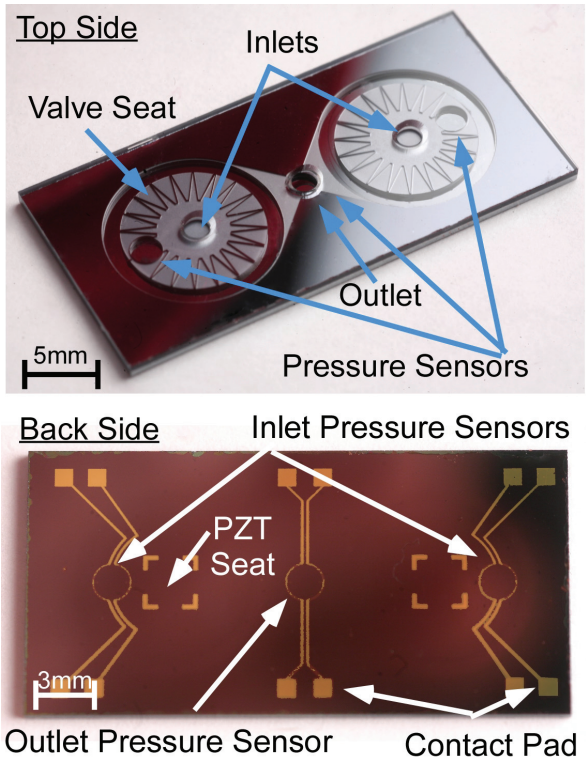

Fig. 3-19: Photographs of the top and back sides of a fabricated valve manifold. The glass inlets and outlets, the two valve seats, and the pressure sensor cavities are clearly visible on the top. The gold contact pads and traces for the pressure sensors, and the gold to define the PZT locations are clearly visible on the back side of the device.

After the thermal oxidation and anneal, vias are etched in the oxide using BHF to create contacts to the buried piezoresistors and metal is deposited on the wafer to make ohmic contact with the Boron doped silicon. A platinum/gold layer with a titanium adhesion layer are evaporated onto the wafer and put in acetone to pattern via lift off.

Lastly, more gold is deposited to form the conductive traces and contact pads for easier electrical interface with external wiring. Figure 3-19 shows the fabricated manifold with a standard starburst pattern.

After the device side is processed, the back side of the wafer undergoes a two step Deep Reactive Ion Etch (DRIE) process to create the pressure sensor diaphragms, the membrane suspension, and the serpentine groves that increase the flow perimeter. The two step DRIE process uses aluminum and photoresist masks to achieve desired groove and membrane structures. Figure 3-20 shows the bottom view of the silicon die after these processes. The resulting grooves are 120 μm in depth and provide a seat perimeter that is longer than 30 cm in length to provide larger flow area when the valve opens.

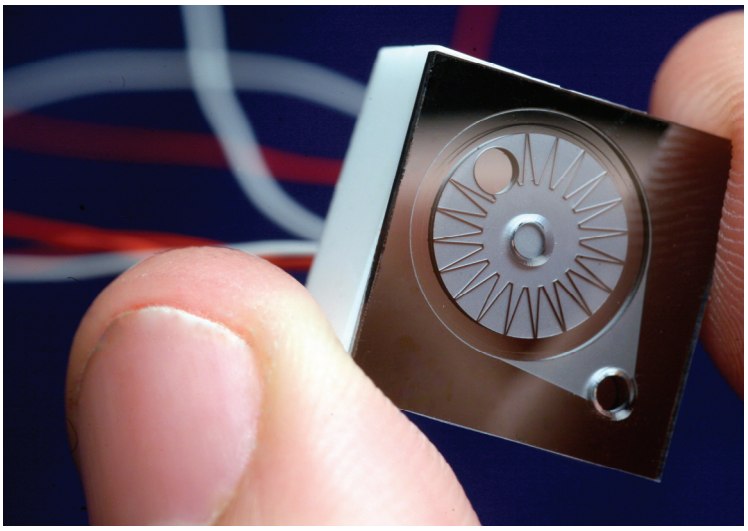

Fig. 3-20: Assembled starburst valve looking from the glass side. The pressure sensor cavities are clearly visible for both the inlet and outlet. The valve is $1.5 \times 1.5 \times 1.1$ cm^3.

A Pyrex glass wafer is patterned with a 1.4 μm recess using BHF, and then undergoes an HF etch to form through vias that act as the valve inlets and outlets. After the recess is formed, both sides of the glass wafer are patterned with chrome, gold, and thick photoresist. The wafer is then placed in HF until the through holes are etched. The SOI

wafer and the glass wafer are anodically bonded at 400ºC, and the wafers are diced to create the final valve die.

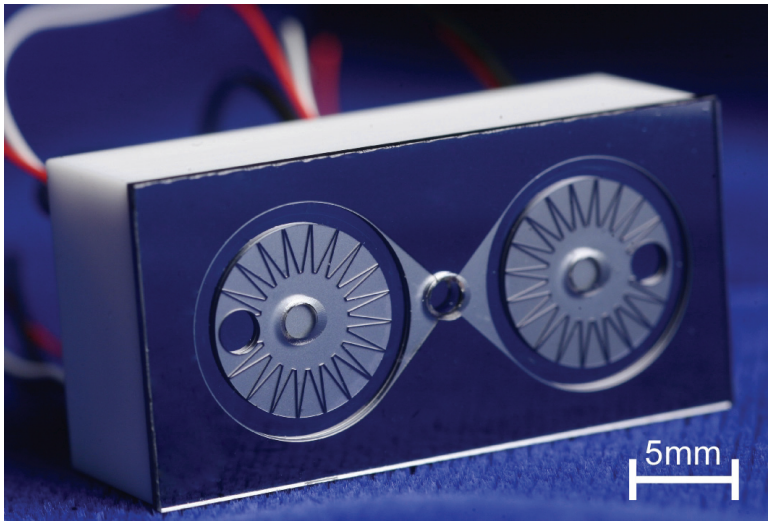

Fig. 3-21: Photograph of an assembled starburst manifold. Both valve plates are clearly visible and the common outlet port is located in the center of the die. The manifold measures 3×1.5×1.1 cm^3.

After the valves are fabricated, solder connections are made to the pressure sensor pads, and they are assembled with a piezoelectric (PZT) actuator stack inside a ceramic Macor cap. The PZT stack is bonded inside the Macor cap using epoxy and assembly continues in the same manner in which the other valves are assembled. The added complications in assembly of a starburst manifold are the two PZT stacks need to be assembled so they are in alignment, and the extra wiring from the plurality of sensors and actuators must be carefully routed. Care in the assembly steps compensate for these difficulties. The valve plates on the manifold can be individually adjusted during the bond step to create a normally open, partially open, or normally closed valve. The final valve structure measures 1.5 x 1.5 x 1.1 cm^3 and is pictured in Fig.3-20, and the manifold structure measures 3 x 1.5 x 1.1 cm^3 and is pictured in Fig. 3-21. The valve and manifold are assembled with a Macor header to provide fluid interconnects (Fig. 3-22).

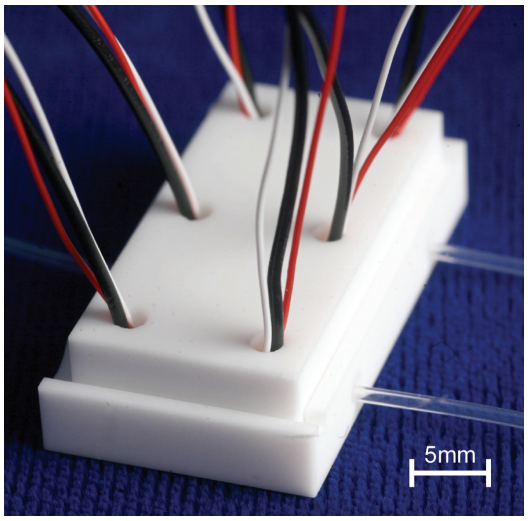

Fig. 3-22: Photograph of an assembled starburst manifold with the attached fluidic header. The inlets and outlet tubes interface with the valve through a Macor connector piece.

3.3.3 Modeling

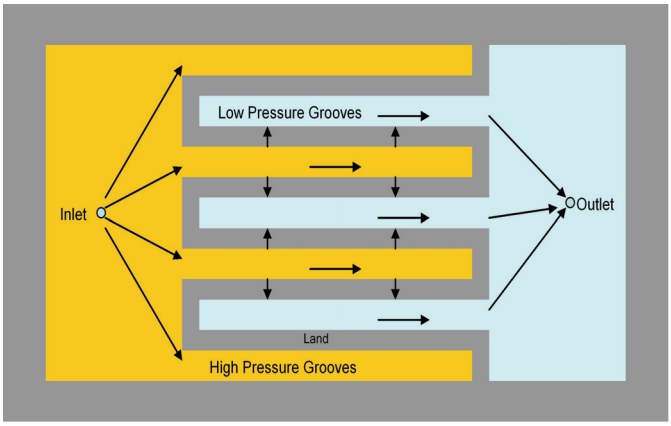

Fig. 3-23: Generalized flow pattern of the valves: Fluid flows from the inlet to the high-pressure grooves, across the land region, the low-pressure grooves, then to the outlet.

A numerical flow model, specific to the perimeter augmented microvalve was developed to examine the flow behavior of the valve [Kle02][†]. The flow through the valve was assumed to be isothermal, laminar, and steady flow. The flow regions are further divided into component level: flow along the grooves and across the land (Fig. 3-

[†] Initial flow enhancement was proposed by Prof. Greg Nellis and initial modeling was performed by Dr. Tyler Brosten at the University of Wisconsin and includes figures 3-23 to 3-25.

23). The flow within the grooves are also assumed to be no slip and fully developed flow while in the land region it is expected that the slip and compressibility will have large effect on the flow characteristics.

The flow through the grooves are represented by

$$-\frac{dP_g}{dx} = \frac{f}{D_h}\frac{\rho}{2}V_g^2 + \rho V_g \frac{dV_g}{dx} \qquad (3\text{-}7)$$

where P_g and V_g are pressure and velocity of the gas at a particular location x within a groove, f is the friction factor, D_h is the groove hydraulic diameter, and ρ is the density (Fig. 3-24). The friction factor f was determined through Computational Fluid Dynamic (CFD) model using FLUENT 6.2.

Variable	**Description**	**Nominal Value**
d	Clearance between land and seat	3.687 µm
L_g	Length of the groove	2800.0 µm
W_{land}, W_{tip}	Width of the land and top	50.0 µm
W_g, D_g	Width and depth of the groove	100.0 µm
P_H	Inlet high pressure	135.8 kPa
P_L	Outlet low pressure	101.3 kPa
r	Density of water (25 °C and 5 atm)	997.1 kg/m^3
m	Viscosity of air (25 °C and 5 atm)	0.0008905 kg/m-s

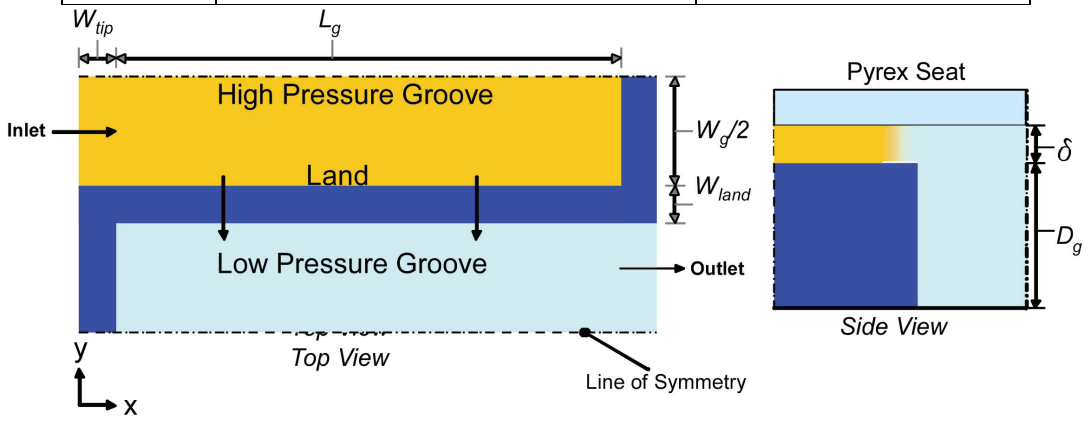

Fig. 3-24: An overview of the parameters used during the analysis of the valve seat geometry,

Component level model for flow through the land is based on rarefied compressible gas through parallel plates and can be represented as

$$\dot{m}' = \frac{\delta^3 P_o^2}{24\mu LRT}\left[P_r^2 - 1 + 12K_n(P_r - 1)\right] \qquad (3\text{-}8)$$

where $\dot{m}'$ is the mass flow rate per unit channel width, δ is the gap height, P_o is the outlet pressure, L is the channel length, R is the ideal gas constant, T is the temperature, K_n is the Knudsen number based on δ, and P_r is the ratio of inlet pressure to the outlet pressure.

The component level model for flow through the land is based on the one-dimensional flow of a rarefied compressible gas through a channel. These physical groove, y-based component level models are interconnected through the steady state numerical solution of interconnected governing equations; these algebraic equations are based on satisfying continuity. The resulting system of equations is solved using the Engineering Equation Solver (EES) [Kim83]. Differential control volumes within the grooves and the land are shown in Figure 3-25.

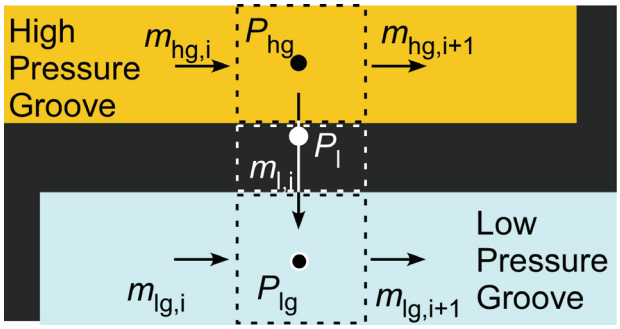

Fig. 3-25 Mass balance terms for the control volumes of the numerical solution.

The governing equation for the flow in the high-pressure groove expresses the pressure drop in terms of a viscous loss and an inertial term. The governing equation is discretized so that the gas velocity in the groove is related to the mass flow rate. For a

complete discussion of the numerical solution scheme, including boundary conditions and the coupling to the manifolds, please refer to [Bro07]. The solution of the system of equations provides the flow through the valve given its actuation state (i.e., the valve clearance) and operating conditions (i.e., the pressures at the inlet and exit, the inlet conditions, and the type of fluid).

An optimization study was done using the flow model developed for the first generation valves to design the valve seat for the starburst pattern[‡]. It was found that are four primary parameters that can be adjusted to increase flow modulation capabilities of the valve. The arbitrary values used for optimization of the individual parameters are listed in the below and graphically represented in Fig. 3-24. (The value of the parameter being optimized changes during optimization).

The model predicts that it would be advantageous to use a saw-toothed groove pattern as opposed to the rectangular pattern used for the flexure and membrane suspended valves. The flow modulation is enhanced using a groove pattern because of decreased flow pressure losses along the groove. The mass flow is progressively reduced as it proceeds into the groove on the inlet side because some material crosses the land area and enters the adjacent groove on the outlet side. Saw-toothed grooves give the entrance to the land, which has the highest mass flow of any point in the groove, the largest amount of area. As the mass flow decreases, so does the groove width. The flow area is proportional to the amount of mass going through the groove. The model predicts the potential increase in flow modulation by using saw-toothed grooves could be 10.4 times

[‡] The saw-tooth serpentine valve structure was proposed by Prof. Greg Nellis and initial modeling was performed by Nick Guldan at the University of Wisconsin and includes figures 3-26 to 3-29

the modulation using rectangular valve seat augmentation. See Fig. 3-26 for an illustration of a saw-tooted valve seat.

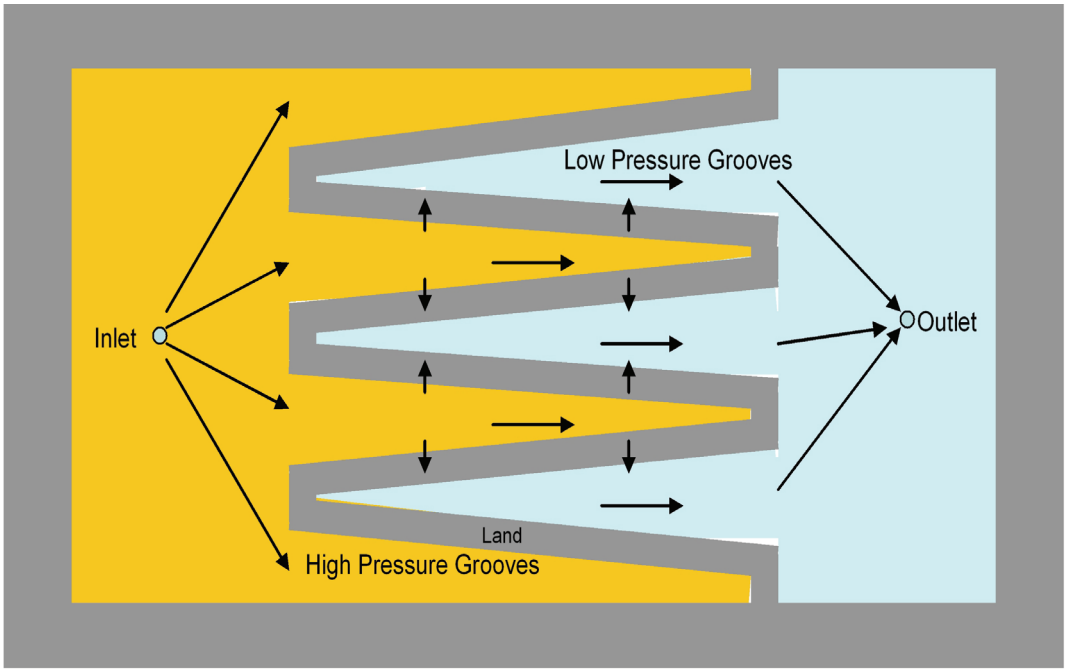

Fig. 3-26: A representation of a saw-toothed valve seat that relies on larger groove openings on the inlet side of the valve. A saw-tooth valve geometry can yield up to 10 times the flow for set valve seat length.

The angle applied to create a saw-tooth valve has significant initial impact that marginally diminishes with an increasing angle (Fig. 3-27). The ratio of inlet over outlet is an effective measure of the degree the valves are saw-toothed. A value of one implies rectangular grooves. A value of 200 implies perfectly saw-toothed grooves.

The model also predicts that flow rate increases with decreasing the land width. In the flexure and membrane suspended valves, the land is 50 micron thick. The limiting factor, outside of manufacturability, is the ability for the thinner valve seat to withstand the pressure drop across it. The valve experiences high pressure on the inlet side and low pressure on the outlet side, and it must maintain enough material to support itself against

that pressure difference. A valve land width of 10 μm would provide 2.86 times the flow of an identical geometry with a 50 μm width (Fig. 3-28).

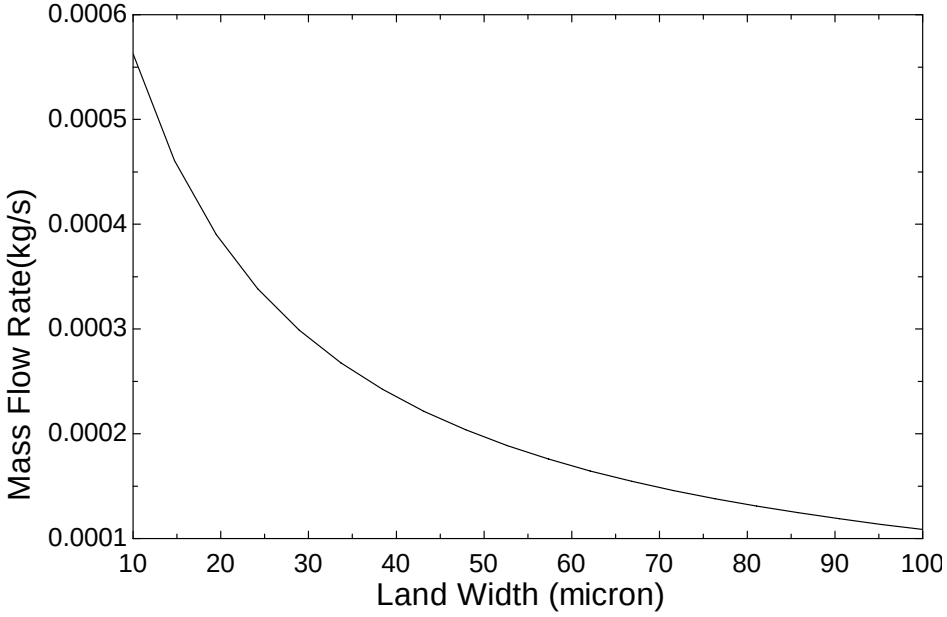

Fig. 3-27: A graphical representation of the increase in relative flow rates through valves with different groove ratios but the same valve seat perimeter. The more pronounced the saw-tooth effect, the greater the flow rate. Valve parameters for the simulation are summarized in the table in Fig 3-23.

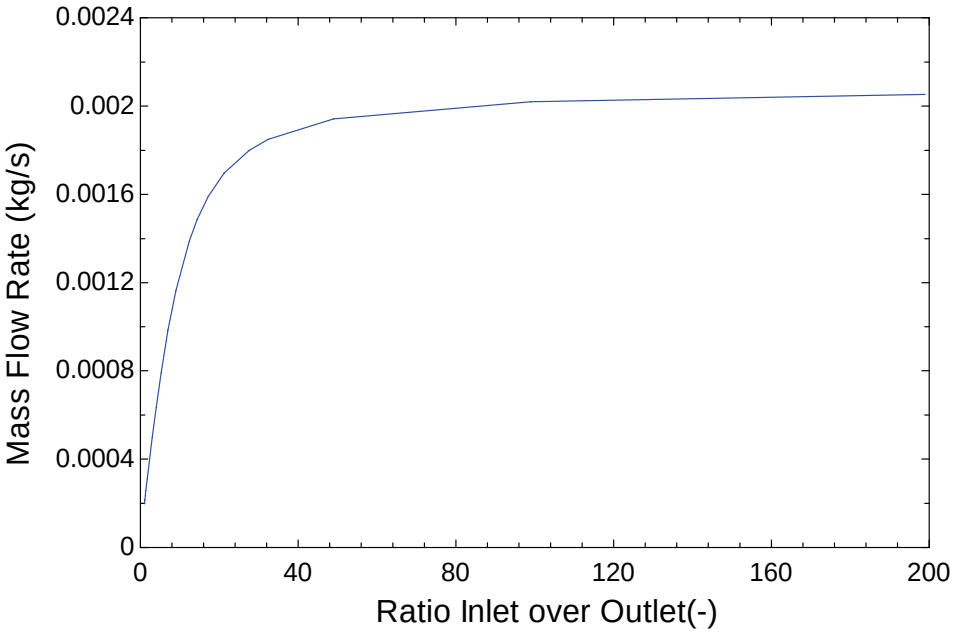

Fig. 3-28: Analysis of the relative flow rates of similar valves with a change in the width of the valve seat. Valve parameters for the simulation are summarized in Fig 3-23.

Increasing the depth of the grooves provides another mechanism for increasing the flow rate through the valve. Increasing the groove depth reduce loss by allowing more flow area for the fluid travelling through the valve. This groove depth is limited primarily by the manufacturing aspect ratio, but also by the same structural limitations listed above. Increasing the groove depth increases the stress on the valve seat. The model predicts increases in groove depth from 100 to 500 μm would increase flow modulation by a factor of 1.21 (Fig. 3-29).

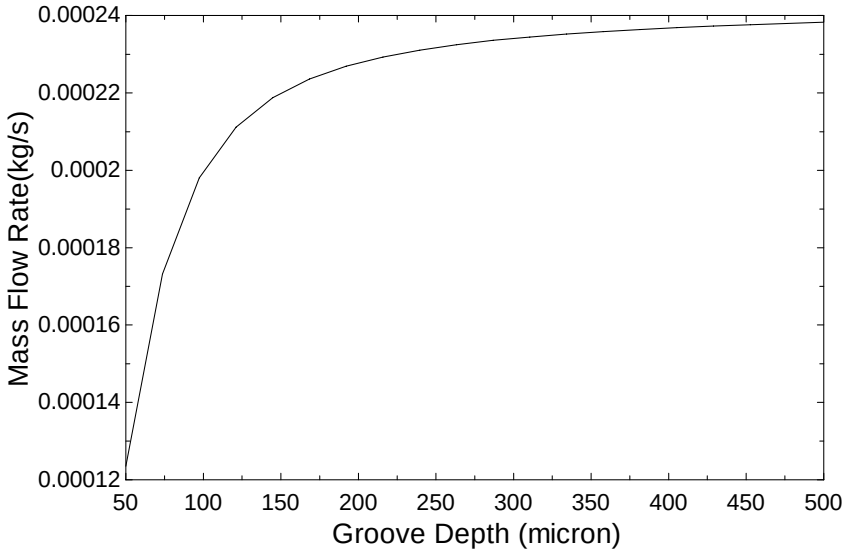

Fig. 3-29: Analysis of the flow rate variations for valves with identical parameters except for the depth of the groove that resides on either side of the valve seat. Valve parameters for the simulation are summarized in the table in Fig 3-23.

One method of creating saw-tooth valves is to create a pinwheel or starburst pattern with the inlet of the valve on the interior of the circle and the outlet of the valve located external to the starburst geometry. This allows for a concentric, uniform design that maximizes both the total valve seat perimeter and the inlet to outlet ratio required to

gain the benefits of a saw-tooth structure. The design parameters for a starburst valve geometry are summarized below (Fig. 3-30)

Variable	Description	Min	Max
A	Width of the tip of a valve seat wedge	5 μm	20 μm
B	Width of the base of the valve seat wedge	50 μm	400 μm
L	Length of the valve seat wedge	100 μm	3000 μm
α	The angle that the ends of the wedge form	1°	45°
r1	This is the outer radius of the boss area	4000 μm	5000 μm
r2	Imaginary radius of the ends of the wedge	800 μm	4000 μm

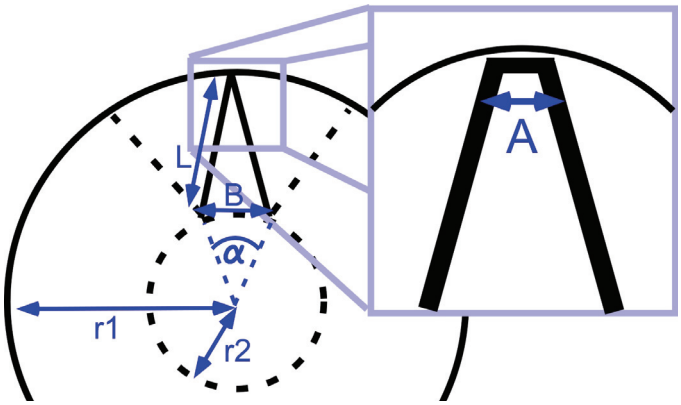

Fig. 3-30: A graphical representation of the parameters used to optimize the starburst pattern designs.

The total length of the valve seat is and the advantage gained from using saw-tooth grooves are the most important factors in maximizing the flow rate through the valve. An analytical model for the total flow area (tF) through the valve with a 30 μm wide seat (Eqn. 3-9) was developed that takes into account the total valve seat length (tL) and the advantages from the saw-tooth geometry (fM).

$$tF = tL \times fM = \frac{2L \times 2\pi \times (r1 - L)}{B + 30\mu m} \times (1 + \frac{2B}{5A}) \quad (3\text{-}9)$$

The total length of the valve seat analytically calculated from the valve geometry and is dependent upon the length of a wedge (L), and the total number of wedges (nW) in an entire circle. If the wedge angle (α) is relatively small (<10°) the number of wedges can

be approximated (Eqn. 3-10) from the imaginary inner circle radius (r2) and the width of the base of a wedge (B).

$$nW \approx 2\pi(r2)/(B+30\mu m) \qquad (3\text{-}10)$$

The improvement in flow rate the results from the saw-tooth groove structures is the "flow multiplier" (fM). A linear approximation for the flow multiplier was extracted from the saw-tooth analysis presented earlier is provided in Eqn. 3-11. This equation only applies for a B/A ratio of 20 or less. Anything beyond that is considered to have an fM of 10.

$$fM = 1+(B/A)\times(2/5) \qquad (3\text{-}11)$$

The total flow area for a valve with a boss radius (r1) of 4500 µm and a width tip width (A) of 10 µm is graphically represented in figure 3-31 with varying widths of the wedge base (B) and wedge lengths (L).

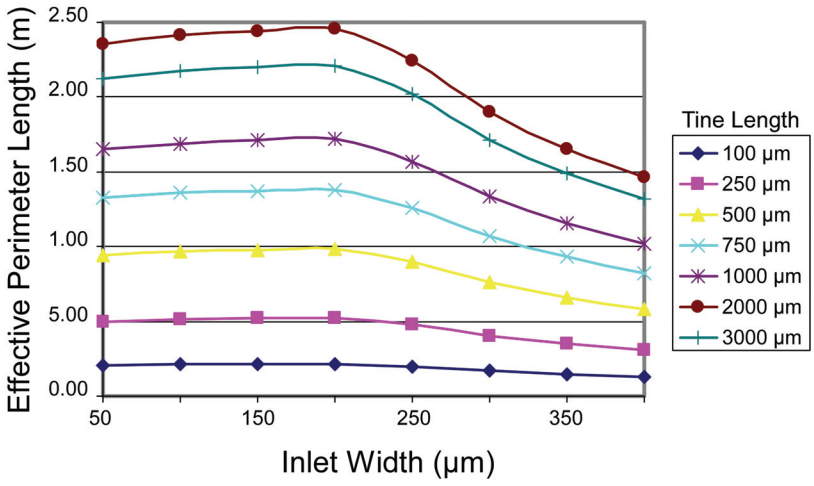

Fig. 3-31: The total effective perimeter length (left axis) as a function of the inlet width of a single valve wedge for different wedge lengths. Simulations are for valves with a boss radius of 4500 µm, wedge tip width of 10 µm, and a valve seat width of 30 µm.

This diagram suggests that the optimal length of B is approximately 200 μm, but this is slightly inaccurate due to the linear assumptions made about the flow multiplier. Instead, a wedge gap (B) of about 150 μm was used because it compensates for mathematical errors in an adjustment direction that is unlikely to have a negative impact. Using these values (B = 150 μm, r1 = 4500 μm, and A = 10 μm) we can solve the value of L that yields the maximum effective flow rate. This value is at exactly one half of the length of r1, or 2250 μm. This dictates a valve geometry with 97 wedges each requiring less than 4° of the outer arc.

In addition to analytically designing the valve geometries to provide high flow rates, pressure sensors are simulated to function in the range of system pressures. This analysis allows maximization of the pressure sensitivity while maintaining functionality up to one atmosphere of pressure (100 kPa). The diaphragm stress for 100 kPa of differential pressure should not exceed ~600 MPa. The following table highlights the maximum sensor diaphragm radius for various thicknesses (in steps of 250 μm) that have stress at differential pressures of 100 kPa of less than 500 MPa.

Membrane Thickness									
10 μm		20 μm		30 μm		40 μm		50 μm	
S (MPa)	Rad	S (MPa)	Rad	S (MPa)	Rad	S (MPa)	Rad	S (MPa)	Rad
385	750	385	1500	477	2500	385	3000	245	3000

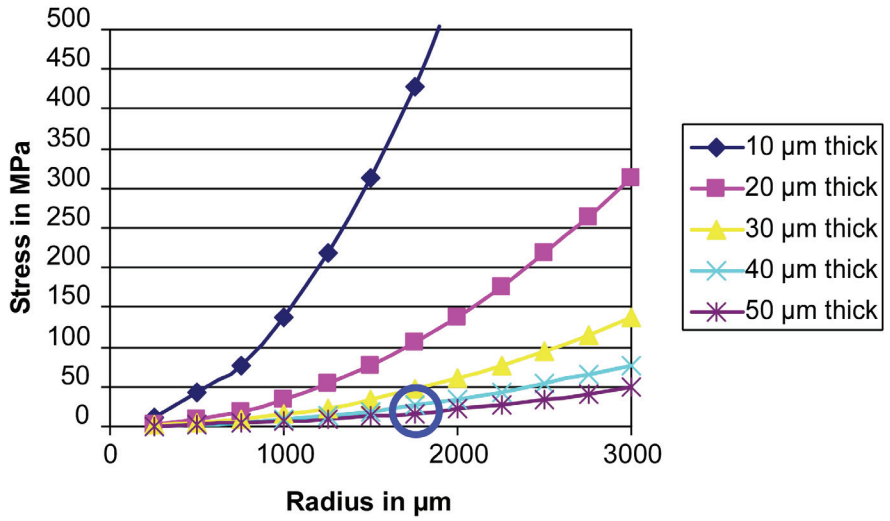

Fig. 3-32: FEA simulated diaphragm stress for sensor membranes of varying thickness and radius at 20 kPa of differential pressure. The circle represents the operating point of the membrane suspended valve.

The membrane suspended valve has a 40 µm thick sensor membrane with a radius just under 1750 µm. This membrane deflects 16 µm and experiences 130 MPa of stress at 100 kPa of differential pressure. The starburst valve must have smaller sensors that approach three times the sensitivity to improve delivery control (Fig. 3-32).

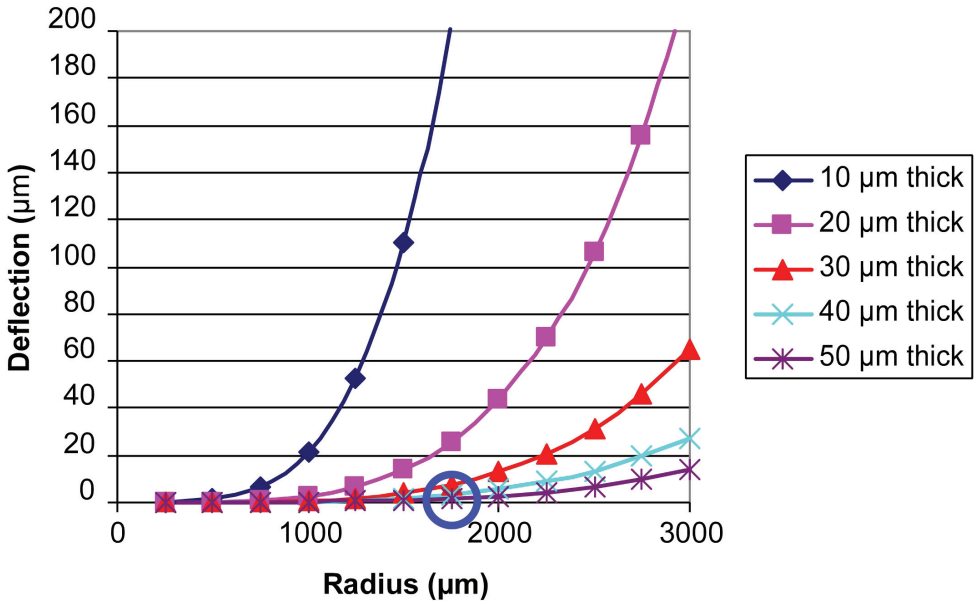

Fig. 3-33: Simulated diaphragm deflection for sensor membranes of varying thickness and radius at 20 kPa of differential pressure. The circle represents the operating point of the membrane suspended valve.

Figure 3-33 indicates that different geometries may experience different membrane deflections for various operating points. A potential linear approximation error occurs when the deflection is larger than a small percentage of the radius. Predictable and linear sensor designs should avoid this condition because of the deviations that result.

When comparing sensitivities to the membrane suspended pressure sensor, relative sensitivities can be calculated by comparing simulated stress in various manifold sensor designs (Table . This is accomplished by comparing membrane induced stress at an arbitrary operating point (differential pressure of 100 kPa). The highlighted value is the membrane suspended pressure sensor.

Table. 3-1: Simulated diaphragm stress and deflection comparison for various sensor geometries

Membrane Thickness	**1X**	**2X**	**3X**
10 µm			
Radius (µm)	Not simulated	500	750
Stress (MPa)	Not simulated	209.5	385.4
Deflection (µm)	Not simulated	6.7	34.4
20µm			
Radius (µm)	1000	1275	1500
Stress (MPa)	170	266.7	385.4
Deflection (µm)	13.6	33.2	68.8
30 µm			
Radius (µm)	1500	1750	2250
Stress (MPa)	170	232	385.4
Deflection (µm)	20.4	237.7	103.2
40 µm			
Radius (µm)	1750	2500	3000
Stress (MPa)	130	266.7	385.4
Deflection (µm)	15.9	66.3	137.5

This analysis assumes the dopant implantation will be near enough to the surface to mitigate the effects of variable membrane depths relative t stress. While this analysis suggests the best sensor can be achieved with a 10 µm membrane thickness, a larger thickness is used for structural support to increase processing yield. During processing, the ring thickness and radius have to sustain pressures that push against an unsupported

boss. These forces include liquid pressure involved in wet etching or cleaning the wafer. Additionally, after assembly, the operational deflection (and stress) occurs across the ring membrane when the valve is closed. The process information is necessary to determine the risks associated with various designs, and the device needs to successfully operate with at least 100 kPa of differential pressure in typical operation modes.

Two dimensional axis-symmetric simulations were done using ANSYS to determine different device layer sizes with different ring radii that would not mechanically fail during processing or device operation. Failure during processing occurs when the pressures on the diaphragm from fabrication steps cause the boss to deflect (Fig. 3-34a). If deflection and stress exceed the mechanical limits of silicon, the valve boss and membrane would burst; leaving a gap in the wafer and ruining the valve. The valve can also fail during device. This occurs if the fluid in the valve is at a high pressure; the high internal pressure causes the unsupported ring of the diaphragm to bend and potentially burst (Fig. 3-34b). The boss does not deflect in this case because it is mechanically supported by the PZT stack actuator. These simulations are used to determine valve geometries that should not experience more than 500 MPa of stress to prevent mechanical failure during fabrication or operation. The simulations assume a boss thickness of 500 μm, a boss radius of 4500 μm, and a diaphragm radius of 5500 μm. These values are close enough to final geometries that the simulations below are applicable for variations of 30% in any dimension.

Processing pressures on the diaphragm are not likely to exceed 20 kPa if care is taken in fabrication steps that involve moving the wafer back and forth when immersed in aqueous solutions (like BHF). Simulations with 20 kPa pressure were done to understand

the effects of processing on the entire membrane and boss for determining fabrication tolerances. The simulations assume a boss thickness of 500 µm and a boss radius of 4500 µm (Fig. 3-34cd). A wafer with a 10 µm thick diaphragm requires more delicate handling during force inducing process steps than a 20 µm diaphragm. It also suggests that a 10 µm device layer should have a ring radius less than 1000 µm to prevent mechanical failure due to 500 MPa of stress; a 20 µm thick device could be designed with a ring radius of up to 1600 µm without mechanically failing. Additionally, the greater the deflection, the less mechanical resistance the membrane has against valve actuation. It is apparent that a 10 µm membrane with a ring radius of 400 µm or greater will not significantly alter the mechanics of the valve. This is also true of a 20 µm membrane with a ring radius of 800 µm or greater.

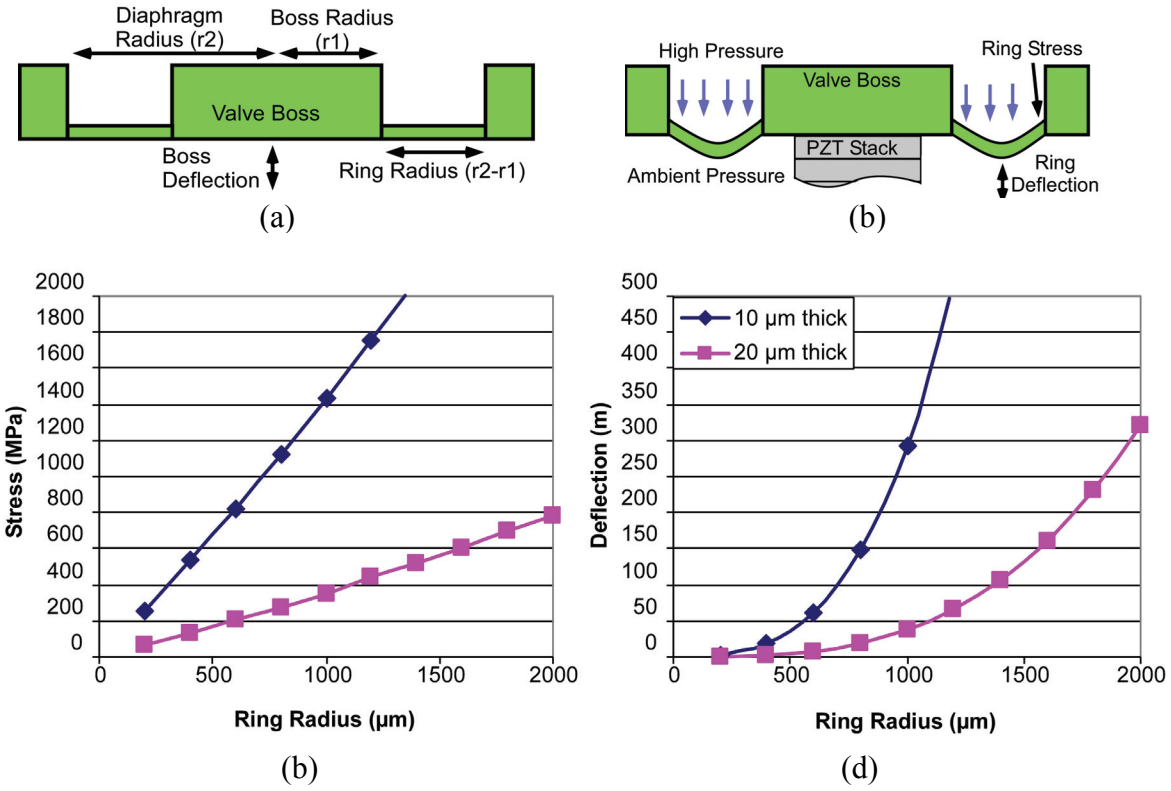

Fig. 3-34: (a) A profile of the valve showing the boss, diaphragm, and bulk silicon on the perimeter of the device. The boss will experience significant pressures during

fabrication, and because it is unsupported it will deflect and cause stress at the boss/ring joint that could cause mechanical failure (b) A profile of the valve showing a boss supported by a PZT stack. Pressure differences between the operating fluid and the ambient environment will cause diaphragm ring around the boss to deflect. This deflection and associated stress may cause mechanical failure during valve operation. (c) Stress induced on the membrane caused by boss deflection for 20 kPa of processing pressure for different ring radii and diaphragm thicknesses (d) Boss deflection under the same conditions

Typical inlet pressures during valve operation are expected to range from 0 to 100 kPa. The stress induced at 100 kPa differential pressure should not exceed 500 MPa to prevent mechanical failure during operation. To meet these conditions the radius of a 10 µm thick membrane can not exceed 1000 µm and the radius of a 20 µm device layer can not exceed 2000 µm. Ring deflection with these geometric constraints is less than 20 µm. Simulations to determine geometries unlikely to mechanically fail during processing and operation suggest the valve should be designed with a 20 µm membrane.

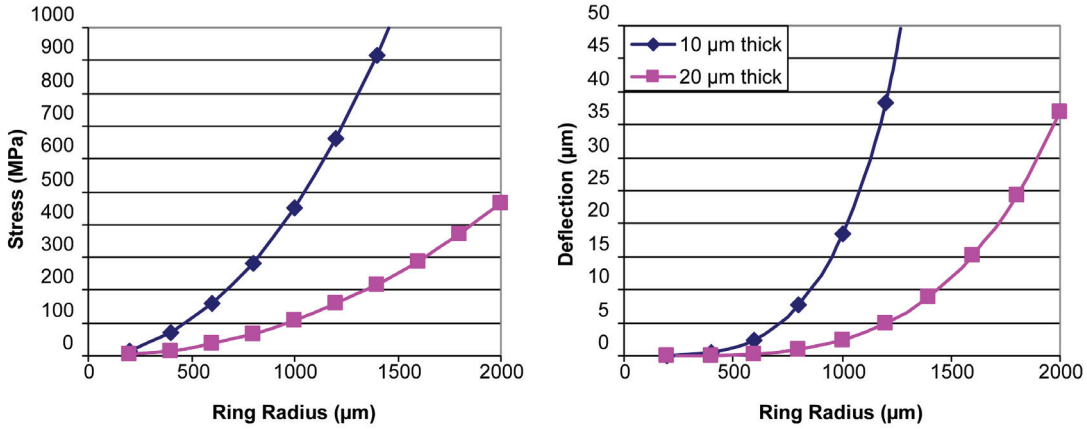

(a) (b)

Fig. 3-35: (a) Stress induced in the diaphragm ring for operating pressures of 100 kPa with varying diaphragm thicknesses and ring radii (b) Deflection of the center of the diaphragm ring for the same operating conditions

3.3.4 Experimental Results

Partially-open starburst valves and manifolds were tested at room temperature with N_2 gas flow and isopropyl alcohol (IPA). N_2 gas was introduced to the inlet of the valve at

varying gauge pressures, while the outlet was connected to a flow meter and vented to atmosphere (Fig. 3-36). The flow rate was measured as both regular and high-flow valves were actuated with various voltages. Normal flow valves were tested with valve actuation voltages ranging from -30 to 90V. Flow was modulated with inlet pressures from 0 to 23.5 kPa with a maximum flow rate of 521 ml/min (Fig. 3-37).

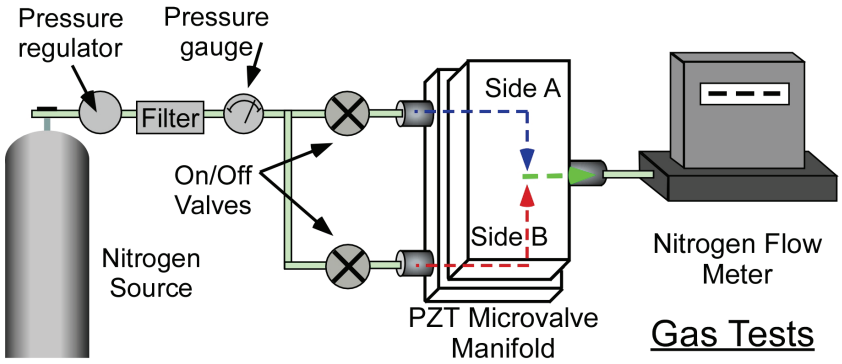

Fig. 3-36: Schematic of the gas tests. Nitrogen is routed to both sides of the manifold and is controlled by inlet valves. The manifold regulates flow rates for pressures, and the flow meter detects the actual rate. Single starburst valves are tested in a similar manner with only a single inlet channel used for testing.

In a similar test using the same experimental structure, high-flow valves (assembled at 0V) demonstrate flow modulation with lower valve actuation voltages ranging from -20 to 40V. Flow was modulated with inlet pressures from 0 to 23.5 kPa with a maximum flow rate of 419 ml/min (Fig. 3-38). These flow rates are 5x greater than those exhibited by either the flexure or membrane suspended valves with the same voltage difference.

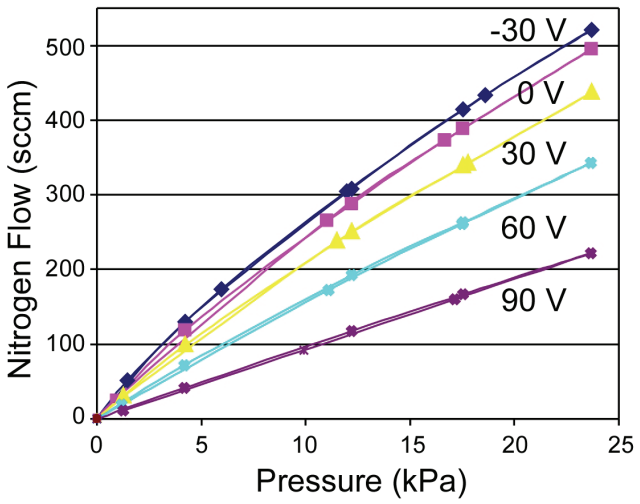

Fig. 3-37: Flow rates in a normal-flow starburst valve for actuations voltages ranging from -30 – 90 V with differential pressures up to 23.5 kPa and a maximum flow rate of 521 ml/min

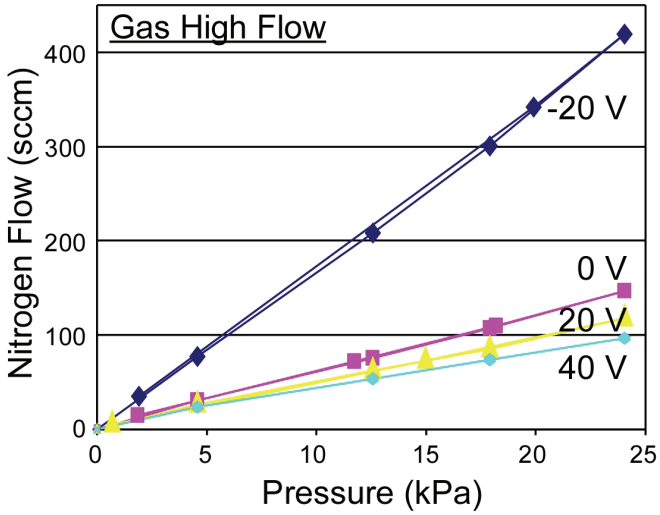

Fig. 3-38: Flow rates in a normal-flow starburst valve for actuations voltages ranging from -30 – 90 V with differential pressures up to 23.5 kPa and a maximum flow rate of 521 ml/min

Both normal and high-flow valves were tested at 14 kPa of differential pressure with a wide range of differential actuation voltages. The hysteresis due to piezoelectric actuation can be seen in the flow rate variations for various set voltages (Fig. 3-39). The hysteresis curve direction is repeatable and dependent upon the polarity applied to the

actuator. The flow rate ranged from 445 to 57 ml/min in the high flow valve and from 336 to 64 ml/min in the normal flow valve.

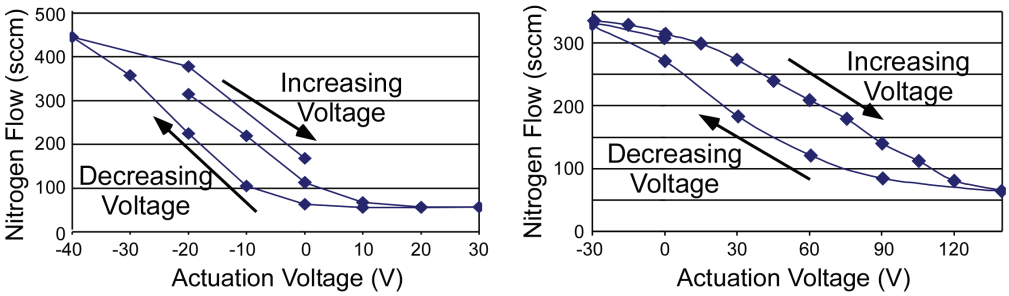

Fig. 3-39: left: hysteresis of a high-flow starburst valve for increasing and decreasing actuation voltage with flow ranging from 445 to 57 ml/min; right: hysteresis of a normal-flow valve at 14 kPa with flow ranging from 336 to 64 ml/min

The preferred voltages for use in a drug delivery system range from 0-80 V due to limitations of charge pumps and power regulation. Normal-flow valves modulated gas flow from 100% when fully open to 64% of this flow within this preferred actuation range. In contrast, high-flow valves provided a dynamic range of 100% to 12% of total flow with the same actuation (Fig. 3-40). Further gas flow data and information on a capillary-driven sealant technique can be found in Appendix A.

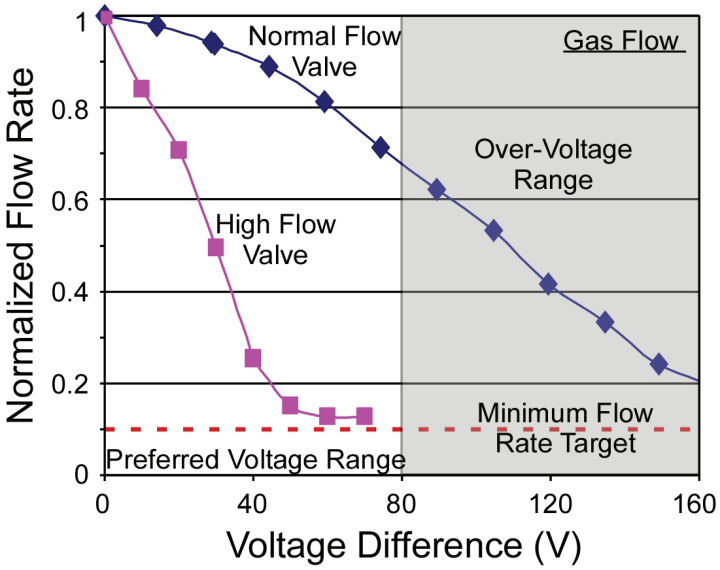

Fig. 3-40: Normal and high-flow valve performance at 14 kPa of differential pressure. High-flow valves provide greater dynamic range using actuation voltages preferred by the drug delivery system design.

For liquid modulation, experiments were conducted using regulated Ni gas to pressure a liquid reservoir. Pressure driven IPA flow is regulated into the individual inlets of the manifold by external valves (Fig. 3-41). Flow leaving the valve manifold (or single valve) is determined by recording the travel of air bubbles through a 1 m catheter at the outlet of the device. The catheter is similar in length and size to those used in intrathecal drug delivery implants. This mimics the output resistance experienced in the drug delivery system and allows for more accurate characterization of the liquid flow rate as it pertains to the targeted system application. Liquid tests conducted on a normal-flow valve with pressurized IPA demonstrate flow modulation ranges necessary for intrathecal drug delivery. A dynamic flow range regulation of 100% down to 8% is realized in the preferred 80 V actuation range (Fig. 3-42).

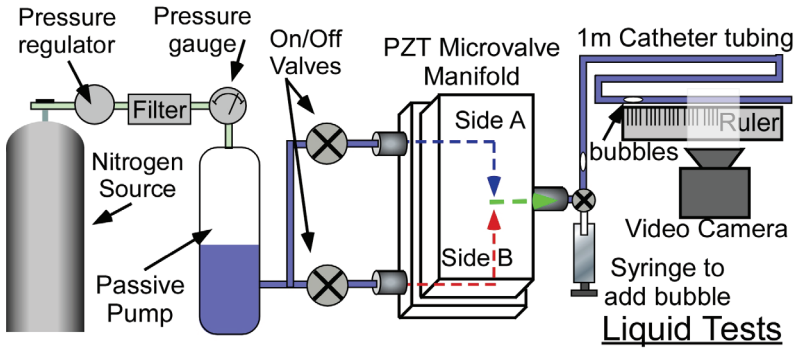

Fig. 3-41: Schematic of the liquid tests. Nitrogen is used to pressure fluid in a large reservoir. The pressurized fluid is independently routed to each side of the manifold, and a video camera records the travel of bubbles through a 1 m catheter tube to determine the flow rate through the valve.

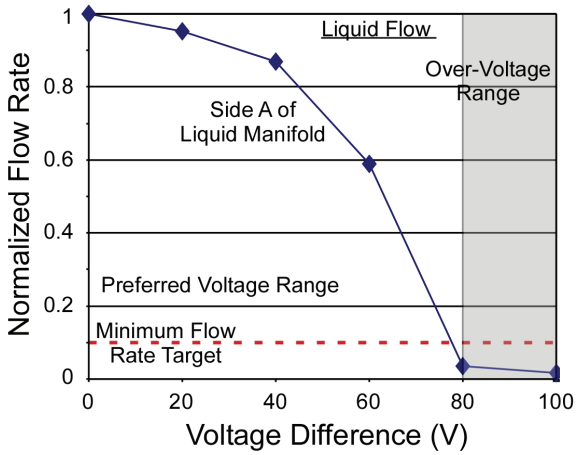

Fig. 3-42: Normalized flow rate of one side of a normal-flow starburst manifold at 14 kPa differential pressure for varying actuation voltage. The target dynamic range is realized in the preferred 80 volt operating range. The flow is regulated from 100% down to below 10%.

Further tests were conducted on a normal-flow manifold to determine mixing from the independently regulated flow channels. Flow from valve A (one side of the manifold) varied from 1.77 mL/hr to 0.028 mL/hr and valve B varied from 2.12 mL/hr to 0.38 mL/hr (Fig.3-43). This flow range represents typical intrathecal drug delivery flow rates. When both valve A and B were open together, flow rates combined from each valve within two separate regimes. At high flow rates, the catheter resistance dominated flow. At lower flow rates, valve resistance dominated, and the combined flow rates were close to the individual flow rates of each valve added together.

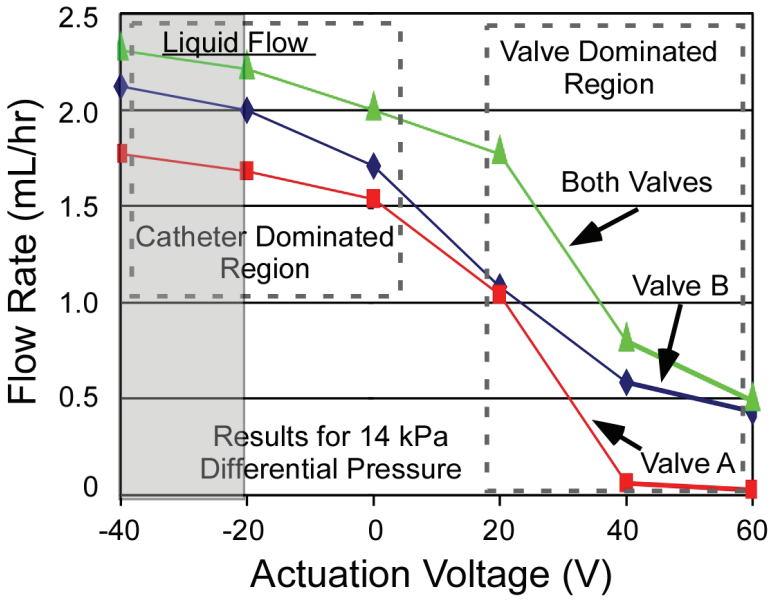

Fig. 3-43: Flow rate of alcohol through individual and combined valves in a manifold at 14 kPa. Catheter resistance is greater than valve resistance at low voltages outside preferred operating region. This results in reduced modulation. Mixing also functions as expected, and is particularly evident in the lower flow rate regimes.

The pressure sensors are comprised of four boron doped piezoresistors on a silicon diaphragm. T-Supreme 4 was used in conjunction with the data from the pressure sensor in the membrane suspended valve design to simulate and design the Boron piezoresistors. The results indicate that the resistors should have a sheet resistance of about 5.3×10^3 Ω/□ and a resistance of 112.6 kΩ. Several resistors were tested at room temperature and resistance varied between 100 kΩ and 150 kΩ indicating close correspondence with simulation. The resistors are arranged in a Wheatstone bridge configuration. The pressure sensor was driven at 5 V as the differential output voltage was monitored. Multiple pressure sensors were monitored over 3 days to determine linearity and sensitivity (Fig. 3-44).

At room temperature, the pressure sensors have a sensitivity of 698 ppm/kPa. This is almost double the sensitivity of the sensors used in the membrane suspended valve design.

The device does exhibit a change in offset and sensitivity associated with temperature that needs to be accounted when it will be used in an implant.

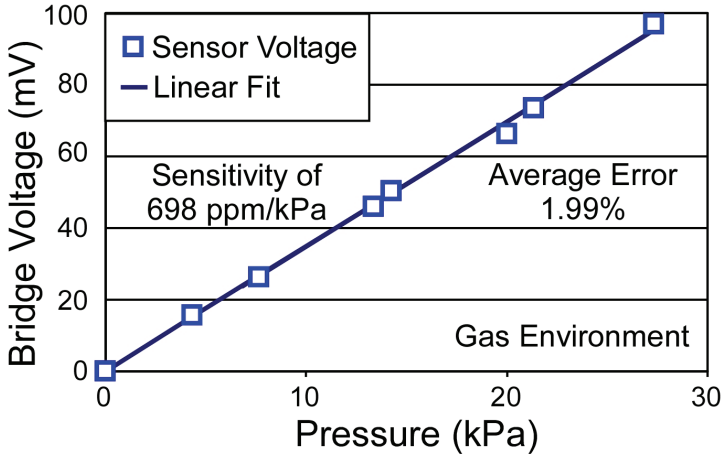

Fig. 3-44: Characterization of pressure sensors with nitrogen gas. Typical differential voltage from a piezoresitive pressure sensor Wheatstone bridge in a manifold has sensitivity of 698 ppm/kPa and an average error of 1.99% of the expected value.

3.4 Discussion

Different types of valves were developed to address the design specifications for the throttle element in the implantable drug delivery architecture. This work also addresses preliminary investigation into embedding sensors and using versatile assembly techniques and geometries. The multiple valve designs and associated testing provide a robust background against which future regulatory designs can be compared and evaluated to meet specific drug dosing requirements.

This work involved the design, fabrication, assembly, and early stage testing of three types of valves; one of which was designed as a manifold. The first valve was suspended by flexure springs and was fabricated using an SOI wafer and a glass wafer. The second valve design was a membrane suspended valve. The third valve design utilized a starburst geometry and was fabricated in a manifold. Membrane suspension allows for

easily embedded sensors, and also reduces the liquid channel dead volume when compared to flexure suspension. The fabrication was modified from the flexure suspended valve process to include sensors and to increase device yield. Further process modification was done for the starburst design to allow for greater pressure sensitivity and more accurate flow range regulation. The valves were assembled with a PZT actuator in a ceramic encasing in a process that can set the gap to a predetermined un-actuated height.

All valves were tested for gas flow regulation across variable pressures. Actuation voltage and respective valve seat displacement is very similar in all valves because they share a common actuation mechanism. This allows for uniform control mechanisms to be developed regardless of the specific valve suspension or seat geometry. Additionally, liquid flows have been characterized using both styles of valve and both sides of the manifold. Results suggest that a membrane suspension is more suited for use to regulate delivery of a drug from a liquid reservoir in an implantable drug delivery device, and multiple pressure sensors are better for accurately monitoring system performance.

Membrane suspended valves have positive and negative characteristics when compared to flexure suspended valves for use in delivery medication. The membrane suspended valves are greater than twice the volume (2.25 cm^3 compared to 1 cm^3), deflect slightly less for a given voltage (due to the stiffer suspension), and have a lower maximum inlet pressure because of the bursting of the pressure sensor cavities. This lower inlet burst pressure is due to a lower failure point of the pressure sensor membrane. This is further reduced when attempting to increase sensitivity by reducing the stiffness of the sensor membrane. This lower pressure limit reduces the maximum pressure that

the reservoirs can generate, and ultimately reduces the maximum flow rates the drug delivery device can achieve. Despite these relative drawbacks, membrane suspension is used in the preliminary system because of the use of embedded sensors, lower leakage levels, reduced channel volume, and higher fabrication and assembly yield.

In summary, this piezoelectric design process allows for application specific microvalve variations while retaining a common assembly and actuation technique throughout. Membrane suspended valves are easily integrated with embedded sensors to form throttles that are able to provide feedback for control algorithms to manage flow. Furthermore, a starburst geometry and manifold fabrication allow for membrane suspended valves to be integrated on the same substrate. Valves were tested with gas and liquid flow across a variety of conditions to determine static and dynamic response over extended time periods. These preliminary results provide the necessary components to design and fabricate the rest of an implantable drug delivery system.

CHAPTER 4:

RESERVOIR SPRING DESIGN, FABRICATION, AND PERFORMANCE

The compressive reservoirs that provide mechanical pressure to drive drug delivery from the system (Fig 2-1) can be designed in a variety of ways. The two mechanical spring designs used in this work are very different in structure, material, and fabrication, but they both apply force to a polymer balloon to pressurize liquid. More detail on the design, fabrication, operation and modeling of silicon torsion springs is in Section 4.1, metal compressive sleeves is in Section 4.2, and discussion on reservoir design is in Section 4.3.

4.1 Silicon Torsion Springs

4.1.1 Device Structure and Operation

Using silicon bulk fabrication techniques to create z-axis mechanical springs is a relatively well developed technique. An example of this technique is a valve that uses flexure springs to allow for deflection while creating the spring force necessary to return the membrane back to its initial position. Traditional z-axis springs are designed with serpentine patterns in silicon to form "leaf" springs. A 15 mL reservoir that operates by pressurizing polymer chambers with traditional leaf springs would require large, long devices. This is due to springs generating force proportional to their length and displacement. Our PET balloon reservoir is 4 mm in diameter. In order to generate

reasonable force and achieve 4 mm of out-of-plane deflection, leaf springs would have to be approximately 10 cm long on each side of the balloon. Torsion springs are a compact alternative because the torque (T) is dependent upon the spring constant (K_θ) and the angle of deflection (θ). The tangential force at the end of an arm is the torque divided by the length of the arm (Eqn. 4-1)

$$T = F \times l = K_\theta \times \theta \qquad (4\text{-}1)$$

This means that the z-axis force from a torsion spring depends on the incident angle of the spring, the torsion spring constant, and torsion arm length (l) (Eqn. 4-2).

$$F_z = \cos(\theta) \times (K_\theta \times \theta) / l \qquad (4\text{-}2)$$

Torsion springs are less dependent upon spring size for force generation than traditional leaf springs because the rotational spring constant and the arm length affect the final size. In order to increase the total force and, subsequently, the pressure generated by the PET reservoir, many parallel springs can used in conjunction.

Torsion springs with the rotational plane set orthogonally to the spring arm would require wide spacing between parallel springs. This limits the number of parallel springs that could apply force to a polymer balloon. To increase the number of parallel springs, the torsion arms are set at 60˚ to the rotation plane. This increases the overall width of the device, but it allows significantly more springs to generate pressure simultaneously. The torsion springs are designed to deliver the most torque in the smallest area while not exceeding the physical constraints of bulk silicon or the limits of fabrication technology. They were iteratively simulated using ANSYS. The final serpentine torsion springs consist of bends that measure 40 μm deep, 60 μm wide, and 150 μm long. The reservoir is pressurized by 50 springs in parallel. The springs at the rear of the reservoir are stiffer

then the springs at the front. This creates a force gradient that allows the reservoir to be emptied from the rear before the front like a tube of toothpaste. The average total spring length is 3500 μm on either side of the reservoir.

4.1.2 Device Fabrication

The microspring fabrication process uses a silicon-on-insulator (SOI) wafer which has an epitaxial layer, a buried oxide layer, and bulk wafer thicknesses of 40 μm, 0.5 μm, and 400 μm, respectively (Fig. 4-1). The use of the SOI wafer in the fabrication process permits the buried oxide layer to provide an etch stop for deep reactive ion etching (DRIE), while the epitaxial layer provides a well-controlled spring thickness and bulk Si properties. PECVD oxide is deposited on the front side of the wafer.

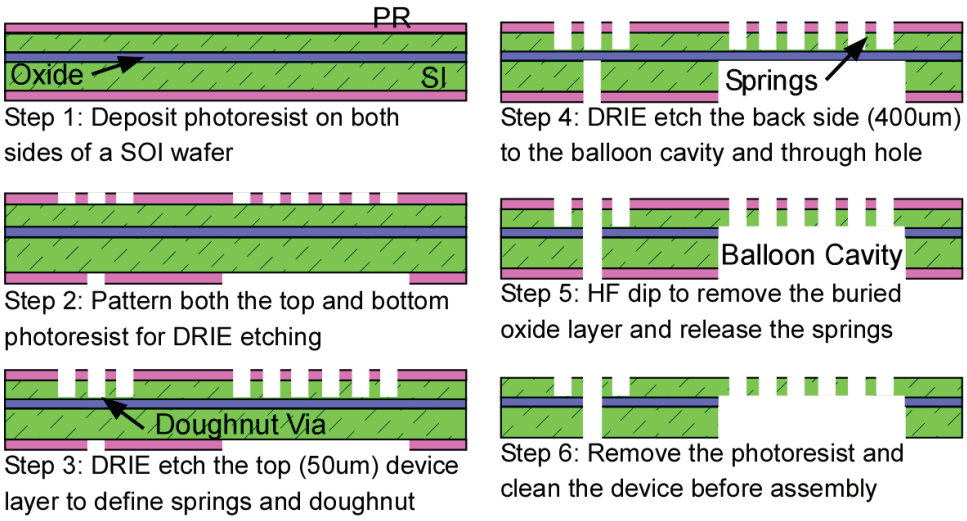

Fig. 4-1: Process for spring SOI wafer with DRIE etch to define springs and backside release DRIE etch and HF dip

Photoresist is deposited on top of the oxide and lithographically patterned to define the torsion springs. The oxide is then plasma etched. Both the photoresist and oxide act as a mask while a DRIE etch down to the insulating layer from the top side of the wafer

defines the bulk silicon springs. About 5 μm of PECVD oxide is deposited on the back side of the wafer. Photoresist is deposited on top of this oxide layer and patterned into release windows. The PECVD oxide is plasma etched. Next, both the oxide and photoresist act as a mask for a 400 μm DRIE etch to the insulating layer. Lastly, the device wafer is etched in HF to remove the insulating and oxide masking layers and release the springs. To prevent stiction from destroying the springs, the wafer is rinsed with water and then immersed in methanol. The methanol is evaporated to finish the spring release.

The reservoir is assembled from the silicon bulk springs, a PET angioplasty balloon, and a bulk plastic substrate. The PET balloon is secured to the plastic base using epoxy. The torsion springs are then aligned to the balloon, and the edges of the die are secured to the plastic base using epoxy. The PET tubing for the inlet and the outlet of the reservoir are connected to nozzles that act as an interface between the balloon reservoir and the Tygon tubing (ID 1.52 mm) used to interconnect the entire system.

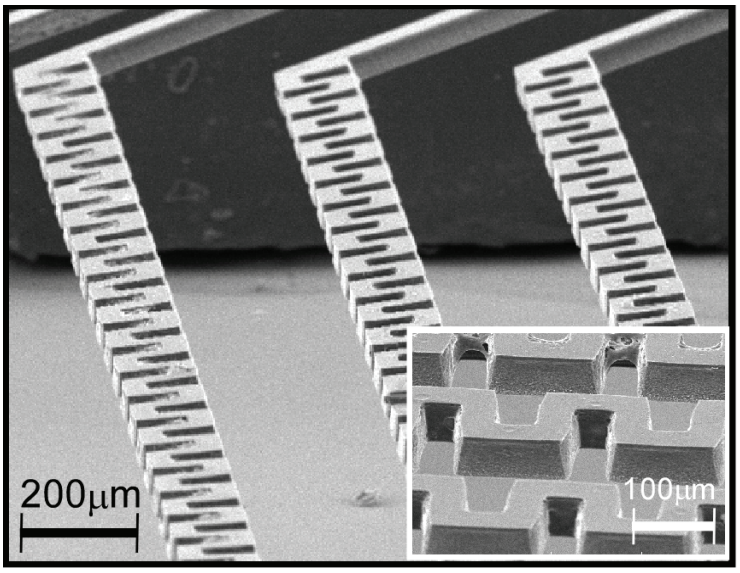

Fig. 4-2: SEM of the torsion springs showing twists of torsion beams

4.1.3 Modeling and Experimental Results

Rotational spring deflection was achieved by inserting solid tubing into the springs (Fig. 4-2). The springs rotated to achieve the necessary deflection. Reservoirs can be characterized by monitoring resultant pressures as they are. The experimental setup (Fig. 4-3) used a gas to liquid pressure conversion method that was very similar to the valve flow rate tests. The gas pressure was slowly increased and then held constant as the deflection of the valve was measured.

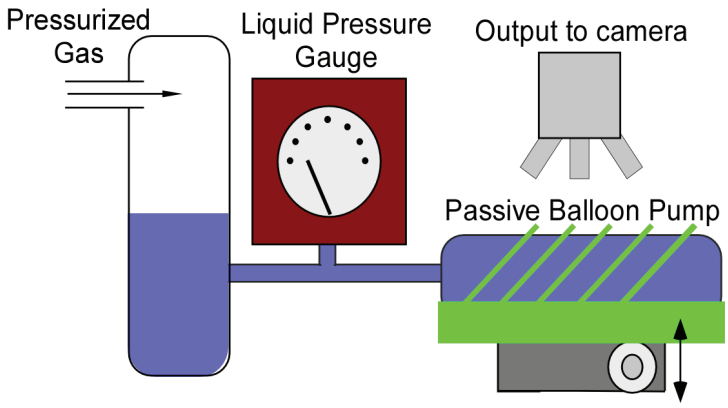

Fig. 4-3: Setup to measure deflection of springs using z-axis focal adjustment

After the measurement, the pressure was again increased and the process was repeated until the balloon was completely filled. The balloon was then allowed to empty. The process was repeated several times to verify functionality. As the PET reservoir was inflated, the springs underwent z-axis deflection and lost focus. This deflection was measured by setting the springs into focus on an optical microscope before applying pressure, and then lowering the entire device with a z-axis micrometer stage actuator after pressure was applied. Once the image of the springs returned to focus, the distance the stage travelled was recorded as the deflection of the springs for a given inlet pressure. To prevent measurement errors, the stage was only lowered, never raised. Also, the entire measurement structure was reset for each empty-to-full reservoir test. The optical

deflection measurement techniques have an error of ± 5 µm. The torsion springs deflected up to 4 mm as the reservoir was inflated (Fig. 4-4). The spring deflection for various pressures (Fig. 4-5) is nonlinear, and required up to 80 kPa to fully fill the reservoir.

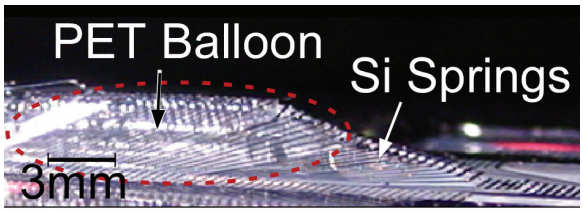

Fig. 4-4: Photo of springs after balloon insertion showing 4 mm out of plane deflection

ANSYS simulation data was used in a MatLab model of deflection and z-axis force. The spring force translates into reservoir pressure via the cross sectional area of the beams that are in contact with the PET balloon. The predicted results from simulation are plotted against the actual measured results of spring pressure and deflection (Fig. 4-5). The simulated results are of the same order of magnitude, but the actual results show a deviation from simulation at both low and high pressures.

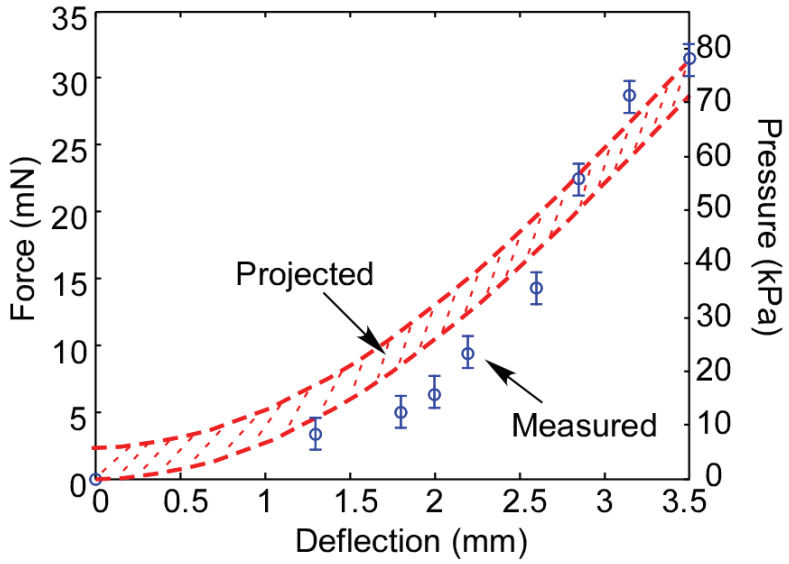

Fig. 4-5: Measured and predicted z-axis spring deflection and resultant force and pressure.

The variations can be due to differences in fabricated spring dimensions versus modeled dimensions. They can also be the result of the mechanical properties of the PET balloon. It was modeled as contributing no effect, but it takes force to initially expand, and requires a high force to expand after it is filled to its nominal volume.

4.2 Metal Compressive Sleeve Springs

4.2.1 Device Structure and Operation

Traditional methods for pressurizing reservoirs in drug delivery systems include using gas, mechanical springs, material elasticity, or osmotic pressures. Most require significant volume when compared to the volume necessary for the fluid itself, which diminishes the VER of the final implantable system. This problem is magnified if the system is scaled down in overall volume. In contrast, elastic compression of the reservoir may have low dead volume if properly designed. Compressive springs are used to pressurize the reservoir because they take little volume, generate necessary pressures, and plastically deform instead of break.

The compression reservoir springs are fabricated in a mesh. The springs are batch fabricated in a sheet, and wrapped around the balloon to form the compressive sleeves (Fig. 4-6).

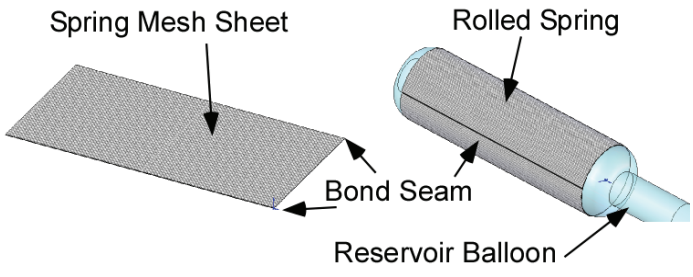

Fig 4-6: The springs are designed as flat mesh sheets that are rolled around the balloon to compress the liquid inside and generate pressure

The liquid container is a PET balloon measuring 20 mm in diameter, and 60 mm in length. This provides a total reservoir volume of 18.85 mL. This is comparable to the volumes of the current intrathecal drug pumps made by either Medtronic or Codman (ranging from 15 mL to 50 mL).

The material used to form the spring is 45% cold-reduced sheet Elgiloy. Elgiloy is a Co-Cr-Ni alloy in 100 μm sheets. Material information for Elgiloy was found for 40% and 50% cold-reduced, so the material properties used in spring design were taken as an average of the two. This material was chosen for springs because of its high elasticity. It also is ductile, so plastic deformation occurs before the springs physically break. Actual and estimated material properties were taken from Matweb (www.matweb.com) and are summarized in Table 4-1.

Table 4-1: Elgiloy Sheet Material Properties

	40% Cold Reduction	50% Cold Reduction	45% Cold Reduction (Estimated)
Density	8.3g/cc	8.3g/cc	8.3g/cc
Tensile Strength (ultimate)	1440 MPa	1620 MPa	1530 MPa
Tensile Strength (yield)	1170 MPa	1310 MPa	1240 MPa
Poisson's Ratio	0.226	0.226	0.226
Modulus of Elasticity	189.6 GPa	189.6 GPa	189.6 GPa
Elongation at Break	4%	3%	3.5%

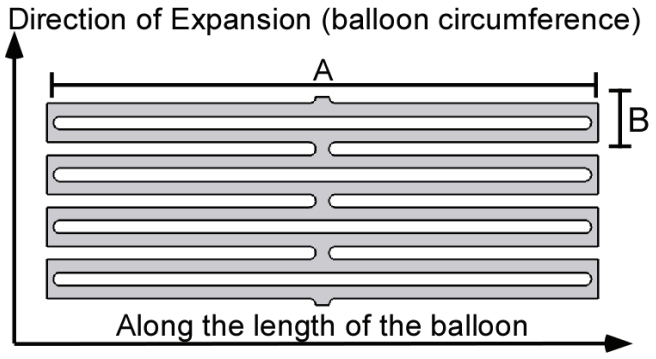

Fig. 4-7: Four Cells of a balloon mesh are shown. Stiffer springs have dimensions (A: 6 mm; B: 600 μm). More expandable springs have dimensions (A: 10 mm; B: 600 μm)

The springs were designed as a mesh that consists of a single cell that is continuously repeated to form a sheet that can be rolled into the compression sleeve. Four cells with the direction of expansion are shown with relevant dimensions (Fig. 4-7).

4.2.2 Device Fabrication

Fabrication of the planar springs is done by photochemical machining (PCM) of a bulk metal sheet. PCM, or chemical blanking, is a process that utilizes a laser-defined mask to lithographically pattern a photoresist (PR) layer covering the base metal layer [ASM89]. The PR is developed and the unprotected metal is etched with a heated spray of etchant. In this way, intricately patterned flat metal parts can be produced, with thicknesses ranging from 10 μm to 1.6 mm. The base metal sheet is typically 300 x 450 mm, although larger sheets can easily be processed.

PCM is derived from printed circuit board etching processes, so most common photoresists and etchants are geared towards processing copper. However, with appropriate surface treatment (to promote photoresist adhesion) and modified etchants, many other metals can be processed. The photoresist is typically laminated onto both sides of the base metal layer, and both sides are exposed simultaneously. Typical etchants include ferric chloride, cupric chloride, sodium hydroxide, hydrochloric acid, or even hydrofluoric acid for especially chemically resistant metals. Among others, copper, aluminum, stainless steel, nickel alloys, platinum, tungsten, and even titanium can be processed with an appropriate etchant. The etching is an isotropic process, so masks are adjusted for undercut based on the thickness of the part. Feature sizes are constrained, and the minimum size is usually equal to the thickness of the work piece. Tolerances of

+/- 10% of the part thickness are typical. Material removal rates are approximately 10 - 50 µm/min, although looser tolerances can allow for faster etching.

One advantage of PCM includes burr-free processing of thin metal without distortion or other physical changes to the work piece. Additionally, very hard and brittle metals are machined without difficulty. Of importance to this work, Elgiloy can be processed with PCM. Chief disadvantages of PCM include the limitations imposed by the chemistry of the work piece, as well as the fact that sharp radii cannot be produced due to the undercut involved in the isotropic process.

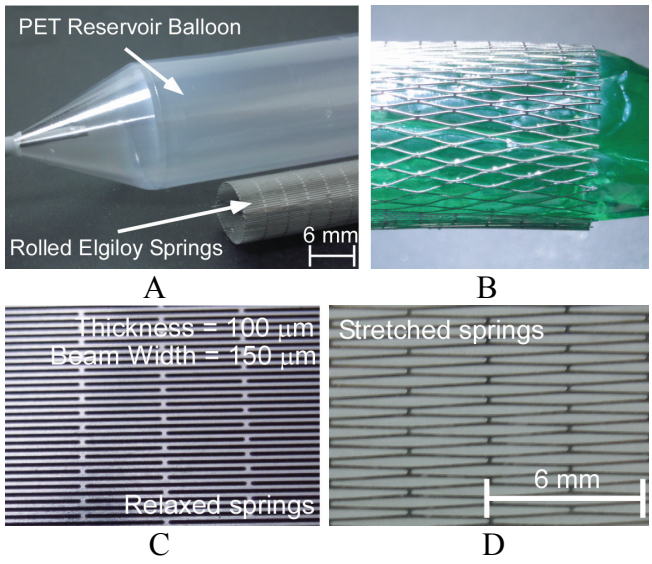

Fig. 4-8: (a) The compressive sleeve and the polymer balloon used to form an 18.8 mL reservoir. (b) A reservoir filled with green water inside an expanded sleeve demonstrating the expansion of the diamond shape cells. (c) Relaxed Elgiloy® spring mesh showing the springs cells in an un-actuated rectangular shape. (d) Stretched springs in a diamond shape. In all cases, the cell windows are each 600 µm x 6 mm.

Once the springs are fabricated, the planar sheets are rolled into sleeves and bonded at the seam with epoxy. The reservoirs are assembled by inserting a 60 mm long 20 mm diameter PET angioplasty balloon into the metal springs (Fig. 4-8a). Once the balloon has been inserted into the compressive sleeve, it is inflated with nitrogen gas to condition

the springs. The first generation springs are 100 μm thick, the beams are 150 μm wide, and the mesh cell size is 600 μm by 6 mm. An unrolled sleeve is 60 mm long by 10mm wide. The reservoirs each hold 18.8 mL and have an un-pressurized volume of 4.7 mm. A fully inflated liquid reservoir (Fig. 4-8b) clearly demonstrates the uniform expansion of the mesh cells of the springs.

4.2.3 Modeling and Experimental Results

The spring mesh was modeled by simulating half of a cell with correct boundary conditions in ANSYS and extrapolating the results for application to the entire sheet. The cell was tested by deflecting the spring 600 μm. The simulation software then partially relaxes the springs to ease extreme transitions that may cause simulation error. A final step is conducted in which the springs are released entirely and are allowed to relax to a default state. This is different then the initial state to due to plastic deformation that occurs during the initial expansion. This simulation uses in-plane forces and stresses to predict the forces the compressive springs will provide when curled around a balloon. The assumption is that the out of plane deflections (total bend angle of a cell is about 4 degrees) will not have a dramatic impact on the final device performance. This simulation mechanism was tested by simulating both a single half-cell (with the correct simulation parameters), and simulating an entire sheet. The results were the same.

Two different mesh sizes were chosen for the trade-off between total deflection and total pressure. Spring type A is designed with a higher spring constant. It delivers higher forces, but deflects a smaller amount before plastic deformation occurs. The second

spring is designed to deflect much more (this reduces "dead" volume) but it has a lower spring constant and generates smaller forces.

The volume change of reservoirs designed from two spring types are compared in Fig. 4-9. The stiffer springs expand from an initial diameter of 10 mm to a final diameter of 20 mm. This leaves a 25% unpressurized reservoir volume when they are un-stressed. The second spring geometry has an initial diameter of 6.66 mm. These springs have only an 11% unused volume.

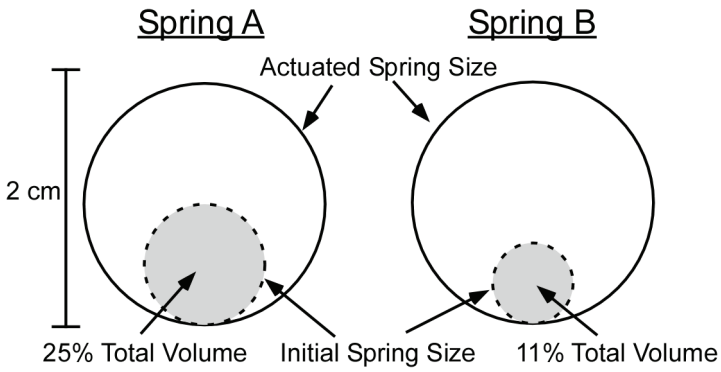

Fig 4-9: Comparison of initial and fully actuated spring sizes and reservoir volumes

The spring model parameters were determined by using the forces and stresses from ANSYS coupled with calculations based on hoop-stress equations. The stiffer springs are designed to generate about 18 kPa of pressure when the reservoir is full. The softer, larger deflection springs generate about 5.3 kPa when full. An interesting option with these types of springs is the ability to apply them in parallel. Two or more sleeve springs can be wrapped around the same balloon to double (or triple etc) the pressure generated from a single reservoir. This allows many different configurations with very limited changes to fabrication.

The planar metal springs are tested by stretching and measuring force generation for varying displacements. Each side of an unrolled spring sheet is affixed to a metal rod. This acts as a simulacrum for pressurized expansion because it distributes the force applied to the mid-point of the rod along the sheet evenly. Fixing one side of the sheet and attaching the other side of the spring sheet to a force transducer on a micrometer stage distributes forces along the bonding edge of the spring uniformly. The micrometer stage slowly deflects the springs while the force is measured (Fig. 4-10). The springs are measured after fabrication and again after they are stretched 20 mm to condition them with plastic deformation similar to that which occurs when they are used in a fully inflated reservoir. Conditioned springs have a spring constant of 305.7 N/m. The measured spring constant and plastic deformation closely match the finite element analysis (FEA) simulation results from ANSYS software during the design phase (predicted 18 kPa when fully inflated).

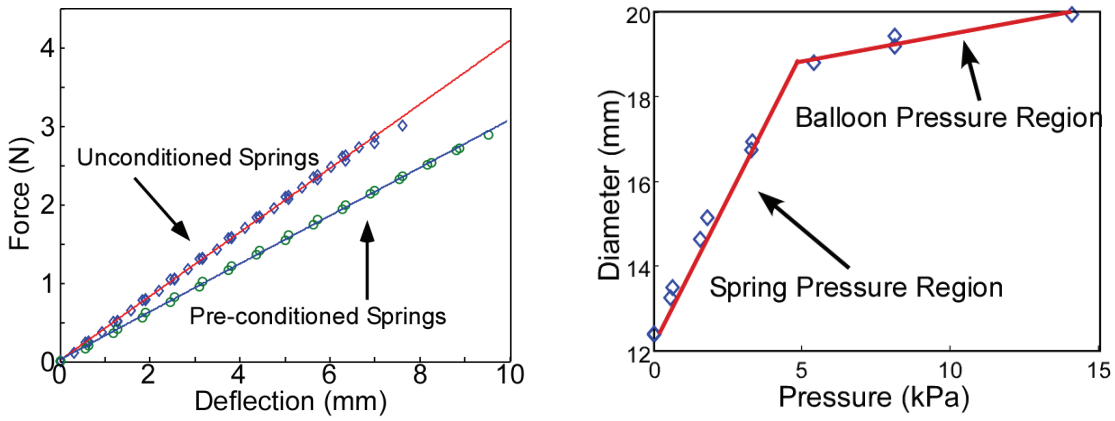

Fig. 4-10: (a) Measured load characteristics of the mesh springs as a function of linear conditioning (stretching). The unconditioned spring constant is 407.3 N/m and the pre-conditioned spring constant is 305.7 N/m. (b) Measured reservoir pressure generated for various balloon/sleeve distension. From 12 mm to 19 mm, the pressure is generated by the springs. Beyond 19 mm, the balloon elasticity changes the profile. Fully inflated, the reservoir is 20 mm in diameter and generates almost 15 kPa.

4.3 Discussion

Reservoir development addresses the need to store and pressurize medication in an IDDD with a valve regulated architecture. This work investigates multiple balloon pressurization methods by using two different spring types. In one type, silicon was etched into planar torsion springs, and in the second type, Elgiloy was fabricated in planar mesh sheets and rolled into compressive sleeves. The torsion springs and the compressive sleeves are combined with a PET angioplasty balloon to transfer the spring force into pressure. Both methods generate pressures for most of the liquid volume of the reservoir, and the mechanisms themselves take relatively little volume.

Pressure was applied using nitrogen gas, and the displacement of the springs was measured. The experimental results agreed with design simulations reasonably well. Additionally, both reservoir types have been filled with liquid and exhibit similar decreasing volume with decreasing pressure tendencies. Results suggest that spring pressure can be used to regulate delivery of a drug from a liquid reservoir in an implantable drug delivery device. The multiple reservoirs and associated testing provide a robust background that allows for similar development methods to be used in designing future devices for other target applications.

Compressive Elgiloy springs have both positive and negative characteristics when compared to silicon torsion springs for use as the mechanical force transducer in a pressurized reservoir. The metal springs have less device volume, are cylindrical in shape, are liable to plastic deformation instead of breaking, and are easier to fabricate and assemble. The principal drawbacks of the metal springs are lower pressure generation when fully inflated (15 kPa compared to almost 80 kPa), the use of a metal instead of

silicon (making integration of sensors more difficult), and greater unused liquid volumes. This lower pressure limit reduces the maximum flow rates the drug delivery device can achieve. Despite these relative drawbacks, the metal sleeves are used in the preliminary system because of robustness, reusability, smaller dead volumes, and ease of fabrication.

In summary, reservoirs have been designed that meet system requirements. Compressive sleeve springs are easily designed and assembled with PET balloons into reservoirs that have title total dead volume. Reservoirs were characterized with gas and liquid to determine their properties for use with the PZT throttle valve. These preliminary results provide the necessary reservoirs to use in conjunction with membrane suspended valves for the design and fabrication of a complete drug delivery system.

CHAPTER 5:

PRELIMINARY SYSTEM RESULTS

This work describes the development of a preliminary drug delivery system using a less complicated architecture than the design suggested in Chapter 2 (Fig 5-1). A single valve and reservoir are used to regulate flow from the implantable device while maintaining a relatively high volume efficiency. More details on partial assemblies, demonstrated diffusion, control algorithms, electronic circuit implementation, and complete system results are in the following sections.

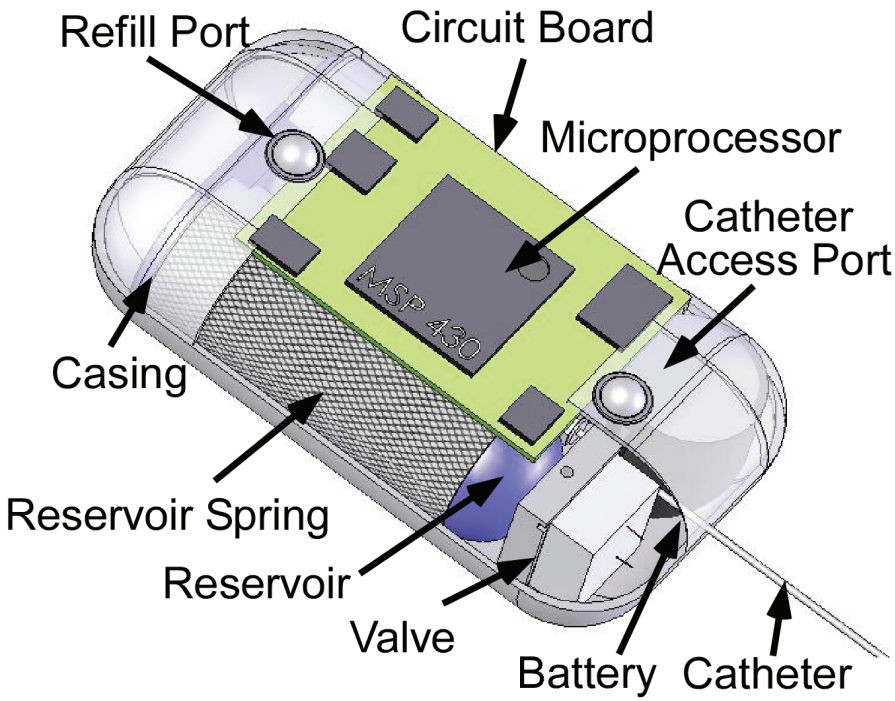

Fig.5-1: System overview: A large reservoir is pressurized with compressive sleeves and regulated by a microvalve to control drug delivery rates. Control is regulated by onboard electronics that allow for pressure monitoring and reprogramming.

5.1 Control Algorithms and Electronics

5.1.1 Circuitry and Power Consumption

Drug delivery system lifetimes are typically dependent upon battery life. Battery life can be extended by enlarging the battery, or by reducing the power consumption. The reservoir uses no electrical power, and the PZT valves only consume significant amounts of power when they are adjusted. The primary source of power consumption is the electronic circuit board. This requires board design, component selection, system functionality, and programming to be optimized for power consumption. The electronics should be powered from a single battery. The system should include multiple sensor inputs, storage of complex delivery programs, drive the valves across operating voltages, and wirelessly communicate with an external programmer used by a medical professional. This functionality should be implemented with the smallest battery possible that allows the entire system to run for 5 years.

The circuit has several functions, the most important of which is control of the delivery rate. Control is achieved as follows: the input from the differential pressure sensor is amplified and read into the microcontroller. This sensor data is processed, used in control algorithms, and the valve actuation voltage needed to realize the desired flow is generated by the charge pump amplifier. Minimally, the control system includes multiple sensor inputs, storage of complex delivery programs, and capacity to drive the valves across operating voltages. Circuit board design, component selection, system functionality, and programming optimization for power consumption may yield substantial reductions in battery requirements. The system electronics are designed with the long term goal of a 5 year system lifetime.

The prototype control PCB (Fig. 5-2) is designed to use feedback from the embedded sensors to operate the system. The circuit is designed to operate from a battery providing 3-4 volts. The battery regulator is selected for power efficiency and is the LT 1761 from Linear Technologies. The microprocessor selected to control the chip is the MSP430F169 made by Texas Instruments. It is well suited to this application because it has the necessary peripherals (ADC and DAC), a low power sleep mode in which it consumes 2 μW, and power consumption of 600 μW when active. Capacitive boost-boost amplifiers (LT3482, Linear Technologies, California) are used to amplify the output signals from the microprocessor to power the PZT actuators. The differential input from the piezoresistive Wheatstone bridge pressure sensors are amplified and converted to a single-ended output voltage by AD623 instrumentation amplifiers from Analog Devices. These amplifiers are shut-down when they are not reading pressure, greatly reducing their power draw. The preliminary circuit board is a double-sided, two metal layer board that measures 4 cm x 6 cm. The CC1100 from Texas Instruments is the chip used for wireless communications in the ISM band. The preliminary circuit board is a double-sided, two metal layer board that measures 4 cm X 6 cm.

Different control algorithms can both be implemented using the embedded pressure sensors, the compressive spring pressurized reservoir, and PZT microvalves. The sensors can be used in multiple ways to determine the flow rate. Given this flow information, continuous delivery can be regulated by slowly adjusting the aperture of the valve to compensate for decreasing pressure. It could also be regulated by using duty cycle control that appears continuous to the patient at the catheter/CSF interface because of fluidic capacitance effects.

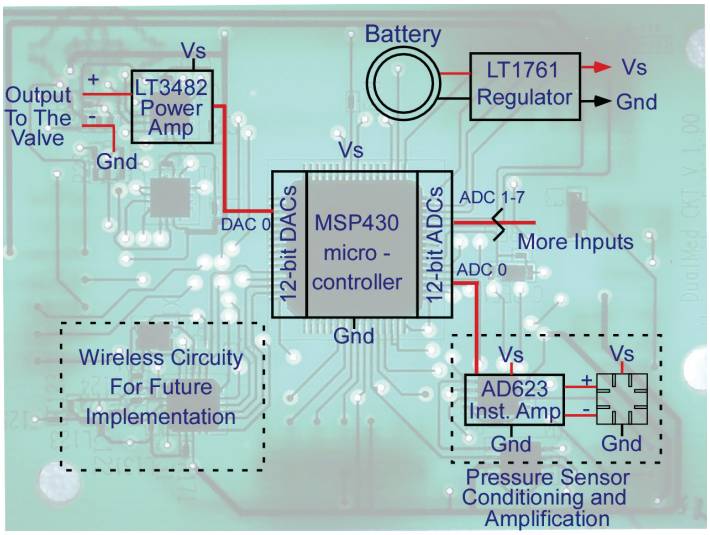

Fig. 5-2: A block diagram outline of the electronics is overlaid on an image of the actual control PCB that is 4 cm X 6 cm and powered from a 3V battery. The pressure sensor input is amplified and read by an ADC. This data is used in the closed loop control algorithms implemented in the microcontroller. The PCB is capable of independently controlling two valves and has the circuitry necessary to enable wireless communication for data readout and reprogramming.

Additionally, a bolus dose can be delivered by fully opening the valve until the desired volume is delivered. These continuous and bolus control algorithms can be combined to generate unique delivery profiles or respond to environmental stimuli. The implementation of the control algorithms and other circuit functions will dominate the power consumption of the device, but there are several trade-offs between power consumption and delivery accuracy that can be used to reduce the battery drain.

5.1.2 Control Algorithms and Valve Power Consumption.

In analyzing the power consumption of continuous flow, it is necessary to consider the reservoirs and the actuation of the valves. The reservoirs generate pressure as a continuous function of stored volume (V) (Eqn. 5-1).

$$P = f(V) \qquad (5\text{-}1)$$

The flow rate (Q) is related to the differential pressure (P) between the reservoir and the delivery load through the hydraulic resistance of the serial combination of the valve and catheter. For an unactuated open valve, the minimum hydraulic resistance is 7.32 x 10^{12} Pa/m^3, which is 10 times the resistance for a 1 m long catheter (6.519 x 10^{11} Pa/m^3). Therefore, the valve approximately defines the resistance of the system, and regulates flow by changing this resistance (Eqn. 5-2).

$$Q = P/R_{system} \approx P/R_{valve} = \partial[f^{-1}(P)]/\partial t \qquad (5\text{-}2)$$

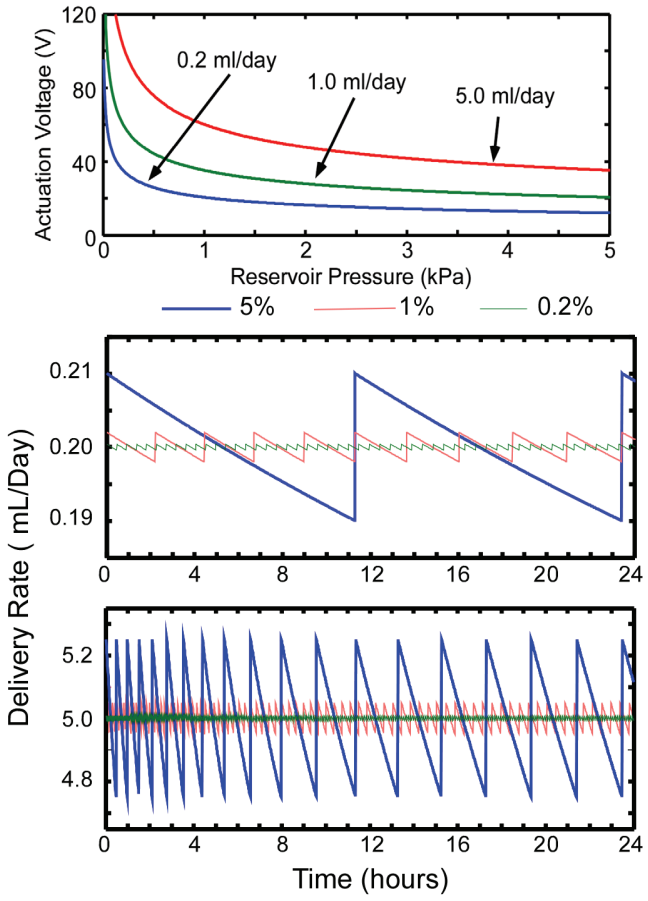

Fig. 5-3: (top) Calculated voltage needed to actuate the valve to maintain a set flow rate for various reservoir pressures (middle and bottom) Calculated change in flow rate over time due to changes in valve constriction at various error rates. The frequency of valve adjustments decreases over time due to non-linearity in the reservoir.

The delivery rate can be determined by monitoring the change in reservoir pressure (Figure 5-3). This mechanism requires no information about the valve for accurate continuous and bolus flow regulation.

Another regulation mechanism involves setting an initial flow rate and maintaining it by periodically increasing the throttle aperture to compensate for the decrease in the reservoir pressure as the reservoir is emptied. Assuming the valve is at a particular set aperture, the flow rate is determined by the differential pressure across the valve divided by the flow resistance. The reservoir pressure changes as material flows from it, so the flow rate for a specific aperture is a function of volume and consequently, time (Eqn. 5-3). The highest possible actuation voltage is 120 V, and at this voltage, a flow rate of 5.0 mL/day requires a minimum differential pressure of 130 Pa.

$$Q = Q_{set} + Q_{err} = {P(t)}/{R_{valve}} = h(t) \qquad (5\text{-}3)$$

For a constant set point, there is a set flow (Q_{set}) and an acceptable deviation from this set point (Q_{err}) such that the flow rate remains within an acceptable error range. The flow rate function *h(t)* will slowly decay because the reservoir pressure drops as material flows out of it. The initial time (t_a) and the final time (t_b) that the flow rate will be within the error bounds for a particular set point can be determined (Eqn. 5-4).

$$t_a = h^{-1}(Q_{set} + Q_{err});\ t_b = h^{-1}(Q_{set} - Q_{err}) \qquad (5\text{-}4)$$

The power consumption (U) of the valve is a combination of the continuous power draw and the valve transition energy multiplied by the switching frequency (Eqn. 5-5). The transient energy consumption (E_{change}) is estimated at 376.8 μJ per switch based on experimental observations for a valve assembled with three PZT actuators (PLO55.31,

Physik Instrumente, Germany). The transient power consumption is much greater than the leakage for actuation frequencies that are greater than one stroke every 5 minutes.

$$U_{total} = U_{trans} + U_{cont} \approx U_{trans} = E_{change} \times f_{change} \quad (5\text{-}5)$$

$$U_{total} \approx E_{change} \times (\frac{1}{t}) = E_{change} \times (\frac{1}{h^{-1}(Q_{set} + Q_{err}) - h^{-1}(Q_{set} - Q_{err})}) \quad (5\text{-}6)$$

The stroke frequency for a specific error rate is the inverse of the error period and is used to determine the power consumption. The result (Eqn. 5-6) is an analytical formula that allows the error rate, set point, and power consumption levels to be adjusted with respect to each other for any chosen application.

The typical range of delivery for intrathecal medication varies from 0.2-5.0 mL/day. Analytical models were built from empirical data taken from the PZT microvalve and the compressive spring reservoir. These models were used to simulate drug delivery from the system at various constant flow rates. Figure 5-3 represents the regulation of delivery from a typical reservoir with varying error (5%, 1%, .02%) over one day. The stroke frequency for delivering 0.2 mL/day with a 5% error is 2.1 adjustments/day. The primary power consumption at this switching rate is due to current leakage through the piezoelectric actuator. Conversely, the worst case power consumption scenario requires one adjustment every four minutes to regulate 5.0 mL/day with 0.2% accuracy. Using a maximum accuracy of 0.2%, the average power consumption of the throttle is 1.68 μW. This worst case power draw also represents the power consumption of the valve for duty cycle regulation.

5.1.3 System Power Consumption and Noise of First Generation Systems

A worst case power consumption of the valve for any possible operation was determined to be 1.6 μW. Additionally, a preliminary circuit design consumes less than 10 mW of power when not communicating via the wireless interface. The current power consumption is due to added features not necessary for operation, and should be reduced to at most 1 mW with the implementation of power management features. Further power optimization techniques (software implementation) could reduce the non-communicating power to approximately 100 μW without any hardware restructuring. Communications only occur once every 3 months and currently consume approximately 30 mW of power; so they can be ignored. Circuit consumption of 1 mW will yield a battery life of 120 days with a standard rechargeable AA battery. After fluid flow and medical issues are addressed, power consumption can be reduced. This should yield a system with a battery life of 3-5 years powered from a single AA Li-on cell.

The circuitry is very important in accurately reading the pressure from the embedded sensors. Sensitivity of the circuit, drift, and repeatability are the parameters that determine the ability to regulate delivery within tolerance and need to be addressed in the readout circuitry.

The pressure of the reservoir is linearly related to the flow rate through the reservoir. A medically viable flow rate can be achieved above 500 Pa. The maximum error in delivery due to sensor properties will occur at this minimum pressure, and it needs to be less than 2.5% of the delivery rate. The minimum resolvable pressure difference needs to be 12.5 Pa to achieve this. The embedded pressure sensors are piezoresistive Wheatstone bridges that provide a linear (within 2%) differential voltage. The pressure sensors

exhibit slightly different initial offset voltages (within +/- 2% of the supply), and have a sensitivity of 250 ppm/kPa. The pressure sensors are calibrated before and after assembly of the device, and a polynomial linearization is used to create a memory model that the microcontroller uses to determine the actual pressure. The full scale pressure range the sensor needs to realize is 0-20 kPa with a 3.3 V power source. The sensor output enters a differential amplifier. From there the amplified signal is converted by a 12-bit analog-to-digital converter (ADC). The minimum pressure step the electronics can resolve is 4.886 Pa. This corresponds to an ADC input of 0.8 mV. The electronic sensitivity is well below the 4.886 Pa threshold required. The pressure sensor is not limited by the DAC, but it may be limited by noise.

Noise in piezoresitive diaphragm circuits come from three sources: mechanical vibrations, electrical noise in the piezoresistors, and electrical noise in the interface circuit. The mechanical noise is dominated by viscous forces. The second noise source is electrical noise from the piezoresistors and is Brownian in origin. These noise sources are usually dominated by interface circuit. The noise from these three components, respectively, is provided in pressure-equivalent units by Eqn. 5-7:

$$P_{n\_RMS} = \sqrt{4kTR_a + \frac{4kTRB}{(V_s S)^2} + \frac{\Delta V_{\min}}{(V_s S)}} \qquad (5\text{-}7)$$

Here, R_a is the mechanical resistance coefficient per unit area; B is the system bandwidth; V_s is the source voltage; and S is the sensitivity. In this case, the interface circuit is an AD623 with a minimum resolvable voltage difference (ΔV_{min}) of 200 μV. The pressure resolution limit due to this is 0.24 Pa. The noise generated from the interface circuit is at least an order of magnitude less then the minimum resolvable unit of the ADC, and is well with the specifications of the pressure sensor.

Another source of pressure sensor error can occur from drift. Long term drift needs to be studied to verify that it is within tolerable limits. If necessary, the pressure sensor can be re-calibrated every time the reservoirs are refilled. Temperature can also cause sensor drift, and this can be calibrated out when used in conjunction with the internal temperature sensor.

Additional flow rate errors can arise from hysteresis in the PZT valve. The effect of hysteresis varies on the method of control being employed. If continuous flow regulation is the only technique employed, hysteresis can be accounted for by following one side of the actuation vs. deflection curve. This is accomplished by slowly opening the valve and never closing it until there is a refill. If bolus or mixed regulation methods are employed, the hysteresis needs to be calibrated and an internal model that accounts for increasing or decreasing voltage needs to be coupled with the pressure sensor linearization to derive the flow rate.

5.2 Diffusion Regulation

5.2.1 Experimental Results

Intrathecal drug pumps deliver medication into cerebral fluid in the spine by pressure-driven diffusion. Tests to confirm diffusion regulation were conducted using integrated valves and reservoirs filled with fluorescent dye for regulating delivery into agar gel. These tests were conducted with normally closed valves that were actuated at 30 V during assembly. A silicon spring reservoir was completely filled before each diffusion experiment was conducted. Fluorescent images of dye diffusion were taken every 30 s for 5 min for various actuation voltages. This test demonstrates control over a wide range

of diffusion rates with varying voltage (Figure 5-4). A beveled needle tip resulted in the noticeable non-circular diffusion patterns. The results indicate that the mechanism of diffusion does not present a barrier to this delivery architecture.

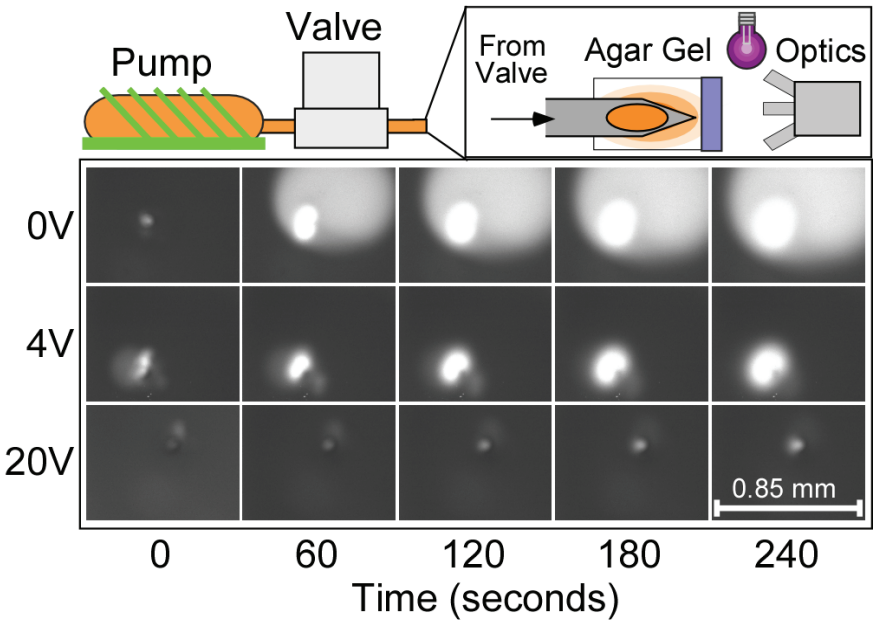

Fig. 5-4: Microvalve regulated fluorescent dye diffusion from a spring pump into agar gel. The setup is on top and typical fluorescent images taken for different valve actuation voltages are shown over time.

5.2.2 Analysis

In order to verify that valve regulation is the only element responsible for the changes in diffusion rate, analysis of the experimental data has been done. Constant-source diffusion models based on Fick's law (Eqn. 5-8) were mapped to fluorescent intensity at various modulation levels presented by the valve (Fig. 5-5) using specialized Matlab® image analysis software.

$$N(x,t) = N_0 \times erfc\left(\frac{x}{2\sqrt{Dt}}\right) \qquad (5\text{-}8)$$

The model assumes spherical diffusion from the needle that acts like a constant source. The software was used to determine constants for every point independently.

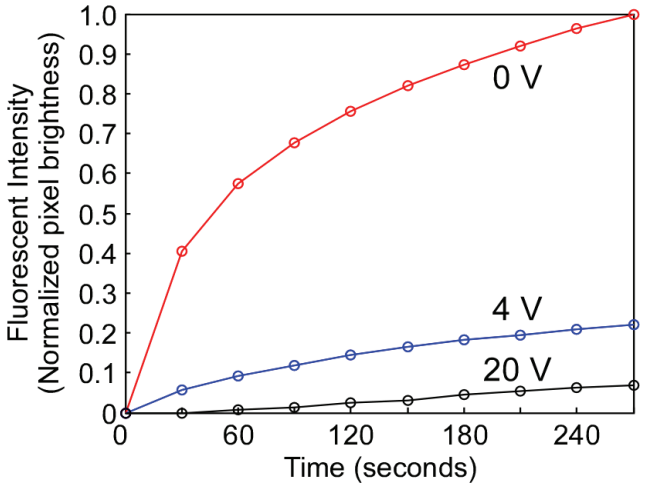

Fig. 5-5: The normalized output of total fluorescent intensity of diffusion into agar gel for actuation voltages over time.

The *Dt* product for every point was determined using the constant source diffusion model and a least squares fit (Fig. 5-6). The slope of the *Dt* products is the time independent diffusion constant for a given modulation voltage applied to the valve. The very close linear fit of these independently determined diffusion constants is expected, and it lends credence to the model.

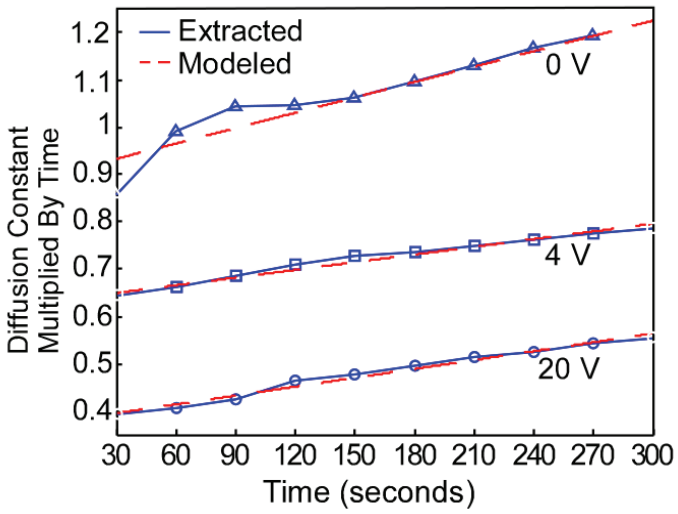

Fig. 5-6: Extracted *Dt* values for infinite source diffusion plotted with modeled diffusion *Dt* values showing close fit validating the model

The determined diffusion constants were inserted in the constant source model, and it was then used to predict time-based diffusion distances for particular fluorescent concentrations across actuation voltages (Fig. 5-7). This model makes several assumptions for simplification, but accuracy suggests that valves can be used to achieve active control over diffusion into cerebrospinal tissue in ways that concord with Fick's diffusion principals.

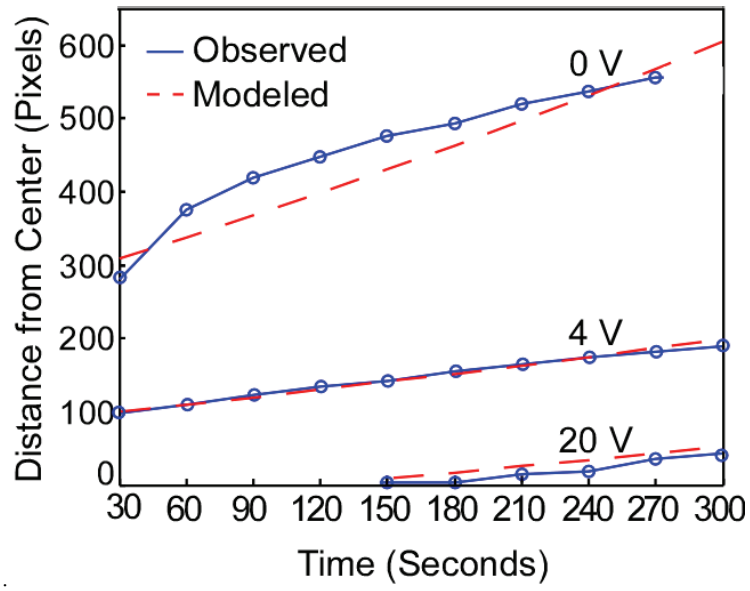

Fig. 5-7: Observed distance of a set intensity compared to the expected distance based on the diffusion model of the system.

5.3 Housing and Assembly

A complete system requires the development of a long-term biologically compatible housing containing the components necessary for drug delivery. The preliminary prototype is made from aluminum; the final device for implants will likely be made from biocompatible titanium. The metal encasement contains a microvalve, a large reservoir, the control circuitry, a battery, and has two ports for refilling the reservoir and accessing the catheter. The prototype housing measures 4.5 cm X 8.5 cm X 3.4 cm with 1 cm

beveled edges. The housing has a total volume of 113 cm^3 with a total reservoir volume of 37 cm^3. This prototype has a relatively high VER, but it can be further increased by improving the component form factors and the assembly procedure.

Table 5-1: Comparison prototype device with current commercial intrathecal implantable pumps.

	SynchroMed EL	**SynchroMed II**	**IsoMed**	**Proposed Device**
Manufacturer	Medtronic	Medtronic	Medtronic	U. Michigan
Volume (cm^3)	123 cm^3, 156.7 cm^3	91 cm^3, 121 cm^3	111.7 cm^3, 135 cm^3,172.2 cm^3	73.9 cm^3
Weight (empty)	185, 205 g	165, 175 g	113, 116, 120 g	80g
Reservoir Size	10, 18 ml	20, 40 ml	20, 35, 60 ml	37 ml
Battery Life	6.5 years at 0.5 ml /day	7 years at 0.5 ml /day	No battery	15+ years
Flow Rate (ml/day)	0.5 – 20 (programmable)	0.048-20 (programmable)	0.3, 0.5, 1.0, 1.5, 4.0 (constant flow)	0.1 – 30 (programmable)

The current ports attached to the prototype are micro vascular access ports made by Instech Laboratories. The access ports are designed for long term subcutaneous implantation and are designed to sustain hundreds of needle punctures and up to 690 kPa back pressure. The assembled prototype in the housing can be seen in Figure 5-8.

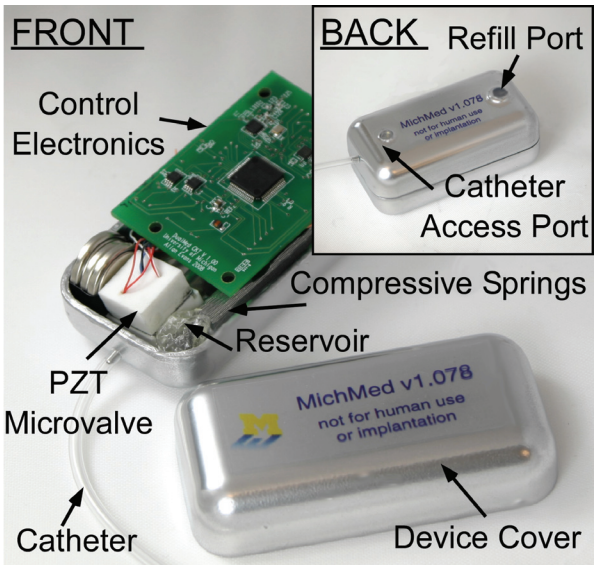

Fig. 5-8: A drug delivery prototype pictured during assembly. A polymer reservoir is pressurized with Elgiloy compressive sleeve springs and regulated by the PZT microvalve to control drug delivery rates. The entire device takes up about 130 cm^3. The inset is a photograph of the closed device with the refill and catheter access ports prominently displayed.

5.4 System Results

5.4.1 Pressure Sensor Control and Delivery

Continuous flow delivery requiring differential pressure and duty cycle based regulation both require characterization of the valve to be properly implemented. In contrast, bolus flow regulation requires a pressure sensor and characterization of the reservoir. With proper sensor arrangement, both techniques are combined to provide information about the delivery rate, reservoir volume, and increase delivery accuracy.

Pressure sensor errors may be caused by non-linearity in the piezoresistors, the resolution of the digital-to-analog converter, and unaccounted differences between the operating temperature and the calibration temperature. During laboratory testing and calibration, photocurrents induced in the wires connecting the valve to the circuit may also contribute to errors. Since the pressure sensor readings are used to determine valve settings in this architecture, errors in pressure measurement will translate into flow inaccuracies. Additional flow inaccuracies may result from approximations used for the valve response, unforeseen drift in piezoelectric actuation, or changes in the mechanical loading along the length of the catheter. The compounding effects of these errors may be reduced by simultaneously characterizing the system for pressure and flow in two-dimensions.

Pressure and flow properties were characterized by flowing nitrogen gas through valves at several actuation voltages. The inlet pressure was monitored with the embedded PZT pressure sensor as well as a capacitance manometer (727A Baratron®, MKS Instruments, Massachusetts) that provided an accurate reference pressure. Sensor error was recorded as the discrepancy between the embedded sensor and the reference.

Averaging 128 pressure sensor measurements over a time period of one second reduced the error in the system. Pressure sensor and flow rate results for a typical valve are partially displayed in a two-dimensional error map in Figure 5-9. The flow rates that were evaluated were typical of intrathecal delivery ranges. The average pressure sensor error was less than 1.04 kPa, and the average deviation from the target flow rate at any pressure was less than 6.4% of the maximum flow rate for that pressure. Well characterized valve mappings may be interpolated to create continuous functions or look-up tables to control the system with acceptable delivery error.

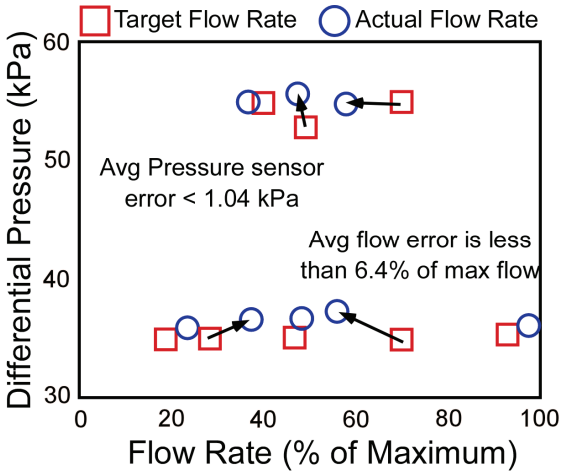

Fig. 5-9: A two dimensional mapping of continuous flow regulation measuring the average pressure sensor error and the corresponding actual flow versus the target flow rate. The pressure sensor average error is less than 1.04 kPa and the average deviation from target flow is less than 6.4% of the maximum flow for a particular pressure.

Tests were conducted for both continuous and bolus delivery. Third order polynomial models were built from empirical data taken from the PZT microvalve and the spring pressurized reservoir and incorporated into a microprocessor program to regulate continuous flow, Flow measurement was performed by observing the distance travelled by an air bubble in a delivery catheter. Tests typically ran from 8 hrs to as long

as a week. One typical test (Figure 5-10a), demonstrated average delivery accuracies of 3.22% with no deviation from the flow rate worse than 9.09% at delivery rates of less than 0.2 mL/day. Additionally, the total delivered volume over the 6 day period was 3.003 mL with the expected total volume being 3.015 mL. This represents a long term delivery error of less than 0.4% of the target volume.

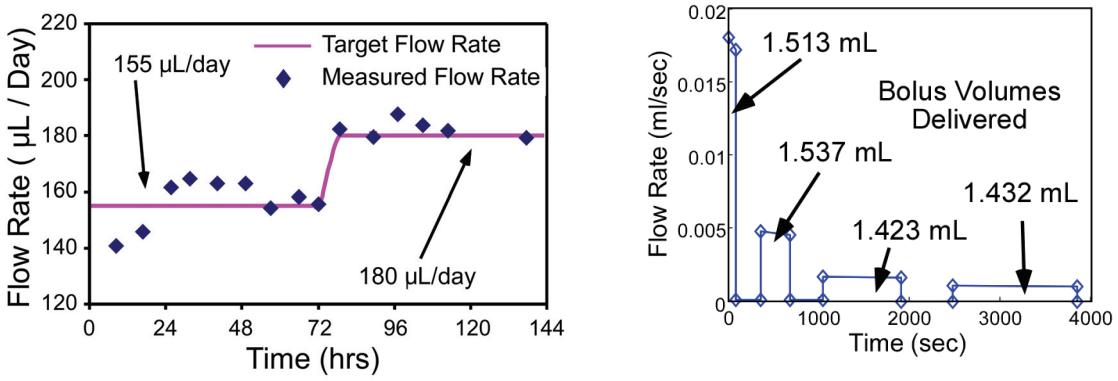

(a) (b)

Fig. 5-10:(a) Controlled long term flow from the assembled system in a typical reliability test. In these tests, reservoirs were refilled through the insertion port and were programmed with specific delivery schedules. In this instance, a system was programmed to deliver 155 µL/day for three days followed by 180 µL/day for the next three days. Actual flow rates are recorded by monitoring the distance an air bubble traveled along a catheter. The flow rates for each set-point have a maximum deviation from the target flow rate of 9.09% and an average deviation of 3.22%. The total volume delivered was within 0.39% of the target volume for the time period. (b) Programmed delivery of 6 mL in four boluses of 1.5 mL. The volume delivered was 5.971 mL.

Bolus delivery was conducted with a microvalve and reservoir model using a calibrated pressure-volume relationship. A program was implemented to deliver a total volume of 6 mL in four 1.5 mL bolus doses. The throttle valves were actuated at 40 V according to the pressure-volume relationship of the reservoir that had been previously determined (Figure 11b). These results suggest the methodology used to regulate flow can achieve high accuracies.

5.5 Discussion

This effort has resulted in the successful design and realization of a prototype system for eventual use in intrathecal drug delivery. Piezoelectric microvalves were assembled and used as the throttle mechanism to regulate flow. Compressive springs made from rolled Elgiloy sheets generate fully inflated reservoir pressures of almost 15 kPa and were pre-conditioned to increase repeatability. Control electronics were designed to regulate flow using embedded pressure sensors within the valve. The valves, reservoirs, electronics, and access ports were integrated with a metal casing to form a complete prototype with a total volume of 113 cm^3 and a reservoir volume of 37 cm^3. With appropriate refinements to the component form factors and assembly procedures, the reservoir volume can be doubled leading to a VER of approximately 60%. Several delivery tests were conducted for both bolus and continuous flow delivery. Four bolus units were delivered with a total error of 0.48%. Continuous flow programs were also implemented in one of two ways. Either the valve was slowly adjusted (opened) to maintain a set flow rate, or a changing duty cycle was used to maintain a set flow rate. In six day tests conducted at low flow rates (0.1-0.2 mL/day), delivery was regulated with average accuracies of 3.22% and a total delivered volume that was within 0.4% of the target.

Drug delivery systems utilizing this architecture can be scaled up or down for various applications; this can be done by changing the reservoir size, shape, or the valve modulation range. Additionally, specific un-powered flow rates can be set by assembling the throttle valves with a nominal gap that meets delivery needs. This can be used to

create a failsafe delivery (in cases of power loss) that can prevent hazardous withdrawal or overdose effects. The valve can be easily altered to include embedded sensors that measure other physical properties to increase the information available to the clinician. Additionally, the current sensors can be used to improve the accuracy and the safety of the device. In summary, valve regulated drug delivery holds promise as a volume efficient, versatile, and safe architecture for an intrathecal system.

CHAPTER 6:

SECOND PROTOTYPE SYSTEM RESULTS

This chapter describes the development of a second generation preliminary drug delivery system using a different architecture than the design in Chapter 2 (Fig 6-1). A two-valve manifold and two reservoirs are used to regulate flow from the implantable device. Section 6.1 details the housing assembly and component; section 6.2 reviews system testing, and section 6.3 is a summary discussion.

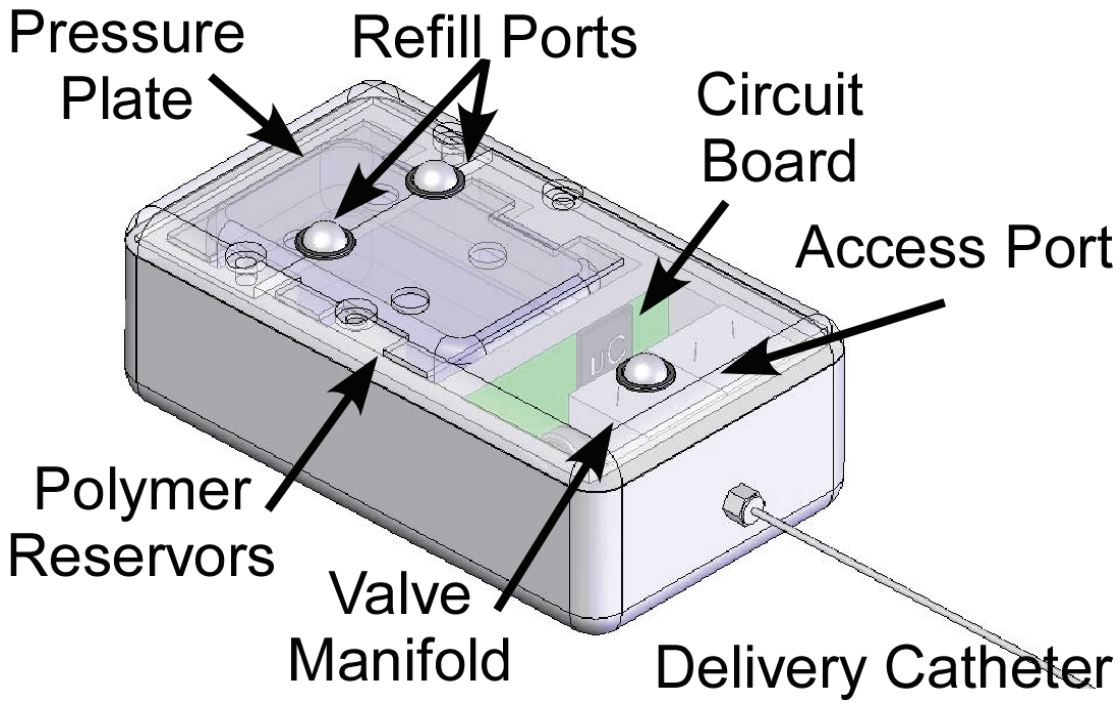

Fig.6-1: System overview: Two polymer reservoirs are pressed by a plate attached to compressive springs to generate pressure. Two valves in a manifold are used to regulate drug delivery rates. Control is regulated by onboard electronics that allow for pressure monitoring and reprogramming.

6.1 Housing Assembly, and Components

The complete system requires the development of a long-term biologically compatible housing with integrated components necessary for delivery monitoring and regulation. This prototype is made from stainless steel using traditional machining processes. An actual realization of the implant would likely be made of biocompatible titanium. The stainless steel housing contains a two-valve manifold, control circuitry, two PE reservoirs, a steel pressure plate, traditional springs, three access ports, and a battery. The system housing measures 5.08 cm X 9 cm X 3 cm with 5 mm beveled edges. The housing has a total volume of 130 cm^3 with a total reservoir volume of 40 cm^3. This prototype has a VER of 30.7 % but it can be increased by integrating system components into the housing more efficiently. The assembled prototype in the housing can be seen in Figure 6-2.

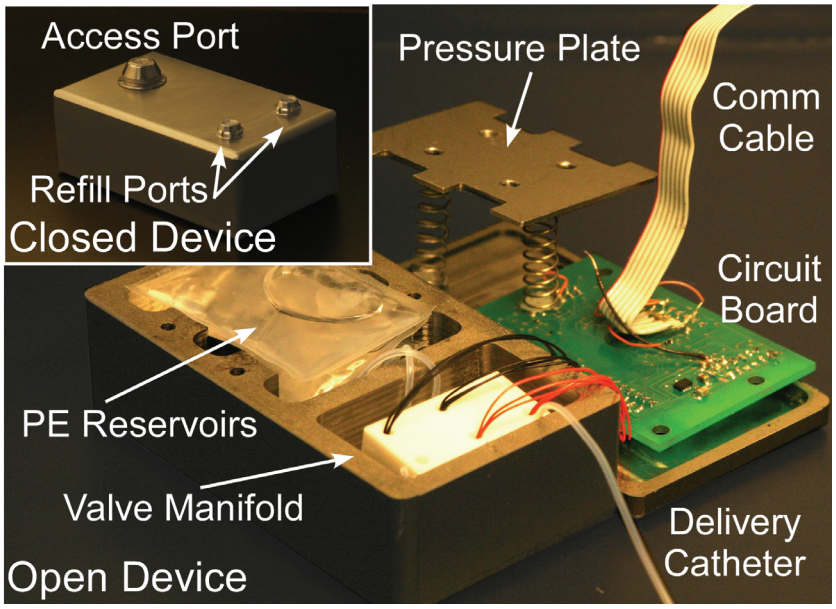

Fig. 6-2: A second generation drug delivery prototype pictured during assembly. Two polymer reservoirs are pressurized using a spring-loaded plate. Flow is monitored and regulated by a PZT actuated valve manifold with embedded pressure sensors. The entire system takes up about 130 cm^3. Inset is a photograph of the closed system with the refill and catheter access ports.

The reservoirs in this prototype are made from Polyethylene (PE) and are pressurized through compression by a metal plate (Fig. 6-3). The reservoirs have an inlet tube from the refill port and exit tubing to the manifold and inlet pressure sensor. The reservoirs are fabricated by heat sealing sheet polyethylene into the desired shape to fit within the housing cavity designed for the pressure plate. The reservoirs are stacked on top of one another and compressed traditional springs drive the pressure plate against the top reservoir, which, in turn, presses against the bottom reservoir. There are tracks in the plate and in the casing to maintain alignment of the plate, springs, and reservoirs. The pressure response of the reservoir is adapted to specific system needs by altering the compressive springs used to drive the pressure plate

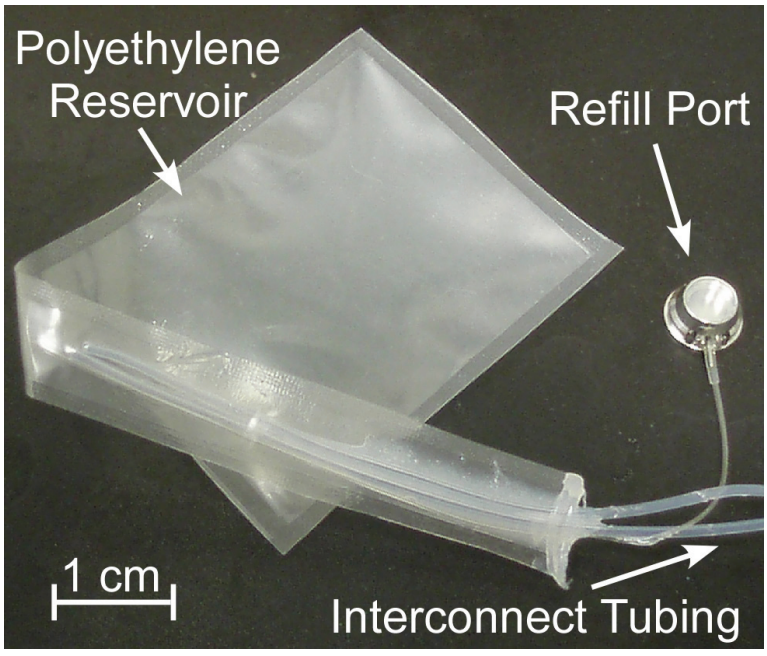

Fig. 6-3: A photograph of a reservoir before it is inserted into the system. There reservoir is connected to the refill port and interconnect tubing that leads to the manifold and a pressure sensor.

A prototype was developed using two centralized compressive springs designed to generate forces necessary to drive flow at intrathecal drug delivery rates. The reservoirs

were characterized inside of the housing by filling each one with 1 mL of isopropyl alcohol and measuring the resultant pressure using the internal pressure sensors (Fig. 6-4). The outlet tubes were sealed closed to prevent outflow and subsequent transient pressure measurement variation. The most sensitive pressures occur when the reservoirs are significantly depleted. Reservoirs generated pressures from 0 kPa when completely empty up to 5.17 kPa at 10 mL of total volume. This represents a typical increase of 0.52 kPa/mL which is an acceptable pressure profile for system functionality.

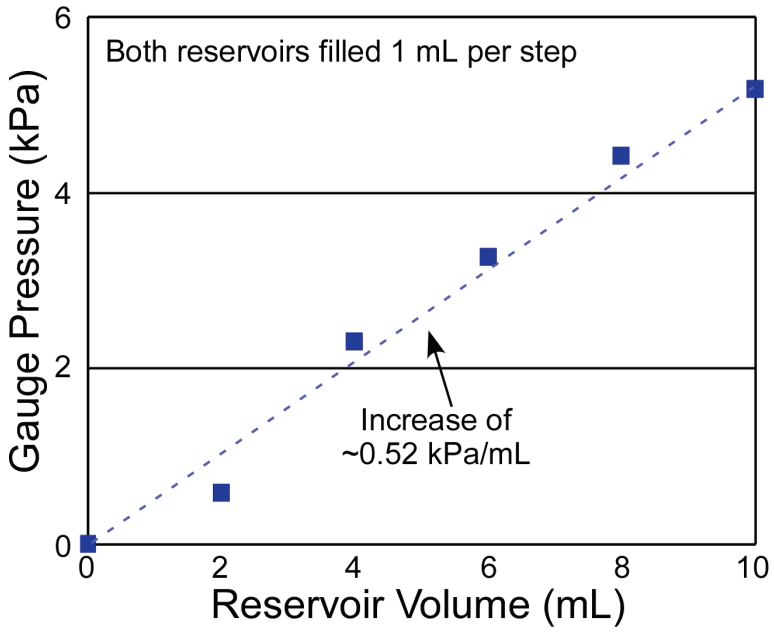

Fig. 6-4: Results from one reservoir filling test where each reservoir was filled with IPA in 1 mL increments. Results for fill volumes up to 10 mL suggest a linear pressure profile of 0.52 kPa/mL.

6.2 System Tests

6.2.1 Testing Methods

The changes in implementation from the first prototype to the second allow for a series of testing that is more analogous to the use of the final system in multi-drug delivery protocols. This is principally enabled by the use of multiple reservoirs and the

use of inlet and outlet pressure sensors. An experimental method was developed to allow for both the testing of the regulation of multiple flow paths and preliminary testing of medically relevant techniques.

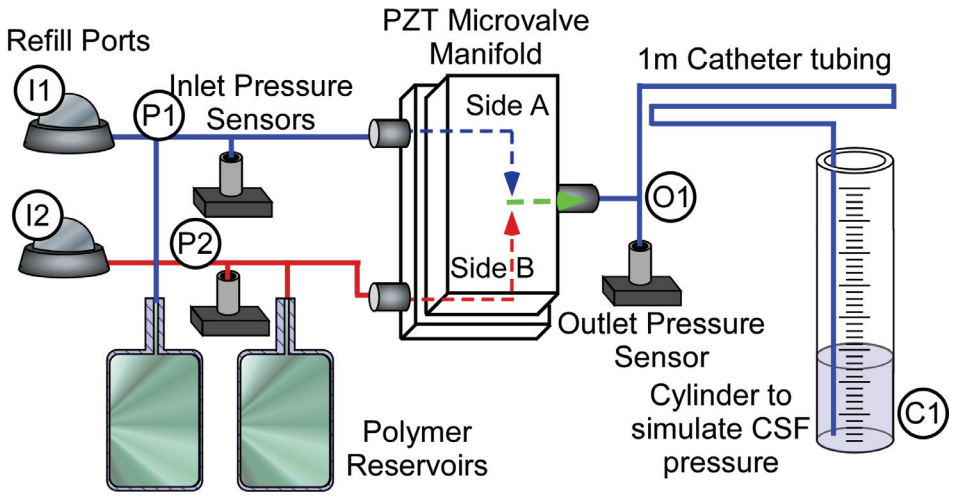

Fig. 6-5: A schematic of the entire system under test. A cylinder at the outlet of the device is used to simulate intrathecal pressure. The schematic is labeled to signify important nodes at which partial system test results may be monitored.

A complete schematic of the experimental set-up includes refilling the reservoirs from the refill port through delivering medication into a pressurized cylinder to mimic pressures in the intrathecal space (Fig 6-5). The schematic is labeled at the major branches for reference; for example, the outlet of the manifold is labeled as O1. The structures for individual tests are described in relation to this schematic. For example, the reservoir characterization discussed previously could be referred to as a test where IPA was driven into the inlet ports (I1 and I2) and the reservoir outlets (P1 and P2) were sealed while the pressure was monitored.

During testing, three variants were most commonly used. The complete system tests used absolute pressure sensors at the inlet and outlet ports. The inlet pressure sensors are MEMS absolute pressure sensors from Freescale with a range of 0-200 kPa (MPXA4250)

and the outlet pressure sensor was a MPXA6115 from Freescale (range of 0-115 kPa). A one channel variant replaces the polymer reservoirs with gas pressurized liquid from an N_2 canister using feedback and set-point control. In this scheme, only one side of the manifold is used for testing. The second valve in the manifold was flooded with IPA (to remove all air bubbles from the device) and was sealed at the inlet to allow no air in or alcohol out. The inlet pressure sensor was a Baratron absolute pressure sensor from MKS. A second one sided variant uses the complete system schematic, except, instead of using two pressurized reservoirs, on channel was sealed and only one reservoir was used. This variant was used to test individual channels via superposition before testing the finished system.

6.2.2 Catheter Kinks, Catheter Disconnects, and MRI Compatibility

There are several failure and compatibility issues with implantable intrathecal drug pumps that are of medical interest. Three of these issues are delivery catheter kinks (or tip occlusions), catheter disconnects from the pump or displacement from the intrathecal space, and functionality of the device during an MRI. Addressing catheter changes and MRI compatibility allows for a high level of patient safety when using an implant.

Traditionally, changes in the state of the catheter are detected by symptoms related to alterations in medication rates due to the state change. Basically, the patient receives a change in dosing due to an occluded or disconnected catheter, realizes it, and informs a physician. The physician may then use one of several techniques to determine the actual alterations in the catheters; from tracing radioactive dye through the delivery chain to surgery to physically investigate. The use of embedded sensors within the device may

allow for the system to detect potential catheter state changes before a patient may notice them. This rapid information dissemination could reduce the time or effects of an acute withdrawal of the medication being delivered by the drug pump.

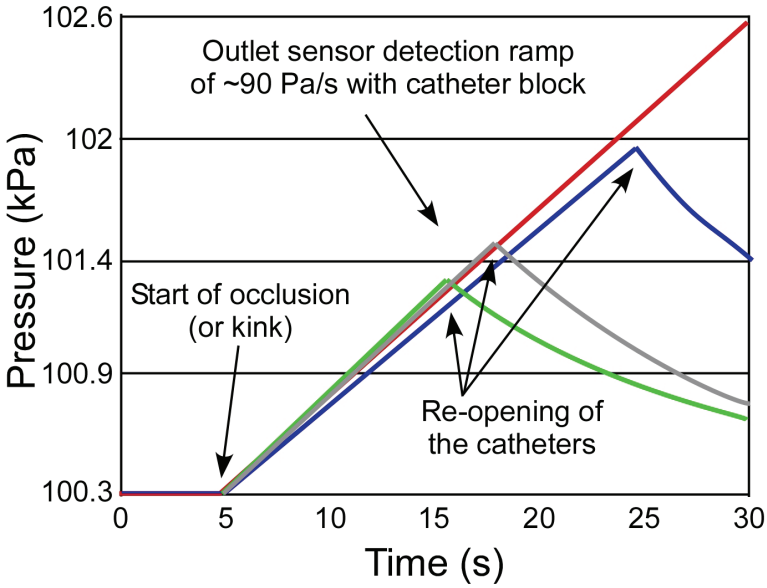

Fig. 6-6: The outlet pressure sensor before, during, and after the catheter is blocked. The sensor detects a pressure ramp of about 90 Pa/s when the catheter is occluded.

The sensor response for catheter kinks was tested by flowing IPA at a constant rate through the manifold, and out the catheter into an air ambient environment. In an effort to simulate the effects of a kink or occlusion, the tip of the catheter was completely blocked (C1) and the response was measured on an oscilloscope. The length of the block was varied to determine the sensor response to temporary blocks or severe kinks (Fig 6-6). The outlet pressure sensor measured 100.3 kPa of absolute pressure while IPA was flowing from an unrestricted catheter. Once the catheter was occluded, the output sensor detected an average pressure ramp of 90 Pa/s while the catheter remained blocked. This consistent pressure change for a blocked catheter was repeatable and occurred at a much faster rate than pressure changes occur during normal operation of an implantable drug delivery device. This test represents a preliminary investigation into acute catheter

occlusion and suggest that detection of a significant pressure ramp can occur within several seconds; at which time the delivery system could beep or otherwise notify the user of the situation.

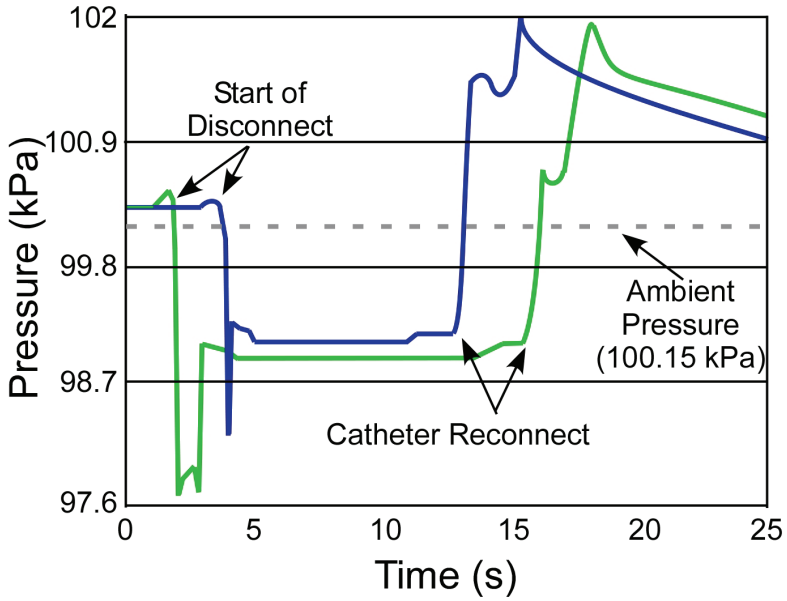

Fig. 6-7: Oscilloscope traces of the outlet pressure sensor when the catheter is acutely disconnected and later reattached to the drug delivery device. The tests were conducted in air ambient; some artifacts of the sensor response may be due to test conditions.

The sensor response for catheter disconnects was tested in a manner similar to the tests for catheter occlusions. Instead of blocking the catheter at the delivery point, the catheter was manually disconnected from the system at connection point (O1). The sensor output was measured before the disconnect, during the disconnect, and after re-attachment of the catheter to investigate the capacity of the outlet sensor to determine disconnects (Fig 6-7). Initial tests indicate a significant initial drop in pressure at the time of the disconnect. The sensor then settles at a new output. This tendency is repeatable in the air ambient tests with an acute disconnect. Some elements of the disconnect pattern may be artifacts of the test procedure. In particular, the magnitude of the pressure drop

that is observed at the disconnection of the catheter might be diminished in a pressurized liquid ambient. Further tests to confirm these disconnect results should be conducted with various conditions; such as submerged in saline, in tissue, or with an alternative disconnection means. If such tests confirm the capacity for the outlet sensor to almost immediately detect acute disconnects, the delivery system could notify the patient and reduce the effects of acute drug withdrawal.

Magnetic Resonance Imaging (MRI) is a relatively common medical diagnostic technique in which the patient is exposed to very strong magnetic fields (~3 tesla). The long-term implantation of an intrathecal drug delivery device makes it likely that some patients with implants will experience an MRI. It is important that the effects of the strong magnetic field on the delivery profile are understood so patients undergoing an MRI do not experience unexpected changes in dosing.

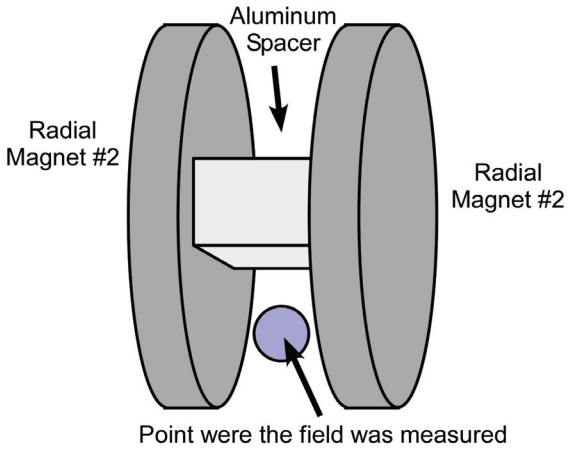

Fig. 6-8: A diagram of the two radial magnets used for the MRI compatibility test and the location of the hall sensor for field strength testing. The minimum measured field strength the manifold experienced was 453 gauss.

Preliminary magnetic compatibility tests for the system were conducted on the manifold to determine changes that occur due to the presence and orientation of a magnetic field. Test fields were generated by separating two radial magnets by 3.5 cm

with an aluminum spacer that kept the plates parallel and maintained a constant separation (Fig. 6-8).

The manifold was placed between the disc magnets in various orientations to test the effects of different magnetic field directions. A hall sensor was placed in the center of the radial discs to determine that 453 gauss was the minimum field strength the manifold would experience. This field was significantly weaker than the strongest fields generated by MRI machines, but it was still strong enough to displace ferromagnetic material and suffices for a preliminary magnetic compatibility test.

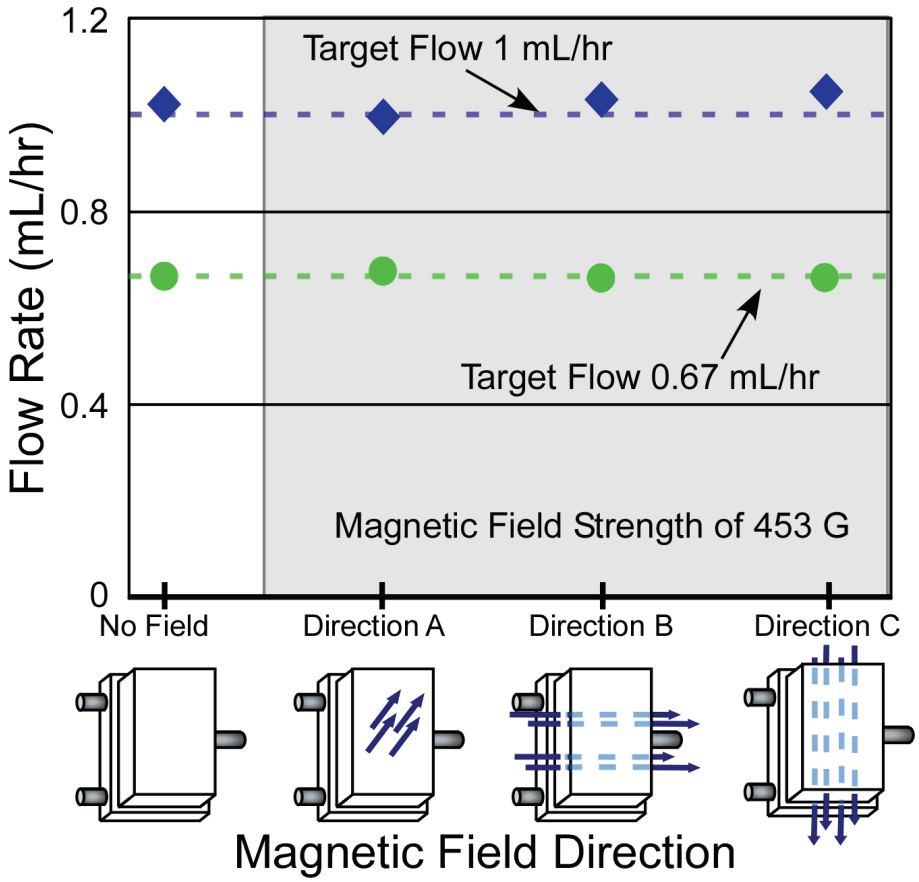

Fig. 6-9: Magnetic field compatibility tests at two target flow rates. Magnetic field orientation and strength caused no significant alteration in flow profiles through the manifold.

Compatibility tests were conducted by constantly flowing IPA through one inlet at two different flow rates while blocking the second inlet (Fig 6-9). Tests were conducted

with no magnetic field, with a field going from bottom to the top of the manifold (Direction A), with a field going from the inlets to the outlet (Direction B), and with a field going across the width of the valve (Direction C). For set flow rates of both 1 mL/hr and 0.67 mL/hr, there was no significant variation due to the presence or orientation of magnetic fields. These initial tests suggest that PZT actuators in a valve manifold are unaffected by magnetic fields. Further testing is necessary to determine if a regulatory system based on this component is MRI compatible, or if magnetic effects cause changes in other features of the system that are not detected in this preliminary test.

6.2.3 System Level Delivery

In the first preliminary device, successful valve regulation of fluid flow was demonstrated using both continuous and duty cycle regulation techniques. The manifold regulated two-reservoir system provides the means for more pertinent tests as they relate to intrathecal delivery of mixed drug protocols. This occurs in two ways; first, having inlet and outlet sensors allows the system to regulate flow with varying CSF pressure. Second, a two-valve manifold allows the regulation of multiple flow streams to occur within a single device.

Intrathecal drug delivery devices have to drive against the CSF pressure to deliver medication. This pressure varies from person to person, and varies within the same person over time based. Typically, intrathecal pressure varies from 0.7 kPa to 1.8 kPa in healthy adults. Detection and compensation for this pressure variation can be achieved by using the outlet pressure sensor.

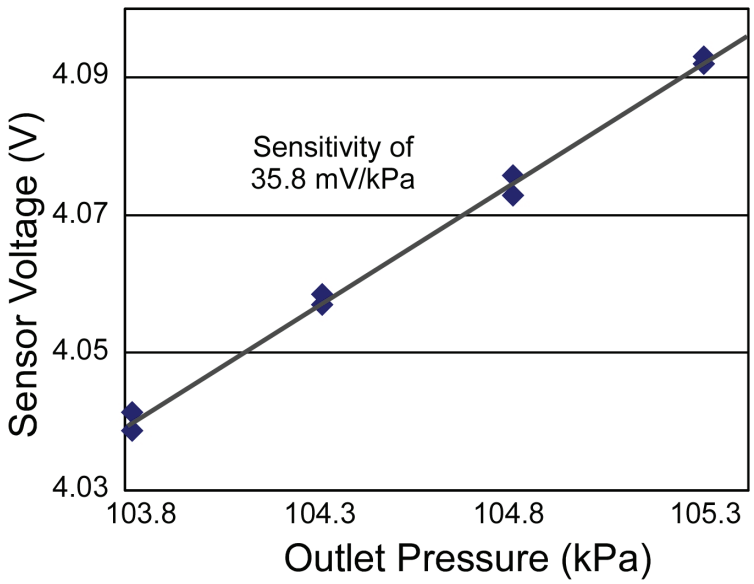

Fig. 6-10: Tests to assess system capability for outlet pressure variation detection in which the sensor voltage at the outlet of the manifold compared varied 35.8 mV/kPa to the actual changes in pressure at the outlet of the catheter

To test the outlet pressure sensor for the capacity to detect intrathecal pressure changes, the outlet catheter was inserted into the bottom of a column of water. The level in the column was varied to reflect the ranges of pressure differences that can occur in the human body. A graph of the pressure sensor characterization for varying flow with a fixed valve width indicates a linear relationship between the sensor pressure and the cylinder pressure with a sensitivity of 35.8 mV/ kPa (Fig 6-10).

The pressure sensor calibration was then used with flow characterizations of the manifold to create a program compensated the aperture to maintain a set flow rate. In a second test, the pressure in the water column was varied while flow rates for uncompensated and compensated delivery were monitored (Fig. 6-11). For valves that remained unadjusted by the compensation program, the flow rate behaved as expected and decreased from 0.58 mL/hr down to 0.21 mL/hr. In contrast, the compensated flow program adjusted the manifold to maintain a flow rate of 0.58 mL/hr while remaining within 0.5 % across outlet pressures.

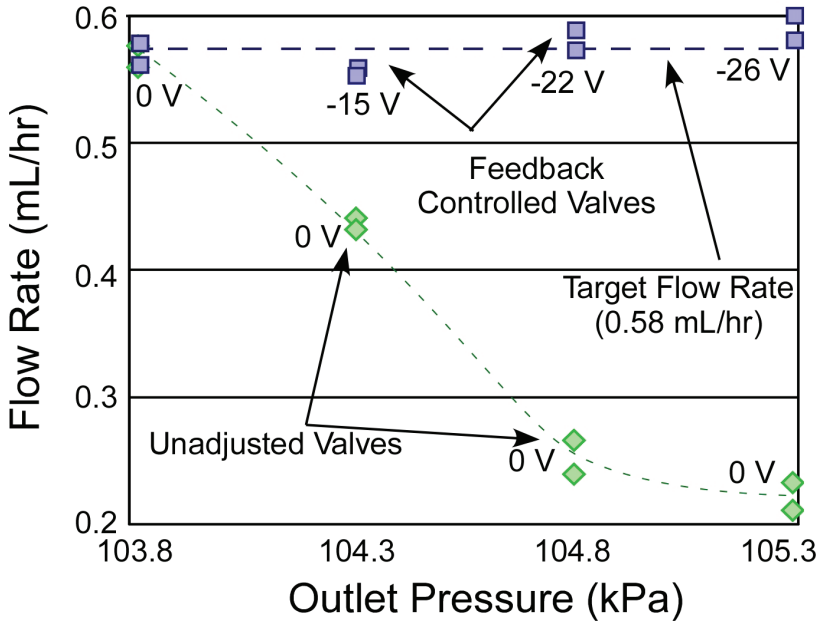

Fig. 6-11: Flow and actuation voltages for changing heights of cylinder pressures to represent unregulated and regulated flow using the internal pressure sensor. Unregulated flow varied from 0.58 mL/hr to 0.21 mL/hr while regulated flow remained within 0.5 % of the target flow rate.

The system was designed to independently regulate delivery from each reservoir. Complete system tests were conducted using previously characterized reservoirs and manifolds in a system assembled with the same control electronics used for the first prototype. Each inlet was driven from a reservoir that was at the same pressure due to the nature of the plate pressurization mechanism. The inlet pressure was recorded and was held constant at 18 kPa. Flow mixed inside the manifold, and was delivered through a 1 m long, 500 μm diameter catheter into an air ambient. One side of the manifold was varied from -30 to 90 V of actuation while the second side was held constant at either -30 or +30 V (Fig. 6-12). The resultant flow rates represented independent regulation of each channel in a manner that is consistent with changing flow resistances along a delivery chain. This is particularly prevalent when Side 1 was either fully open or fully closed. When it was fully open, it had a very low resistance and dominated the flow profile.

When it was fully closed, it had a very high flow resistance and the set state of Side 2 dominated the flow profile.

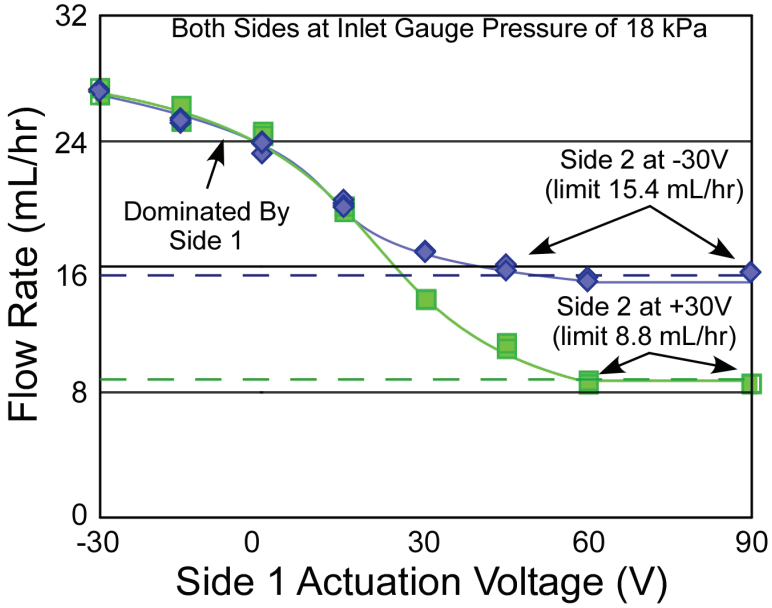

Fig. 6-12: Both sides of the manifold independently regulate flow. Flow rates typically fall within two regimes. In one regime, one side is significantly more open then the other and dominates flow (side of the graph). In the second regime, both valves have similar apertures and contribute to the flow rate (middle).

In controlled flow tests, both reservoirs were pressurized by the spring driven plate, filled via the refill ports, and controlled using a 0-60 V duty cycle powering each side of the manifold from the control PCB. A program was instituted to control the flow at various target flow rates that were altered during the tests. The average supply voltage to the system was 3.3025 V and the average current draw was 18 mA. This resulted in an un-optimized power draw of 57.6 mWhr for the entire system during operation. The device in its current state could only run 100 hrs from a single NiMH AA battery. Additionally, flow rates were well within medical limits of less than 15 % deviation from the target delivery rate. One typical test of this regulation technique is illustrated in Fig. 6-13. In this test, three target flow rates were programmed over a 200 minute period, and

the resultant flow rates were measured with an instantaneous deviated from the set flow rate of no more than 0.01 mL/hr.

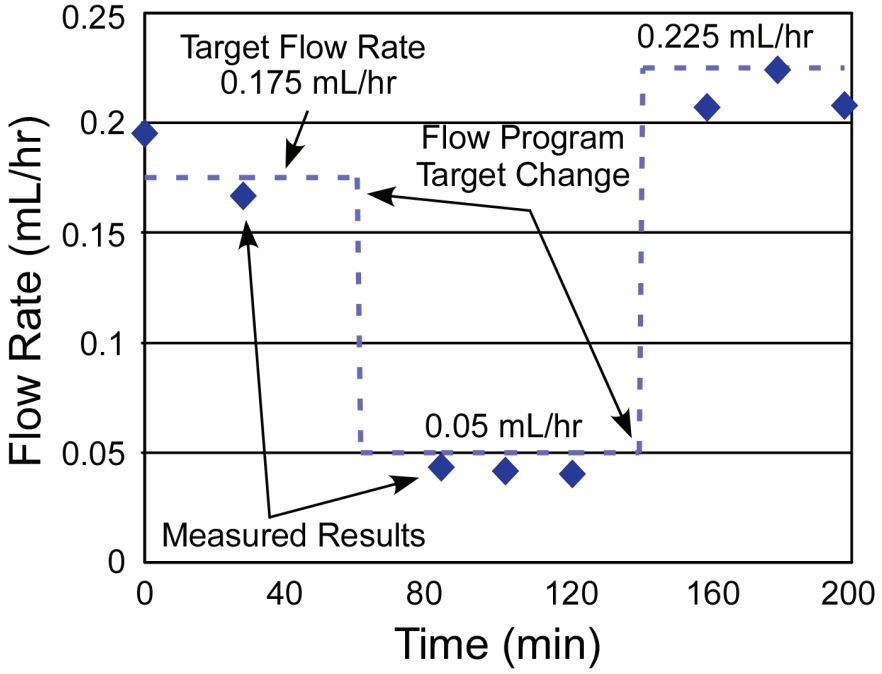

Fig. 6-13: A typical duty cycle regulation of flow through the manifold with multiple set points. In this instance, the duty cycle of a 60 V square wave at 0.02 Hz is altered to achieve mixed flow at the target delivery rates.

6.3 Discussion

This effort has resulted in the successful design and realization of a second prototype system for use in testing aspects of multi-drug protocols with a valve regulated architecture. Piezoelectric valve manifolds with embedded inlet and outlets sensors were assembled and used to regulate flow. A pressurized plate was driven against two PE reservoirs to generate pressures that linearly increased 0.52 kPa per milliliter of volume added. The components were integrated into a stainless steel housing with a total volume of 130 cm^3 and a reservoir volume of 40 cm^3. Several delivery tests were conducted as preliminary investigations into various aspects of intrathecal delivery. Power consumption was 57.6 mWhr, but shows promise for reduction to 100 μWhr with

software optimization. Further reduction to 10 μWhr could be achieved with an alternative low-power microcontroller [Han08]. Initial results suggest possible detection of catheter occlusions and disconnects. Testing also indicates that a system based on this preliminary design should be unaffected by during an MRI and can compensate for changes in spinal fluid pressure. Several delivery tests were conducted for both bolus and continuous flow delivery using flow from two reservoirs. In summary, valve regulated drug delivery holds promise as a volume efficient, versatile, and safe architecture for an multi-drug protocol system.

CHAPTER 7:

TRANSDERMAL POWER TRANSFER MECHANISM

The power transfer mechanism used to recharge the battery in the implantable system (Fig. 2-1) can be designed using several techniques. This chapter describes a power transfer mechanism that was designed to allow for direct contact between the recharging source and the implanted device. Further details on the needle and port pairing are in Section 7.1. The device design is discussed in Section 7.2. Details on the fabrication and assembly are in Section 7.3. Experimental results are reviewed in Section 7.4, and Section 7.5 provides are summary discussion.

7.1 Needle and Refill Port Pairing

7.1.1 Device Overview

Recharging the battery of an implantable device provides efficiency and convenience. It allows designs that require a much smaller battery. Architectures taking advantage of this reduced battery size are able to achieve a greater volume efficiency than traditional devices. This is particularly true for devices that have long implant lifetimes and relatively high rates of power consumption like intrathecal drug pumps [Car07].

Implantable batteries can be recharged through either a direct physical connection, through a wireless radio frequency, or an inductive link. While wireless power transfer is possible for very low-power applications [Bov08], DC recharge capability offers higher

current levels and may be more suitable for implantable drug delivery devices [Vip07]. The only connection made between the external environment and the implanted drug delivery device occurs while a needle is inserted into the access port during a reservoir refill session. Refill ports typically consist of an external biocompatible housing, a re-sealing silicone septum, a metal base plate that limits needle penetration, and a gap between the septum and the base plate with an exit channel through which the fluid enters the reservoir [And90, Str86]. The refill port is typically inset within the drug pump housing in a position in which the rounded rim protrudes just above the wall of the housing [Rey96]. A normal refill session begins with the puncturing of the septum using a non-coring Huber needle until the needle tip presses against the base plate. Medication is then driven into the device from an external syringe [Mor92]. Refills generally require 10-20 minutes and occur every 8-10 weeks.

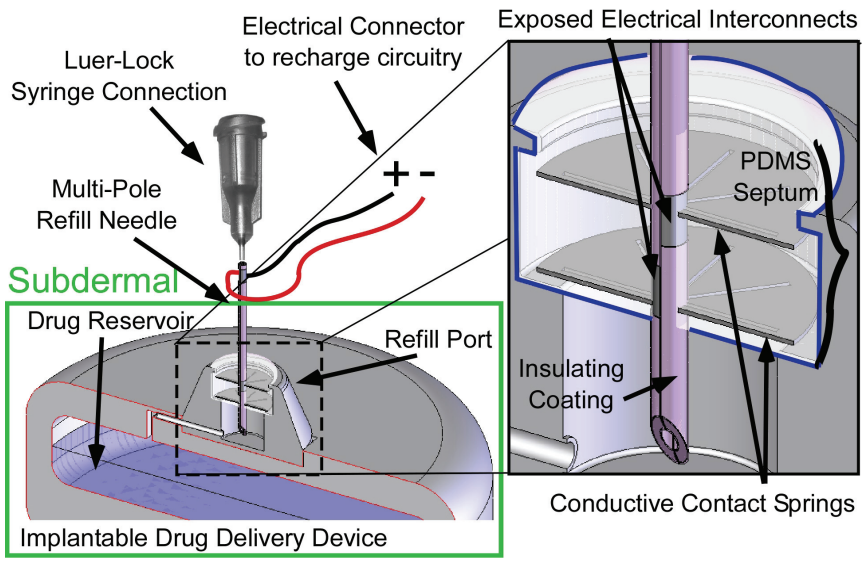

Fig. 7-1: The system view: A two-pole needle is inserted into the refill port of a drug delivery device. Inset: A close view of the two needle halves making electrical contact with springs inside the septum.

A method for power transfer through a customized conductive needle designed to interface with metal spring electrodes embedded in a refill port was developed for implantable drug pumps (Fig. 7-1).

The needle adapts a current model to allow for two isolated conductive pathways. The refill port is designed with embedded metal springs to mate electrically with the modified needle. The system is designed to mate successfully regardless of the rotational orientation or insertion angle of the needle. This prevents the need for the physician to rotate or reinsert the needle to make proper contact, which may otherwise create an additional risk of infection or patient discomfort beyond that which is already experience in the refill process.

7.2 Device Design

The most important aspects of the design are power handling capability, isolation of the drug and tissue from electrical current, and ease of alignment between the needle and the port. In order to transfer DC power, the needle should be composed of at least two conductors, or poles, which must mate with corresponding poles in the refill port. The conductive path should also be electrically isolated. (The isolation is particularly important if the needle is being used to refill the drug reservoir at the same time the battery is being recharged. While this capability is not fundamentally required, it can improve efficiency and convenience.) Structural options for providing multiple conductive paths in a single needle include the use of multiple conductors within the lumen, the use of concentric isolated conductors, or splitting the needle longitudinally

and isolating the halves. The split needle allows for simple alignment because it provides access to both conductors on the exterior of the needle.

7.2.1 Power Transfer and Needle Design

While it is relatively easy to transfer data across most electrical connections, it is more difficult to transfer current at levels of hundreds of milliamps as required to recharge a battery [Sor01]. One challenge is resistive heating in the conductors. For a given conductor, this requires the use of a conductive path with the largest possible cross sectional area. The two methods of creating conductors with the largest cross sectional area are either using the needle itself or filling the needle with a conductor. Using the needle itself is preferable to other methods because the lumen remains unobstructed. Typical refill needles used in implantable drug delivery devices range in size from 22 gauge to as narrow as 28 gauge. The ratio of the inner diameter (r) to outer diameter (R) ranges from 0.55 to 0.6 across this needle range.

7.2.2 Refill Port Design

The refill ports of most implantable drug delivery devices are composed of a polymer septum through which the needle enters the device. The polymer is relatively thick (2-5 mm), and is designed to reseal itself after the refill needle is removed from the device. Below the septum is a small open volume that is connected to the reservoir of the implant. The thickness and insulating properties of the septum make it an appealing candidate for modifications that would allow power transfer.

Fluid ports in conventional implants are typically accessed by non-coring Huber needles. In our design, the power transfer system mates when a multi-pole, non-coring needle punctures the PDMS septum of the refill port and is advanced until the tip of the needle reaches the metal base plate at the bottom of the port. (This metal base plate is electrically floating.) Each longitudinal half of the needle is exposed at a "window" on its exterior; the "window" for each half is at a different point along its length. The location of metal contact springs that are embedded within the septum and the exposed "windows" in the insulation of the needle are designed so the windows align with the mating regions when the needle is fully inserted. This occurs upon every insertion because the tip of the needle presses against the bottom base plate of the refill port. Since two separate springs are located at different heights, rotational alignment of the needle is not necessary to make electrical contact. This prevents the need to twist the needle upon insertion, and it also prevents mating the incorrect conductors to the springs. It should be noted that the needle and the metal springs in the septum are electrically isolated from the casing of the port, the surrounding tissue, and the drug being refilled. The metal contact springs could potentially be replaced by conductive layers that are composed of specialized polymers [Ger02] or conductive fibers in a weave [Taj02]. The most important criteria for determining the structure of the mating springs are the formation of a low resistance contact and the ability to maintain functionality after repeated insertions.

7.3 Fabrication and Assembly

The two system components requiring custom fabrication are the non-coring needle and the refill port. Two-pole Huber needles (700 μm ø, 26 gauge) for use with a smart

refill port are fabricated by lapping two stainless steel needles in half using an oil-based diamond slurry (Fig. 7-2). The needle halves are completely coated in 2.8 μm thick Parylene to electrically isolate the halves from each other and from the environment. Parylene is selectively removed from areas near the needle tip to create the contact windows that mate in the refill port and from the back of the needle to allow contact with the power source. The needle halves are then aligned and bonded [Kim05], with further insulation and sealing strength provided by inserting the needle into a 50 μm thick Kapton tube. Stainless steel needles and Parylene are used to create the two-pole needle because they are biologically compatible materials. Additionally, the thin Parylene coating does not significantly change the inner or outer diameter of the needle.

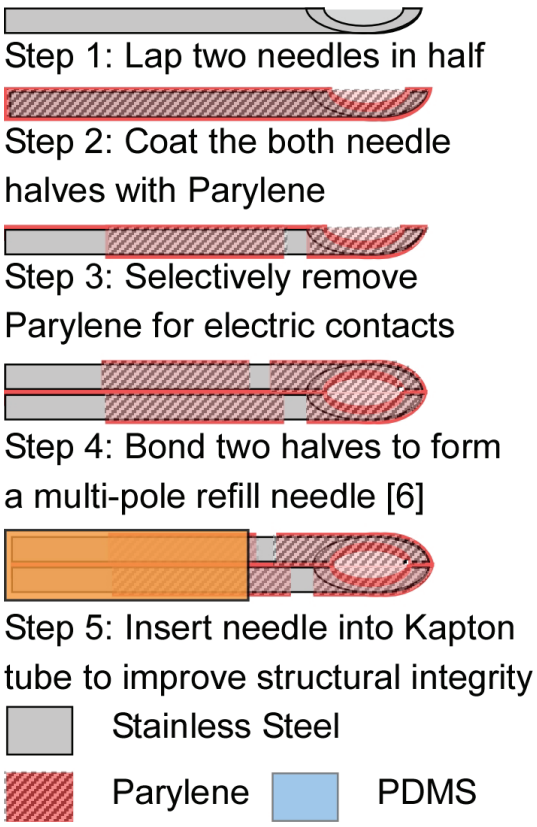

Fig. 7-2: The needle is fabricated from biologically compatible materials. The fabrication process creates open conduction paths or "windows" that are self-aligning once inserted into the port.

The refill port requires a septum designed with contact springs at specific heights to allow for self-aligned mating. The electrical contact springs are fabricated from 100 μm thick stainless steel by micro-electro-discharge machining (μEDM) [Tak02, Ric08]. The contact springs are 5.2 mm in diameter with four quadrants separated by 300 μm wide slots (Fig. 7-3).

The septum is fabricated by inserting two 100 μm thick stainless steel contact springs within the septum at the positions of 4.5 and 5.5 mm above the base plate. The PDMS itself begins at 3.5 mm above the base plate extends to 6.5 mm above the base plate. The septum is 5.88 mm in diameter and is held in place on a shelf in the refill port by compression. A fabricated needle and port are show in Figure 7-4.

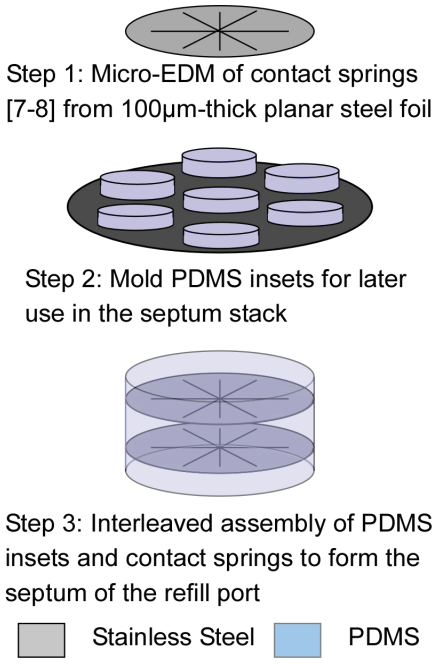

Fig. 7-3: The septum is fabricated from biologically compatible materials. Contact springs of various heights are created to form contact with the openings in the needle coating the conductive needle to allow power transfer.

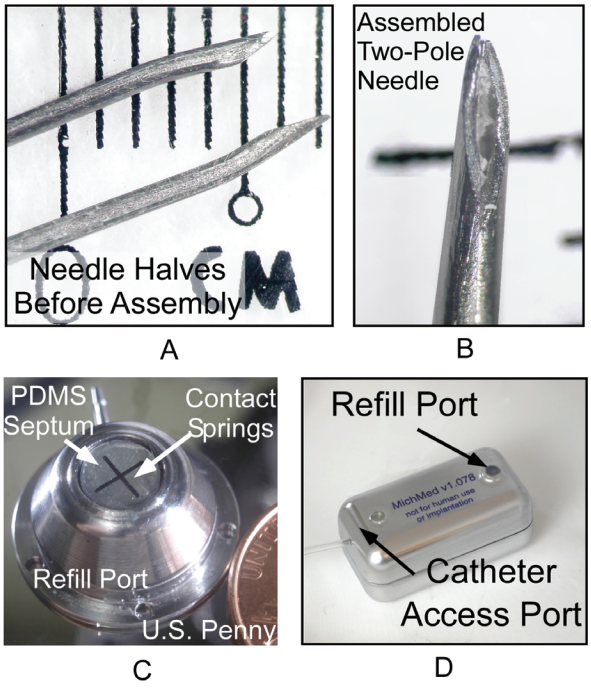

Fig. 7-4: (a) Photographs of 26 gauge coated needle halves before and (b) after assembly taken on a white ruler. (c) A photograph of an assembled refill port in which the top contact spring of the septum is clearly visible. The port is pictured here with a US Penny. (d) An implantable drug delivery device with the refill port and a similar catheter access port.

The springs press against the needle as it is inserted. The pressure forces the needle toward the middle of the refill port, and it also improves the lead transfer conductance by maintaining pressure at the spring/needle junction. The symmetrical nature of the contact springs prevents the need for rotational needle alignment. Additionally, the springs are supported by the PDMS used as the septum polymer and return to their initial positions after the needle is removed. This allows for multiple recharging sessions to occur using a single port.

7.4 Experimental Results

Contact resistance, in both dry and wet ambients, can provide an indication of the integrity and power handling capability between the needle and the port. Higher transfer

currents can alter the contact properties of the mating pair, and these changes can be monitored while recharging batteries. Long term viability can be determined by puncturing the septum multiple times and monitoring the transient changes in resistance and septum deformation. Proper testing allows for determination of both short term and long term properties of the mating pair.

In mating both conventional Huber needles and two-pole needles with assembled refill ports, continuity tests can identify if electrical connections are made as expected (Fig. 7-5). Resistances between the two poles of the needle (A and B), the two septum springs (C and D), and the electrically floating metal base plate (E) were measured as both types of needles were advanced into the septum.

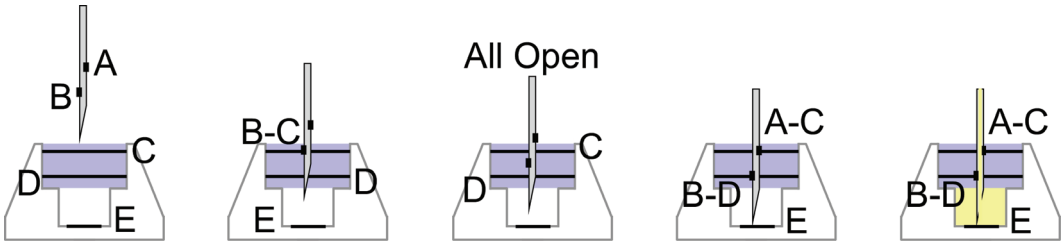

	Not Inserted		Partially In		Disconnect In		Inserted		Saline
Conventional	Expected	Actual	Expected	Actual	Expected	Actual	Expected	Actual	Actual (wet)
A to C	Open	>10M	Short	0.328	Short	0.374	Short	0.367	
A to D	Open	>10M	Short	0.528	Short	0.528	Short	0.532	
A to E	Open	>10M	Open	>10M	Open	>10M	Short	1.09	
Two-pole									
A to C	Open	>10M	Open	>10M	Open	>10M	Short	0.64 -	1.22
B to D	Open	>10M	Open	>10M	Open	>10M	Short	0.83 -	1.65
B to C	Open	>10M	Short	1.4	Open	>10M	Open	>10M	2.3M
A to E	Open	>10M	Open	>10M	Open	>10M	Open	>10M	2.6M

Fig. 7-5: Stages of insertion with resistances color coded to expected states for normal and split needles both dry and completely filled with saline after insertion. (All resistances are in Ω)

In a dry ambient, typical resistances for a fully inserted normal needle were about 0.5 Ω from A to C and D; and 1 Ω between A and E. The two-pole needles had slightly higher resistances from A to C and B to D (~0.7 Ω) but maintained isolation from A to B

(1.6 MΩ) and from A to E (greater than 10 MΩ). The resistance tests also confirmed that C and D were electrically insulated from each other and from E. The slightly higher resistances attributed to the two-pole needles were likely due to the decreased cross sectional area of the needle, and the decreased contact area between the conductors of the split needle and the metallic contact springs. These tests indicated that both the modified and original needles made good electrical contact with the springs. Additionally, the isolation mechanisms of the split needle and the septum functioned as expected. This was verified in the fully inserted state because a normal needle short circuited with both springs and the base plate while the split needle functioned as expected.

Saline is often used as the carrier agent for medication. Saline can also be used to approximate the *in vivo* electrical conditions experienced by implantable devices. In a separate set of tests, saline was introduced into the needle lumen and the port cavity. The exterior of the port was also immersed in saline. Insertion tests, similar to those done in a dry environment, were conducted in this wet ambient. As shown in Figure 7-5, resistances from A to C and B to D were low (less than 2 Ω), and electrical isolation was maintained from B to C and A to E (greater than 2 MΩ). This suggests that the isolation techniques used in the system are effective at isolating the conductive paths from both the medication and the surrounding environment. Additionally, no electrolysis was observed in either the needle or in the mated port during characterization.

One potential limitation on the current levels that can be sustained during a recharging operation is imposed by the parasitic resistive heating of the implantable device, medication, and surrounding tissue. In order to determine the resistive heating in the needle and at the interface between the needle and the contact springs, the change in

temperature was monitored as batteries were recharged. Two 1.2 V NiMH AA batteries were recharged using various current levels at room temperature in a dry environment. The air environment restricts the thermal conductance of heat away from the refill port as compared to a refill port located subcutaneously *in vivo* or in an aqueous medium. Additionally, a lack of liquid located within, or flowing through, the lumen reduces the thermal capacitance of the system and increases the heating of the device for any particular power transfer rate. Typical room temperature recharging with power transfer rates ranging from 10-500 mA demonstrated the expected temperature rises at needle-septum interface (Fig. 7-6) and out on the port housing (Fig. 7-7) of the refill port.

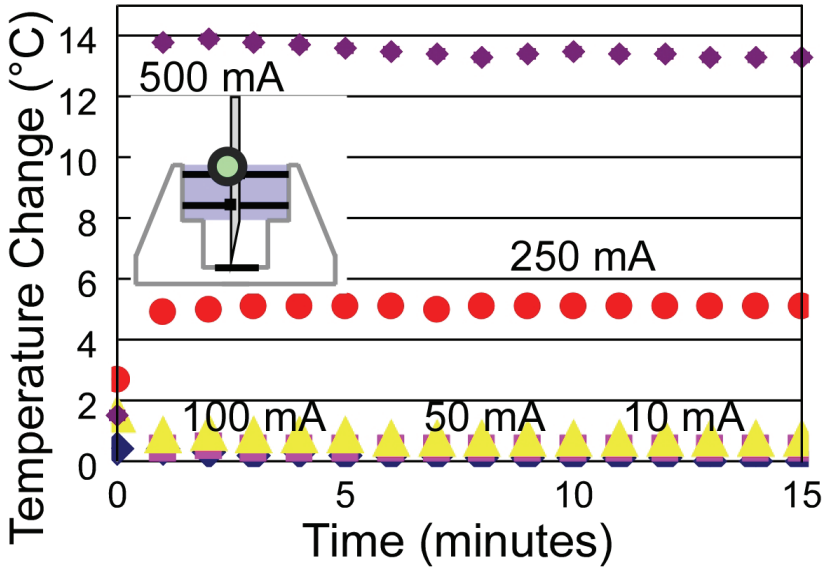

Fig. 7-6: Temperature change at the septum entry point over time for recharging currents from 10-500 mA. The circle in the inset denotes the temperature sampling location. The test was conducted in an air ambient environment with a baseline temperature of 22.4 °C.

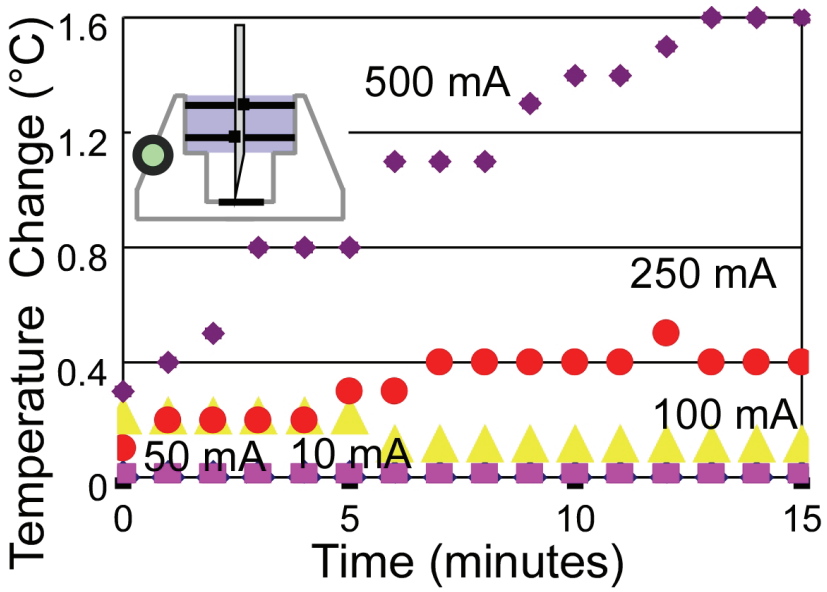

Fig. 7-7: The temperature change of the exterior of the port housing for battery charging currents ranging from 10-500 mA. The temperature increase has resolution of 0.1°C and was conducted in ambient air with a temperature of 22.4 °C. The circle in the inset denotes the temperature sampling location.

The temperature changes at the needle septum entry point exhibited much higher swings because the PDMS septum is not thermally conductive. This is a location in the system that will experience one of the largest temperature increases. The battery voltage was monitored (Fig. 7-8) along with temperature for varying current to confirm the batteries were recharging at rates relative to the transfer current. Typical starting voltages ranged from 1.1 V to 1.4 V. No measureable heating was observed for charging currents of 100 mA or less. At higher current levels (above about 500 mA), modest heating occurred: temperature increases were less than 15°C at the septum and 2°C at the casing. Overall, these results indicate that this type of port is suitable for rapidly recharging a small battery in an implantable drug delivery device.

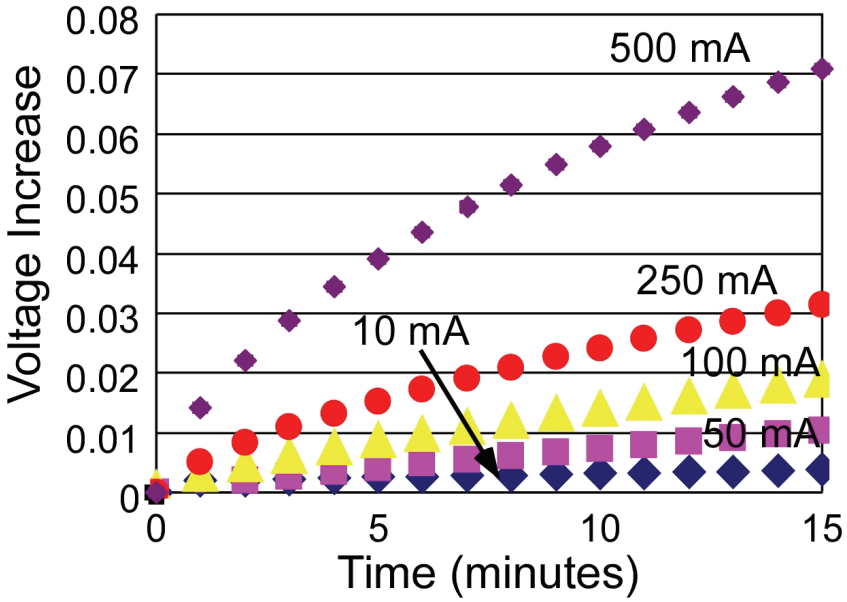

Fig. 7-8: The voltage increase of a NiMH 1.2 V AA battery as it is being recharged across a refill port with various charging currents. Typical starting voltages range from 1.1 V to 1.4 V. Charging profiles match expected values, and demonstrate power transmission with acceptable heating rates for a smart needle and port to be used in implantable drug delivery devices.

In addition to forming good electrical connections and limiting heat generation during battery recharging, this type of power transfer system needs to be reliable over many refill sessions. This is particularly true for mechanical springs because of potential plastic deformation. Typically refill sessions occur once every 6-8 weeks, and device lifetimes range from 5-8 years. Assuming the device is refilled every 6 weeks for 8 years, the refill port could be punctured as many as 70 times. Puncturing the septum many times acts as an approximate simulation of the effect of accumulated refills on the springs, silicone, and device connectivity.

Puncture tests were conducted in an air environment using a refill port and a standard Huber needle. A refill port was punctured one hundred times, and both the resistance and images of the septum were captured. The resistance measurements (Fig. 7-9) varied over

0.27-1.4 Ω and exhibited a roughly logarithmic increase with the number of needle insertions.

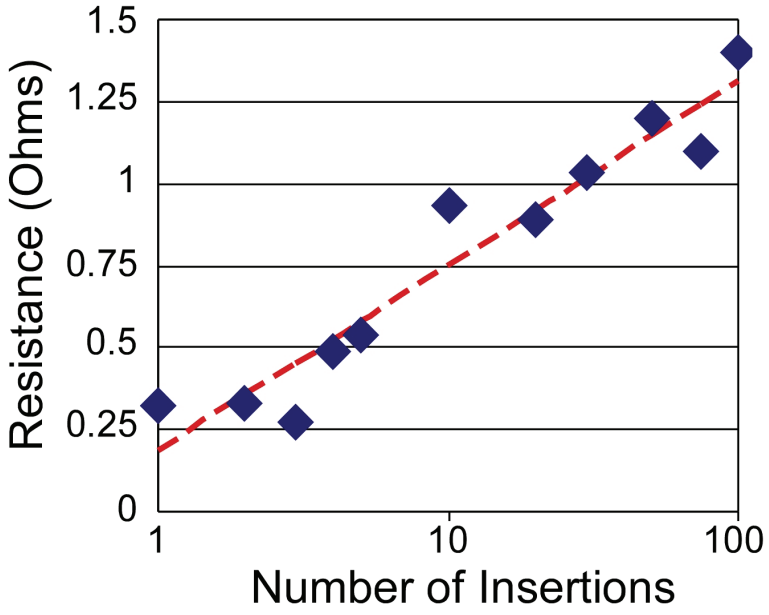

Fig. 7-9: The resistance of the needle and spring contact resistance across many insertions with a logarithmic fit. The resistance varies from 0.27-1.4 Ω over 100 punctures. The logarithmic nature of the resistance indicates that the principal changes to the connection occur early in the life cycle of the refill port.

The image data (Fig. 7-10) clearly displays the plastic deformation that occurs to the septum springs during the initial insertions. Additional punctures caused no apparent changes to the springs, and only slightly altered the PDMS. The image analysis indicates that plastic deformation in the springs and additional mechanical failures in the septum are only likely to manifest themselves during the first few insertions. This logarithmic resistance tendency agrees with the image analysis and further suggests that changes to the mechanical properties of the system occur early on in the lifecycle of the device. The long term tendency to approach a stable operating point, in addition to acceptable electrical and thermal performance from the complete system, indicates that it could be used to recharge batteries in an implantable drug delivery device.

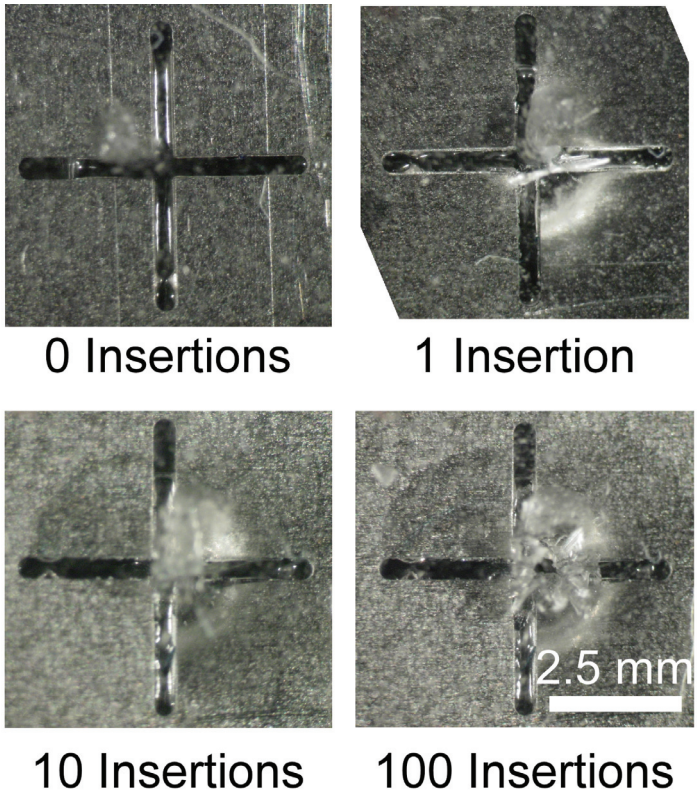

Fig. 7-10: Photographs of the needle septum after a set number of punctures taken under a microscope. The photographs reveal that almost all of the spring deformation occurs during the first needle insertion, and subsequent punctures cause minimal mechanical alteration to the port.

7.5 Discussion

Power transfer development addresses the design and specifications for a potential method of recharging the battery in the implantable drug delivery architecture. This work focuses on recharging the implanted battery during a refill session every 8-12 weeks with enough power to replace what is used between visits. Transferring electrical power through the refill port allows high enough energy densities to be transferred during a refill while minimizing impact to system size and complexity.

This work explored a method for transferring electrical power across a bifurcated needle through the refill port of an implantable drug delivery device. The method is

intended for current levels up to 500 mA and voltage levels up to 3.3 V, as needed to rapidly charge implant batteries. The approach utilized a longitudinally split, two pole Huber needle and a mating port with spring-loaded connections. The refill port connection self-aligns with the needle and makes ohmic contact when the needle is fully inserted. This required no additional alignment. The electrical contact and insulation performed well in both wet and dry ambient environments. The mechanical properties of the refill port remained functional for repeated needle insertions. The modest increases in temperature for even the highest current levels demonstrated that a physical recharging mechanism can work for an implant. The possibility of recharging the battery of an implantable drug delivery device during a drug refill session could result in an implantable drug delivery device size reduction of up to 40%. The recharging capability allows greater system versatility because more energy intensive functions can be implementer. A power transfer connection across the refill port of an implanted device could greatly improve both volume efficiency and system functionality.

CHAPTER 8:

SUMMARY AND FUTURE WORK

A valve regulated active architecture was developed for intrathecal drug delivery devices. The architecture allows for new functionality and high volume efficiency. MEMS components for two prototype systems were developed and tested. Prototypes were assembled and valve regulated delivery was demonstrated. Additionally, a transdermal power transfer mechanism was developed to further reduce device size by allowing the battery to be recharged.

8.1 Dissertation Summary

Chapter 2 outlines the architecture of the final integrated system and component specific parameters. The system is designed with multiple independently regulated microvalves that throttle drug flow from mechanically pressurized reservoirs. The use of regulatory valves allow for high volume efficiency, therapeutic returns from mixed medication, and low power consumption. Additionally, power transfer mechanisms allow for battery recharging and communications.

Potential valve actuation mechanisms were explored to determine a suitable candidate for the system architecture. Piezoelectric actuation was found to be appealing because it can overcome high reservoir pressure and has low power consumption. Metrics for microvalve performance were set at regulation of saline flow from 0.1 – 5 mL/day.

Addionally, the valves should consume less than 1 mW and be smaller then 3 cm^3. The reservoirs were defined as needing volumes between 10-30 mL with dead volumes of 1-3 mL. Compressive pressure mechanisms should pressurize 80% of the reservoir volume at 600 Pa or greater. Also, it was determined that reservoir pressure should not exceed 200 kPa. The system should have linear pressure sensors in the flow path for feedback control of the valves to adjust the delivery rate. An embedded processor is necessary to process the sensor data for the control algorithms, device communication, and error detection. Every element of the circuit must conform to a single supply voltage. A recharging mechanism is necessary to minimize battery size. The circuit needs to provide the full range of clinical functionality while being as power efficient as possible in an effort to further reduce battery volume. These system component definitions should allow an itrathecal drug delivery device the advantages of a valve regulated architecture.

Chapter 3 outlined the PZT microvalves used in the drug delivery system. Three different types of valves were discussed. The first type uses a rectangular serpentine valve seat and flexure suspension. The second type uses a curved valve seat and membrane suspension. It also has an embedded pressure sensor. The third type is a manifold with two starburst valve seats and multiple pressure sensors to determine the differential pressure across the valve.

Flexure suspended valves were assembled with PZT stacks in a ceramic header for a total device size of 1 cm^3. The valves were tested with gas flow at a gauge pressure of 55 kPa and the flow rate could be modulated from 0 to 980 mL/min. At 60 V, valve leakage was below the measurement limit (< 0.1 mL/min.). Preliminary liquid flow tests were performed at room temperature using oil (viscosity 4.5 cP) and the flow rate varied

linearly with the differential pressure over a range of 250-460 μl/min; the corresponding differential pressure drop was 16 - 47 kPa.

Membrane suspended valves were assembled into devices with a total size of 2.25 cm^3 but with a fluid path dead volume of only 0.021 cm^3. The valves were fabricated a boron piezoresistve Wheatstone bridge pressure sensor at the inlet. A normally-open and a normally-closed valve were tested at room temperature with N_2 gas flow at the gage pressure of 52 kPa. The valves were actuated from 0–40 V and the flow rate varied from below the measurement limit (< 1 mL/min) to above 200 mL/min in the normally open valve and above 100 mL/min in the normally-closed valve. Several resistors were tested at room temperature and they averaged around 23.5 kΩ with an average pressure sensitivity of 356 ppm/kPa at room temperature.

Valve manifolds with starburst valve seats were assembled with Macor into devices with a total size of 4.5 cm^3. The manifolds had three Wheatstone bridge pressure sensors to monitor both inlets and the common outlet. Gas flow tests in standard flow valves used actuation voltages ranging from -30 to 90V with inlet pressures from 0 to 23.5 kPa and a maximum flow rate of 521 ml/min. High-flow used lower valve actuation voltages (-20 to 40V) across inlet pressures from 0 to 23.5 kPa with a maximum flow rate of 419 ml/min. Tests were conducted with pressurized IPA on a standard manifold to determine mixing from each channel. Flow from one side of the manifold varied from 1.77 mL/hr to 0.028 mL/hr and the other varied from 2.12 mL/hr to 0.38 mL/hr. Several pressure sensors were tested at room temperature with average resistances between 100-150 kΩ and an average sensitivity of 698 ppm/kPa.

Chapter 4 outlined the design and testing of two types of compression mechanisms that provided mechanical pressure necessary to drive drug delivery. One mechanism utilized compressive metal springs wrapped in a sleeve around a polymer chamber. The alternative mechanism used silicon torsion springs to press against a PET balloon to generate pressure.

Fifty-element springs were fabricated to pressurize a 4 mm thick balloon. The springs consisted of bends that measure 40 μm deep, 60 μm wide, and 150 μm long with a total length of 3.5 mm. Optical techniques were used to measure the spring deflection for various pressures. The torsion springs deflected up to 4 mm as the reservoir was inflated for nonlinearly increasing pressure that reached 80 kPa for a fully filled reservoir. The silicon springs were brittle and difficult to handle.

Planar Elgiloy springs were designed to be used in compressive sleeves that pressurize a PET chamber measuing 20 mm in diameter and 60 mm in length. The springs were fabricated from 100 μm thick sheets with a pattern in which the beams were 150 μm wide, and the mesh cell size was 600 μm by 6 mm. Conditioned springs were found to have a spring constant of 307.5 N/m and generated reservoir pressures up to almost 15 kPa when fully inflated. Compressive sleeve springs were used to pressurize the reservoir in the initial system because they take little volume, offer comparable pressures to traditional springs, and plastically deform instead of break.

Chapter 5 outlined the results of a preliminary drug delivery system using a valve regulated architecture. A single valve was used to regulate fluid flow from a single spring pressurized reservoir. Control circuitry was designed and assembled to operate the system. A housing was developed to encase the system components for testing.

A control PCB was designed that measures 4 cm x 6 cm and powered from a 3 V battery. The pressure sensor input was amplified and read by an ADC. This data can be used in the closed loop control algorithms implemented in the microcontroller. The circuit can actuate the throttle valve with 0-90 V. The maximum power consumption of the valve was 1.68 μW when it was controlled with the PCB. Controlled diffusion into agar gel was demonstrated. Analysis of the images strongly suggested valve regulation is the only element responsible for diffusion rate changes. A preliminary aluminum encasement was developed for the system. It held a microvalve, a large compressive sleeve reservoir, the control circuitry, a battery, and had two ports for refilling the reservoir and accessing the catheter. The housing has a total volume of 113 ccm with a total reservoir volume of 37 ccm giving it a high VER.

The system was tested for both bolus and continuous flow regulation. In one typical test, four boluses of 1.5 mL were delivered using a program targeting 6 mL by actuating a valve with 40 V to open it and 0 V to close it. The actual delivered volume was 5.971 mL. The pressure sensors averaged errors of less than 1.04 kPa. Deviation from target flow for one control algorithm averaged less than 6.4% of the maximum flow for a particular pressure. Testing of the complete system for continuous flow was conducted by re-filling the reservoirs, programming a delivery schedule, and measuring the distance travelled by an air bubble through a catheter. Tests typically ran from 8 hrs to as long as a week. One such long term test (Fig. 5-10a), demonstrated average delivery accuracies of 3.22% with no deviation from the flow rate worse than 9.09% at delivery volumes of less than 0.2 mL/day.

Chapter 6 outlined the results of a second preliminary drug delivery system using a two-valve manifold. The manifold was used to regulate fluid flow from multiple polymer reservoirs pressurized by a spring loaded plate. A stainless steel housing was developed to encase the system components for testing.

Embedded pressure sensors at the outlet of the device were used to determine the potential of the system to detect catheter occlusions. The outlet sensor also demonstrated the potential to detect acute catheter disconnects from the delivery device. Oscilloscope traces of the pressure sensor response provide good preliminary to justify further investigations into the capacity of the outlet sensor to determine the state of the delivery catheter. Magnetic compatibility tests were conducted and no evidence of device alteration was found with magnetic fields of at least 453 gauss is various orientations. A preliminary stainless steel encasement was developed for the system with a total volume of 130 cm^3 and a total reservoir volume of 40 cm^3.

The system was tested for various aspects of flow regulation. A control program was designed to compensate valve apertures to adjust for changes in output pressure that reflect the range of typical intrathecal pressures. The regulated program maintained a steady flow of 0.58 mL/hr across pressures while flow from an unregulated valve diminished from 0.58 mL/hr to 0.21 mL/hr. Various actuation voltages were applied to both sides of a manifold, and resultant flow operated in one of two regimes. Either one valve was significantly more open then the other, in which case it dominated the flow profile, or both valves apertures were comparable and flow was relatively evenly distributed. Regulation tests were conducted by adjusting the duty cycle of a 0-60 V actuation to each side of the manifold. In on such test, three different flow rates were

preprogrammed, and measured flow deviated less than 0.01 mL/hr from the target flow rate.

Chapter 7 outlined a method for power transfer through a customized conductive needle designed to interface with metal spring electrodes embedded in a refill port. The needle adapted a current model to allow for two isolated conductive pathways. The refill port was designed with embedded metal springs to mate electrically with the modified needle. The system was designed to mate successfully regardless of the rotational orientation or insertion angle of the needle.

Two-pole Huber needles (700 μm ø, 26 gauge) for use with a smart refill port were fabricated by lapping two stainless steel needles in half. The needle halves were coated in 2.8 μm thick Parylene for electrical isolation, and further insulation and sealing strength was provided by inserting the needle into a 50 μm thick Kapton tube. The refill port electrical contact springs were fabricated from 100 μm thick stainless steel by μEDM. The contact springs are 5.2 mm in diameter with four quadrants separated by 300 μm wide slots. The septum was fabricated by inserting two contact springs in the septum at 4.5 and 5.5 mm above the base plate. Resistance was tested in both wet and dry ambients and results conformed to expectations. Two 1.2 V NiMH AA batteries were recharged using various current levels at room temperature in a dry environment. Power transfer rates ranging from 10-500 mA demonstrated the expected temperature rises at locations along the refill port. Typical starting voltages ranged from 1.1 V to 1.4 V. No measureable heating was observed for charging currents of 100 mA or less. At higher current levels (above about 500 mA), modest heating occurred: temperature

increases were less than 15°C at the septum and 2°C at the casing. The refill port was punctured one hundred times, and the resistance and varied over 0.27-1.4 Ω.

8.2 Suggestions for Future Work

The tests for each system component and the system as a whole took place at the bench-top, rather than with *in vitro* or *in vivo* conditions. The tests were designed to partially recreate conditions that would be experienced by the components and the system after implantation, while still being simple enough in nature to allow for a first-pass evaluation of sensor and device performance. Crucially, the lessons learned with these first-pass evaluations – allow us to define more complete prototypes with associated key parameters and evaluation methods that accurately simulate medical conditions.

The specifications for additional devices and components are described in more detail. Additionally, the performance of the preliminary systems is discussed in the context of each of these specifications. Where needed, potential design improvements and additional bench-top methods for verifying that the design meets the specification are presented.

Although bench-top testing methods allow for simple characterization, a main goal of this work is to demonstrate a fully function intrathecal drug delivery device. To more rigorously display system performance, *in vitro* testing of an assembled system should be conducted.

8.2.1 Future Device Specifications

The development of future devices should progress toward two goals: the first goal is the improvement of the VER of the system, and the second goal is the development and analysis of medical diagnostic and treatment techniques.

There are several alterations to the preliminary prototypes that can yield higher system VER. Early test results indicate that duty-cycle regulation provides more accurate and reliable control of the drug delivery rate. A new bi-stable valve structure that is either open or closed may be smaller and easier to fabricate than the current multi-state stable PZT valves that are currently used. Advances in the valve design using alternative actuation mechanisms and valve structures would allow for some scaling in the system. Additionally, efficient space employment in the housing coupled with spring advancements could yield significant VER improvements. A restructuring of the second prototype can reduce the total system volume by 30 cm^3 with no change in the included components. The high VER prototype should have two reservoirs that each contain 10-20 mL, flow regulation capabilities from 0.01 – 30 mL/hr, a five year battery life, embedded sensors, wireless communication, and a volume efficiency ratio of at least 50%.

Prototypes for medical diagnostic and delivery characterization could also be developed using modifications to more traditional devices. For example, the COMDMAN 3000 drug pump uses a Freon pressurized reservoir held constant at between 50 - 60 kPa. Drug delivery is realized by driving this fluid through a restrictive glass tube with tight tolerances on diameter. The nominal flow rate is set but the length of the tube. Research groups have altered this restrictor to use the CODMAN 3000 as an

independently set drug delivery device [Bae08]. One future work prototype could use a similar adaptation to a commercial intrathecal drug pump. The adaptation could include embedding sensors or even adding a valve regulator to the output of the device. A prototype fabricated in this way would have poor volume efficiency, but it could be more rapidly developed and deployed in *in vivo* medical studies to determine the diagnostic advantages of embedded sensors. A prototype fabricated using this method should have an output pressure sensor, a method for flow regulation (either a valve, or pump), embedded electronics, and be compatible with long term implantation.

8.2.2 *In Vitro* Testing

Although good performance in initial bench-top testing provides confidence that the system architecture will perform as intended, *in vitro* testing will provide a more accurate assessment of the system. The outlet of the device should run through tissue mediums that simulate the different profiles the catheter experiences including an outlet in a variable pressure saline cylinder. The saline cylinder should have a slowly varying volume that correlates to the changes in intrathecal pressure that occur naturally due to various times of day or body movement. The tests should be conducted without external changes made to the system for time periods varying from 8 hours up to two months with set delivery rates and schedule refills. Additionally, several different delivery profiles and drug ratios should be tested to verify the versatility of the delivery scheme.

After short term *in vitro* tests are conducted to verify system performance, long term experiments should be undertaken. Longevity errors such as granuloma, catheter wear, valve failure, and reservoir consistency can be analyzed by conducting tests for several

months and beyond. The system should also be verified for FDA requirements for implantable devices. This includes a battery of tests that involve EMF radiation, communications power, further MRI compatibility, etc. These tests are extremely important to verify the long-term sustainability of the system and allow development to proceed toward a manufacturable implant.

8.2.3 *In Vivo* Testing

The device modification type should be developed to acquire *in vitro* data and long-term tests should be conducted to determine challenges with a valve regulated system. Preliminary *in vivo* tests should be conducted with the system to confirm the feasibility of long term implantation. One such test should be the implantation of the device into a large animal model without any delivery functionality. This test should determine the biocompatibility of the system and should provide indicators of potential foreign body response that may occur. A second short-term test should be using the system as an external pump to regulate intrathecal delivery into a large animal model. The CSF can be extracted at a location further in the spine while an indicator is delivered by the device. If the extracted CSF demonstrates the expected indicator profile, the system should be delivering medication properly.

Short term diagnostic tests should also be conducted. An implanted device should be used to periodically monitor CSF pressure which can be compared to pressure taken by traditional means. Once baselines are established, catheter occlusions and disconnects should be induced in the animal model. Techniques should be developed to detect these acute catheter alterations *in vivo* from the output pressure sensor and functionality should

be verified during these tests. Also, potential detection of slow changes in the catheter can be studied. One such possibility is the detection of granuloma. This can be tested for by ceasing delivery for 5-10 minutes. After which, the outlet pressure sensor should detect the actual pressure in the CSF because no fluid will be flowing through the catheter; this sets the output of the system and the intrathecal space at equal pressures. Once this pressure is know, a set flow rate can be resumed. The change in the outlet pressure sensor for this set flow rate can be measured and correlated to the resistance of the catheter. If this technique is done at implantation (no granuloma) to establish a baseline, future tests can detect time alterations of the catheter tip. Eventually, the catheters can be removed, and actual conditions can be compared to sensor data.

After short term *in vivo* tests are conducted to verify basic system functionality in an animal model, long term tests should be initiated. A long term large animal study should be conducted with statistically significant numbers, and also multiple control cases. One control group should have a prototype system implanted without any medication delivery. A second control should be comprised of the implantation of a current commercial pump with well known delivery metrics. Results from this long term animal study should provide significant data to support the design of a final system. A final system should be designed based upon the improved VER architecture with additional resources to properly implement the medical diagnostic techniques developed using the medical prototypes. The final system should then be used in human clinical trials and advanced through FDA approval for eventual adoption.

Appendix A: A low leakage liquid seal

Micromachined valves are attractive for a variety of systems with applications ranging from biological analysis to orbital propulsion. Performance metrics such as dynamic range, permitted leakage, response time, maximum pressure, power consumption, size, and material composition are generally determined by the target application [Las04, Oh06, Cha00]. For example, a Joule-Thompson cooler requires high pressure operation and high flow rates for successful operation [Zhu09, Aga04]. On the other hand, a micro gas chromatograph favors valves with a rapid response time to properly determine the chemical composition of an input [Aga05]. Valve performance is dependent upon several factors that include fabrication methods, material composition, and actuation mechanism. For any set valve fabrication and assembly, there are design compromises that allow valve parameters to be adjusted to meet the needs of a specific application.

For many systems, an ideal valve would not limit the flow rate when fully open and would also have no leakage when fully closed. Eliminating leakage in micromachined gas valves has been a major challenge; non-uniformities in the valve seat or the presence of even minute particulates can prevent complete sealing. This problem is further exacerbated by the use of valve actuation mechanisms that provide relatively modest sealing force. In order to address this issue, researchers have explored the use of soft sealing materials for the valve seat [Jeo08, Yan99]. While such polymeric seals are suitable for a variety of valves and applications, the incorporation of such materials can

be a significant challenge for other valves. The operating conditions and environments for certain valves may also limit the use of polymeric valve seats. In such cases, a wet valve seat may provide a solution that is both simple and effective.

Surface tension at solid-liquid interfaces has been exploited for controlling flow within microchannels [Ber93]. For example, hydrophilic and hydrophobic regions along flow channels have been used to modulate pressure driven flow [Bur98, Zha01]. Capillary forces can dominate other forces at typical microchannel dimensions. These forces are proportional to the length of the solid-liquid interface and decrease linearly with size, whereas forces that are proportional to area diminish more rapidly [Sch99]. Based on this favorable scaling, capillary forces can be useful for sealing against gas leakage.

In this paper, we explore how capillary force can be used to prevent gas leakage in a valve that operates by moving a valve seat against a plate to modulate the height of a flow channel. The valve is similar to one reported in [Par08] and [Par09], but it utilizes a more elongated valve seat (Fig. A-1). The valve seat is microfabricated on a silicon-on-insulator (SOI) wafer and suspended above a glass substrate that has perforations for the flow inlet and outlet. A piezoelectric stack mounted above the glass-silicon sandwich modulates the separation between the valve seat and substrate.

The valve seat is designed in a starburst pattern that is axisymmetric with the gas inlet below it and the piezoelectric actuator above it. The elongated valve seat creates a wide flow channel even at a relatively small separation from the substrate to compensate for actuation distances of less than 10 μm. This reduces flow resistance, but also permits

higher leakage if a particle or structural non-uniformity occurs at any point along its 81 mm long serpentine perimeter.

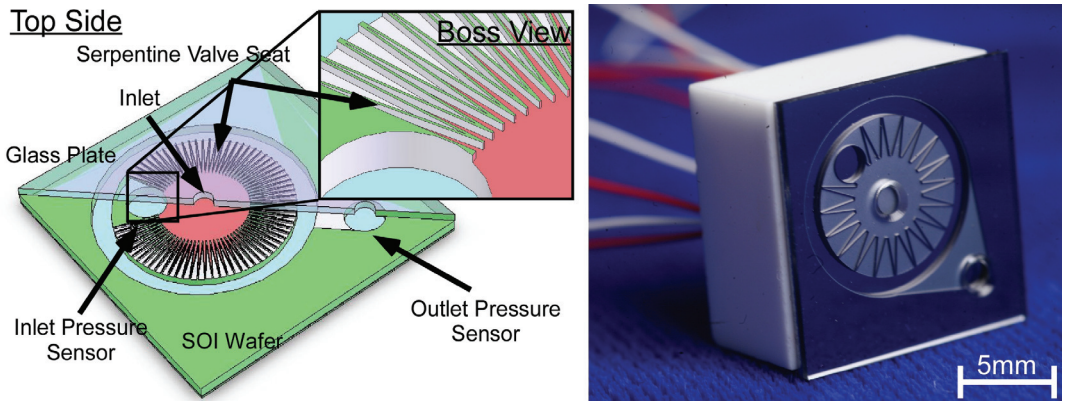

(a) (b)

Fig. A-1: (a) The microvalve plate is designed from silicon and glass with a serpentine valve seat in a starburst pattern. The valve membrane is pressed against the glass plate to close the valve. The valve regulates gas, but because utilizes membrane suspension, a sealant can be introduced into the valve channel without leaking. The valve also has embedded pressure sensors at the inlet and outlet. (b) A photograph of the top surface of the silicon microvalve assembled with a piezoelectric stack inside a ceramic housing.

A capillary seal for gas flow is formed by introducing liquid – water or isopropyl alcohol (IPA) – into the region between the valve seat and substrate and then draining or evaporating it away from the other regions. The liquid-gas interface formed in this gap provides a capillary force that seals the valve from gas flow when it is closed (Figure A-2a). When the valve is opened, surface tension and capillary forces drive the liquid toward places in the channel that have smaller gaps. This permits retention of the liquid on the valve seat. The axisymmetric actuation of the valve seat opens the inner points of the starburst pattern sooner then the outer edges. This drives the sealant from the center of the valve seat to the edges when it is opened (Figure A-2b).

The effectiveness of the capillary seal formed by the liquid in the flow channel is dependent upon both the liquid/solid and liquid/gas interfaces. The seal pressure can be

determined mathematically from the liquid meniscus. Using the Young-Laplace equation, the pressure drop across the meniscus (ΔP) can be determined from the liquid surface free energy (γ) and the vertical and parallel radii of curvature (R_1 and R_2) [Kun04].

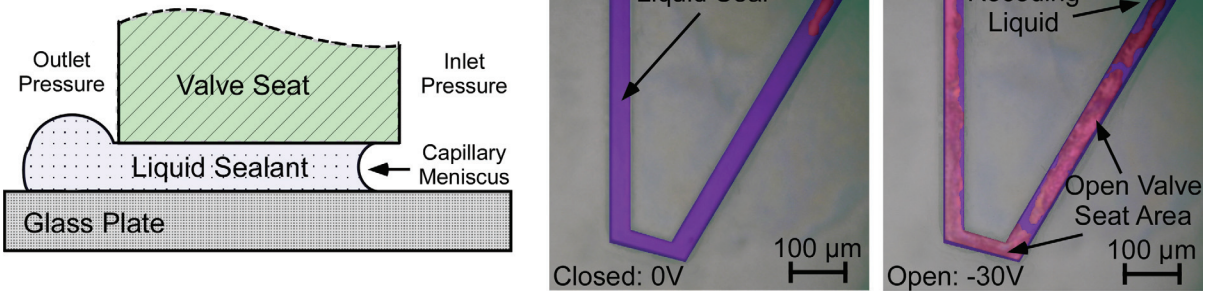

(a) (b)

Fig. A-2**:**(a) Liquid sealant is in the channel between the valve seat and the glass plate. On the high pressure (inlet) side of the channel, a meniscus is formed that generates forces that oppose the pressure. This mechanism creates capillary forces that hold the valve sealed against pressure driven flow. This reduces the leakage of a closed valve. (b) Color enhanced photographs of the wet valve seat, showing the meniscus receding from the inner starburst points that are closer to the actuator, when the valve is opened. Prior to testing the valve for gas flow, the introduction and removal of isopropyl alcohol leaves a residual liquid as the valve seal.

$$\Delta P = \gamma \times (\frac{1}{R_1} + \frac{1}{R_2}) \quad (1)$$

For a long serpentine valve seat, R_2 is essentially infinite. With a contact angle of 20° between water and glass, and a valve channel height of 1.4 µm, the differential pressure that the liquid seal should be able withstand at room temperature is approximately 92 kPa.

The presence of a liquid seal also has an effect on flow characteristics when the valve is opened. For short term effects, it can be assumed that the liquid volume on the valve seat is constant as it migrates toward the outer points of the starburst valve seat when the valve is opened. Simulations that take this into account, assuming an initial gap of 1.3

μm, a linear actuation approximation of 0.05 μm/V, and a closing voltage of 10 V are presented in Figure A-3.

The evaporation rate of the water used as a sealant can be determined from the mass transfer into gas flowing through the valve. Analytical approximations of this effect have also taken into account gas flow across a set surface area of water exposed to various gas flow rates [War88, Huh70]. According to these models, at 25°C, with low humidity and fast gas flow rates, water for the seal should be retained for at least 11 days. Once a valve seat dries out, it can be easily re-wetted. For some applications, a non-volatile liquid such as oil may be more appropriate.

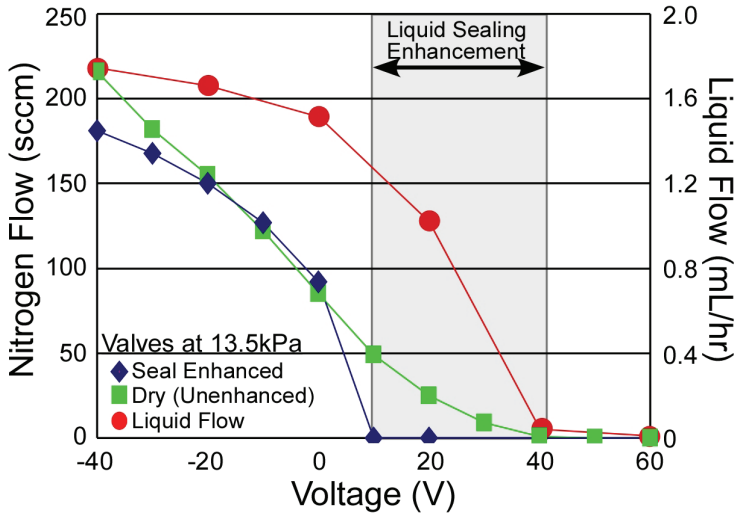

Fig. A-3: Nitrogen flow through valves assembled with a water seal. Gas pressures varied from 4.1-23.6 kPa and flow ranged from 400 mL/min down to below the measurable limit (<1 mL/min) when the valve was closed. The liquid seal prevented pressure flow from generating significant leakage for gas flow. Gas flow rates are compared to flow simulations assuming a constant liquid volume and valve geometry.

For the purpose of this study, valves were fabricated by a process similar to one previously reported in [14]. The silicon valve seat was spaced 1.3-1.4 μm from the glass substrate. This is a partially-open state; the gap is increased or decreased by the polarity and amplitude of the actuation voltage. This spacing, which is the flow channel, was

primed with water after assembly. The narrow valve channel area prevented the water from evaporating from the valve seat at a significant rate and allowed the valve to retain the liquid beyond thirty days in laboratory conditions.

The fabricated valves were tested using nitrogen gas that was used to generate differential pressures ranging from 4.1 to 23.6 kPa across the valves while they were actuated from -30 to 60 volts (Figure A-3). Dry valves remained open until they were actuated with at least 40 V (Figure A-4). In contrast, the seal enhanced valves remained closed over an actuation range of 10 to 60 V for the entire range of tested pressures. Flow rates ranged from 403 mL/min down to flow rates below the measurable range of the test setup (less than 1 mL/min).

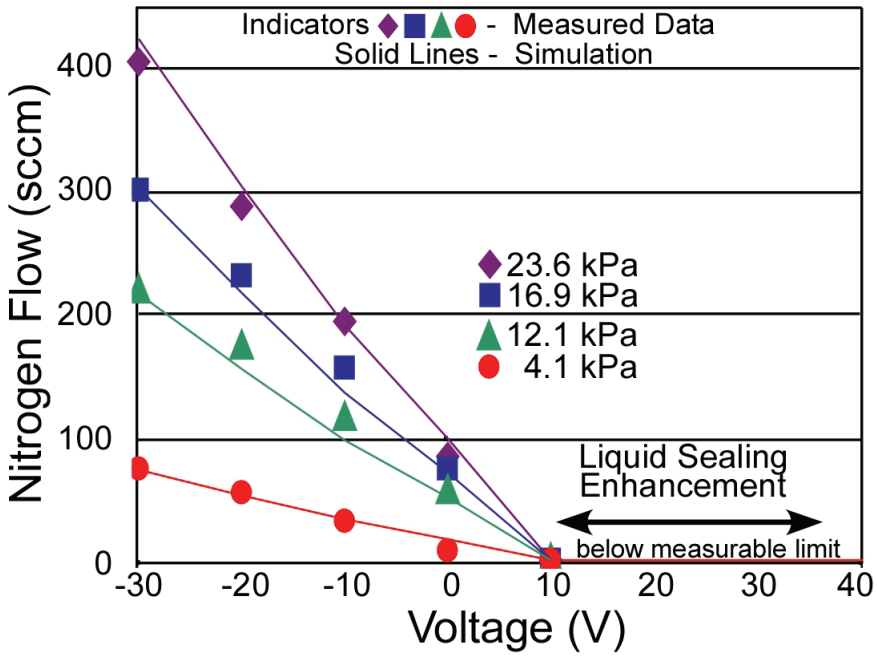

Fig. A-4: Nitrogen and isopropyl alcohol flow through valves assembled with and without a water seal. Gas pressures were maintained between 13.4 and 13.6 kPa and nitrogen flow ranged from 216 mL/min down to below the measurable limit (< 1mL/min) when the valve was closed. The liquid seal prevented pressure flow from generating significant leakage for gas flow, but it did not affect sealing for liquid flow. Liquid sealing enhancement can be clearly seen as a both a closing voltage difference and a leakage difference for gas and liquid flow through an unenhanced valve.

The same valves were also tested with IPA flow to determine the closing point and leakage rates for liquid media, which also do not benefit from a capillary seal. Alcohol flow rates for the valves at 13.3 kPa differential pressure ranged from 1.767 to 0.06 mL/hr across the same voltage range. The valves required 40 V actuation to close against liquid flow; the leakage rate was 0.0283 mL/hr.

The ratio of the maximum gas flow rate to the leakage rate was at least 322 with a liquid seal while the ratio for a dry valve was 216. This suggests that the liquid in the valve is effective at improving the seal and reducing leakage. Additionally, the difference in closing voltages (10 V for a wet valve seat, 40 V when dry) suggests that the capillary seal effect is taking place when the channel gap is approximately 1.4 μm, which is consistent with the gap distance targeted during fabrication.

These results indicate the effectiveness of capillary forces in providing a seal against inadvertent gas flow in a closed microvalve. It has been tested with both IPA and water as sealants, and provides a significant seal improvement. This technique is easy to implement and is potentially useful with a variety of liquids, materials, and pressures.

Appendix B: PCB Overview

Introduction

This effort requires a printed circuit board (PCB) with all of the chips and passive components necessary to drive the device from a single battery source. In an effort to begin the transition to a final battery powered system with complete circuitry, the PCB has been laid out, fabricated, and populated. Testing for every functional system except the wireless communication has been completed. The MSP430F169 from Texas Instruments has been demonstrated to be programmable and can control every element of the board. Additionally, errors and the necessary corrections for the first generation board (DualMed v1.00) are presented.

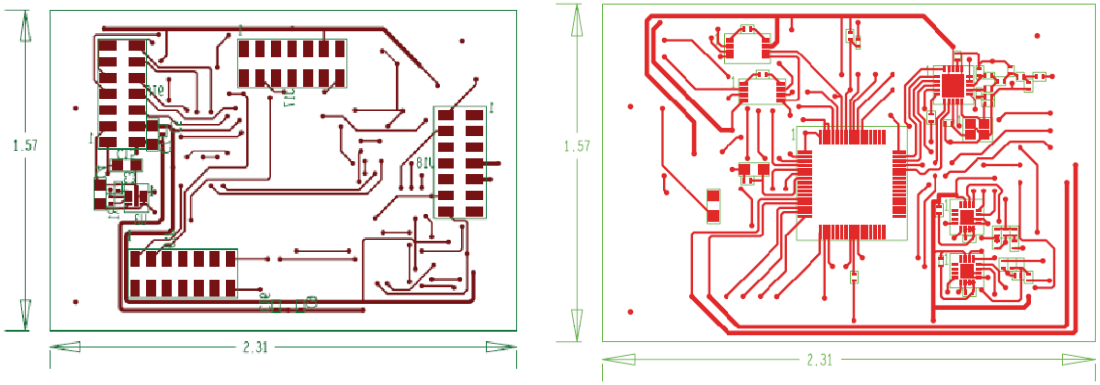

Fig. B-1: PCB layout of the bottom and top sides of the DualMed v1.00 board.

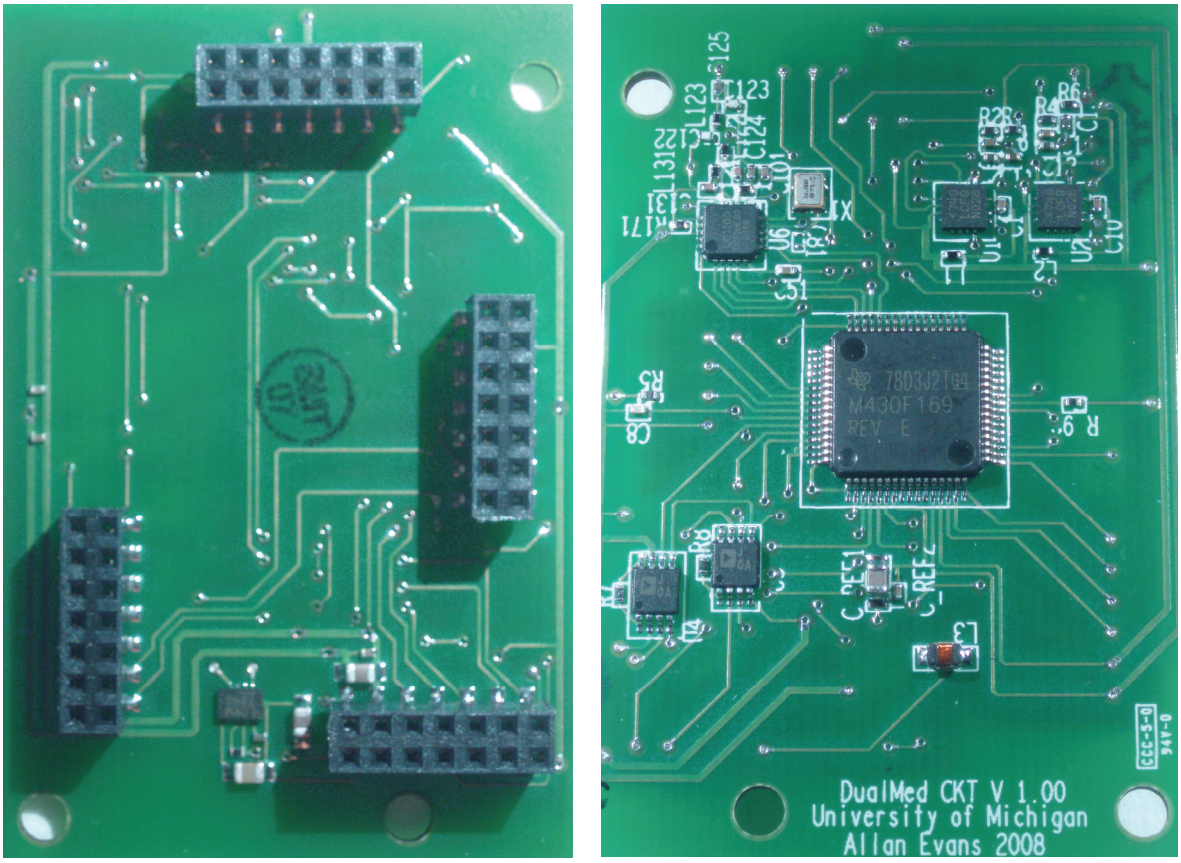

Fig. B-2:Photographs of the populated DualMed v1.00 board taken from the bottom (left), and the top (right). The bottom has the connector ports for interfacing the board with everything else.

PCB Errors

Various elements of the DualMed PCB v1.00 have been tested, and the various known errors and solutions are assembled here. The only untested element is the wireless communications.

First issue: The RST_NMI pin on the JTAG communications bus was being set at the wrong voltage, and this prevented communication with a computer to program the microcontroller.

Problem: See figure B-3. The capacitor (C8) and the resistor (R5) to form the pull-up circuit were switched.

Solution: The easiest solution is to remove both of them and leave the RST_NMI pin disconnected. It is optional for communication, and the current device programs correctly with this solution. For future generations of PCB, the two elements just need to be switched.

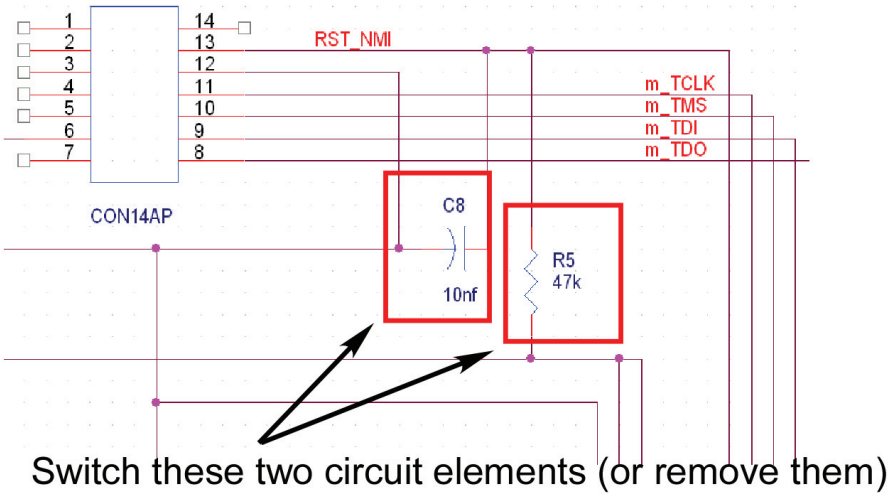

Fig. B-3: The resistor and capacitor locations are reversed. They can just be removed.

Second issue: The output power amplifier can not drive the output above 9V regardless of the input from the DAC.

Problem: See figure B-4. The on chip inductor is only 10nH. The necessary inductor for full amplification should be 10 μH.

Solution: The easiest solution is to remove the inductor, solder to the SW pad of the inductor and attach an external 10 µH between that pad and VCC. The solution for future versions of the chip should just be to make it a 10 µH surface mount inductor with a current rating of at least 300 mA.

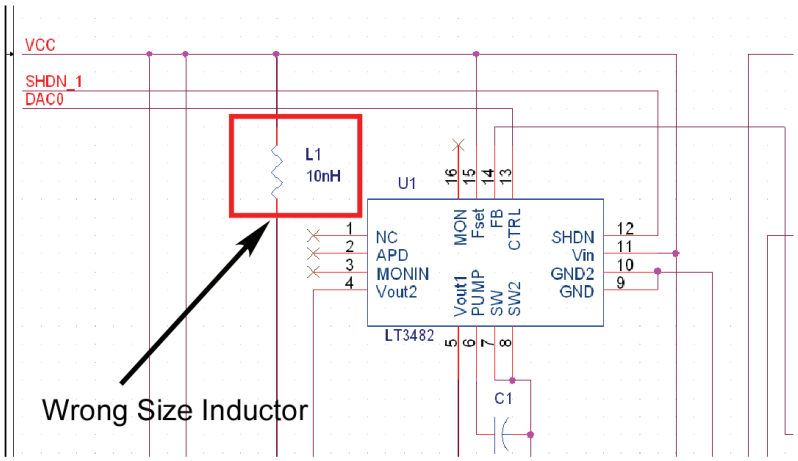

Fig. B-4: The inductor is an order of magnitude small. It needs to be replaced

Third issue: The output power amplifier does not accurately track the control voltage input above 15V. This is after the inductor problem is corrected.

Problem: See figure B-5. The capacitor from Vout1 that is part of the charge pump is connected to the feedback pin instead of to ground. An AC circuit leaks through this pin to the feedback node causing errors in the control voltage.

Solution: The easiest solution is to capacitor, solder to the Vout1 side of where the capacitor previously was, and attach an external 0.47 µF capacitor between this node and

ground. A solution for a future PCB board will need to include a change in layout to correct this error.

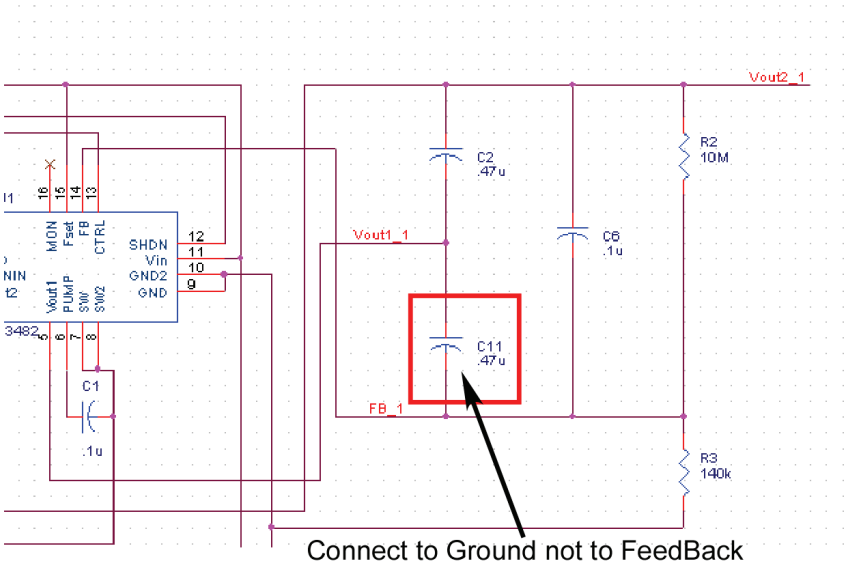

Fig. B-5: The capacitor is incorrectly connected to FB1 instead of Ground.

Additionally, the components currently on the board are only rated at about 20V. So far, everything has worked properly up to 60V, but I suspect there may be lifetime issues with extended use and possible breakdown. This should be corrected in the next assembly run, and may require a change in the layout to allow for larger components that meet this specification.

Appendix C: Software Overview

Introduction

In order to successfully communicate and control an implantable drug delivery device, several elements are needed. The most complex elements of this type of control system are the microcontroller and the wireless communication system. In an effort to ease the transition to a final battery powered PCB with complete circuitry, these elements have been developed. Preliminary programming for every functional system has been demonstrated. The MSP430F169 from Texas Instruments was used with the CC1100 wireless chip in the 433MHz bandwidth for development of the preliminary microcontroller and wireless protocols.

System Overview

The programming of the microcontroller (and by extension all peripherals) follow a very compartmentalized structure. The device is initially powered, and undergoes the start up process. This is also same process that would be undertaken if it was forced to re-boot wirelessly. After it starts up, it goes into a loop where it "sleeps" for one minute to conserve power. Upon waking, it checks for a wireless signal. If there is an input signal, it suspends the loop as it processes all communications requests. After communications are checked, all inputs (ADCs) are processed. The input data is processed and if no changes are necessary, the device goes back to sleep. Otherwise, outputs are changed to meet demands and the device goes back to sleep.

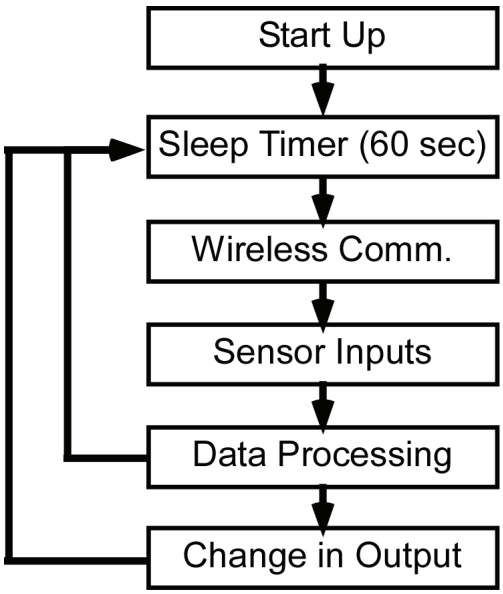

Fig C-1: Software block overview. After startup, the system constantly loops through functions.

1. Start Up: the init() function

Start up, or reset, is a relatively straightforward process. All initial constants are fixed. All communications protocols are implemented. The watchdog timer is suspended. Within this function, there are several sub-functions. The ADCs are initialized as inputs with 6 potential inputs. The DACs are set as output ports with the correct multiplier ratios to match further processing needs. The SPI init establishes the communications standards with the CC1100 chip and uploads the necessary parameters for 433 MHz communication. Basically, this functionality occurs only once, but it sets all protocols and ports to do input, output, and wireless communications.

2. Sleep Timer: the lpm() function

The TI MSP430 has several different low power modes. These modes have several timer interrupts that can be triggered after certain delays, or changed on the input lines. The sleep situation requires the wireless receiver to be shut down (to conserve power), all

outputs to be held constant (to maintain flow), and an activation every minute. To achieve this, low power mode three is used, and is exited out of with a timer event. When it is interrupted, it runs through various sub-functions starting with wireless(). Sleeping power consumption is less than 10mW.

3. Sensor Inputs: the ADC_read() function

The sensors are configured earlier on. The sensor input function quickly reads six individual inputs.

4. Wireless Communications: the wireless() function

The wireless system works by the microcontroller sending commands via the SPI interface to the CC1100. The function starts by waking up the CC1100 from power saving mode. It then checks for any incoming packets that would trigger full bi-directional communication. If it receives and activation command, it goes into receive mode and halts the rest of the process. If it does not receive the communication packet, it puts the CC1100 back to sleep (power savings) and continues on. In the communication mode, several packets are received. They are coded with a (1) a validation bit, (2) a series of adjustment bits (i.e. adjust flow rate table position 5; reset; etc) and then (3) a set of values. All the processing is done with arrays to make changing the values easy and seamless. After a transmission finished packet is sent, all requested data is then output from the chip, and the wireless communications are shut off.

5. Sensor Inputs: the sensor() function

The sensor inputs are activated every minute. All of the inputs are attached to the multiplexed ADC. The ADC's are all very quickly read in sequential order and the values are stored for data processing later on. The 6 inputs allow 3 inputs for each valve to be wired up.

6. Data Processing: the data_proc() function

The data processing is the core of the control. The input data is compared to the calibration functions (set as a polynomial array) to get an effective value (actual pressure, or other value). These input values are then used to calculate flow rate and check for any system failures (like low battery or clogged catheter). The flow rate is compared to the set rate (also in an array) and adjusted as necessary to maintain the set-point. If there are errors, the error output is set.

7. Change in output: the output() function

The output values from the data processing are taken and sent to the correct registers with the values adjusted to get the correct output. Any error signal is activated or de-activated and is sent to a digital output that will power a PZT buzzer. Additional power management techniques (like turning off the valves etc) are also be implemented in this stage.

Code in objective C

```
#include "include.h"
#include  <msp430x16x.h>
```

```
extern char paTable[];
extern char paTableLen;

char txBuffer[4];
char rxBuffer[4];
unsigned int output = 0;
unsigned int recieve = 0;
unsigned int time_switch = 0;
unsigned int r_time = 0;

void main (void)
{
  WDTCTL = WDTPW + WDTHOLD;                   // Stop WDT

  P1DIR = 0x01;                          // set port to outputs
  P1OUT = 0;                            // reset port outputs

  //timer stuff
  CCTL0 = CCIE;                             // CCR0 interrupt enabled
  CCR0 = 20000;
  TACTL = TASSEL_2 + ID_3 + MC_1;               // SMCLK, upmode

  TI_CC_SPISetup();                          // Initialize SPI port

  TI_CC_PowerupResetCCxxxx();                  // Reset CCxxxx
  writeRFSettings();                        // Write RF settings to config reg
  TI_CC_SPIWriteBurstReg(TI_CCxxx0_PATABLE, paTable, paTableLen); //Write PATABLE


  // Configure ports -- switch inputs, LEDs, GDO0 to RX packet info from CCxxxx

  TI_CC_SW_PxIES = TI_CC_SW1+TI_CC_SW2+TI_CC_SW3+TI_CC_SW4;             //Int on falling edge
  TI_CC_SW_PxIFG &= ~(TI_CC_SW1+TI_CC_SW2+TI_CC_SW3+TI_CC_SW4);        //Clr flags
  TI_CC_SW_PxIE = TI_CC_SW1+TI_CC_SW2+TI_CC_SW3+TI_CC_SW4;             //Activate enables
  TI_CC_LED_PxDIR = TI_CC_LED1 + TI_CC_LED2 + TI_CC_LED3 + TI_CC_LED4;  //Outputs
  TI_CC_GDO0_PxIES |= TI_CC_GDO0_PIN;                              // Int on falling edge (end of pkt)
  TI_CC_GDO0_PxIFG &= ~TI_CC_GDO0_PIN;                               // Clear flag
  TI_CC_GDO0_PxIE |= TI_CC_GDO0_PIN;                              // Enable int on end of packet



  //testing sleep and idle
 unsigned int i;

  TI_CC_SPIStrobe(TI_CCxxx0_SIDLE);                              //Put CCxxxx in Idle

  TI_CC_SPIStrobe(TI_CCxxx0_SPWD);                               // Go into power down mode
  i = 5000;                           // Delay
  do (i--);
  while (i != 0);

  _BIS_SR(LPM0_bits + GIE);                                  // Enter LPM0, enable interrupts

  //My code transmit for loop
 // for (;;)
 // {
 //   volatile unsigned int i;



    // Build packet
 //   txBuffer[0] = 2;                        // Packet length
 //   txBuffer[1] = 0x01;                       // Packet address
 //   txBuffer[2] = output;                     // Load output

 //   output++;
  //  if(output == 32)
//      {output = 0;
//      }
```

```
  //  RFSendPacket(txBuffer, 3);              // Send value over RF

 //   P2IFG &= ~TI_CC_GDO0_PIN;               // After pkt TX, this flag is set.

 //   i = 50000;                          // Delay
 //   do (i--);
 //   while (i != 0);
 // }

}


// Timer A0 interrupt service routine
#pragma vector=TIMERA0_VECTOR
__interrupt void Timer_A (void)
{
   unsigned int i;


  if(recieve == 1)
  {
    r_time++;
    P1OUT ^= 0x01;

    if(r_time == 10)
    {
      P1OUT = 0;
      TI_CC_SPIStrobe(TI_CCxxx0_SIDLE);

      TI_CC_SPIStrobe(TI_CCxxx0_SPWD);                  //Put CCxxxx in Idle
      i = 5000;                         // Delay
      do (i--);
      while (i != 0);

      r_time = 0;
      recieve = 0;
      time_switch = 0;
    }
  }

  if(recieve == 0)
  {
    time_switch++;

    if(time_switch == 99)
    {
      TI_CC_SPIStrobe(TI_CCxxx0_SIDLE);                 //Put CCxxxx in Idle
      i = 5000;                         // Delay
      do (i--);
      while (i != 0);


       TI_CC_SPIStrobe(TI_CCxxx0_SRX);
    }

    if(time_switch == 100)
    {
       TI_CC_SPIStrobe(TI_CCxxx0_SIDLE);

      TI_CC_SPIStrobe(TI_CCxxx0_SPWD);                  //Put CCxxxx in Idle
      i = 5000;                         // Delay
      do (i--);
      while (i != 0);

       time_switch = 0;
    }
  }
}
```

```
// The ISR assumes the int came from the pin attached to GDO0 and therefore
// does not check the other seven inputs.  Interprets this as a signal from
// CCxxxx indicating packet received.

#pragma vector=PORT2_VECTOR
__interrupt void port2_ISR (void)
{
  char len=2;                           // Len of pkt to be RXed (only addr
                                        // plus data; size byte not incl b/c
                                        // stripped away within RX function)
  if (RFReceivePacket(rxBuffer,&len))       // Fetch packet from CCxxxx
  {
    if (rxBuffer[1] == 01)
    {
      r_time = 0;
     recieve = 1;// Toggle P1.1 using exclusive-OR
    }
  }


  P2IFG &= ~TI_CC_GDO0_PIN;                 // Clear flag

}




//*****************************************************************************
//  ADC DAC implementation
//
//
//  Built with IAR Embedded Workbench Version: 3.21A
//*****************************************************************************

#define ROWS 10
#define COLS 2

#include  <msp430x16x.h>

int results = 0;
int DAC[ROWS][COLS];

void DAC_Program(void);
void ADC_DAC_Init(void);

void main(void)
{
  WDTCTL = WDTPW + WDTHOLD;                     // Stop WDT
  DAC_Program();                            // Program the DAC output
  ADC_DAC_Init();                           // Initialize ADC12
  ADC12CTL0 |= ENC;                             // Enable conversions

  _BIS_SR(CPUOFF + GIE);                        // LPM0, ADC12_ISR will force exit
}


void DAC_Program(void)                          // Initialize the DAC output program
{
  int row;                                  // The first value is the time
      for (row = 0; row < ROWS; row++)        // Second value is the DAC output (to be replaced with flow rate)
      {
            DAC[row][0] = 10 * (row +1);
            DAC[row][1] = row * .1 * 2048;
      }

}
```

```
void ADC_DAC_Init(void)
{
  P1DIR = 0x01;                          // set port to outputs
  P1OUT = 0;                             // reset port outputs

  //timer stuff
  CCTL0 = CCIE;                              // CCR0 interrupt enabled
  CCR0 = 20000;
  TACTL = TASSEL_2 + ID_3 + MC_1;              // SMCLK, upmode

  // ADC stuff
  P6SEL |= 0x01;                         // select A0 input
  ADC12CTL0 = ADC12ON+SHT0_1+REF2_5V+REFON; // Setup ADC12
  ADC12CTL1 = SHP;                           // Use sampling timer
  ADC12MCTL0 = SREF_1;                       // Vr+=Vref+
  ADC12IE = 0x01;                        // Enable interrupt



  //DAC stuff

  DAC12_0CTL = DAC12IR + DAC12AMP_5 +DAC12ENC;  // Internal ref gain 1
  DAC12_0DAT = 0;
}



// Timer A0 interrupt service routine
#pragma vector=TIMERA0_VECTOR
__interrupt void Timer_A (void)
{

  static unsigned int i = 0;
  static unsigned int time = 0;
  static unsigned int row_1 = 0;

  if(i == 10)                            // Delay Sampling every 10 interrupts
  {
    i = 0;
    time++;

     for (row_1 = 0; row_1 < ROWS; row_1++)         // Check to see where if we are at a new stage
     {
          if(time == DAC[row_1][0] )           // If the time is at a new stage then change output
          {

             DAC12_0DAT = DAC[row_1][1];       // Update with the new output
             row_1++;

                if(time == DAC[ROWS-1][0])    // If we reach the end of a cycle then reset (ie... new day)
                time = 0;
          }
     }

    ADC12CTL0 |= ADC12SC;                  // Sampling open
  }
  i++;

}

// ADC12 Interrupt Service Routine
#pragma vector=ADC_VECTOR
__interrupt void ADC12ISR (void)
{
    results = ADC12MEM0;                   // Put ADC values on DAV
    P1OUT ^= 0x01;                         // Toggle LED
}
```

Appendix D: Fabrication Details

The processing done for the third generation PZT microvalve manifolds took place during May-June 2009 in the Lurie Nanofabrication Facility (LNF) at the University of Michigan. This appendix is meant to be used in conjunction with the third generation fabrication run sheet. The run sheet is referenced by both number and with excerpts from the text itself. This appendix also contains opinions and thoughts about potential future modifications that may either improve yield or ease of fabrication. Fabrication changes made to the originally proposed process are justified, and the purpose of the change is noted.

Fabrication Summary
(run sheet excerpts are italicized)

Wafer: (100) N-type SOI: 20 μm device, 450 μm handle, 2 μm oxide, >5 Ω resistivity
500 μm 4" glass wafer from Plan Optik (PN: V015.04-0001)

This is a deviation from the proposed 30 μm device wafer with a 400 μm handle. These changes were made to reflect a more aggressive design that allows from smaller pressure sensor membranes. Three SOI wafers were processed and several N-type blanks and glass wafers were used for process splits.

1. *SOI wafer processing*
    a. *Cleaning: Piranha clean*

The wafers either come pre-cleaned (as the SOI wafers did), or can be cleaned once opened in the clean room. This step is optional and can be ignored if the wafers are already clean.

b. Thermal Oxidation

This step did not occur in the original process. It was added because Boron implantation at the energy levels originally proposed do not leave visible marks on the wafer. This oxidation step was necessary to create the alignment marks for later lithography steps. The lithographical changes are required to properly align the metal interconnects to the doped resistors. Three SOI wafers and two blanks were pre-cleaned and then oxidized. The thickness and timing of this step are not sensitive to process variations.

c. Resistor Formation

Once the thermal oxidation was completed, the resistors were patterned in using photoresist, and the underlying oxide was etched. One blank wafer was cleaned to confirm that the oxide was completely etched, and the alignment marks were visible for future lithography.

d. Ion Implantation

Three SOI wafers and one blank wafer were sent for ion implantation to Innovion. Total time from ship-out to wafer return was approximately one week. An earlier process split utilizing two blank wafers demonstrated that the implantation parameters fell within simulation and process tolerances.

e. Thermal Oxidation and Boron Drive-In

This step creates a field oxide and drives in the boron to properly create the resistors. This stage is very sensitive to variation in parameters, and could cause faulty resistors if not properly done.

f. Via formation

The metal layers for the second step in via formation were altered from platinum to gold. This change was made because the third generation valves do not have RTDs, and gold interconnects are used to solder external wires to the die. This process change allows the removal of the platinum mask. One SOI wafer was set aside at this stage as a process split. Two SOI wafers and two single sided wafers were processed.

g. Metal Interconnects

Two SOI wafers and two single sided wafers were processed through this step (Figs. D1-5). This is the point where the single sided wafers were used to test the implantation. Preliminary tests on pad-to-pad resistances were conducted on single sided wafers that were removed from this process split. The measured resistances varied from approximately 100 kΩ to 140 kΩ depending on the location of the pads and the Wheatstone bridge arrangement. The expected resistance (based on simulation) was 112.3 kΩ, so the range and results were well within expected tolerances. The results suggested that the sensors and interconnects operate within tolerance.

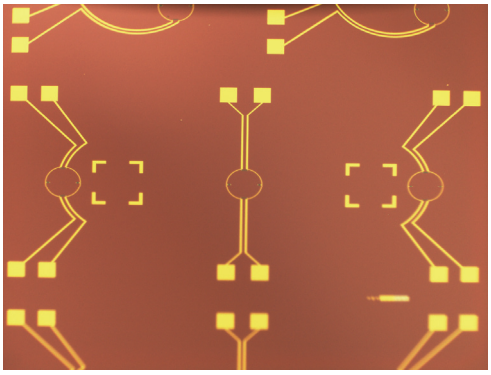

Fig. D-1: A photograph of the gold traces of a two-valve third generation manifold

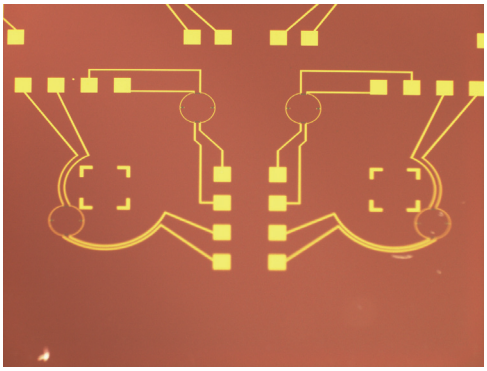

Fig. D-2: A photograph of the gold traces of two third generation single valves.

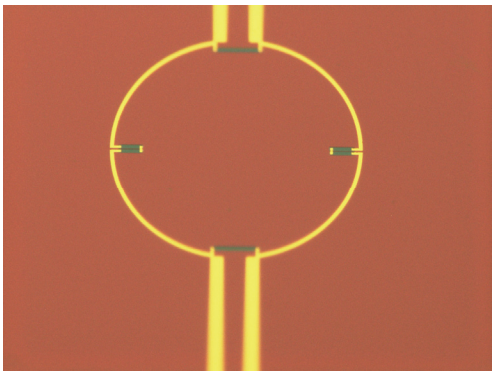

Fig. D-3: A photograph the reverse side of a pressure sensor membrane showing the piezoresistors and gold traces.

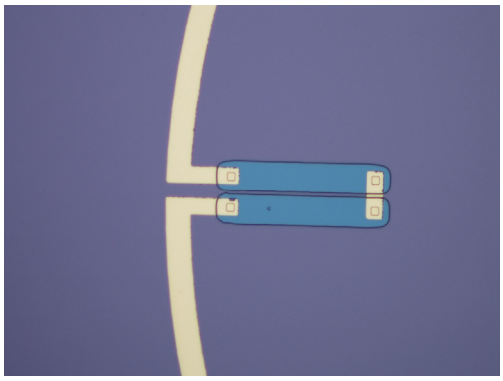

Fig. D-4: A photograph the folded piezoresistor on the left side of the membrane. The interconnect squares are visible.

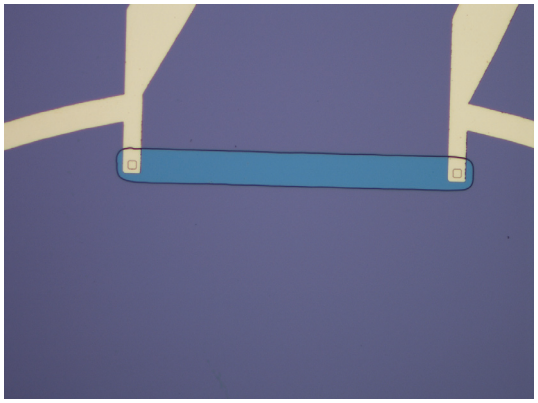

Fig. D-5: A photograph the long piezoresistor on the top side of the membrane. The interconnect squares are visible on the left and right sides of the resistor.

2. SOI wafer backside processing

a. Al pattern for STS

This step altered an etch step to a lift-off step. Additionally, the process is sensitive to under exposure or under development because it can cause the small features in the valve seat to be the incorrect size. Two SOI wafers and four blanks were sent through this process step.

b. DRIE

As an alternative to using photo resist techniques to bond the carrier wafers, conductive oil was used. This oil has the disadvantage of being more difficult to clean (it requires an IPA wipe down), but it has thermally conductive properties that allow for a more uniform deep etch. Additionally, the second DRIE etch is sensitive to recipe variations. Most DRIE steps either scallop in or out. This corresponds to trenches either getting smaller as they get deeper (like a V), or getting wider as they get deeper (like an A). If the recipe has a tendency to scallop out, the membrane can be undermined and weakened. This happened in two of the early wafer splits, and the 20 μm thick valve seat membranes were undermined and broke apart. In order to correct this, the recipe for the second etch was modified to scallop in. Four single side and two SOI wafers were processed through this step.

3. Glass wafer processing

a-l. Cleaning through first etch

BHF was used for the shallow etch for ease of masking and etching instead of HF nitric. This step otherwise was simply used to create the gap where the valve seat sits after anodic bonding. Six glass wafers went through these steps with an recesses between 1.3-1.4 μm.

m-r. Through hole preparation and etch

A Cr/Au etch mask with the maximum thicknesses for both layers was used. The evaporator can take up to nine wafers at once, so processing six glass wafers at a time is easier using evaporation when compared to sputtering. Also, a mask processed this way with photoresist still on it is a better mask for long HF etches. This has been demonstrated in papers, and through personal experience. Six glass wafers were processed through this step.

s. Use Al to prevent bonding at the center area.

Instead of using a photoresist process, a shadow mask was used to deposit the aluminum. The photoresist was difficult to properly spin on the previously etched glass wafer with through holes. Several photoresist etch techniques used when processing the second generation valve process were attempted and all had poor results. Instead, DRIE etching of single sided wafers was used to make shadow masks. The silicon shadow masks were aligned to the glass wafer using visual techniques (1 mm tolerance). These masks make evaporation deposition of aluminum easier and faster with higher yield and retention then previous photoresist steps. Three shadow masks were made, and three glass wafers were deposited with Al.

4. Bonding

a,b,c. Cleaning through the bond

A blank glass wafer was stacked with the processed glass wafer during the anodic bond. This was necessary because Na from the glass migrates into the chuck if the glass side is down, and the gold forms a Eutectic bond with the carbon chuck if the device side of the wafer stack is down. By adding a second glass wafer, the surface of the second wafer at

the glass to glass interface absorbed all of the migrating Na from the anodic bond itself. In order to compensate for this added glass wafer, the voltage of the anodic bond was increased to 800 volts. The anodic bond was tested with two wafers, and demonstrates better bonding if a tack bond was NOT used in advance of the actual bond. One test wafer and two SOI wafers were bonded during this step.

d. Al removal in Al etch well

This step took three days and two batches of aluminum etchant to fully remove the aluminum. It works reliably with no problems otherwise

e. Etch in DI water and soak in SI

This step worked fine. The DI soak was maintained for 2 days.

f. Dry w/ hotplate or oven

Two SOI wafers were placed into an oven at 65°. This caused two pressure sensor membranes to burst as water rapidly evaporated and created pressure buildup inside the pressure sensor cavities. Soaking the wafers in IPA before drying may prevent evaporation from causing similar pressure builds ups.

5. Dicing

There were no issues with this step. Final device yield was between 60 – 70%.

3nd Gen Micromachined Valve Runsheet
Allan T Evans
July 8, 2009

Wafer: (100) N-type SOI: 20 µm device, 450 µm handle, 2 µm oxide, >5 Ω resistivity
500 µm 4" glass wafer from Plan Optik (PN: V015.04-0001)

6. SOI wafer processing
    a. Cleaning: Piranha clean
        i. H_2O_2:H_2SO_4=1:1, 10 mins
        ii. DI water Rinse 5 min & Spin Rinse Dry
    b. Thermal Oxidation
        i. Pre-furnace Clean
        ii. B2 Furnace: Temperature: 1000ºC, Dry/Wet/Dry: 5/40/5 mins
            N_2 anneal: 20 min, thickness: 2438 Å
    c. Resistor formation
        i. Pattern with PR (1827):
            1. HMDS
            2. 1827 PR: spread: 500 rpm 4sec, spin: 3000rpm 30 sec
            3. Expose 15 sec
            4. Develop 1 min (MF 319)
        ii. O_2 plasma 60 sec (80 W)
        iii. Oxide etch in BHF 9 min
        iv. DI water rinse
    d. Ion Implantation
        i. Send out with PR and Oxide mask to INNOViON
        ii. Boron implantation: Dose: 1e13, Energy: 20 Kev, Tilt: 7
    e. Thermal Oxidation and Boron Drive-In
        i. Strip PR and PreFurnace Clean
        ii. B2 Furnace: Temperature: 1000ºC, Dry/Wet/Dry: 5/20/5 mins
            N_2 anneal: 20 min, thickness: ~1000 Å
    f. Via formation
        i. Pattern with PR (1827):
            1. HMDS
            2. 1827 PR: spread: 500 rpm 4sec, spin: 3000rpm 30 sec
            3. Expose 15 sec
            4. Develop 1 min (MF 319)
        ii. O_2 plasma 60 sec (80 W)
        iii. Oxide etch in BHF 9 min
        iv. DI water rinse
        v. Metal deposition (for ohmic contact before PR removal)
            1. Descum 30 sec @ 80 W
            2. Ti/Pt/Au (50/500/1000 Å)
            3. lift off: 1~2 hours in acetone
            4. ultrasonic: 5 min in acetone, 5 min in IPA

5. rinse with DI water

vi. Examine under microscope

g. Metal Interconnects
   i. Pattern with PR (1827): same as above
   ii. Descum
   iii. Evaporate Cr/Au (300/1000 Å) Enerjet evaporator
   iv. Acetone lift off
   v. Followed by ultrasonic in 5 min acetone, 5 min IPA and DI water rinse

7. SOI wafer backside processing
   a. Al pattern for STS
      i. Spin 1827 @2000 rpm on the front side (processed) of the wafer for protection and bake for 1 min @115ºC hot plate (can be longer)
      ii. Spin 1827 @ 3000 rpm and pattern on the back side for Al lift-off
      iii. Evaporate 4000 Å Al on the backside
      iv. Acetone lift-off
      v. PRS 2000, followed by DI rinse
   b. DRIE
      i. Wafer mounting
         1. use wafer mounting oil by STS
         2. mount to a blank carrier wafer
      ii. PR pattern for STS
         1. Spin 9260 @ 1500 rpm
         2. bake 30 mins @ 90ºC Oven
         3. Expose 80 secs using MA6
         4. Develop in AZ400K: DI H_2O=1:3 for 4 mins
      iii. DRIE using STS for ~ 2 hours and 40 mins (check often near end) depth near 400-420 μm
      iv. 2nd DRIE etch after PR strip and remount – 35 mins

8. Glass wafer processing
   a. Piranha clean
   b. BHF dip for 5 mins
   c. DI rinse and spin rinse dry
   d. Evaporate Cr/Au (1000/5000 Å) for glass etch mask
   e. Pattern w/ 9260 @ 1000 rpm
      i. Bake 30 min @ 90ºC oven
      ii. Expose 90 secs using MA6
      iii. Develop in AZ400K:DI=1:3 for 2 mins
   f. Back side protection w/ 9260, use manual spinner(solitec) w/ rubber ring
      i. Spin 9260 @ 1000 rpm, bake 30 mins @ 90ºC oven
   g. O_2 plasma 60 sec @ 80 W (right before the Au etch)
   h. Au etch – 4 min, DI rinse – 1 min, Cr etch – 2 min, DI rinse – 2 min
   i. BHF etch for 90 min approximate depth is 1.4 μm
   j. Strip PR in PRS 2000 then measure the depth.
   k. Strip Au ~ 5 mins, strip Cr ~ 3 min
   l. Piranha clean

m. Evaporate Cr/Au (1000/4000 Å) on both sides twice
n. Pattern the front side w/ 9260 (1000 rpm, 90 sec expose, 2 min develop)
o. Hard bake in 110ºC oven 5 mins
p. Pattern back side w/ 9260
q. Get ready for HF etch
    i. Wrap the edges w/ parafilm
    ii. Cover up the alignment marks w/ white tape
    iii. O_2 plasma on both sides (60 secs, 80 W)
    iv. Dip in DI H_2O then Au etch 4 min
    v. Dip in DI H_2O then Cr etch 4 min
    vi. Dip in DI H_2O then Au etch 4 min
    vii. Dip in DI H_2O then Cr etch 4 min
    viii. Etch in HF for 60 mins
    ix. Inspect the little holes are through
r. Strip Au and Cr
s. Use Al to prevent bonding at the center area
    i. STS blank silicon wafers all the way through to form shadow masks
    ii. Manually align glass wafers to shadow masks
    iii. Evaporate 1000 Å Al then lift-off shadow mask.

9. Bonding
    a. Piranha clean glass wafer before bonding
    b. Use a second glass wafer as a Na catch in the bonder
    c. Anodic bonding at 800 V, 400ºC
    d. Al removal in Al etch well (several days)
    e. Rinse in DI water and soak in DI water for several hours.
    f. Dry w/ hotplate or oven
10. Dicing

Appendix E: System Housing Designs

This section contains the machine drawings for the housings mechanically manufactured for the first and second prototypes presented in the body of the thesis. All measurements are presented in millimeters with the values for inches in brackets.

Half of the shell for the first generation prototype:

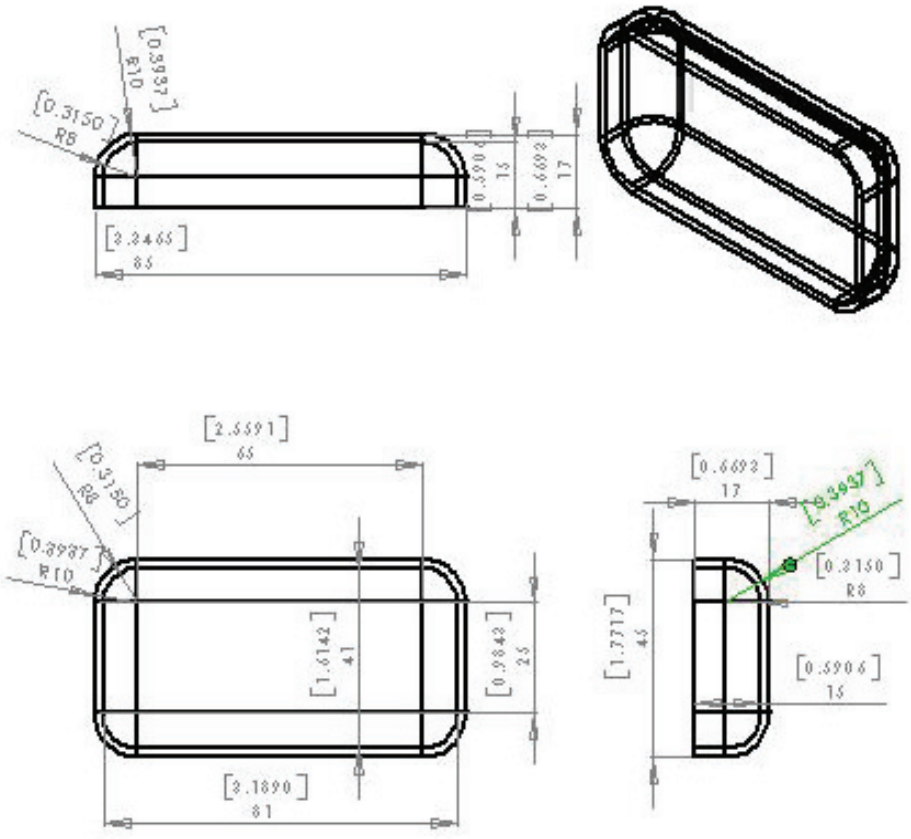

Bottom compartment for the second generation prototype:

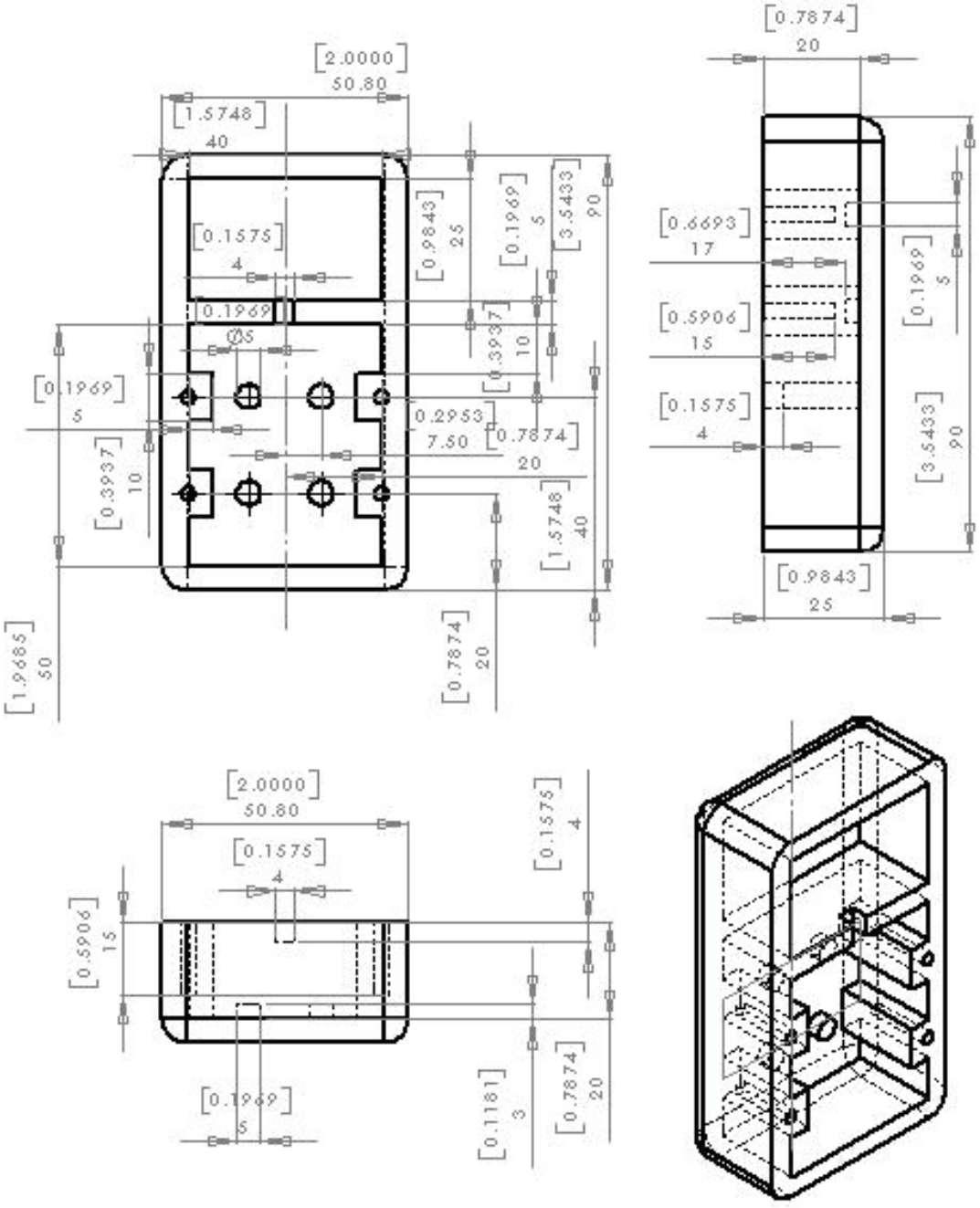

Stainless steel top for the second generation prototype:

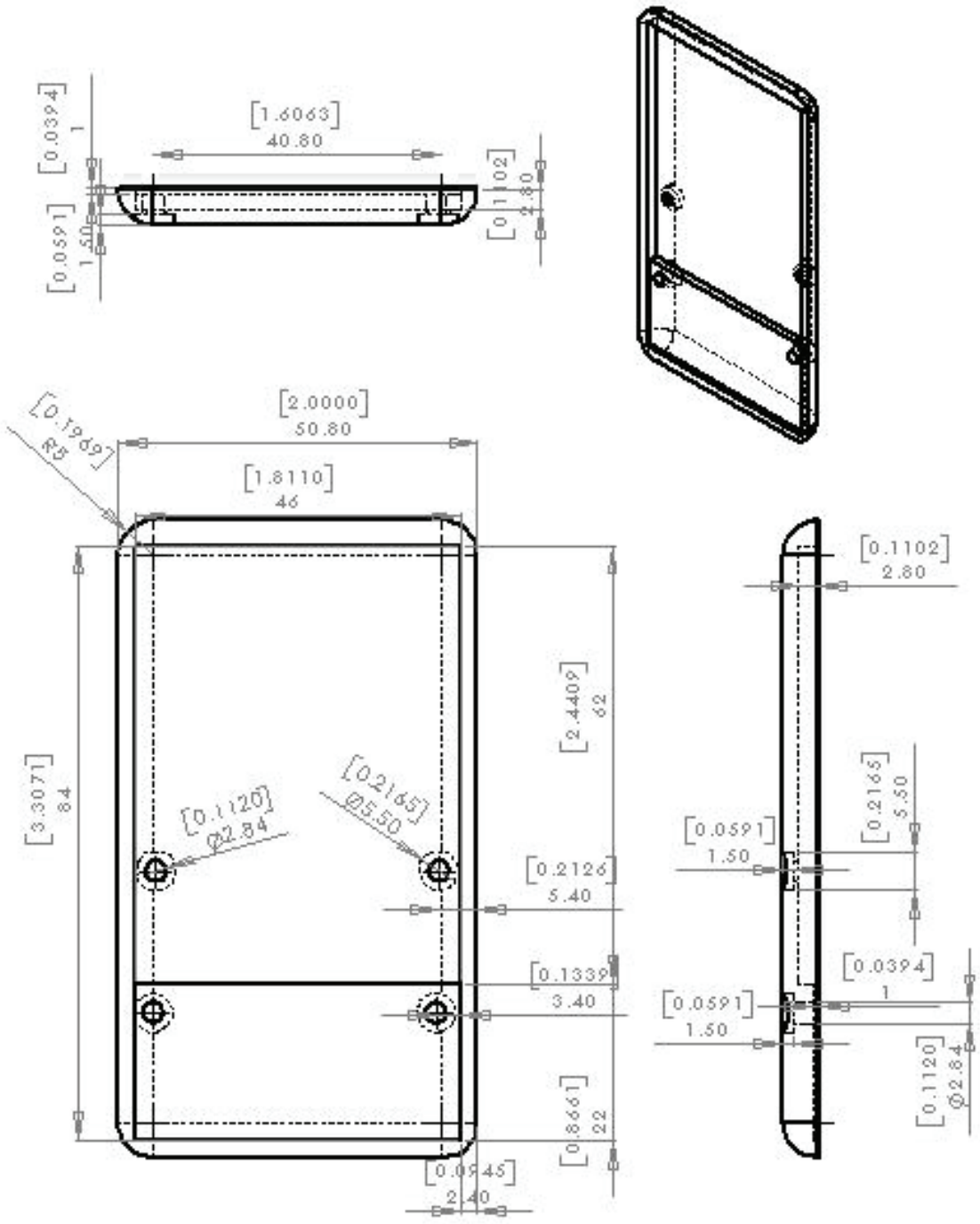

BIBLIOGRAPHY

[Adv08] Advanced Infusion, "Our products", Available online at http://advancedinfusion.com, Accessed October 9, 2008.

[Aga04] M. Agah, G.R. Lambertus, R.D. Sacks and K.D. Wise, "High-speed MEMS-based gas chromatography," *Proceedings of the IEEE International Electron Devices Meeting San Francisco (December 2004)*, pp. 27–30, 2004.

[Aga05] M. Agah, J.A. Potkay, G. Lambertus, R. Sacks and K.D. Wise, "High-performance temperature-programmed microfabricated gas chromatography columns," *J. Microelectromech. Syst.*, vol. 14, pp. 1039–1050, 2005.

[Alj02] U. Aljancic, D. Resnik, D. Vrtacnik, M. Mozek, and S. Amon, "Temperature Effects Modeling in Silicon Piezoresistive Pressure Sensor," *IEEE Mediterranean Electrotechnical Conference*, Cairo, Egypt, pp. 36-40, May 2002.

[Alz08] "Alzet Osmotic Pumps" Available online at http://www.alzet.com, Accessed October 08, 2008

[And90] J.C. Andrews, S.C. Walker-Andrews, and W.D. Ensminger, "Long-term central venous access with a peripherally placed subcutaneous infusion port: initial results," *Radiology*, vol. 176, pp. 45-47, March 1990

[And99] V.C. Anderson, and K.J. Burchiel, "A prospective study of long-term intrathecal morphine in the management of chronic nonmalignant pain", *Neurosurgery*, Vol. 44, No. 2, pp. 289-301, 1999.

[ASH00] "ASHP guidelines on quality assurance for pharmacy-prepared sterile products. American Society of Health System Pharmacists", *American Journal Health Syst. Pharm*, Vol. 57, No. 12, pp. 1150-1169, 2000.

[Bae02] B. Bae, N. Kim, H. Kee, S. Kim, Y. Lee, S. Lee, and K. Park, "Feasibility test of an electromagnetically driven valve actuator for glaucoma treatment," *Journal of Microelectromechanical Systems*, vol. 11, n. 4, pp. 344-54, 2002.

[Bae08] L. Baert, L. Schueller, Y. Tardy, D. Macbride, G.V. Klooster, H. Borghys, E. Clessens, G.V.D. Mooter, E. Van Gyseghem, P. Van Remoortere, P. Wigerinck, and J. Rosier, "Development of an implantable infusion pump for

sustained anti-HIV drug administration," *International Journal of Pharmaceutics*, vol. 355, n. 1-2, pp. 38-44, 2008.

[Bar82] A. Baraka, "Rostral spread of intrathecal morphine in man", *Middle East J Anaesthesiol*, Vol. 6, No. 4, pp. 178-180, 1982.

[Bar94] P. W. Barth, C. C. Beatty, L. A. Field, J. W. Baker, and G. B. Gordon, "A robust normally-closed silicon microvalve," *Solid-State Sensor and Actuator Workshop*, pp. 248-50, 1994.

[Ber93] J.C. Berg, Editor, "Wettability. Surfactant Science Series," vol. 49, New York, Marcel Dekker (1993).

[Bin05] J. S. Bintoro, P. J. Hesketh, and Y. H. Berthelot, "CMOS compatible bistable electromagnetic microvalve on a single wafer," *Microelectronics Journal*, vol. 36, n. 7, pp. 667-72, 2005.

[Bor06] R.T. Borno, J.D. Steinmeyer and M.M. Maharbiz, "Transpiration actuation: the design, fabrication and characterization of biomimetic microactuators driven by the surface tension of water," *J. Micromechanics and Microengineering*, Vol.16, pp.2375-2383, 2006

[Bov08] B. R. Boveja and A. Widhany, "Method and system for providing pulsed electrical stimulation to provide therapy for erectile/sexual dysfunction, prostatitis, prostatitis pain, and chronic pelvic pain," U. S. Patent 7,330,762, Feb. 12, 2008.

[Bra03] A. Brask, G. Goranovic, and H. Bruus, "Theoretical analysis of the low-voltage cascade electro-osmtic pump", *Sensors and Actuators B: Chemica,* Vol. 92, pp.127-132, 2003.

[Bro07] T.R. Brosten, J.M. Park, A.T. Evans, K. Rasmussen, G.F. Nellis, S.A. Klein, J.R. Feller, L. Salerno, and Y.B. Gianchandani, "A Numerical Flow Model and Experimental Reslts of a Cryogenic Micro-Valve for Distributed Cooling Applications," *Cryogenics*, vol.47, no.9-10, pp.501-9, 2007

[Buf26] R.M. Buffington and W.M. Latimer, "Coefficients of Expansion at Low Temperatures and Thermodynamic Applications of Expansion Data," *Journal of the American Chemical Society*, vol.48, pp.2305-19, 1926

[Bur98] M.A. Burns, B.N. Johnson, S.N. Brahmasandra, K. Handique, J.R. Webster, M. Krishnam, T.S. Sammarco, P.M. Man, D. Jones, D. Heldsinger, C.H. Mastrangelo, and D.T. Burke, "An Integrated Nanoliter DNA Analysis Device," *Science*, vol. 282, no. 5388, pp. 484-487, 1998.

[Car07] M. Carmichael, “The Changing Science of Pain,” *Newsweek,* pp. 40-47, June 4, 2007.

[Cha00] I. Chakraborty, W. C. Tang, D. P. Bame, and T. K. Tang, "MEMS Micro-valve for Space Application," *Sensors and Actuators*, vol. 83, pp. 188-193, 2000.

[Cod03] Codman, “CODMAN® Model 3000 Series Constant Flow Implantable Pump with Bolus Safety Valve”, Product Brochure, 2003.

[Coo91] D.W. Coombs and N. Fine, “Spinal anesthesia using subcutaneously implanted pumps for intrathecal drug infusion”, *Anesth Analg*, Vol. 73, No. 2, pp. 226-231, 1991.

[Coo04] C.G. Cooney and B.C. Towe, “A thermopneumatic dispensing micropump,” *Sensors and Actuators*, Vol.116, No.3, pp.519-524, 2004

[Cra80] J.S. Crawford, “Site of action of intrathecal morphine”, *Br Med J*, Vol. 281, No. 6248, pp. 1144, 1980.

[Deer02] T.R. Deer, et al., “Clinical experience with intrathecal bupivacaine in combination with opioid for the treatment of chronic pain related to failed back surgery syndrome and metastatic cancer pain of the spine”, *Spine J*, Vol. 2, No. 4, pp. 274-278., 2002.

[Deer04] T. Deer, et al., “intrathecal drug delivery for treatment of chronic low back pain: report from the National Outcomes Registry for Low Back Pain”, *Pain Med*, Vol. 5 No. 1, pp. 6-13, 2004.

[Dia08] DiabetesNet.com, “Diabetes pump comparison chart”, Available online at www.diabetesnet.com/diabetes_technology/insulin_pump_models.php, Accessed October 9, 2008.

[Dub01] P. Dubois, B. Guldimann, M. A. Gretillat, and N. F. d. Rooij, "Electrostatically actuated gas microvalve based on a Ta-Si-N membrane," *14th IEEE International Conference on Micro Electro Mechanical Systems*, pp. 535-8, 2001.

[Dub01-2] P. Dubois, B. Guldimann, and N. F. d. Rooij, "High-speed electrostatic gas microvalve switching behavior," *Proceedings of the SPIE - The International Society for Optical Engineering*, vol. 4560, pp. 217-26, 2001.

[Eth05] K.D. Ethans, O.I. Schryvers, P.W. Nance and A.R. Casey, “intrathecal drug therapy using the Codman Model 3000 Constant Flow Implantable Infusion Pumps: experience with 17 cases”, *Spinal Cord*, Vol. 43, pp. 214-218, 2005.

[Erd06] S. Erdine and J. De Andres, “Drug delivery systems”, *Pain Practi*ce, Vol. 6, No.1, pp. 51-57., 2006.

[Esa89] M. Esashi, S. Shoji, and A. Nakano, "Normally Closed Microvalve and Micropump Fabricated on a Silicon Wafer," *Sensors and Actuators*, vol. 20, pp. 163-9, 1989.

[Esa90] M. Esashi, "Integrated Micro Flow Control Systems," *Sensors and Actuators, A: Physical*, vol. A21, n. 1-3, pp. 161-7, 1990.

[Eva07] A.T. Evans, J.M. Park, G.F. Nellis, S.A. Klein, J. Feller, L. Salerno, and Y. B. Gianchandani, “A Low Power, Microvalve-Regulated Drug Delivery System Using a Si Micro-Spring Pressurized Balloon Reservoir”, *IEEE Intl. Conf. on Solid-State Sensors and Actuators (Transducers)*, Lyon, Paris, pp. 359-63, June 2007.

[Eva08] A.T. Evans, J.M. Park, S. Chiravuri, and Y.B. Gianchandani, “Dual drug delivery device for chronic pain management using micromachined elastic metal structures and silicon microvalves”, *Micro Electro Mechanical Systems*, pp. 252-255, 2008.

[Fas99] V. Fascio, R. Wuthrich, D. Viquerat, and H. Langen, "3D Microstructuring of Glass Using Electrochemical Discharge Machining (ECDM)," *International Symposium on Micromechatronics and Human Science*, Nagoya, Japan, Nov. '99, pp.179-83, 1999.

[FDA08] “Insulin” Available online at http://www.fda.gov/Diabetes/insulin.html, Accessed October 08, 2008

[Gra01] T.S. Grabow, D. Derdzinski, and P.S. Staats, “Spinal drug delivery”, *Current Pain Headache Rep*, Vol. 5, No. 6, pp. 510-516, 2001.

[Gra03] A. Grayson, I. Choi, B. Tyler, P. Wang, H. Brem, M.J. Cima, and R. Langer, "Multi-pulse drug delivery from a resorbable polymeric microchip device", *Nature Materials,* Vol. 2, pp. 767-772, 2003.

[Ger02] M. Gerard, A. Chaubey, B. D. Malhotra, “Application of conducting polymers to biosensors, Biosensors and Bioelectronics,” *Biosensors and Bioelectronics,* vol. 17(5), pp. 345-359, May 2002

[Gol97] C. Goll, W. Bacher, B. Bustgens, D. Maas, R. Ruprecht, and W. K. Schomburg, "An electrostatically actuated polymer microvalve equipped with a movable membrane electrode," *Journal of Micromechanics and Microengineering*, vol. 7, n. 3, pp. 224-6, 1997.

[Han08] S. Hanson, B. Zhai, M. Seok, B. Cline, K. Zhou, M. Singhal, M. Minuth, J. Olson, L. Nazhandali, T. Austin, D. Sylvester, and D. Blaauw, “Exploring variability and performance in a sub-200mV processor,” *IEEE Journal of Solid-State Circuits*, pp. 881-891, April 2008.

[Has00] S.J. Hassenbusch and R.K. Portenoy, “Current practices in intraspinal therapy--a survey of clinical trends and decision making”, *J. Pain Symptom Manage*ment, Vol. 20, No. 2, pp. S4-11, 2000.

[Has04] S.J. Hassenbusch, et al., “Polyanalgesic Consensus Conference 2003: an update on the management of pain by intraspinal drug delivery-- report of an expert panel”, *J. Pain Symptom Manage*, Vol. 27 No. 6, pp. 540-563, 2004.

[Hea08] Health A to Z, “Cerebrospinal fluid (CSF) analysis”, Available online at www.healthatoz.com Last accessed October 9, 2008.

[Hir97] M. Hirano, K. Yanagisawa, H. Kuwano, and S. Nakano, "Microvalve with Ultra-Low Leakage," *Proceedings IEEE. The Tenth Annual International Workshop on Micro Electro Mechanical Systems. An Investigation of Micro Structures, Sensors, Actuators, Machines and Robots*, pp. 323-6, 1997.

[Hon04] S. Hong, et al., "Development of an Implantable intrathecal Drug Infusion Pump," *Engineering in Medicine and Biology Society, 2004. IEMBS '04. 26th Annual International Conference of the IEEE* , vol.2, no., pp. 3440-3442, 1-5 Sept. 2004

[Huf90] M. A. Huff, M. S. Mettner, T. A. Lober, and M. A. Schmidt, "A pressure-balanced electrostatically-actuated microvalve," *IEEE Solid-State Sensor and Actuator Workshop*, pp. 123-7, 1990.

[Huf93] M. A. Huff, J. R. Gilbert, and M. A. Schmidt, "Flow characteristics of a pressure-balanced microvalve," *The 7th International Conference on Solid-State Sensors and Actuators (Transducers '93)*, pp. 98-101, 1993.

[Huh70] C. Huh and L.E. Scriven, “Hydrodynamic model of steady movement of a solid/liquid/fluid contact line,” *Journal of Colloid and Interface Science,* vol 35, no. 1, pp. 85-101, 1970.

[Ike97] T. Ikehara, H. Yamagishi, and K. Ikeda, "Electromagnetically driven silicon microvalve for large-flow pneumatic controls," *Proceedings of the SPIE - The International Society for Optical Engineering*, vol. 3242, pp. 136-44, 1997.

[Jeo08] O.C. Jeong and S. Konishi, “Pneumatic gas regulator with cascaded PDMS seal valves,” *Sensors and Actuators A: Physical*, vol. 143, no. 1, pp. 84-89, 2008.

[Jer94] H. Jerman, "Electrically activated normally closed diaphragm valves," *Journal of Micromechanics and Microengineering*, vol. 4, n. 4, pp. 210-16, 1994.

[JCT99] "New standards to assess and manage pain" *Jt Comm Perspect*, Vol. 19 No. 5, pp. 5, 1999.

[Kan82] Y. Kanda, "Graphical Represenstation of the Piezoresistance Coefficients in Silicon," *IEEE Transactions on Electron Devices*, vol.ED-29, no.1, pp.64-70, 1982

[Kim83] S.-C. Kim and K.D. Wise, "Temperature Sensitivity in Silicon Piezoresistive Pressure Transducers," *IEEE Transactions on Electron Devices*, vol.ED-30, no.7, pp.802-10, 1983

[Kim05] H. Kim and K. Najafi, "Characterization of Parylene-assisted wafer bonding: Long-term stability and influence of process chemicals," in *The 13th International Conference on Solid-State Sensors, Actuators and Microsystems*, 2005, pp. 2015-2018

[Kle02] S.A. Klein, "Engineering Equation Solver," The University of Wisconsin - Madison, 2002, http://sel.me.wisc.edu/ees/new_ees.html

[Koh99] M. Kohl, D. Dittmann, E. Quandt, B. Winzek, S. Miyazaki, and D. M. Allen, "Shape memory microvalves based on thin films or rolled sheets," *Materials Science & Engineering A (Structural Materials: Properties, Microstructure and Processing)*, vol. A273-275, pp. 784-8, 1999.

[Koh99-2] M. Kohl, K. D. Skrobanek, and S. Miyazaki, "Development of stress-optimised shape memory microvalves," *Sensors and Actuators, A: Physical*, vol. A72, n. 3, pp. 243-50, 1999.

[Koh00] M. Kohl, D. Dittmann, E. Quandt, and B. Winzek, "Thin film shape memory microvalves with adjustable operation temperature," *Sensors and Actuators, A: Physical*, vol. A83, n. 1-3, pp. 214-19, 2000.

[Kra97] E.S. Krames, and K. Olson, *Clinical realities and economic considerations: patient selection in intrathecal therapy*. J Pain Symptom Manage, Vol. 14**,** No. 3, pp. S3-13, 1997.

[Kra99] E.S. Krames, "Practical issues when using neuraxial infusion", *Oncology (Williston Park)*, Vol. 13, No. 5 Supplement 2, pp. 37-44, 1999.

[Kun04] P.K. Kundu and I.M. Cohen, Fluid Mechanics (third ed.), Elsevier, Oxford (2004).

[Lan76] R. Langer and J. Folkman, "Polymers for the sustained release of proteins and other macromolecules", *Nature,* Vol. 263, pp. 797-800, 1976.

[Lan90] R. Langer, "New Methods of Drug Delivery," *Science*, vol.249, pp.1527-1533, 1990

[Las04] D.J. Laser and J.G. Santiago, "A review of micropumps," *J. Micromech. Microeng.*, vol. 14, no. 6, pp. R35-R64, 2004.

[Lee04] C. Lee and E. H. Yang, "A Piezoelectric Liquid-Compatible Microvalve for Integrated Micropropulsion," in *Technical Digest of the 2004 Solid-State Sensor and Actuator Workshop*. Hilton Head Isl., SC, pp. 160-163. 2004.

[Lee06] C. Lee, E. H. Yang, S. M. Saeidi, and J. M. Khodadadi, "Fabrication, characterization, and computational modeling of a piezoelectrically actuated microvalve for liquid flow control," *Journal of Microelectromechanical Systems*, vol. 15, n. 3, pp. 686-96, 2006.

[Li04] H. Q. Li, D. C. R. J. L. Steyn, K. T. Turner, O. Yaglioglu, N. W. Hagood, S. M. Spearing, and M. A. Schmidt, "Fabrication of a high frequency piezoelectric microvalve," *Sensors and Actuators, A: Physical*, vol. A111, n. 1, pp. 51-6, 2004.

[Lik06] R. Likar, et al., "Importance of intrathecal pain therapy", *Schmerz*, 2006.

[Lo08] R. Lo, et al., "A refillable microfabricated drug delivery device for treatment of ocular diseases," *Lab on a chip*, Vol.8, No. 7, pp. 1027-1030, 2008.

[Lob07] E.B. Lobato, N. Gravenstein, R.R. Kirby, *Complications in Anesthesiology*, Lippincott Williams & Wilkins, 2007, pp. 732.

[Mal05] J. Maloney, et al., "Electrothermally activated microchips for implantable drug delivery and biosensing", *J. Controlled Release,* Vol. 109, pp. 211-219, 2005.

[Med06] Medtronic, "SynchroMed® II Implantable Infusion Pump (Models 8637-20 and 8637-40) Missing Propellant Physician Letter – Enclosure", Accessed online at www.medtronic.com/neuro/spasticity/itbtherapy/downloads/Propellant_Enclosure_detail_explanation.pdf, last accessed on October 9, 2008.

[Med08] "Medtronic Sychromed II Pump" Available online at www.medtronic.com/your-health/multiple-sclerosis/device/our-baclofen pump/synchromed-ii-pump/index.htm. Accessed October 08, 2008

[Mer01] S. Mercadante and R.K. Portenoy, "Opioid poorly-responsive cancer pain. Part 2: basic mechanisms that could shift dose response for analgesia", *J Pain Symptom Manage*, Vol. 21, No. 3, pp. 255-264, 2001.

[Mer03] S. Mercadante, et al., "Hyperalgesia: an emerging iatrogenic syndrome", *J Pain Symptom Manage*, Vol. 26, No. 2, pp. 769-775, 2003.

[Mes98] S. Messner, M. Muller, V. Burger, J. Schaible, H. Sandmaier, and R. Zengerle, "A normally-closed, bimetallically actuated 3-way microvalve for pneumatic applications," *Eleventh Annual International Workshop on Micro Electro Mechanical Systems. An Investigation of Micro Structures, Sensors, Actuators, Machines and Systems*, pp. 40-4, 1998.

[Mic08] Available online at http://www.mchips.com/, Accessed October 08, 2008.

[Mor92] S. L. Morris, P. F. Jaques, and M. A. Mauro, "Radiology-assisted placement of implantable subcutaneous infusion ports for long-term venous access," *Radiology*, vol. 184(1), pp. 149-151, July 1992

[Nay93] M.M. Nayak, N. Gunasekaran, A.E. Muthunayagam, K. Rajanna, S. Mohan, "Diaphragm-Type Sputtered Platinum Thin Film Strain Gauge Pressure Transducer," *Measurement Science & Technology*, vol.4, no.12, pp.1319-1322, 1993

[Oh06] K.W. Oh and C.H. Ahn, "A review of microvalves," *J. Micromechanics Microengineering,* vol.16, pp. R13–R39, 2006.

[Ohn90] T. Ohnstein, T. Fukinura, J. Ridley, and U. Bonne, "Micromachined silicon microvalve," *IEEE Micro Electro Mechanical Systems-An Investigation of Micro Structures, Sensors, Actuators, Machines*, pp. 95-8, 1990.

[Pai96] J.A. Paice, R.D. Penn, and S. Shott, "Intraspinal morphine for chronic pain: a retrospective, multicenter study," *J Pain Symptom Manage*, Vol. 11, No. 2, pp. 71-80, 1996.

[Par07] J.M. Park, T.R. Brosten, A.T. Evans, K. Rasmussen, G.F. Nellis, S.A. Klein, J. Feller, L. Salerno, and Y.B. Gianchandani, "A Piezoelectric Microvalve with Integrated Sensors for Cryogenic Applications", *IEEE/ASME International Conference of Micro Electro Mechanical Systems*, pp. 647-650, 2007.

[Par08] J.M Park, R.P. Taylor, A.T. Evans, T.R. Brosten, G.F. Nellis, S.A. Klein, J.R. Feller, L. Salerno, and Y.B. Gianchandani, "A Piezoelectric Microvalve for

Cryogenic Applications," *IOP Journal for Micromechanics and Microengineering*, vol. 18, no. 1, pp. 15-23, 2008.

[Par09] J.M. Park, A.T. Evans, K. Rasmussen, T.R. Brosten, G.F. Nellis, S.A. Klein, and Y.B. Gianchandani, "A Microvalve with Integrated Sensors and Customizable Normal State for Low Temperature Operation," *IEEE/ASME J. Microelectromechanical Systems,* vol. 18, no. 4, pp. 868-879, 2009.

[Phi03]. C.J. Phillips, "Pain management: health economics and quality of life considerations." *Drugs*. Vol. 63 No 2, pp. 47-50. 2003

[PoC08] Population Council, "Jadelle General Information" Available online at http://www.popcouncil.org/biomed/jadellefaqgeninfo.html, Accessed October 08, 2008.

[Pot05] J. A. Potkay and K. D. Wise, "An electrostatically latching thermopneumatic microvalve with closed-loop position sensing," *18th IEEE International Conference on Micro Electro Mechanical Systems*, pp. 415-18, 2005.

[Rai07] N.G. Rainov, and V. Heidecke, "Management of chronic back and leg pain by intrathecal drug delivery", *Acta Neurochir Suppl*, Vol. 97, Pt. 1, pp. 49-56, 2007.

[Rau03] R.L. Rauck, et al., "Long-term intrathecal opioid therapy with a patient-activated, implanted delivery system for the treatment of refractory cancer pain", *J. Pain*, Vol. 4, No. 8, pp. 441-447, 2003.

[Rey96] D. Reynaerts, J. Peirs, and H. Van Brussel, "A SMA-Actuated Implantable System for Delivery of Liquid Drugs," in *Proceedings of the Fifth International Conference on New Actuators*, 1996, pp. 379-382

[Ric03] C. A. Rich and K. D. Wise, "A high-flow thermopneumatic microvalve with improved efficiency and integrated state sensing," *Journal of Microelectromechanical Systems*, vol. 12, n. 2, pp. 201-8, 2003.

[Ric08] M. T. Richardson, and Y. B. Gianchandani, "Achieving precision in high density batch mode micro-electro-discharge-machining," *Journal of Micromechanics and Microengineering,* 12 pp, Jan. 2008.

[Rob94] J. K. Robertson and K. D. Wise, "A nested electrostatically-actuated microvalve for an integrated microflow controller," *Micro Electro Mechanical Systems. An Investigation of Micro Structures, Sensors, Actuators, Machines and Robotic Systems*, pp. 7-12, 1994.

[Rob98] J. K. Robertson and K. D. Wise, "A Low Pressure Micromachined Flow Modulator," *Sensors and Actuators A*, vol. 71, n. 1-2, pp. 98-106, 1998.

[Rob03] D. C. Roberts, L. Hanqing, J. L. Steyn, O. Yaglioglu, S. M. Spearing, M. A. Schmidt, and N. W. Hagood, "A piezoelectric microvalve for compact high-frequency, high-differential pressure hydraulic micropumping systems," *Journal of Microelectromechanical Systems*, vol. 12, n. 1, pp. 81-92, 2003.

[Rog04] T. Rogge, Z. Rummler, and W. K. Schomburg, "Polymer micro valve with a hydraulic piezo-drive fabricated by the AMANDA process," *Sensors and Actuators, A: Physical*, vol. A110, n. 1-3, pp. 206-12, 2004.

[Rum03] C. Fu, Z. Rummler, and W. Schomburg, "Magnetically driven micro ball valves fabricated by multilayer adhesive film bonding," *Journal of Micromechanics and Microengineering*, vol. 13, n. 4, pp. S96-102, 2003.

[Sad98] D. J. Sadler, T. M. Liakopoulos, J. Cropp, C. H. Ahn, and H. T. Henderson, "Prototype microvalve using a new magnetic microactuator," *Proceedings of the SPIE - The International Society for Optical Engineering*, vol. 3515, pp. 46-52, 1998.

[Sak05] T. Sakurada, T. Komatsu, and S. Sakurada, "Mechanisms of nociception evoked by intrathecal high-dose morphine", *Neurotoxicology*, Vol. 26, No. 5, pp. 801-809., 2005.

[San99] J.T. Santini, M.J. Cima, and R. Langer, "A controlled-release microchip", *Nature,* Vol. 397, pp. 335-338, 1999.

[Sat94] K. Sato and M. Shikida, "An electrostatically actuated gas valve with an S-shaped film element," *Journal of Micromechanics and Microengineering*, vol. 4, n. 4, pp. 205-9, 1994.

[Sau94] K. Sauter, et al., "Treatment of high-dose intrathecal morphine overdose. Case report," *J. Neurosurg,* Vol. 81, No. 1, pp. 143-146, 1994.

[Sch99] M. Scherge, X. Li, and J.A. Schaefer, "The effect of water on friction of MEMS," *Tribol. Lett.*, vol. 6, no. 3-4, pp. 215–220, 1999.

[Sch06] S.A. Schug, et al., "Neuraxial drug administration: a review of treatment options for anaesthesia and analgesia," *CNS Drugs*, Vol. 20 No. 11, pp. 917-933, 2006.

[Sha04] P. Shao, Z. Rummler, and W. K. Schomburg, "Polymer micro piezo valve with a small dead volume," *Journal of Micromechanics and Microengineering*, vol. 14, n. 12, pp. 305-9, 2004.

[Shi94] M. Shikida, K. Sato, S. Tanaka, Y. Kawamura, and Y. Fujisaki, "Electrostatically driven gas valve with high conductance," *Journal of Microelectromechanical Systems*, vol. 3, n. 2, pp. 76-80, 1994.

[Shi97] Y. Shinozawa, T. Abe, and T. Kondo, "A proportional microvalve using a bi-stable magnetic actuator," *Proceedings IEEE. The Tenth Annual International Workshop on Micro Electro Mechanical Systems. An Investigation of Micro Structures, Sensors, Actuators, Machines and Robots*, pp. 233-7, 1997.

[Sho91] S. Shoji, B. Schoot, N. Rooij, and M. Esashi, "Smallest Dead Volume Microvalves for Integrated Chemical Analyzing Systems," *International Conference on Solid-State Sensors and Actuators (Transducers)*, pp. 1052-5, 1991.

[Skr97] K. D. Skrobanek, M. Kohl, and S. Miyazaki, "Stress-optimized shape memory microvalves," *Proceedings of the IEEE Micro Electro Mechanical Systems (MEMS)*, pp. 256-61, 1997.

[Smi90] R. L. Smith, R. W. Bower, and S. D. Collins, "The design and fabrication of a magnetically actuated micromachined flow valve," *Sensors and Actuators A: Physical*, vol. 24, n. 1, pp. 47-53, 1990.

[Smi07] S. Smith, et al., "Development of a miniaturised drug delivery system with wireless power transfer and communication," *IET Nanobiotechnol.*, Vol.1, No. 5, pp. 80-86, 2007.

[Sor01] M. L. Soria, J. Chacon, J. C. Hernandez, "Metal hydride electrodes and Ni/MH batteries for automotive high power applications," *Journal of Power Sources*, vol. 102(1-2), pp. 97-104, Dec. 2001

[Str86] S. Strum, J. McDermed, A. Korn and C. Joseph, "Improved methods for venous access: the Port-A-Cath, a totally implanted catheter system," *Journal of Clinical Oncology*, vol. 4, pp. 596-603, 1986

[Sut06] J. Sutanto, P. J. Hesketh, and Y. H. Berthelot, "Design, microfabrication and testing of a CMOS compatible bistable electromagnetic microvalve with latching/unlatching mechanism on a single wafer," *Journal of Micromechanics and Microengineering*, vol. 16, n. 2, pp. 266-75, 2006.

[Taj02] R. Tajima, K. Satoshi, M. Inaba, and H. Inoue, "Development of soft and distributed tactile sensors and the application to a humanoid robot," *Advanced Robotics,* vol. 16(4), pp. 381-397, 2002.

[Tak02] K. Takahata, and Y. B. Gianchandani, "Batch Mode Micro-Electro-Discharge Machining," *IEEE/ASME Journal of Microelectromechanical Systems*, vol. 11(2), pp. 102-110, 2002.

[Tak05] H. Takao, K. Miyamura, H. Ebi, M. Ashiki, K. Sawada, and M. Ishida, "A MEMS microvalve with PDMS diaphragm and two-chamber configuration of

thermo-pneumatic actuator for integrated blood test system on silicon," *Sensors and Actuators A: Physical*, vol. 119, n. 2, pp. 468-75, 2005.

[Tay06] H.K. Taylor, H. Sun, T.F. Hill, A. Farahanchi, and D.S. Boning, "Characterizing and Predicting Spatial Nonuniformity in the Deep Reactive Ion Etching of Silicon," *Journal of the Electrochemical Society*, vol. 153, no. 8, pp. C575-85, 2006

[Ter79] S. C. Terry, J. H. Jerman, and J. B. Angell, "A Gas Chromatographic Air Analyzer Fabricated on a Silicon Wafer," *IEEE Transactions on Electron Devices*, vol. ED-26, n. 12, pp. 1880-6, 1979.

[Tur07] J.A. Turner, J.M. Sears, and J.D. Loeser, "Programmable intrathecal opioid delivery systems for chronic noncancer pain: a systematic review of effectiveness and complications", *Clin J Pain*, Vol. 23, No. 2, pp. 180-195, 2007

[Vip07] R. Vipul, "Vipul's lifetime lifeline permanent pacemaker and implantable cardioverter-defibrillator," U. S. Patent 7,239,917, Jul. 3, 2007.

[War88] K. Warnaka and L. Pochop, "Analyses of equations for free water evaporation estimates," *Water Resour. Res.,* vol. 24, no. 7, pp 979-984, 1988.

[Wat97] T. Watanabe and H. Kuwano, "A microvalve matrix using piezoelectric actuators," *Microsystem Technologies*, vol. 3, n. 3, pp. 107-11, 1997.

[Wer05] D.P. Wermeling, "Ziconotide, an intrathecally administered N-type calcium channel antagonist for the treatment of chronic pain", *Pharmacotherapy*, Vol. 25 No. 8, pp. 1084-1094, 2005.

[Wij02] W. v. d. Wijngaart, H. Ask, P. Enoksson, and G. Stemme, "A high-stroke, high-pressure electrostatic actuator for valve applications," *Sensors and Actuators, A: Physical*, vol. 100, n. 2-3, pp. 264-71, 2002.

[Win96] M. Winkelmuller and W. Winkelmuller, "Long-term effects of continuous intrathecal opioid treatment in chronic pain of nonmalignant etiology", *J Neurosurg*, Vol. 85 No. 3, p. 458-467. 1996

[Won07] R. WonHyoung, et al., " Biodegradable micro-osmotic pump for long-term and controlled release of basic fibroblast growth factor", J. Controlled Release, Vol. 124, No. 4, pp. 98-100, 2007

[Yan95] K. Yanagisawa, H. Kuwano, and A. Tago, "Electromagetically driven microvalve," *Microsystem Technologies*, vol. 2, n. 1, pp. 22-5, 1995.

[Yan99] X. Yang, C. Groasjean and Y.C. Tai, “Design, fabrication and testing of micromachined silicone rubber membrane valves,” *IEEE/ASME J. of Microelectromechanical Systems (J. MEMS)*, vol. 8, no. 4, pp.393-402, 1999.

[Yan04] X. Yang, A. Holke, S. A. Jacobson, J. H. Lang, M. A. Schmidt, and S. D. Umans, "An electrostatic, on/off microvalve designed for gas fuel delivery for the MIT microengine," *Journal of Microelectromechanical Systems*, vol. 13, n. 4, pp. 660-8, 2004.

[Yan04-2] E. H. Yang, C. Lee, J. Mueller, and T. George, "Leak-tight piezoelectric microvalve for high-pressure gas micropropulsion," *Journal of Microelectromechanical Systems*, vol. 13, n. 5, pp. 799-807, 2004.

[Yea01] C.J. Yeager, “A Review of Cryogenic Thermometry and Common Temperature Sensors,” *IEEE Sensors Journal*, vol.1, no.4, pp.352-60, 2001

[Yob01] L. Yobas, M. A. Huff, F. J. Lisy, and D. M. Durand, "A novel bulk micromachined electrostatic microvalve with a curved-compliant structure applicable for a pneumatic tactile display," *Journal of Microelectromechanical Systems*, vol. 10, n. 2, pp. 187-96, 2001.

[Yob03] L. Yobas, D. M. Durand, G. G. Skebe, F. J. Lisy, and M. A. Huff, "A novel integrable microvalve for refreshable Braille display system," *Journal of Microelectromechanical Systems*, vol. 12, n. 3, pp. 252-63, 2003.

[Zde87] M. J. Zdeblick and J. B. Angell, "A microminiature electric-to-fluidic valve," *The 4th International Conference on Solid-State Sensors and Actuators (Transducers '87)*, pp. 437-39, 1987.

[Zha01] B. Zhao, J.S.Moore, and D.J. Beebe, “Surface-Directed Liquid Flow Inside Microchannels,” *Science*, vol. 291, no.5506, pp. 1023-1026, 2001.

[Zhe00] A.P. Zhernov, “Lattice Constant and Coefficient of Linear Thermal Expansion of the Silicon Crystal. Influence of Isotopic Composition,” *Low Temperature Physics*, vol.26, no.12, pp.908-915, 2000

[Zhu09] W. Zhu, M.J. White, G.F. Nellis, S.A. Klein, Y.B. Gianchandani, “A Si/Glass Bulk Micromachined Cryogenic Heat Exchanger for High Heat Loads: Fabrication, Test and Application Results,” *IEEE/ASME J. Microelectromechanical Systems*, in press, Apr. 2009